The optical polarization of M82 and the local spiral arm

Axon, D. J.

THE OPTICAL POLARIZATION OF M82 AND THE LOCAL SPIRAL ARM

BY

D. J. AXON B.Sc.

A THESIS SUBMITTED TO THE UNIVERSITY OF DURHAM FOR THE DEGREE OF DOCTOR OF PHILOSOPHY

August 1977

TO MY PARENTS

PREFACE

The work described in this thesis was carried out during the period 1973-1976 while the author was a research student under the supervision of Dr S. M. Scarrott in the Astronomy Group of the Physics Department, University of Durham.

The analysis of the structure of the local galactic magnetic field was carried out in collaboration with Dr R. S. Ellis. The methods used were developed and applied jointly and the interpretation of the results is a hybrid of our ideas. The reduction and collation of the data for the polarization catalogue was begun by the author.

The idea of investigating the spatial variations of the polarization in extragalactic systems was stimulated by this work. The project became a reality following a series of informal discussions with my supervisor and Dr R. G. Bingham of the Royal Greenwich Observatory, which led to the collaborative design of the Durham Nebula Polarimeter. The observations of M82 made with this instrument were obtained on the 36" Yapp telescope at the RGO by the author. An electronographic camera designed by Dr D. McMullan of the RGO was used as the polarimeter's detection system.

The digital procedures used to analyze the polarization results are based on the ideas of the author and his supervisor, but the approach described here follows the author's bias on the subject. All the computer programmes used in the analysis were written by the author with the exception of a "clear plate and sky subtraction" routine, written by Dr Stuart Pallister, the use of which is gratefully acknowledged.

All the other work presented in the thesis is the original work of the author except where explicitly cited in the text.

ABSTRACT

This thesis comprises two separate but related topics in the study of optical polarization of galaxies. In part I we investigate interstellar polarization within 2 kpc of the sun and attempt to quantify the local structure of the galactic magnetic field. In part II we report the results of polarization measurements of the peculiar galaxy M82, obtained using a new polarimeter and digital reduction techniques, and discuss models of the origin of the polarization.

Measurements of the linear polarization of starlight have been collated into a catalogue containing the Stokes' parameters in galactic coordinates for those stars for which reliable distances could be determined. The catalogue is presented in the form of vector maps on the sky in several distance intervals.

Assuming a magnetic alignment hypothesis we have investigated the direction and form of the galactic magnetic field through e-vector plots and from the periodicity of the Stokes' parameters $Q(l)$ and $U(l)$ with galactic longitude. The results show the existence of a longitudinal field directed towards $l = 45^{o} \pm 10^{o}$ within 500 pc, and beyond this there is much confusion with a possible change in direction, associated with the bifurcation of the spiral arm, to $l = 74^{o} \pm 10^{o}$. There is no evidence for a field directed towards $l = 90^{o}$. It is clear however that a simple longitudinal model of the field is rather naive. The $U(l)$ plots show strong evidence for an inclination of the field by 15^{o} to the plane, and this is not associated with a helical structure. The possible significance of this conclusion to the origin of the field is discussed.

Incremental polarization maps have been produced but show little correlation with the spiral structure of the galaxy. There is strong evidence for irregularities in the field. The polarization appears to saturate in all directions at about 1 kpc from the sun. We interpret this as an

observational selection effect. The major part of this work is directed towards studying the importance of irregularities in the field structure. Autocorrelation techniques have been used and unlike previous authors we can find no coherence in this component on scales greater than 50 pc.

In the second part of the thesis we describe an imaging polarimeter constructed for use with a McMullan electronographic camera and designed to operate at an f/15 focus. This is the first polarimeter to use electronographic detection and the principles, construction and method of operation are described. The instrument is intended for observations of galaxies and other nebulae to diameters of up to 8 minutes of arc and has been successfully used to observe the irregular galaxy M82 in the B-band. The results of these observations are reported in this thesis. The polarimeter enables the simultaneous measurement of the linear polarization at more than 1500 locations in a 40 mm field of view to be made. This information is obtained in a series of eight exposures, which enables the effect of cathode sensitivity variations to be removed. The method is independent of variations in background sky brightness and polarization, and in atmospheric transparency. A review of the existing designs of polarimeter, their advantages and disadvantages and the possible sources of systematic errors are discussed. The optical system is also suitable for use with two-dimensional digital detectors but so far none have been used with the instrument.

In order to take full advantage of the vast amount of information contained on each electronograph an entirely new digital analysis technique has been developed. Attempts have been made to locate features such as stars, grid overlaps, scratches and dirt blobs automatically using a random search technique. This proved unsatisfactory, and possible explanations and refinement in the approach are outlined. A simple contour method is shown to be a satisfactory means of carrying out the feature extraction with manual assistance. A highly accurate image registration method capable of producing

a picture to picture registration better than 2μ is developed and the method takes into account small scale flaws, saturation effects, cathode sensitivity variations and differing exposure times. The technique is vastly superior to conventional methods of plate analysis and future refinements are discussed. The performance of the instrument in the laboratory and at the telescope is reported, the existence of severe instrumental effects established, and corrections derived and applied to the polarization data. Their eradication from the instrument is described and results of calibration measurements of standard stars with the improved optics presented, showing the instrument is capable of reaching a precision of ±0.5% in p and ± 3^{o} in θ. The results of polarization measurements of M82 are presented and compared with previous observations. These results have a spatial resolution of between 5 and 8 times that of previous observations, are 20 times as numerous and have comparable accuracy (± 2.5% in p and ± 4^{o} in θ). These results represent the first complete mapping of the linear polarization in an extragalactic system at optical wavelengths.

A review of the existing observational material on M82 is presented and the relevance of the current observations established.

The predictions of simple scattering models for producing the observed polarization are compared with the observations and show moderate agreement. The active region of the galaxy is located and the evolutionary status and energetics of M82 are discussed. The current problems in our understanding of the galaxy and suggestions for future work are detailed.

CONTENTS

	Page
Introduction	1
Chapter 1 THE QUANTITATIVE DESCRIPTION OF POLARISED LIGHT	7
1.1 The States of Polarization	7
1.2 The Stokes Parameters	9
PART 1: THE LOCAL SPIRAL ARM	
Chapter 2 STELLAR POLARIZATION AND THE LOCAL STRUCTURE OF THE GALACTIC MAGNETIC FIELD	
2.1 A critique of the methods of Measuring the Galactic Magnetic Field	14
2.2 The conflict over the Direction of the Galactic Magnetic Field, and the possible existence of irregularities	19
2.3 The Optical polarization Data	25
2.4 E-vector Plots of the Starlight	36
2.5 Variations of the Stokes Parameters with Galactic Longitude	40
2.6 Incremental Polarization; The Magnetic Field and the Spiral Arms	44
2.7 Irregularities in the Magnetic Field: A correlation analysis	49
2.8 Discussion and Conclusions	57
PART 2: M82	
Chapter 3 THE NEBULA POLARIMETER	
3.1 The Designs and Techniques Used in Polarimetry	69
3.1.1 Photographic polarimeters	69
3.1.2 Photoelectric polarimeters	70
3.2 The Nebula Polarimeter	73
3.2.1 The Optical System	74
3.2.2 The Mechanical Construction of the Polarimeter	79

Page

3.2.3 The Electronographic Camera

3.3 The Theory of the Polarimeter 85

3.4 Discussion of Systematic Errors 89

3.4.1 The Problem of Foreground Illumination

3.4.2 Errors Introduced by the Telescope 90

3.4.3 Errors Intrinsic to the Polarimeter 93

3.5 The Observing Procedure 95

3.6 The Observations 97

Chapter 4 THE DIGITAL ANALYSIS OF POLARIZATION

4.1 The problems Associated with Analogue Reduction Techniques 105

4.2 The production of a Digital Picture 111

4.3 Feature Extraction 115

4.4 The Method of Image Registration 119

4.5 Seeing-disc cells: The Subtraction of the clear plate background 128

4.6 The f-factors, e-factors and Stokes parameters 130

4.7 The Subtraction of the Sky background 133

Chapter 5 POLARIZATION RESULTS AND CORRECTIONS

5.1 Laboratory Measurements 138

5.1.1 The Polarimeter Transmission Characteristics 139

5.1.2 The angular divergence and polarizing efficiency of the Wollaston prism 139

5.1.3 The Behaviour of the Chromatic $\lambda/2$-plate 139

5.1.4 Corrections for Instrumental Vignetting 152

5.2 Calibration Measurements at the telescope 154

5.2.1 Observations of Standard Stars

Page

5.2.2 Cloth Measurements 159

5.3 The M82 Polarization Results 162

5.3.1 Polarization error analysis: A comparison with previous observations 165

Chapter 6 OBSERVATIONAL PROPERTIES OF THE GALAXY M82

6.1 Optical Polarization of M82; the Historical Development 179

6.2 Failure of the Synchrotron Hypothesis 181

6.2.1 The Radio Spectrum

6.2.2 Optical polarization measurements in the outer Filaments and the Polarization of the Hα emission line 183

6.3 The Electron Scattering Model 186

6.4 Dust Scattering 189

Chapter 7 THE POLARIZATION STRUCTURE OF M82

7.1 Introduction 198

7.2 The Centre of Symmetry of the Polarization Pattern 198

7.3 Scattering Models 203

7.4 The Central Region of M82 209

7.4.1 The Velocity Field 214

7.4.2 The evolutionary status of irr II galaxies 217

CONCLUDING REMARKS 221

APPENDIX I Theory of the Measurement of the Wave-Plate Retardance.

APPENDIX II The Solinger and Markert (1976) Model.

APPENDIX III The Geometry for Scattering Models with Line of Sight Integration.

ACKNOWLEDGEMENTS

INTRODUCTION

The methods of determining the physical conditions in a celestial object are somewhat restricted and rather difficult. Most of our information comes from studying the electromagnetic radiation (and in particular that in the visible part of the spectrum) emitted by these objects. Photometry and spectroscopy provide useful estimates of distance, kinematics, temperature and chemical composition. Valuable information can also be obtained from studies of the state of polarization of the light, as generally one expects light not to show any preference in its vibrational pattern. If the light is found to be polarized an anisotropy producing mechanism must therefore be in operation in the object.

There are several mechanisms for producing polarized light; usually, though not necessarily, they are associated with the presence of a magnetic field. If an object is known to have a magnetic field, e.g. evidence from Zeeman splitting of spectral lines, then a more detailed picture of the behaviour of this field can be obtained from polarization studies. In the absence of a magnetic field the observed polarization must be reconciled with that expected from other viable mechanisms and this will also provide valuable information on the structure and conditions in the object.

The first objects investigated for polarization effects were those in, or associated with, our own solar system. It is well over a hundred years since Arago and Mavius (1835) made the first unsuccessful search for polarization in the Solar Corona. It was not until 1908 however, that strong polarization effects were observed in sunspots by Hale, and their origin established as the Inverse Zeeman Effect.

Polarization effects were observed in the reflected light from the Moon and planets by Lyot (1929), and detailed studies of the variation of this polarization with phase of the moon, and wavelength, have subsequently been carried out by Öhman (1939), and Clarke (1969). Attempts to extend polarization measurements to more distant, and fainter objects proved to be difficult, as most polarization effects appearing in celestial light sources are small, and high sensitivity is therefore required. The measurements were further hampered by the faintness of the objects themselves, restricting the most accurate methods to the brightest sources.

Before 1946 it was generally believed that starlight was not polarized, as no anisotropy producing mechanisms were predicted. It was not until Babcock (1947) discovered the circular polarized Zeeman components of the absorption lines in spectra of peculiar A-type stars that views began to change. About the same time work on theoretical models of early-type star atmospheres (Chandresakhar 1946, Chandresakhar and Breen 1947), in which photon-free electron scattering was important, indicated that light emanating from a given point on the stellar limb might be linearly polarized by as much as 11.7%, with the "electric vector" parallel to the limb. Chandresakhar (1946) suggested that it would be possible to detect this effect in eclipsing binary pairs containing an early-type, and a late-type star, if the limb of the early-type star was observed as it was being occulted by the late-type star. While trying to verify these predictions, Hall (1949) and Hiltner (1949a, b) independently discovered that not only early-type stars, but also other stars exhibited linear polarization.

The stars which showed the largest polarization were those that also showed the largest "reddenings", thus Hall (1949) concluded that the polarization was not associated with individual stars, but was an effect caused while the light was passing through interstellar space on its way to the Earth. Hiltner (1949a, b) then suggested that the polarization was due to the selective extinction of starlight by interstellar dust particles, or "grains", the dust particles being unsymmetrical in cross-section, and systematically aligned by some force. Many mechanisms for orientating these interstellar "grains" have been suggested. Usually the aligning force is assumed to be a magnetic field embedded in the spiral arms, as suggested by Fermi and Chandresakhar (1953). The most widely invoked of these theories is due to Davis and Greenstein (1951), in which the particles, in trying to obtain the lowest rotational kinetic energy state they can, for their given angular momentum, tend to rotate about their short axes. The composition of the particles is such that paramagnetic relaxation results in these axes becoming aligned parallel to the galactic magnetic field.

This rather fortuitous discovery of interstellar polarization opened the way for considerable theoretical speculation as to the exact form of the galactic magnetic field, as indicated by the many subsequent large-scale polarization surveys. Nearly 8000 stars have now been measured for linear polarization, and in all but the strong magnetic stars, where self-polarization is important, the polarization is less than 5%.

The interpretation of these results in terms of galactic field models have proved to be unsatisfactory as ambiguous results as to its exact form have been obtained by applying different statistical techniques to the same data. Several other observational techniques are available for studying the galactic magnetic field structure and provide estimates of the field parameters which disagree markedly with those deduced from the optical polarization data.

In an attempt to resolve these many contradictions we have reinvestigated the problem, based on an analysis of the optical polarization data; and the results are presented in part I of the thesis. It is also quite possible that the galactic field, though basically regular, might well contain numerous irregularities, and we have also considered this problem in some detail. In the presence of irregularities our unfavourable observing position would then make accurate interpretations very difficult.

Probably the only way to overcome this difficulty is to observe galaxies other than our own, where we are presented with a view of light from the whole galaxy. We would then expect to be able to see the general field composition manifested in the observed polarization. The main problems with attempting such observations are the low surface brightness of such objects, and the high sensitivity required to be able to detect any polarization at all.

Early attempts to measure polarization in M64 by Reynolds (1911) and Green (1917), and in NGC 2261 by Meyer (1919) proved inconclusive, while later attempts to measure polarization in M32 by Sinclair-Smith (1935) gave null results. The first convincing evidence for extragalactic polarization came from observations of M31 by Öhman (1939).

Since then many attempts have been made to measure polarization in other galaxies. (Elvius 1956a, b and references therein). Most recent observers have abandoned the tedious and inaccurate large-scale photographic techniques, requiring exposure times of several hours, and concentrated on the use of modified stellar polarimeters of the standard photoelectric type. (Elvius 1962). Because these devices were designed for observing point sources the fields of most galaxies have only been "sampled" at various points, this results in the measurements being far from extensive, though very reliable.

The basic lack of an extensive mapping of polarization in extra-galactic systems has instigated the work presented in part II of the thesis. A new instrument designed specifically for extended object studies has been built, with the intention of making detailed optical polarization maps of extra-galactic objects. The observations reported in this thesis are the first in the project and concentrate on the interesting irr II galaxy M82.

REFERENCES

Arago and Mavius	1835	Astronomie Popularie, III, p. 609
Babcock, H.W.	1947	Ap. J., <u>109</u>, p.105
Chandresakhar, S.	1946	Ap. J., <u>103</u>, p.351
Chandresakhar, S. and Breen, F.H	1947	ibid., <u>109</u>, p.435
Clarke, D.	1965	M.N.R.A.S., <u>129</u>, p.71
Davis, L. and Greenstein, J.L.	1951	Ap. J., <u>114</u>, p.206
Elvius, A.	1962	Lowell Obs. Bulletin, <u>5</u>, p.271
Elvius, A.	1956a	Stockholm Obs. Ann. <u>18</u>, No. 9
Elvius, A.	1956b	ibid. <u>19</u>, No. 1
Fermi, E. and Chandresakhar, S	1953	Ap. J., <u>128</u>, p.113
Green, W.K.	1917	Pub. A.S.P., <u>29</u>, p.108
Hall, J.C.	1949	Science, <u>109</u>, p.166
Hiltner, W.A.	1949a	Science, <u>106</u>, p.165
	1949b	Ap. J., <u>109</u>, p.471
Lyot, B.	1929	Annles de L'Observatoire de Meadon, <u>5</u>, Phase 1.
Meyer, W.F.	1919	Pub. A.S.P., <u>31</u>, p.194
Ohman, Y.	1939	M.N.R.A.S., <u>78</u>, p.553
Reynolds, J.H.	1911	M.N.R.A.S., <u>13</u>, p.6
Sinclair-Smith	1935	Mount Wilson Cont., p.524

CHAPTER 1

THE QUANTITATIVE DESCRIPTION OF POLARIZED LIGHT

1.1 The States of Polarization

When discussing polarization it has become standard practice to consider the sectional pattern of the electric field vector (E-vector) as defining the state of polarization (though the use of the magnetic field vector would be equally valid) and throughout the subsequent discussions the state of polarization will be specified in this manner. Similarly, "the direction" of polarization for linearly polarized light will be understood to mean the direction of the E-vector, and the plane of polarization as "that plane defined by the E-vector and the direction of propagation of the light". Thus, in terms of a formal definition, "polarized light" is light whose E-vector sectional pattern exhibits a preference for a particular transverse direction or for a particular handedness.

There are three basic polarization types: Linear Polarization, Circular Polarization and Elliptical Polarization (the first two being special cases of the latter with ellipticities 0 and 1 respectively). The state of linear polarization can exist in an infinite number of forms, as defined by the azimuthal angle of the E-vector. Circularly polarized light comes in only two different forms, differing in their handedness. Elliptically polarized light also exists in an infinite number of forms, differing as to azimuthal angle, ellipticity, and handedness (fig. 1.1).

To these three states of polarization can be added a fourth, the "Unpolarized State" (this title is somewhat ambiguous since instantaneously the light will always show one of the above patterns. However, the sense of polarization changes rapidly with time, thus showing no long term preference (Hurwitz, 1945)). Probably the best definition of the unpolarized state is to say that "if light, when submitted to a device which splits it up into orthogonal polarization forms yields subbeams of equal intensity, then it is unpolarized" (Birge and Durbridge 1935). The existence of this unpolarized state enables light to be in a state of "partial polarization", where it is composed of a combination of one of the three polarized states and the unpolarized form. The possibility of the existence of these admixtures leads to the concept of "degree of polarization". This is a measure of the proportions of linearly or elliptically polarized light and unpolarized light that constitute a given beam. If this beam, of intensity I, is divided into a pair of completely orthogonal polarized components, with maximum intensity difference, with intensities I_1 and I_2 respectively; then the degree of polarization P is defined to be

$$P = \frac{I_1 - I_2}{I_1 + I_2} = \frac{I_1 - I_2}{I} \tag{1.1}$$

In practical terms this is usually the quantity measured in polarization studies; however, this does not give information as to which polarization form is present, but only how much of it is present.

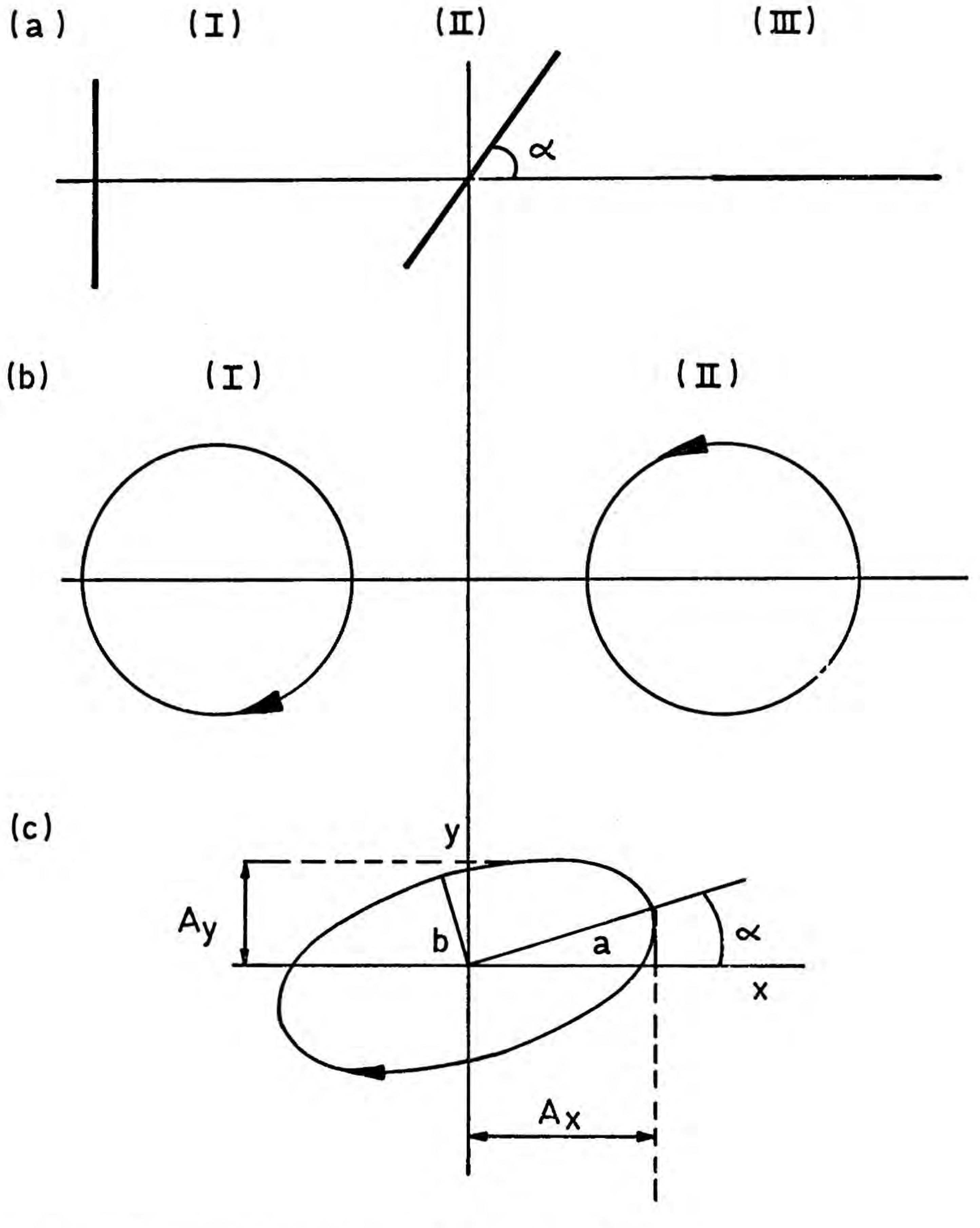

Figure 1.1 Sectional Patterns of Polarized Light Forms

(a) Linearly polarized light (I) vertical (II) at azimuth α (III) horizontal.

(b) Circularly polarized light (I) Left Circularly Polarized, (II) Right Circularly Polarized.

(c) Elliptically polarized light at azimuth angle α to horizontal with ellipticity $e = {}^{b}/a$ and clockwise handedness.

1.2 The Stokes Parameters

Stokes (1852) discovered that the state of polarization of a beam of light could be completely specified by just four quantities, now called the "Stokes Parameters". These parameters describe both the intensity and the polarization of a beam of light, and are applicable to all forms of polarized light, whether it be monochromatic, or polychromatic. Each parameter has dimensions of intensity (a time average intensity rather than an instantaneous value) and define a column vector (the Stokes' Vector), in the four-spaces they form, which rather elegantly represents the state of polarization and intensity of a light beam in one quantity.

Following Walker (1954) these parameters will be designated I, Q, U, V, and written in column matrix form as

$$\begin{bmatrix} I \\ Q \\ U \\ V \end{bmatrix}$$

The first parameter, I, represents the "intensity" of a given beam of light. The second parameter, Q, is a measure of the "horizontal preference" displayed by the E-vector, and is positive for polarization forms closer to a horizontal line than a vertical line, negative if the other preference is shown, and zero if no preference is shown, e.g. right-handed circular polarization. The parameter U is similarly a preference indicator, but this time a "45^o preference guide", that is polarization forms closer to $+45^o$ than -45^o are positive etc. The fourth parameter V distinguishes the handedness of a beam, being positive for right handed polarization forms, negative for left-handed forms, and zero for linear forms.

The formal definitions of the parameters in terms of the electromagnetic theory are given by Perrin (1942), and require the assumption that the light is sufficiently monochromatic for a definite phase angle, γ, to instantaneously exist between the components A_x and A_y of the E-vector, and yet at the same time be of sufficiently large bandwidth so that the unpolarized state is not precluded. The resulting definitions of the parameters are as follows:

$$\begin{aligned} I &= \langle A_x^2 + A_y^2 \rangle \\ Q &= \langle A_x^2 - A_y^2 \rangle \\ U &= \langle 2A_xA_y \cos\gamma \rangle \\ V &= \langle 2A_xA_y \sin\gamma \rangle \end{aligned} \tag{1.2}$$

Where the brackets designate time averaging of the enclosed quantities . For unpolarized light there is no time-averaged preference for A_x or A_y and the Stokes' parameters reduce to

$$\begin{aligned} I &= \langle 2A_x^2 \rangle \\ Q &= 0 \\ U &= 0 \\ V &= 0 \end{aligned}$$

Similarly for a horizontally polarized beam the parameters become

$$\begin{aligned} I &= A_x^2 \\ Q &= A_x^2 \\ U &= 0 \\ V &= 0 \end{aligned}$$

In general the four parameters satisfy the inequality

$$I \geq (Q^2 + U^2 + V^2)^{\frac{1}{2}} \tag{1.3}$$

The equality only being true for a completely polarized beam. If a beam of light is completely unpolarized then $Q = U = V = o$, thus a partially polarized beam can be considered to be a superposition of a natural beam of intensity

$$I_U = I - (Q^2 + U^2 + V^2)^{\frac{1}{2}} \tag{1.4}$$

and a completely polarized beam

$$I_P = (Q^2 + U^2 + V^2)^{\frac{1}{2}} \tag{1.5}$$

The degree of polarization, P, is then given by

$$P = I_P/I = (Q^2 + U^2 + V^2)^{\frac{1}{2}}/I \tag{1.6}$$

This identity illustrates one of the fundamental properties of the Stokes' parameters, namely their additivity. When combining two independent beams it is not necessary to take into account any difference of phase or amplitude. If we have the Stokes' parameters for two beams 1 and 2, and wish to find the properties of a beam formed by combining the two, this is simply:

$$\begin{aligned} I_C &= I_1 + I_2 \\ Q_C &= Q_1 + Q_2 \\ U_C &= U_1 + U_2 \\ V_C &= V_1 + V_2 \end{aligned} \tag{1.7}$$

Using other representations of the beam the additivity process becomes far more complicated. If the measurements are made relative to a fixed reference direction then the position angle of the partially linearly polarized beam, θ, is given by

$$\theta = \tfrac{1}{2} \tan^{-1} \frac{U}{Q} \tag{1.8}$$

Furthermore, Solleillet (1929) pointed out that the Stokes' vectors transform linearly when acted on by optical devices, where the coefficients defining the transformation matrices are representative of the optical device and its azimuthal angle. Mueller (1948) was able to determine these matrices phenomenologically. The resulting combination of these matrices with the Stokes' parameters in the "Mueller Algebra" provides a powerful, and simple, tool in complicated optical problems, where for example a beam of polarized light is passed through a succession of optical components, i.e. in a polarimeter or the interstellar medium. The resultant outgoing polarization form is, by conventional means, difficult to calculate; however, with the Mueller Algebra the Stokes' vector of the original beam has only to be acted on from the left by the matrices representing the series of optical devices, applying the normal rules of matrix algebra, to enable the outgoing polarization form to be calculated.

REFERENCES

Birge, R.T. and Dubridge, L.A.	1935	J. Opt. Soc. Amer., 25, p. 179
Hurwitz, H. Jr.	1946	J. Opt. Soc. Amer., 35, p. 525
Perrin, F.	1942	Chemical Physics, 10, p. 418
Mueller, H.	1948	J. Opt. Soc. Amer., 38, p. 661
Soleillet, P.	1929	Ann. de Physique, 12, p. 23
Stokes, G.G.	1852	Trans. Cambridge Phil. Soc. 9, p. 399
Walker, W.	1954	Am. J. Phys., 22, p. 170

PART I

CHAPTER 2

STELLAR POLARIZATION AND THE LOCAL STRUCTURE OF THE GALACTIC MAGNETIC FIELD

2.1 A Critique of the Methods of Measuring the Galactic Magnetic Field

Information about the local structure of the galactic magnetic field is obtained from observations of :

a) The Zeeman splitting of the 21 cm line of neutral hydrogen.

b) Faraday rotation of extragalactic radio sources.

c) The brightness and Faraday rotation of the galactic radio emission.

d) The rotation measures of pulsars.

e) The polarization of starlight.

Of these, only method (a) provides a direct measurement of the magnitude and direction of the magnetic field (see Galt et al 1960, or Davis and Berge 1967, for details). However, the field strengths obtained by this method are an order of magnitude larger ($\sim 50 - 100\mu$ G) than those obtained from the other techniques (Verschuur 1968, 1969, a, b, c, Davies et al 1968) and expected from theoretical considerations (Chandresakhar and Fermi 1953, Spitzer 1956). In order to explain this discrepancy Verschuur (1969d, 1970) has suggested that the magnetic field in neutral Hydrogen clouds could be greatly enhanced during their collapse, and this seems to agree well with the results of theoretical work on cloud collapse (Mestel 1976). If this is indeed the case, the resultant amplified field will not be typical of the general interstellar field, either in strength or direction, and in view of this possibility the results obtained by this method will be excluded from the present discussion.

All the other techniques require different constituents of the interstellar medium to "illuminate" the magnetic field; (b) and (d) require thermal electrons, (c) relativistic electrons and (e) interstellar dust.

The sense and magnitude of the magnetic field component along the line of sight, $B_{\parallel}$, can be found from the Faraday rotation observed in polarized radio sources. Since the angle of rotation, θ, is dependent on wavelength, λ, it is possible to determine the intrinsic angle of the source, and the degree of rotation caused by the intervening interstellar medium. The angle of rotation is given by

$$\theta = (\text{R.M.})\ \lambda^2 \text{ radians} \tag{2.1}$$

where R.M. is the Rotation Measure defined as

$$\text{R.M.} = 0.81 \int n_e \vec{B}.\vec{d\ell} \tag{2.2}$$

where n_e is the line of sight electron density in cm^{-3}, B is in μ Gauss and ℓ is the depth of the region over which rotation occurs (in parsecs). The sign of the rotation measure gives the sense of the field, a positive measure indicates a field directed towards the observer.

In order to determine the magnetic field from extragalactic R.M.'s assumptions must be made about the electron density distribution. Possible variations with galactic longitude are generally ignored, the electron density is either assumed to be a constant c.f. $n_e = 0.062\ cm^{-3}$ (Mills 1970), or to decrease with height, z, above the galactic plane cf. $n_e = 0.012 \exp(-z^2/1.443 \times 10^{-2})\ cm^{-3}$ (Davies R.D. 1969). These estimates are probably not all that realistic, as considerable variations of electron density in ionized region are expected (Spitzer 1968), and the uncertainty in the depth of the electron layer complicates the issue further.

A more serious problem is caused by the possibility of intrinsic Faraday rotation in the extragalactic sources. Though the R.M.'s show a pronounced dependence on galactic coordinates (Valleé and Kronberg, 1973), there are nevertheless numerous cases where sources only a few degrees apart have vastly different R.M.'s (Gardner et al 1969). If indeed these "anomalous" R.M.'s are due to self-rotation in the sources then the technique will be invalidated as there is no reliable method for removing such effects.

As the variations of position angle across a pulse are frequency independent, there is no differential rotation across a pulse, implying that intrinsic Faraday rotation is absent in pulsars (Manchester 1972). Thus the serious objection made against extragalactic rotation studies does not apply to the pulsar measurements. Furthermore, it has been shown (Davies, J. G. et al 1968) that the arrival time t, of a radio pulse from a pulsar is different at different frequencies, ν, due to the passage through the magnetized plasma of the interstellar medium. For a uniform plasma

$$\frac{dt}{d\nu} = -\frac{81 \times 10^2}{\nu^3} \times D \text{ Sec Hz}^{-1} \qquad (2.3)$$

where D is the so-called "Dispersion Measure" in $pc\ cm^{-3}$, given by

$$D = \int n_e\, d\ell \ \ pc\ cm^{-3} \qquad (2.4)$$

and is therefore the integral along the line of sight of the electron density. Hence it is possible to measure the average electron density directly, and this removes the difficulty discussed in connection with the extragalactic R.M.'s. The mean line of sight component of the magnetic field is then obtained by combining the Dispersion and Rotation Measures.

$$< B_{\parallel} > = \frac{\int n_e \, \vec{B}.\vec{d\ell}}{\int n_e \, d\ell} \qquad (2.5)$$

However, it must be realized that in order to determine the topography of the magnetic field the distance of the pulsar must be known, and its calculation from the dispersion measure does require assumptions about the electron density. Even taking this into account the pulsar R.M.'s probably provide the best means of studying the magnetic field. Unfortunately only about forty pulsars have known R.M.'s and Dispersion Measures (Manchester 1974), and this lack of data leads to a very incomplete coverage of the sky, making a reliable statistical analysis very difficult.

The background radio emission is assumed to be due to synchroton radiation from relativistic electrons (for a review of the mechanism see Ginzburg and Syrovatski 1964, 1965). This results in the emission being polarized with the direction of the E-vector orthogonal to that of the magnetic field as seen in projection. Theoretically the polarization should be $\sim 73\%$ but observations show that in practice it is only a few per cent, and this is generally regarded as being due to the superposition of contributions with different position angles along the line of sight (Burn 1966). Further information comes from the distribution and brightness of the radio emission since the apparent emissivity of a region is proportional to $|B \sin\theta|^{\beta-1}$ where θ is the angle between the magnetic field, B, and the line of sight, and β is the "temperature spectral index of emission" defined by (Brightness Temperature) $\propto$ (Frequency)$^{-\beta}$ (Bingham and Shakeshaft 1967). There are three disadvantages with this method. Firstly, the magnitude of the magnetic field in the direction orthogonal to the E-vector can be determined, but its sense cannot. Secondly, the complicated line of sight effects are difficult to remove. Thirdly, it is not possible to determine the distance at which the radiation originates. Normally, distance estimates are made on the basis of visible optical features that might be connected with the radio structure, but this is far from being reliable or satisfactory.

The polarization of starlight by anisotropic grains aligned in a weak interstellar magnetic field by the Davis-Greenstein (1951) mechanism has already been mentioned. Other hypotheses have been invoked that do not involve magnetic alignment (Gold 1952, Saltpeter and Wickramasinghe 1961, Harwit 1970) but these are generally regarded as inadequate (Davis 1955, Serkowski 1962, Purcell and Spitzer 1971). With the Davis-Greenstein (DG) mechanism the polarizing particles are aligned with their short axes in the direction of the magnetic field. This results in the direction of maximum extinction for the grains being perpendicular to the magnetic field direction. Thus the E-vector of the resultant polarized light will be parallel to the magnetic field direction.

Quite apart from the tenacity of the link between the DG mechanism and the observations, optical polarization now appears to be regarded by astronomers as a poor way of studying the magnetic field for two reasons. Firstly, as with the background radio emission studies, it gives only a two-dimensional representation, the E-vector of the light being parallel to the projection of the magnetic field vector perpendicular to the line of sight. Secondly, the magnitude of the field cannot be calculated directly from the observations without making assumptions about the nature of the grains. But as we have already seen each of the alternative methods has its accompanying drawbacks, some of which are more severe than these.

There are however, several advantages peculiar to the optical polarization data. Firstly the sheer volume of data now available makes it possible to carry out a meaningful analysis of the variations of the polarization with position, and hence the variations in the magnetic field. Secondly, there are no problems with intrinsic polarization in the sources. Thirdly, the distance of each star can be readily calculated, thus allowing the field topography to be determined. It is for these reasons that we have based our analysis (Ellis and Axon 1976) on a catalogue which we have compiled from the available optical polarization data (Axon and Ellis 1976).

2.2 The Conflict over the Direction of the Galactic Magnetic Field, and the Possible Existence of Irregularities

Numerous models of the galactic magnetic field have been constructed, but basically there are only two principal schools of thought. The oldest is the so-called "Longitudinal Model" (Chandresakhar and Fermi 1953) in which the magnetic field runs parallel to the axis of the spiral arm. Originally it was suggested that this magnetic field was directed towards $\ell = 45^{\circ}$ or $\ell = 225^{\circ}$, but this appeared to conflict with the neutral Hydrogen observations (Oort 1958) which indicated that the spiral arms were directed towards $\ell = 85^{\circ}$. Furthermore the model was unable to account for certain local inhomogeneities, such as the peaking of the background radio emission in the "galactic spurs" (Bingham and Shakeshaft 1967). In order to overcome these problems, Hoyle and Ireland (1961) proposed an alternative configuration in which the magnetic field wound round the spiral arms in a helical pattern.

Considerable impetus was given to this model when Morris and Berge (1964) and Gardener and Davis (1966) interpreted the distribution of extra-galactic R.M. signs as indicating that the magnetic field was pointing in opposite directions above and below the galactic plane, which was exactly what the helical model predicted. This led Hornby (1966) to propose a more detailed helical model, consisting of tightly wound, skewed helices with an axial direction of $\ell = 70^{\circ}$, and this model showed fairly good agreement with the background radio emission and the optical polarization data as well. However, Bingham and Shake-shaft (1967), and Thielheim and Langhoff (1968) concluded that the same data indicated a "quasi-longitudinal" magnetic field, that is a longitudinal field which changes sign as it crosses the plane of the spiral arm, but they assigned different directions to the field, Bingham and Shakeshaft proposed $\ell = 70^{\circ}$, whereas Thielheim and Langhoff preferred $\ell = 90^{\circ}$.

Shortly afterwards, Mathewson (1968) used the optical polarization data to investigate the magnetic field. His analysis was based on plots of the directions of the E-vectors of the starlight, and these revealed areas in which the E-vectors appeared to form "elliptical flow patterns" or looping structures. Mathewson interpreted these patterns as being a consequence of a helical magnetic field seen in projection. He concluded that the model which best fit the data was one in which the field was wound in right-handed helices of pitch angle 7°, the helices lying on the surface of tubes having an elliptical cross-section of axial ratio 3 , and with the semi-major axis parallel to the galactic plane. The helices were also sheared through an angle of 40° on the plane, in an anticlockwise direction, and their axes were directed towards $\ell = 90^{\circ}$ or $\ell = 270^{\circ}$. In addition to fitting the optical polarization data Mathewson (1968) proposed that the radio spurs arose as a consequence of the helical magnetic field in regions of magnetic field compression, and were therefore elongated in the direction of the magnetic field which appeared to agree well with their observed orientations. Later attempts to show that the model was also consistent with the extragalactic R.M.'s (Mathewson and Nicholl 1968, Mathewson 1969) were only partially successful. Good agreement could be obtained only if the helical configuration was confined to within 500 parsecs of the sun, and then beyond this distance a longitudinal field directed towards $\ell = 90^{\circ}$ assumed.

Gardener et al (1969) also analysed the optical polarization data, and disagreed strongly with Mathewson's (1968) interpretation. They concluded that the data indicated that the magnetic field was longitudinal and directed towards $\ell = 50^{\circ}$, but at the same time they reported that the extragalactic R.M.'s indicated that the magnetic field was longitudinal and directed towards $\ell = 80^{\circ}$.

Even in the face of this contradictory evidence the helical model was widely accepted as providing the most complete explanation of the observations (Vershuur 1970). However, recent observations (Reinhardt 1972, Berkhuijsen 1971, Wright 1973, Manchester 1974) have all suggested that the magnetic field is longitudinal in form, but once again each observer proposes a different direction for this magnetic field (table 2.1).

It is indeed quite remarkable how many different directions have in fact been proposed for the magnetic field, and it is very disconcerting that the optical and radio data seem to suggest entirely different directions. Whiteoak (1974) has argued that one need not necessarily expect the same answers from the optical and radio data as they sample different components of the interstellar medium. But even assuming that this accounts for the disagreement between the optical and radio data it cannot satisfactorily explain the discrepancies that exist between independent analyses of the same data, e.g. the optical data alone suggests magnetic field directions that differ by as much as 40°. Nowhere is this disagreement more dramatically illustrated than in the analysis of Klare et al (1970) who find that the minimum values of the optical polarization indicate that the magnetic field is directed towards $\ell = 50^{\circ}$, but that the dispersion in the position angles indicate that the magnetic field is directed towards $\ell = 80^{\circ}$.

In the face of all this contradictory evidence, what then is the direction of the magnetic field ? In order to find the answer to this question, and to try and resolve the aforementioned discrepancies, we have reinvestigated the information contained in the optical polarization data. We have included the recent data of Schroeder (1976) and Klare et al (1971) in the analysis, and particularly in the former case, since all the stars are nearby, it is hoped that the new data will clarify the situation. Of equal importance to our understanding of the magnetic field is its relation to the spiral structure of the galaxy. We have also studied the correlation between the magnetic field, the spiral arms and other prominent structural features.

Previously we remarked that the most important argument in favour of the helical model was that it was capable of explaining the North galactic spurs. Elsewhere there is little difference between the models and therefore this

Table 2.1

Directions for the regular component of the Galactic magnetic field

Reference		Method	Value (1°)
Gardner et al	(1969)	Faraday rotation of extragalactic sources	80 (b_o = 0)
Manchester	(1973)	Faraday rotation of pulsars	94 ± 11
Reinhardt	(1971)	Faraday rotation of quasars	110
Berkuijsen	(1971)	Radio background polarization	60 (b_o = 0)
Spoelstra	(1973)	Galactic loops as supernova remnants	40
Mathewson	(1968)	Optical polarization	90 (helical)
Klare et al	(1968)	Optical polarization	80
Axon and Ellis	(1976)	Optical polarization	60 ± 15 (b_o = 15 ?)

Table 2.2

Source of Data

Observer		No: of stars (approx.)	P mags	θ deg.
Hiltner	(1951-56)	1034	0.003	1-7
Smith	(1956)	123	0.005 - 0.020	5-20
Behr	(1959)	550	0.0005	1-15
Hall	(1958)	1329	0.005	8
Appenzeller	(1966-1968)	230	0.0003-0.0012	1-20
Mathewson and Ford	(1970)	1800	0.0007	1-10
Klare et al	(1971)	1600	0.001-0.004	5
Schroeder	(1976)	511	0.0001-0.0024	2

region provides a critical test between them. Berkhuijsen (1971) has argued that these loops and spurs are in fact due to old supernovae remnants, rather than a helical magnetic field. Spoelstra (1971, 1972 a, b, c) elaborated on this argument and showed that far from providing a good fit to the observations in this region the helical model experienced serious difficulties in explaining them. Spoelstra (1972d) also showed the viability of the supernovae hypothesis as an alternative explanation for the spurs, and the results of his calculations of models of this activity gave an excellent fit to the observations. In view of these results he rejected the helical model in favour of the supernova remnants hypothesis. The conclusion that the North polar spur region is not the result of a regular field structure, but rather a consequence of a large "irregularity", is of considerable importance to our concept of the galactic magnetic field. Up until now we have tacitly discussed the observations in relation to regular magnetic field structure, however, the possibility that the spur region is not an isolated irregularity, but merely a prominent example of a generally smaller widespread phenomena introduces a new dimension into our discussion. There is quite strong evidence to support this idea. For instance the region around $\ell = 80^{\circ}$ is one of the directions proposed for the magnetic field by Klare et al (1971). Here Whiteoak (1974) points out the existence of the Cygnus X complex, and Weaver (1970) has presented radio evidence supporting a merger of the Orion and Sagittarius arms in this direction. Quite clearly this region could be another large irregularity and this could provide a very reasonable explanation for Klare et al's result. Furthermore, the considerable scatter observed in the optical polarization and radio data could indicate that smaller irregularities are very common. If this is the case it would be necessary to revise our model of the magnetic field to include both a regular and irregular component. Manchester (1974) argues strongly in favour of such an idea and suggests that the helical model could be the result of trying to fit a regular field to the irregularities, and Valleé and Kronberg (1973) go as far as to suggest that the whole of the optical polarization data samples a large local irregularity with a radius of one kpc Clearly the whole question of magnetic field irregularities is of great importance and we have searched the data for the possible existence of irregularities and have investigated the evidence for them having a characteristic size.

To summarize then, the aims of the present analysis are as follows:

1. To establish the local direction and form of the galactic magnetic field.
2. To correlate the observed polarization and the magnetic field with the spiral structure of the galaxy.
3. An investigation of the possible existence of irregularities in the magnetic field and to try and establish their scale.

2.3 The Optical Polarization Data

Extensive polarization measurements have been made by Van P. Smith (1956), Hall (1958), Hiltner (1949, 1954a, 1954b, 1956), Behr (1959), Lodén (1960a, 1960b, 1961), Appenzeller (1966, 1968), Mathewson and Ford (1970), Klare et al (1974) and Schroeder (1976). The total number of stars in each of these sources, and the associated experimental errors, are given in table 2.2.

Though the total number of individual measurements exceeds 8500, the number actually used in the analysis, 5070, was considerably reduced for two reasons. Firstly, in order to be able to study the field topography, the distances of the stars must be known. Distances were generally calculated from colour excesses and spectral types as described below, or in some cases, when trignometric parallaxes had been used, values were taken from the source catalogue, e.g. Behr (1959). The paucity of such data meant the exclusion of many stars. Secondly, a considerable number of measurements are duplicated results, which must be removed for the statistical analysis. Where more than one measurement of the same star existed the most accurate value (as determined by the source errors) was used, or in the case of several measurements with the same accuracy an average value taken. Unfortunately these two restrictions have meant the total exclusion of the 1800 stars measured by Lodén. This is because firstly their identification is via an obscure catalogue, thus making removal of duplications difficult (Lodén 1975); and secondly, the only available colour and spectral information is similarly based on a rather obscure and ill-defined photometric system which would possibly introduce spurious distance effects into the analysis.

In our catalogue (Axon and Ellis 1976) and throughout this analysis we express the polarization in terms of the Stokes' parameters so that their additive properties can be used. Both Stokes' parameters are expressed in magnitudes and have been calculated from the relations (after Serkowski 1962)

$$
\begin{aligned}
Q &= p \cos 2 (\theta_G - \pi/2) \\
U &= p \sin 2 (\theta_G - \pi/2)
\end{aligned}
\qquad (2.6)
$$

where p is the degree of polarization in magnitudes, and θ_G is the position angle of the E-vector in the galactic coordinate system (measured from the North galactic pole and increasing anticlockwise from North), determined from the position angle in the equatorial system, θ_E, by

$$\cot(\theta_G - \theta_E) = \frac{\cos b \tan b_N - \cos(\ell - \ell_N) \sin \ell_N}{\sin(\ell - \ell_N)} \tag{2.7}$$

where ℓ and b are the galactic coordinates of the star and ℓ_N and b_N are the galactic coordinates of the equatorial North pole at the equinox of the observations (Appenzeller 1968).

The magnitude system of polarization is described by Behr (1959) and Serkowski (1962) and has been preferred, because of the then obvious connection between polarization and extinction. Conversion to the polarization in per cent, $P_{\%}$, is however, easily accomplished by using the relation

$$P_{\%} = 46.05\, p \tag{2.8}$$

The distance of a star, d, in parsecs is calculated from

$$5 \log_{10} [d(pc)] = m_V - M_V + 5 - A_V \tag{2.9}$$

where m_V and M_V are the apparent and absolute magnitudes of the star respectively, and A_V is the total interstellar absorption for the star.

The total extinction A_V is found from the measurable colour excess, E_{B-V} in the UBV system by assuming the universal reddening law (Blanco 1956; Sharpless 1963)

$$R = A_V / E_{B-V} = \text{constant} . \tag{2.10}$$

The colour excess E_{B-V} is given by

$$E_{B-V} = (B-V) - (B-V)_o \tag{2.11}$$

and is the difference between the observed (B-V) colour index of the star and the intrinsic colour index $(B-V)_o$ of the star, which has to be obtained from the spectral classification of the star, as does the absolute magnitude. It has been demonstrated that variations in R from place to place are quite small (Serkowski, Mathewson and Ford, 1975), although there is some evidence for higher values than normal in dense dust clouds, where the grains might be larger (Carrasco, Strom and Strom 1973), in which case one would expect R to be correlated with A_v. In the absence of any well defined results on such variations there appears to be little justification for a more elaborate form of equation 2.10. Any errors thus incurred will in any case be small compared to those due to the uncertainties in the intrinsic colours and absolute magnitudes. By choosing a value of R, A_v can be calculated from the colour excess, the value of R adopted for the B-V indices was

$$R = 3.0 \pm 0.2 \quad \text{(Blanco 1956, Sharpless 1963)}$$

Spectral types, apparent magnitudes and colour indices are often provided with the original data, and in each case the author quotes the relevant sources. In the cases where one or more of these quantities was not given, we referred to other well known catalogues in the literature, e.g. Blanco et al(1968), Hoffleit(1964,) Neckel (1968), and many more too numerous to mention.

The colour indices were mainly in the UBV system (Johnson 1963), but for some stars in the catalogues of Smith (1956) and Hall (1958) the only colour measurements that were available were in the C_1 system (Stebbins, Huffer and Whitford 1940). For these C_1 indices we adopted a value for R of

$$R = 6.1 \pm 0.4$$

in accordance with the modification suggested by Morgan et al (1953).

The relationship between intrinsic colour and spectral type has been established on a firm basis (Johnson and Morgan 1953, Morgan and Harris 1953, Mendoza 1956) for stars of the main sequence by using the colours of nearby stars, that are probably unaffected by interstellar reddening. For O and B stars the problem is more difficult as few stars of this type are observed nearby. For these stars recourse must be made to galactic clusters that contain O and B stars and also stars around $A0_V$. The difference in colour index between the early-type and late-type stars in the cluster enables the intrinsic colours to be determined. It is in these stars and in the higher luminosity classes where the greatest uncertainty exists.

The calculation of absolute magnitudes is carried out in a somewhat similar manner. For main sequence stars the absolute magnitudes are determined for nearby stars, which have known trignometric parallaxes or proper motions and hence are at a known distance. For O and B stars and supergiants the same problem exists as for the intrinsic colour determinations. Again galactic clusters are used to solve the problem, but this time the situation is more complicated as the results rely on the "Zero Age Main Sequence" (ZAMS) fitting procedure. The Z.A.M.S. is the main sequence of stars which have completed the Kelvin contraction but have not evolved further as a consequence of Hydrogen burning in their interiors. The curve fitting procedure is based on the assumption that for star clusters of the age of the Hyades (10^9 years) and younger, the Z.A.M.S. is identical, and works in the following way. The absolute magnitudes of main sequence stars, determined from local measurements, are plotted against the colour indices of those stars in the cluster, corrected for interstellar reddening. The vertical fit with Z.A.M.S. for the unevolved part of this curve then enables the distance modulus of the cluster to be determined, and hence the absolute magnitudes of the other types of star in the cluster. For further details of the method reference should be made to papers by Johnson and Hiltner (1956), Johnson (1957), and Johnson and Iriarte (1958). Quite clearly the validity of the absolute magnitudes determined in this way hinges on the validity of the assumptions behind the Z.A.M.S., and if these are incorrect then so are the absolute magnitudes. A more detailed discussion on the possible uncertainties in M_V are given by Blaauw (1963) and Keenan (1963).

The intrinsic colours used in this analysis were taken from a compilation of the best available values made by Johnson (1963), and are as given in table 2.3. The absolute magnitudes, taken from Blaauw (1963) and Schmidt-Kaler (1965), are given in table 2.4. Values of absolute magnitude and intrinsic colour were assigned to each star from these tables according to their spectral types designated on the MK system (Morgan and Johnson 1953, Morgan, Keenan and Kellman 1943). For colours measured on the C_1 system intrinsic colours were calculated from the B-V intrinsic colours by using the relations due to Morgan et al (1953)

TABLE 2.3

Intrinsic Colours
from Johnson(1963)

B−V

Sp. Type	V	III	II	Ib	Ia
O5	−0.32	−0.32	−0.32	−0.32	−0.32
O6	− .32	− .32	− .32	− .32	− .32
O7	− .32	− .32	− .32	− .31	− .31
O8	− .31	− .31	− .31	− .29	− .29
O9	− .31	− .31	− .31	− .28	− .28
O9.5	− .30	− .30	− .30	− .27	− .27
B0	− .30	− .30	− .29	− .24	− .24
B0.5	− .28	− .28	− .26	− .22	− .22
B1	− .26	− .26	− .24	− .19	− .19
B2	− .24	− .24	− .22	− .17	− .17
B3	− .20	− .20	− .18	− .13	− .13
B5	− .16	− .16	− .14	− .09	− .09
B6	− .14	− .14	− .12	− .07	− .07
B7	− .12	− .12	− .10	− .05	− .05
B8	− .09	− .09	− .07	− .02	− .02
B9	− .06	− .06	− .04	.00	.00
B9.5	− .03	− .03	− .01	+ .01	+ .01
A0	.00	.00	+0.01	+ .01	+ .01
A1	+ .03	+ .03	...	+ .01	+ .01
A2	+ .06	+ .06	...	.00	.00
A3	+ .09	...	...	.00	.00
A5	+ .15	+0.15	...	+ .07	+ .07
A7	+ .20	...	...	+ .13	+ .13
F0	+ .30	...	...	+ .24	+ .24
F2	+ .38	...	...	+ .34	+ .34
F5	+0.45	...	...	+0.45	+0.45

U−B

Sp. Type	V	III	II	Ib	Ia
O5	−1.15	−1.15	−1.15	−1.15	−1.15
O6	−1.14	−1.14	−1.14	−1.14	−1.14
O7	−1.14	−1.14	−1.14	−1.14	−1.14
O8	−1.13	−1.13	−1.13	−1.13	−1.13
O9	−1.12	−1.12	−1.12	−1.12	−1.12
O9.5	−1.10	−1.11	−1.12	−1.09	−1.10
B0	−1.08	−1.09	−1.10	−1.05	−1.07
B0.5	−1.01	−1.03	−1.05	−1.01	−1.04
B1	−0.93	−0.96	−1.00	−0.96	−1.00
B2	−0.86	−0.89	−0.95	−0.91	−0.96
B3	−0.71	−0.74	−0.83	−0.82	−0.87
B5	−0.56	...	−0.69	−0.72	−0.78
B6	−0.49	...	−0.62	−0.67	−0.73
B7	−0.42	...	...	−0.62	−0.68
B8	−0.30	...	...	−0.53	−0.60
B9	−0.19	...	...	−0.48	−0.56
B9.5	−0.10	...	...	...	...
A0	0.00	...	...	...	...

TABLE 2.4

Mean Visual Absolute Magnitudes

for Mk Luminosity Classes from

Schmidt-Kaler (1965) and Blaauw (1963)

Type	Luminosity Class										
	V	IV-V	IV	III-IV	III	II-III	II	Ib	Iab	Ia	Ia-0
O6...	−5.5										
8...	−5.2										
9...	−4.8		−5.3		−5.7		−6.0	−6.1	−6.2	−6.2	
B0...	−4.4		−4.8		−5.0		−5.4	−5.8	−6.2	−6.2	−8.1
1...	−3.6		−4.1		−4.4		−5.0	−5.7	−6.2	−6.6	−8.2
2...	−2.5		−3.3		−3.6		−4.8	−5.7	−6.3	−6.8	−8.2
3...	−1.7		−2.5		−2.9		−4.6	−5.7	−6.3	−6.8	−8.3
5...	−1.0		−1.8		−2.2		−4.4	−5.7	−6.3	−7.0	−8.3
7...	−0.4		−1.2		−1.6		−4.0	−5.6	−6.4	−7.1	−8.3
8...	− 0.5 +0.1		−0.7		−1.0			−5.6	−6.5	−7.1	−8.3
9...	0.0 +0.6		−0.2		−0.4		−3.8	−5.5	−6.5	−7.1	−8.4
A0...	+ 0.5 +1.0		+0.3					−5.2	−6.6	−7.1	−8.4
1...	+ 0.8 +1.5		+0.7		−0.9		−3.0	−5.1	−6.6	−7.3	−8.4
2...	+ 1.2						−2.9	−5.0	−6.7	−7.5	−8.5
3...	+ 1.5		+1.0:		−0.3		−2.8	−4.8	−6.8	−7.6	−8.5
5...	+ 1.8						−2.7	−4.8	−6.9	−7.7	−8.5
7...	+ 2.0		+1.7:		+0.3		−2.6	−4.8		−8.0	
F0...	+ 2.4						−2.5	−4.7	−6.6	−8.5	−8.7
2...	+ 2.8						−2.5	−4.6	−6.6	−8.4	−8.8
5...	+ 3.2	+2.8	+1.9		+1.0		−2.3	−4.6	−6.4	−8.2	
6...	+ 3.5	+2.8	+1.9				−2.2	−4.6	−6.4	−8.1	
8...	+ 4.0	+2.9	+1.9		+1.0		−2.2	−4.6	−6.3	−8.0	
G0...	+ 4.4		+2.6				−2.1	−4.5	−6.3	−8.0	−9.0
2...	+ 4.7		+2.9		+0.4		−2.0	−4.5	−6.2	−8.0	
5...	+ 5.1		+3.0				−2.6 −2.0	−4.5	−6.2	−8.0	
8...	+ 5.5		+3.0	+1.3	+0.4	−1.0	−2.6 −2.0	−4.5	−6.1	−8.0	
K0...	+ 5.9		+3.0	+1.3	+0.8	−0.8	−2.6 −2.0	−4.4	−6.1	−8.0	
1...	+ 6.1		+3.0	+1.3	+0.8	−0.8	−2.6 −2.0	−4.4	−6.1	−8.0	
2...	+ 6.3				+0.8	−0.8	−2.6 −2.0	−4.4	−6.0	−8.0	
3...	+ 6.5				+0.1	−1.0	−2.6 −2.0	−4.4	−6.0	−8.0	
4...	+ 6.8				−0.1	−1.0	−2.6 −2.0	−4.4	−5.9	−8.0	
5...	+ 7.2				−0.3	−1.0	−2.6 −2.0	−4.4	−5.9	−8.0	
7...	+ 8.1										
M0...	+ 8.7				−0.4		−2.4				
1...	+ 9.4										
2...	+10.1				−0.4		−2.4	−4.8	−5.6	−7.0	
3...	+10.7										
4...	+11.2				−0.5						

$$B\text{-}V = +\ 0.30 + 2.06\ C_1 \qquad \text{for O, B0, Ia - B2 Ia Stars}$$

$$B\text{-}V = +\ 0.18 + 1.76\ C_1 \qquad \text{B1 - A7, Main Sequence Stars}$$

$$B\text{-}V = +\ 0.27 + 1.37\ C_1 \qquad \text{for yellow giants}$$

A more comprehensive discussion of the UBV and C_1 systems is given by Johnson (1963). The error in absolute magnitude for main sequence stars is $\sim \pm\ 0^m.05 - 0^m.15$ (Blaauw 1963), and ignoring any possible inadequacies in the Z.A.M.S. Blaauw (1963) estimates that the typical error in absolute magnitude for O and B stars is $\sim \pm\ 0^m.2 - 0^m.3$, and for luminosity class III, Ia stars $\pm\ 0^m.3 - 0^m.4$. Taking these errors into account the star distances determined from equation 2.9 are uncertain by $\sim$ 7 - 12% for main sequence stars, $\sim$10 - 20% for O and B stars and $\sim$20 - 25% for luminosity class III and Ia stars within 2 kpc, and this must be borne in mind during the following analysis.

Having calculated the distance of the stars it is instructive to examine their spatial distribution. Figure 2.1 shows the overall distribution with distance, and it appears that the majority of the data lies within 2 kpc of the Sun, beyond this distance we feel that the lack of data makes any analysis pointless. Similarly the overall distributions with galactic coordinates are shown in figures 2.2 - 2.4, figure 2.3 being the most informative as it shows that most of the data is within $\pm\ 15^{\circ}$ of the galactic plane. More careful investigation of these latter distributions shows that most of the high latitude stars are within 500 parsecs. We have therefore confined our analysis to stars with $\pm\ 15^{\circ}$ of the galactic plane.

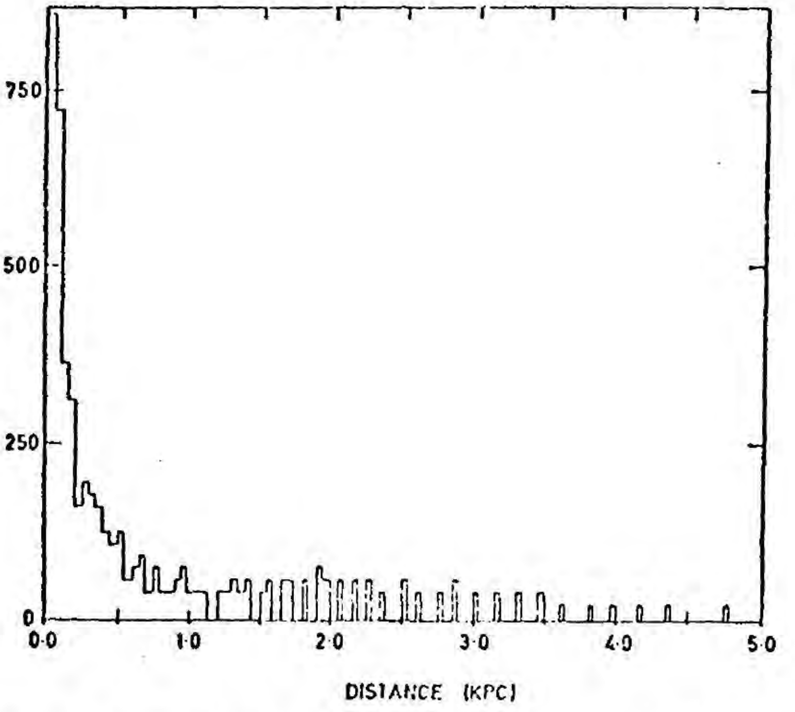

FIGURE 2·1 *The frequency distribution of stars in the catalogue with distance.*

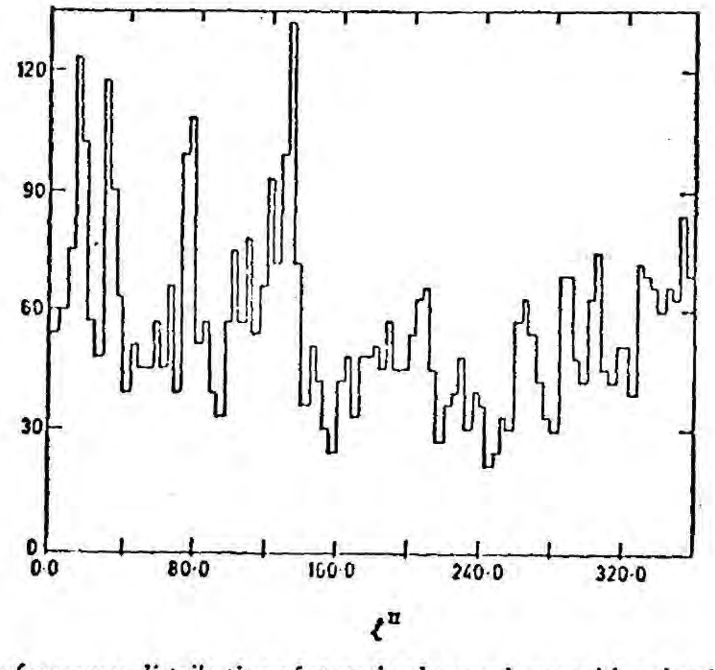

FIGURE 2·2 *The frequency distribution of stars in the catalogue with galactic longitude.*

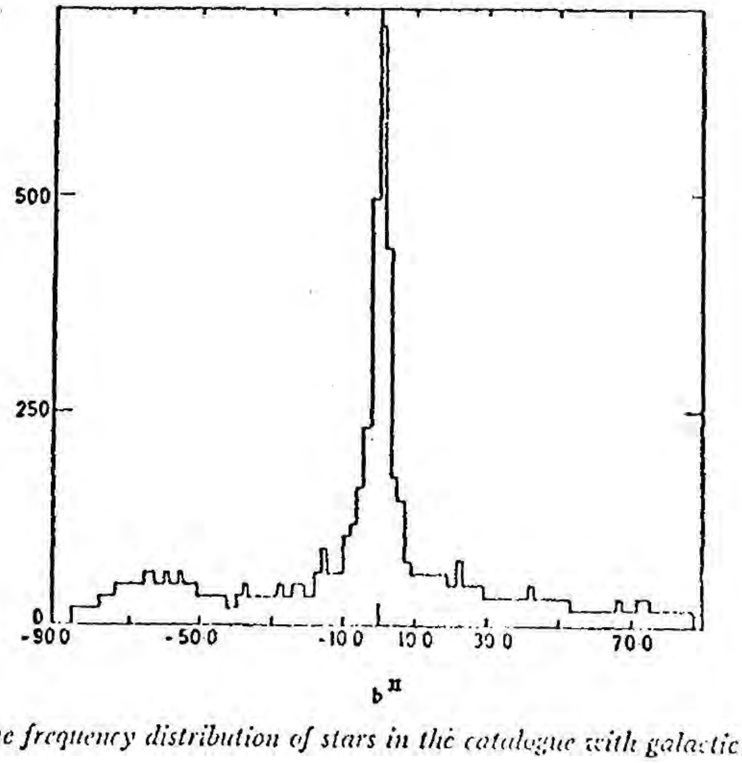

FIGURE 2·3 *The frequency distribution of stars in the catalogue with galactic latitude.*

We now wish to relate the polarization, via the Davis-Greenstein mechanism, to the physical conditions at a given location in the galaxy. Following Osbourne et al (1973) we may use a generalised equation for the degree of polarization δp produced in a volume element which extends $\delta \ell$ along the line of sight

$$\delta p = \frac{\text{const. } K \, . \, B_{\perp}^{2} \rho_{g} \, \delta \ell}{n_{H} \, T^{\frac{1}{2}} \, T_{g}} \qquad (2.12)$$

where T and T_g are the gas and grain temperatures respectively, n_H is the gas density, ρ_g the grain density, and $B_{\perp}$ is the magnetic field in the plane perpendicular to the line of sight. The constant K takes into account the size, shape and composition of the average grain. Clearly the observed Stokes' vectors in a certain direction are the integrals of the incremental polarization vectors along the line of sight. From equation 2.12 it is now easy to understand the physical significance of Q and U. Q is a measure of the degree of alignment, either in the galactic disk $(Q > 0)$, or perpendicular to the disk $(Q < 0)$. If the magnetic field is wholly in either of these directions then $U = 0$. U is largest when $\theta = 45^{\circ}$ $(U < 0)$ or $\theta = 135^{\circ}$ $(U > 0)$ and effectively measures the degree of inclination of the magnetic field. In order to compare the polarization at different places we shall assume that K takes the same value everywhere. This is <u>not</u> the same as assuming that all grains are identical, for certain grains will be more efficient polarizers than others. What is assumed to be constant is the "population" of grains, apart from density variations, and the subset of this population which makes the major contribution to the polarization.

There is some evidence to support this assumption. The wavelength dependence of the polarization is fairly unique (Stokes et al 1974), and this requires a consistent grain population. Chemical variations may be important; although only a few elements are involved their abundance ratios have been shown to vary with direction (Gillett et al 1975). More recently circular polarization measurements (Martin 1974) have imposed exacting requirements on the possible composition of the grains, and it now appears that the grain type is universally constant. When we calculated the stellar distances we made note that R was practically a constant (Serkowski et al 1975), and since R is related to the wavelength of maximum extinction, which is determined by the mean grain size, this would appear to suggest a constant size distribution. As we have already used this concept in calculating the stellar distances we are merely applying a consistent argument to the polarization data. More dangerous assumptions concern the variations of the grain density and magnetic field strength. The distribution of dust is clearly not uniform, and it appears to be concentrated in "clouds" of varying density, with sizes ranging between 100 and 1000 parsecs (Neckel 1967, Fitzgerald 1968, Cahn and Nosek 1973). As a result of this structure the rate of production of polarization along the line of sight will not be constant. The existence of irregularities in the magnetic field will have a similar, but more important, effect as the polarization is proportional to B^2 but only proportional to ρ_g. Unfortunately it is not possible to separate the contributions of these effects in the observed polarization variations. As we are primarily interested in the topography of the magnetic field (subsequently referred to as "the field"), we shall assume that <u>ρ_g is a constant</u>, and use the variations of the polarization to study the field variations.

A better approach would be to use empirically determined dust distributions, but this introduces a degree of complexity which is beyond the scope of the present analysis.

2.4 E-vector Plots of the Starlight

As a first step in our analysis we have made plots of the E-vectors of the starlight against galactic coordinates in a fashion similar to that of Mathewson and Ford (1970). In these plots, the magnitude, p, of the polarization is simply represented by the length of the line as indicated by the accompanying scale; the orientation of the line with respect to the vertical, in an anticlockwise direction, gives the position angle θ of the starlight. We have used distance intervals identical to those of Mathewson and Ford (1970) so that a direct comparison between their maps and ours can be made This enables us to check that systematic errors have not been introduced into the data during the reduction process described in section 2.3, and also enables us to see the effect of the new data. There is one major difference between our representation and that of Mathewson and Ford (1970) which is that we have abandoned the use of lines of two thicknesses in favour of one scale, as in our experience this notation has been the source of considerable confusion. The plots are divided into the following distance ranges 0-50, 50-100, 100-200, 200-400, 400-600, 600-1000, 1000-2000, 2000-4000, 4000 + pc and are shown in figures 2.4 a to i. The effect of the new data is very evident on the nearby plots (0-600 pc), and comparison between the two sets of maps shows many features in common,implying that systematic errors have not been introduced into our data during the reduction processes.

Figures 2.4 (a)-(i) The E-vectors of the linear polarization measurements plotted in galactic coordinates. The length of each line is proportional to the percentage polarization according to the scale marked in the top left-hand corner. The maps contain all stars which lie within the distance interval marked at the top of the diagram.

DISTANCE INTERVAL 0-50pc.

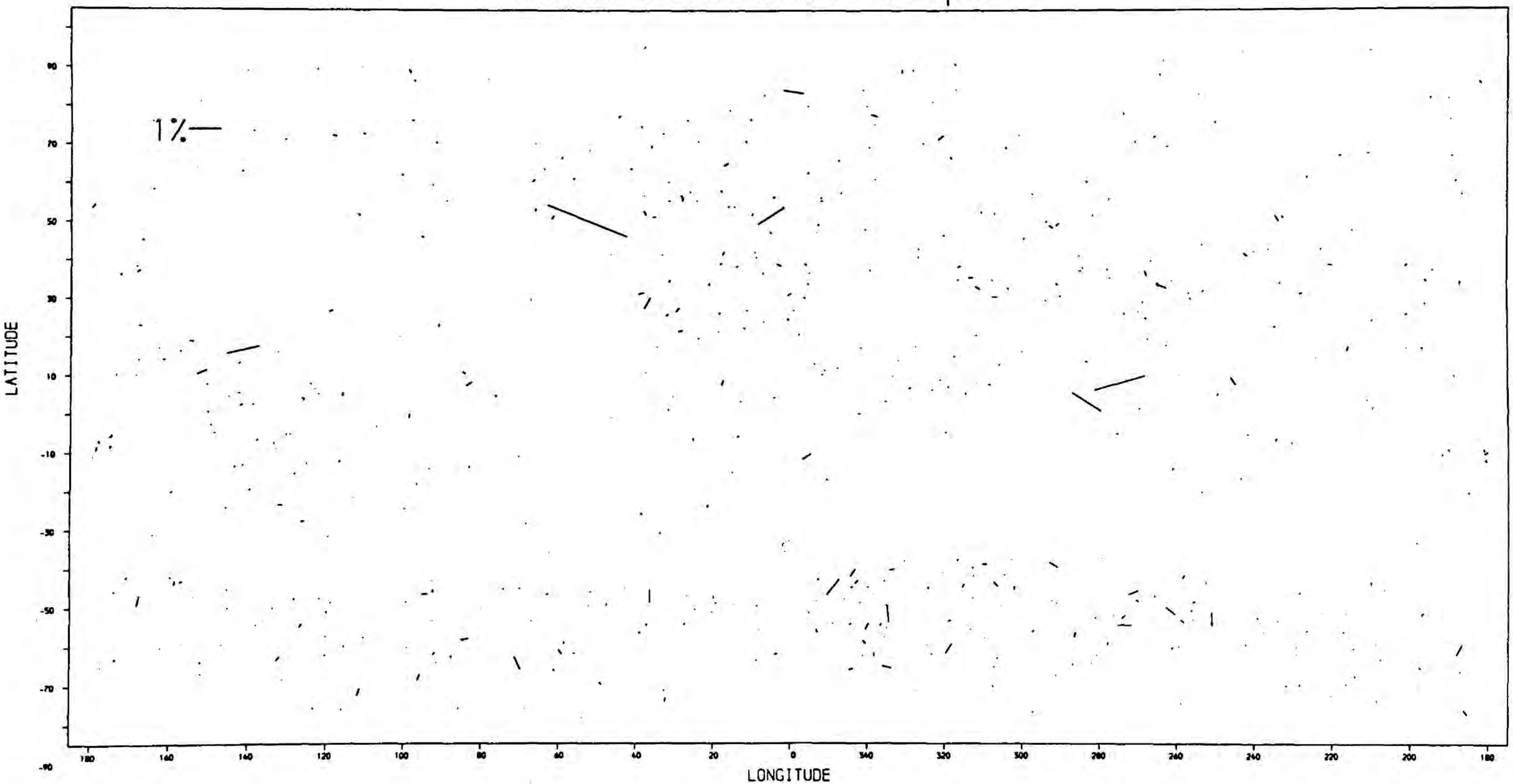

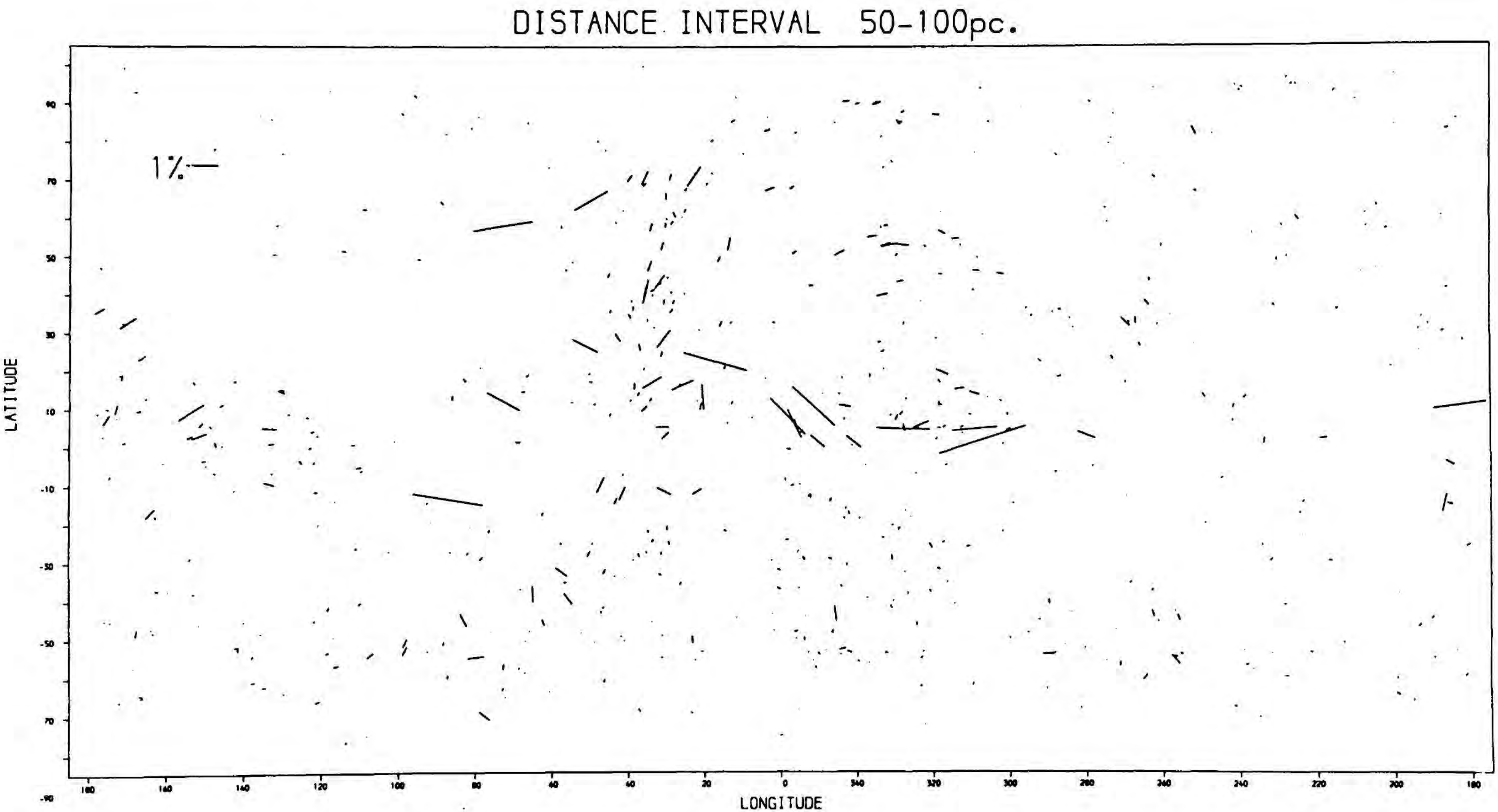
DISTANCE INTERVAL 50-100pc.
1%
LATITUDE
LONGITUDE

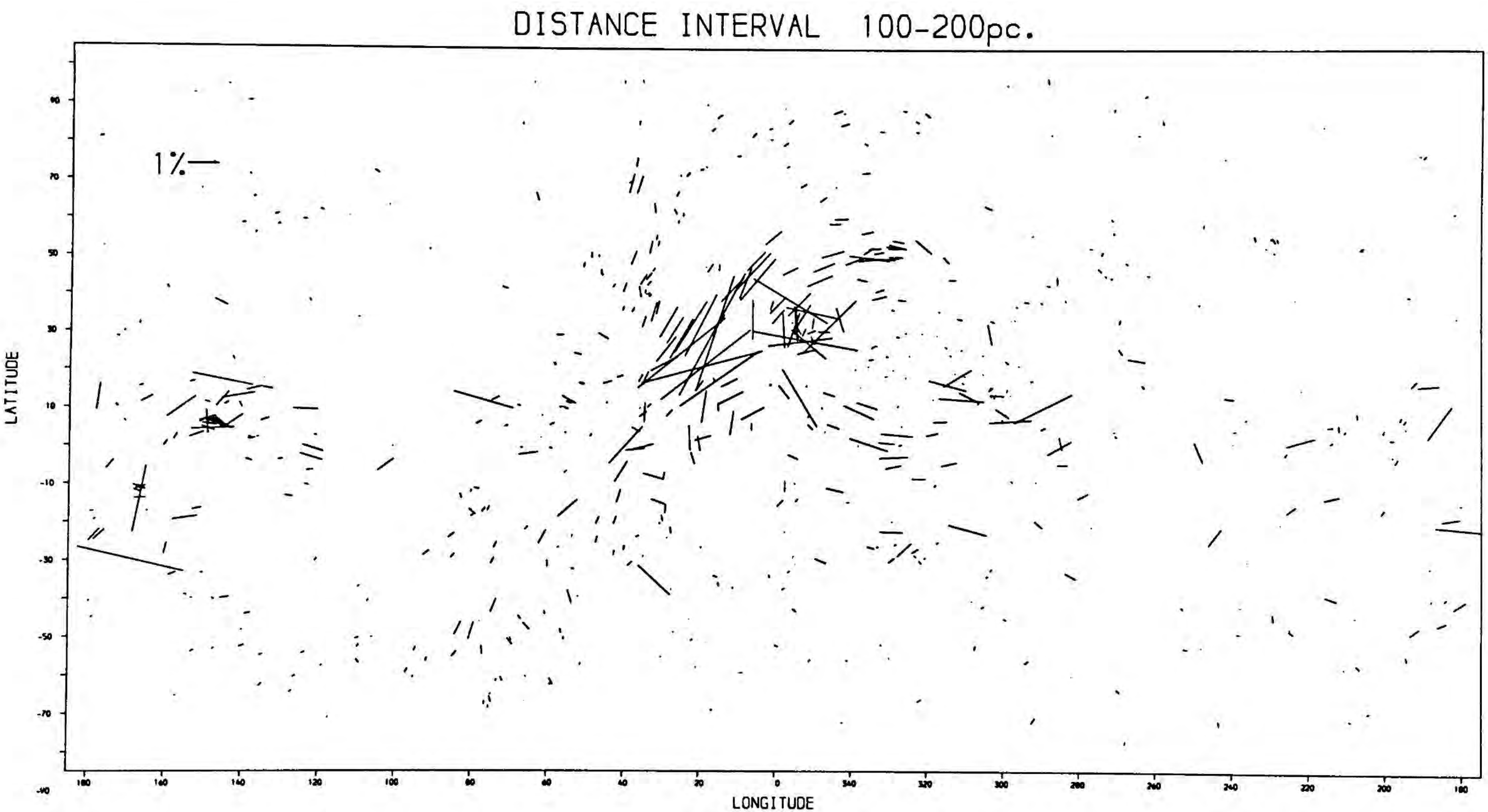
DISTANCE INTERVAL 100-200pc.
1%
LATITUDE
LONGITUDE

DISTANCE INTERVAL 200-400pc.

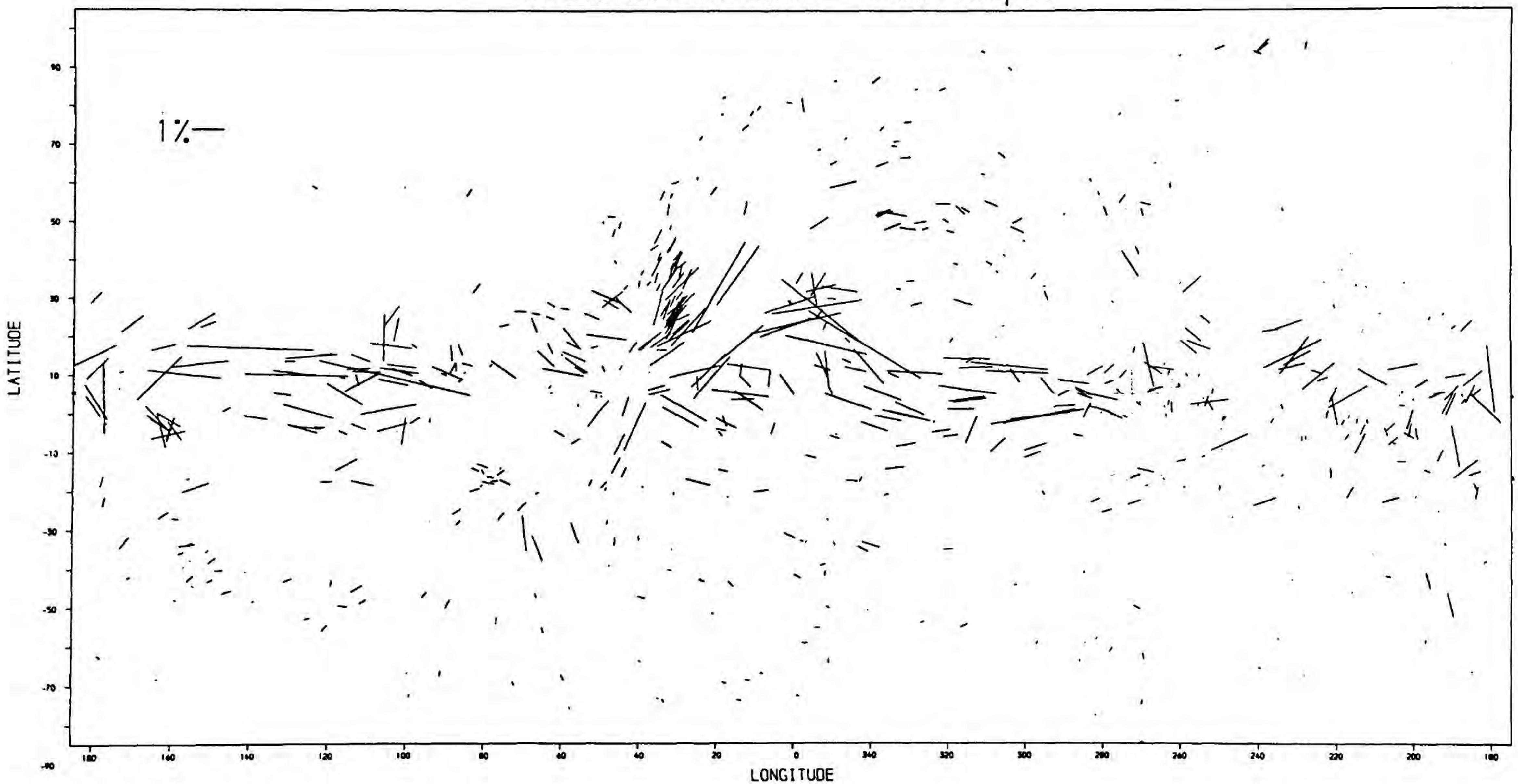

DISTANCE INTERVAL 400-600pc.

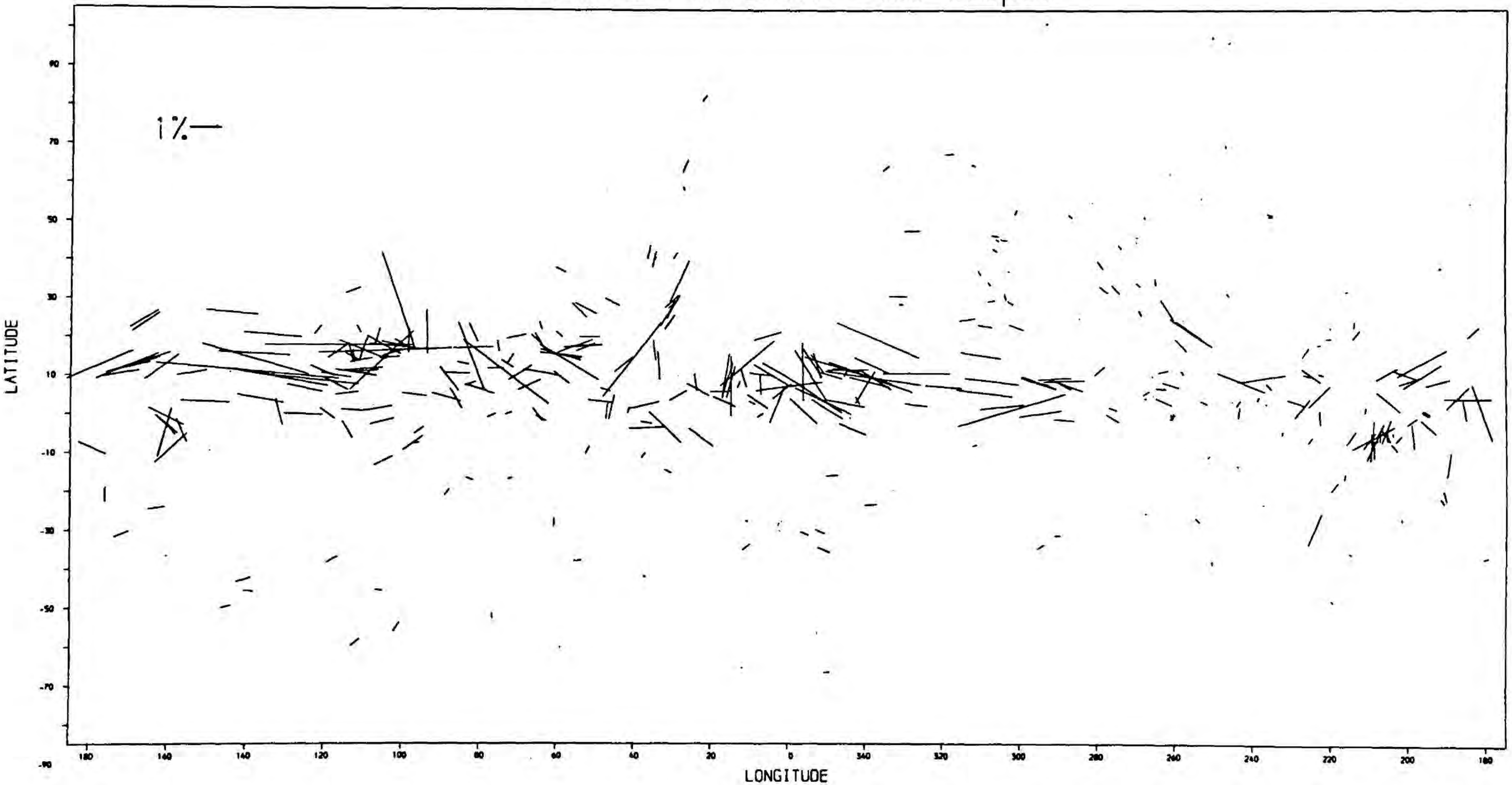

DISTANCE INTERVAL 600-1000pc.

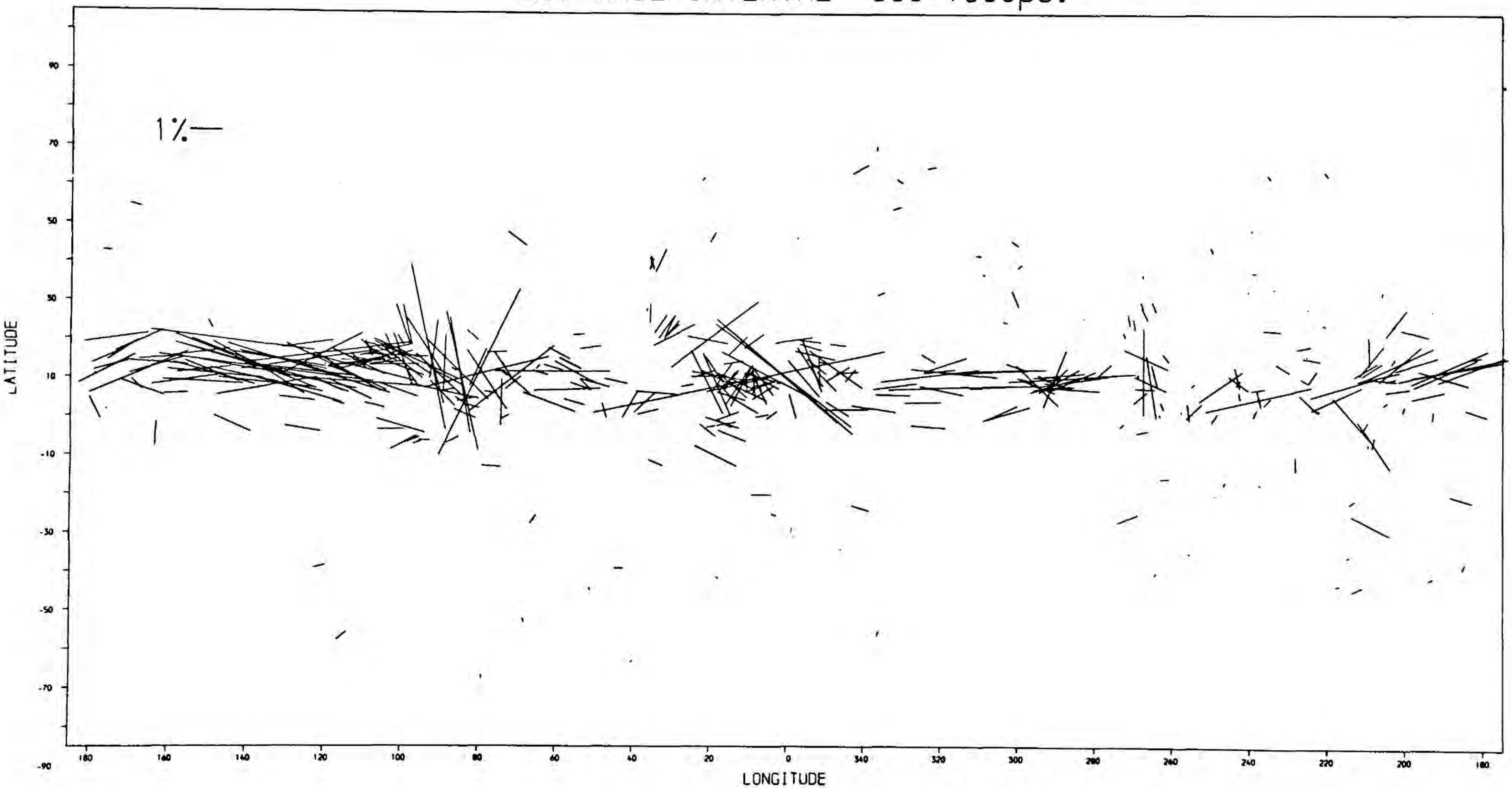

DISTANCE INTERVAL 1000-2000pc.

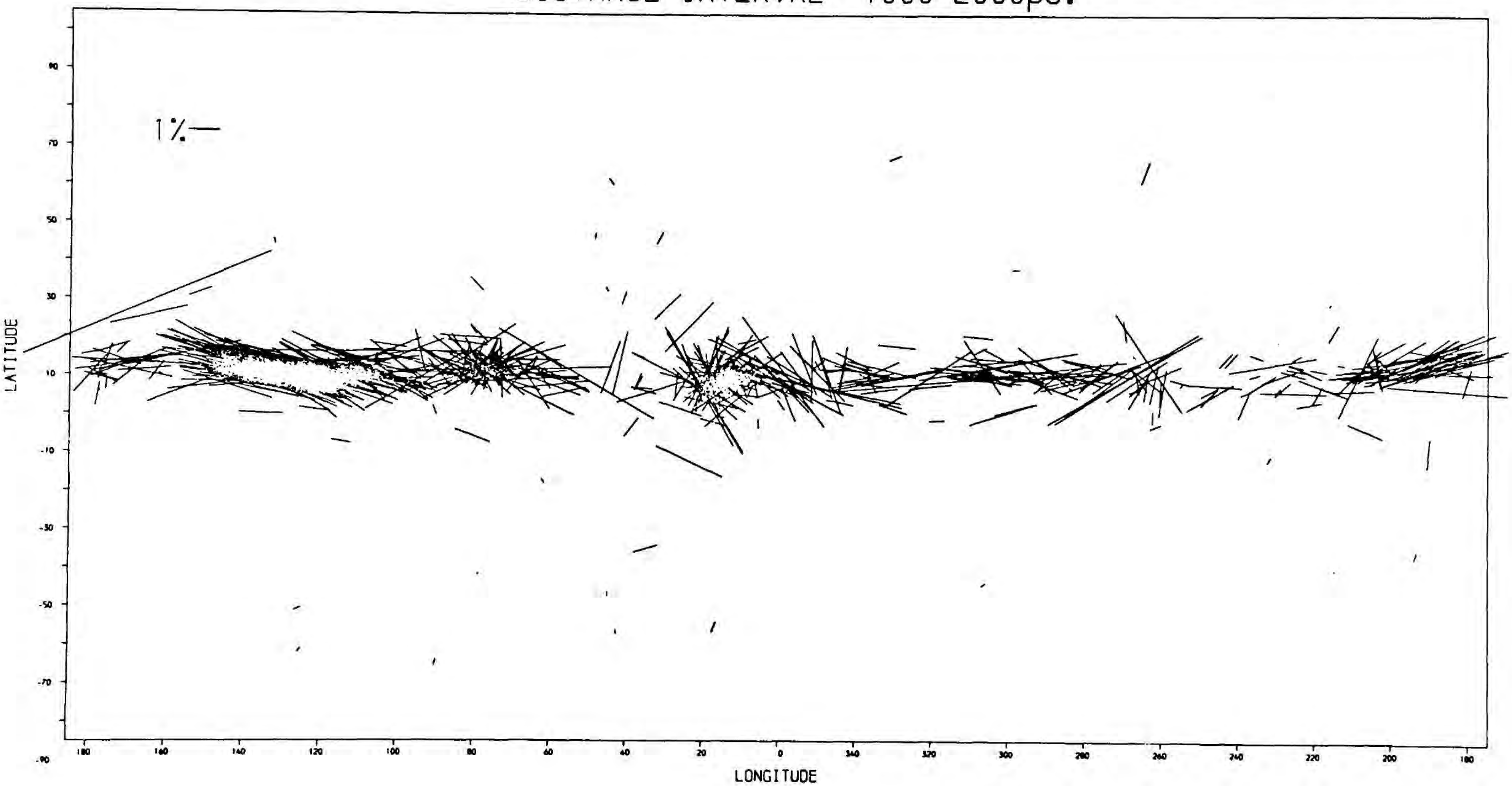

DISTANCE INTERVAL 2000-4000pc.

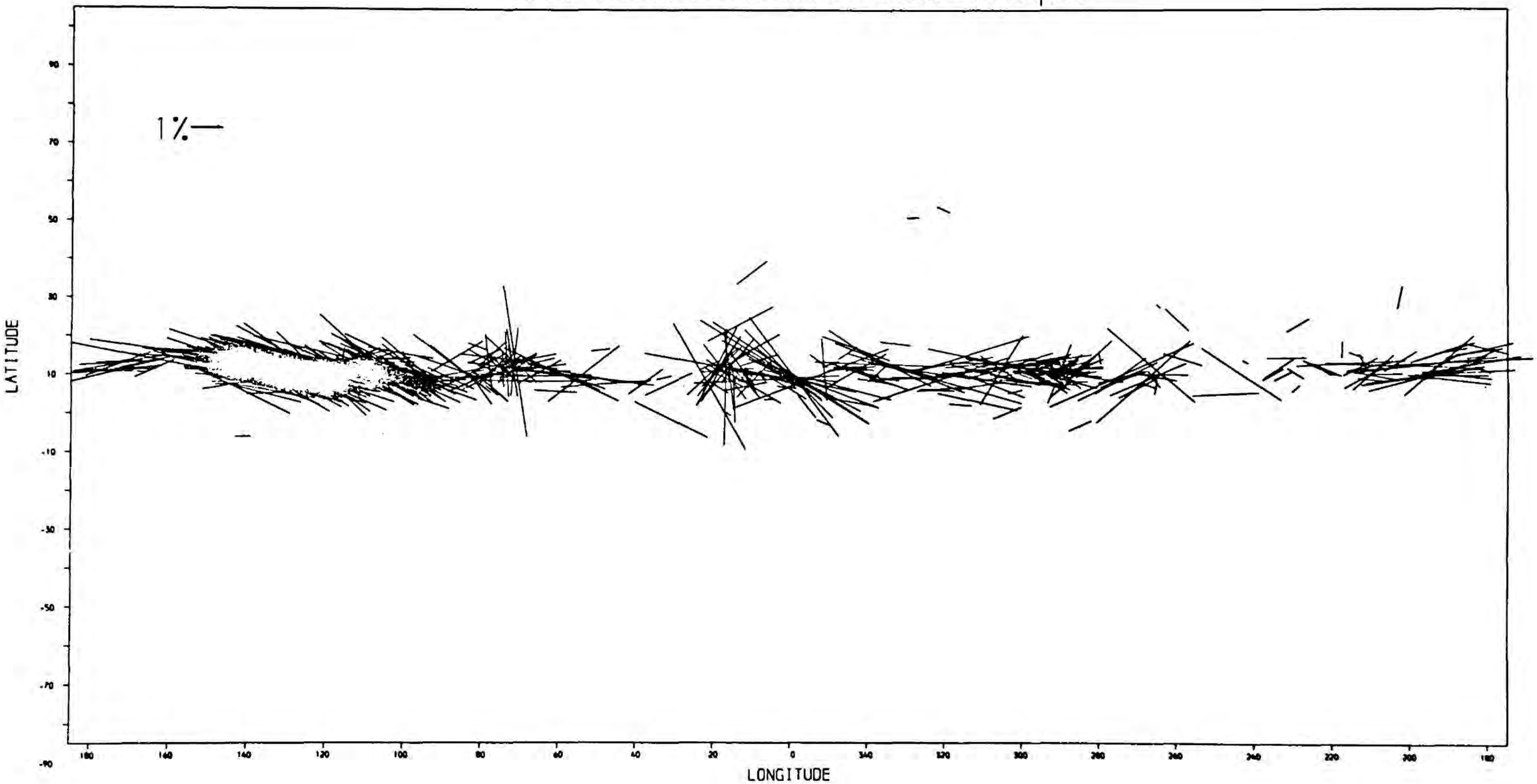

DISTANCE INTERVAL 4000+pc.

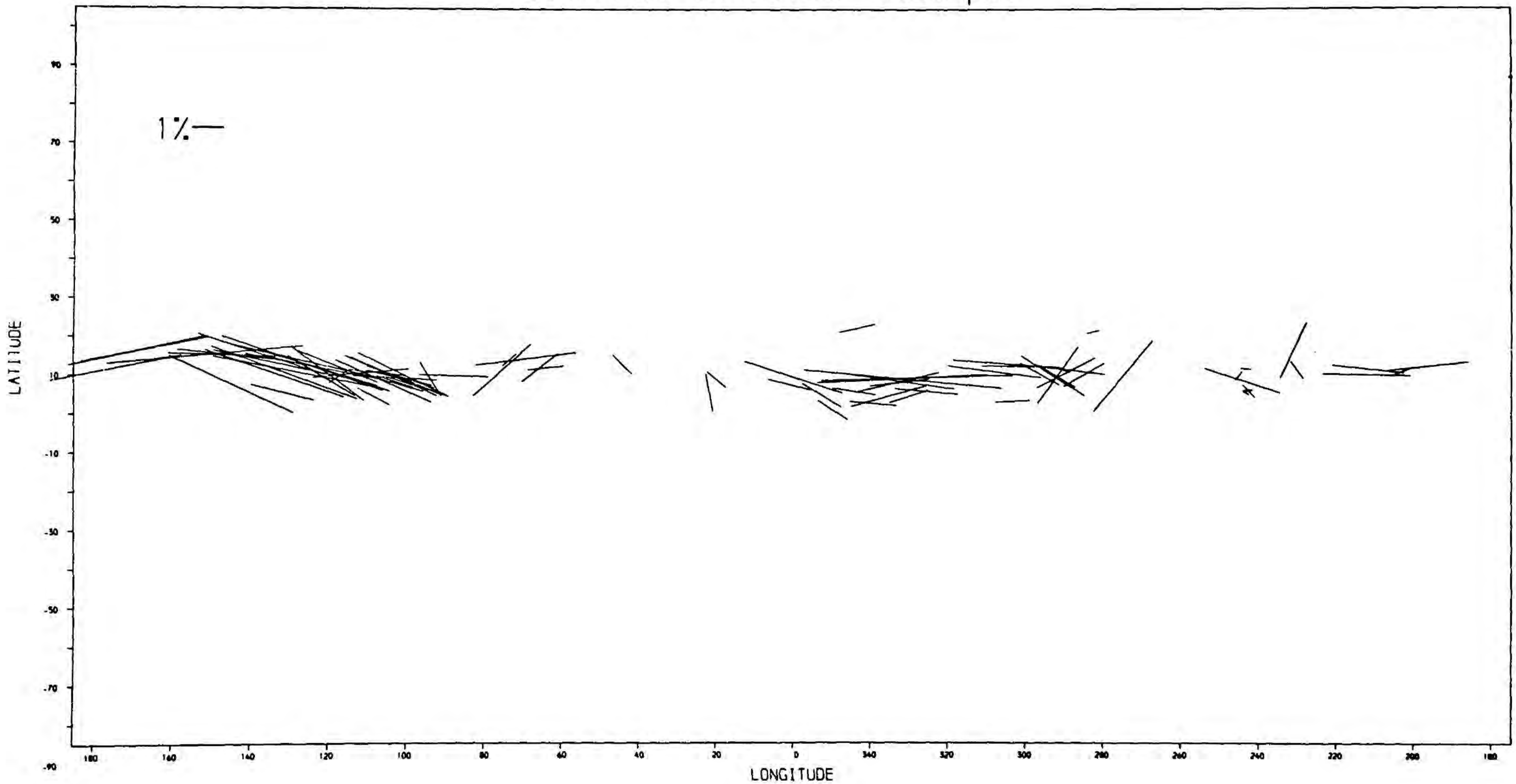

The first major features we notice on the 0-600 maps are the looping structures that first prompted Mathewson (1968) to propose the helical magnetic field. There appears to be so many of these loops visible on our plots that it seems unlikely that they are the result of a helical magnetic field model, and are better explained as the result of a tangled field produced by supernovae explosions (Spoelstra 1973). A list of the positions of these loops is given by Brand and Zealey (1975). Apart from these looping structures no semblance of order can be seen on these maps. An interesting region of "criss-crossing" vectors can be seen at $\ell \sim 45^{\circ}$ on the 100-600 pc maps, which coincides with the galactic spurs and could be a possible joining of the galactic loops. Equally apparent on the nearby maps are occurrences of "spuriously" large vectors which might be indicative of irregular structure in the magnetic field or the interstellar medium. On the 400-600 pc map the beginnings of a region of ordered vectors is visible at $\ell \sim 140^{\circ}$, which would be consistent with a magnetic field directed towards $\ell = 50^{\circ}$ rather than $\ell = 90^{\circ}$. There is no real evidence for such regularity at $\ell = 320^{\circ}$, i.e. 180° away from this direction,or at $\ell = 360^{\circ}$ which would indicate a field towards $\ell = 90^{\circ}$. The overall impression one gets from the nearby plots is the absence of any regular structure which could be attributed to a regular magnetic field (excluding the loops). Beyond 600 pc, however, the picture changes somewhat. The looping structures so prominent on the nearby plots, disappear, but since these are mainly visible at $|b| > 15^{\circ}$ and most of the data beyond this distance is concentrated in the galactic plane this is hardly surprising. Several regions of ordered vectors are distinguishable at $\ell \sim 140^{\circ}$, $\ell \sim 300\text{-}270^{\circ}$ and possibly $\ell \sim 180^{\circ}$. The ordering at $\ell \sim 140^{\circ}$ agrees well with the radio continuum data (Bingham 1967) and suggests that the magnetic field is perpendicular to this direction. The argument is supported by the chaotic pattern of vectors at $\ell \sim 50^{\circ} - 60^{\circ}$ which would be along the field direction. However, the issue is confused somewhat by a region of "criss-crossing" vectors at $\ell \sim 80^{\circ} - 90^{\circ}$ and the region of regularity at $\ell \sim 180^{\circ}$ which could be taken as indicating a field directed towards $\ell = 90^{\circ}$. There is also a possible zone of confusion at $\ell \sim 210^{\circ}$, but this is not well defined. The helical model can readily explain the alignment at $\ell \sim 180^{\circ}$ but can offer no explanation for the ordering at $\ell \sim 140^{\circ}$, and the opposite is true for a field directed towards $\ell = 50^{\circ}$.

By far the most important feature visible on these maps is the inclination of the vectors to the galactic plane in the regions of alignment. This inclination, which is so prominent on our maps appears to have escaped the attention of the other workers, including Mathewson and Ford. However, careful examination of the Mathewson and Ford plots in these regions does show evidence of this inclination, but the effect is masked by their use of two plotting scales. This inclination is $\sim 15^{\circ}$. There are two possible explanations of this effect; either the regular field is itself inclined or this inclination is the consequence of some large cloud with a systematic orientation of its own. If an inclined regular field is the explanation then this would have intriguing consequences from the point of view of the field origin (Piddington 1972). Though the general features of the data can be obtained from these plots their value is limited by the "noise" in the data. To try and overcome this problem, and to obtain a direction for the regular field, we have resorted to binning the data and examining the variations of the mean bin vectors with position. We have considered all stars having $|b| < 15^{\circ}$ and have binned these in 10 distance intervals of 200 pc, at intervals of 15° in ℓ. For each bin the average values of the Stoke parameters $\overline{Q}$ and $\overline{U}$ were calculated from the individual Stokes' parameters and then combined to give the average polarization $< p >$ and position angle $< \theta >$

$$
\begin{aligned}
< p > &= \left(\overline{Q}^2 + \overline{U}^2\right)^{\frac{1}{2}} \\
< \theta > &= \tfrac{1}{2} \tan^{-1} \frac{\overline{U}}{\overline{Q}}
\end{aligned}
\qquad (2.13)
$$

and the resulting distribution is shown in Figure 2.5. As before the magnitude p of the polarization is simply represented by the length of the line as indicated on the accompanying scale. The orientation θ is drawn such that all E-vectors parallel to the galactic plane are parallel to $\ell = 90^{\circ}$, while E-vectors perpendicular to the galactic plane are parallel to $\ell = 0^{\circ}$. This is done irrespective of direction since it facilitates a direct comparison of orientations in different places. The point is an important one, for there is a natural tendency to interpret the vectors as being in the plane of the paper, and hence in the plane of the galactic disk, whereas of course all E-vectors are perpendicular to the line of sight. From Fig. 2.5 we broadly confirm the conclusions of Klare et al that the direction corresponding to a minimum p is that from $\ell = 240^{\circ}$ to $\ell = 60^{\circ}$, though if a bend in this field were allowed, we would prefer a direction $\ell = 75^{\circ}$ beyond $\sim$ 1 kpc. Perpendicular to the field direction the polarization should be a maximum, and there is indeed good evidence for large parallel vectors in the region $\ell = 128 - 195^{\circ}$, and to a lesser extent $\ell = 300^{\circ} - 330^{\circ}$. The maximum polarization appears to be at $\ell = 135^{\circ}$ implying a field direction of $\ell = 45^{\circ}$,

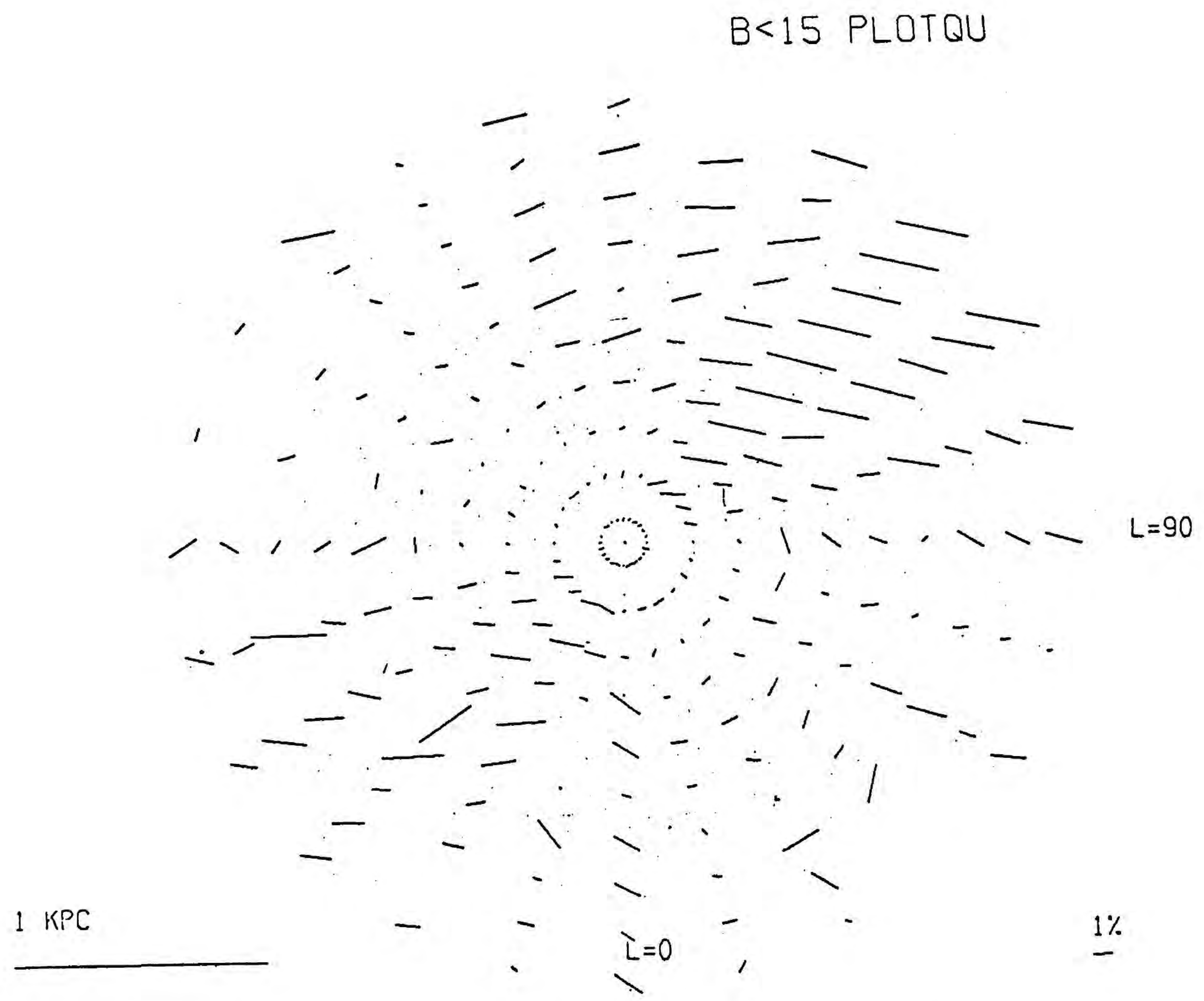

Figure 2.5 Integral polarizations for stars with $|b| \leq 15^o$; the distance scale is linear.

but there may be anomalies in this direction. Again we notice strong evidence for an inclination of $\sim 15^{o}$ in the sector $\ell = 120^{o} - 195^{o}$ and possibly a similar, though less pronounced effect at $\ell \sim 330 - 360^{o}$. A clearer representation of these variations is given by the variation in the mean bin Stokes' parameters with galactic coordinates and their development with distance.

2.5 Variations of the Stokes' Parameters with Galactic Longitude

In order to help us interpret the variation of the Stokes' parameters with galactic coordinates let us now consider a simple model of the magnetic field consisting of a regular component B_{reg} directed towards galactic coordinates (ℓ_o, b_o) and an irregular component of average magnitude B_{irr} which is random in direction. For a direction (ℓ, b) the field parallel and perpendicular to the galactic disk in the plane perpendicular to the line of sight are :

$$\begin{aligned} B_{plane} &= B_{reg} \sin(\ell - \ell_o) \cos(b - b_o) + B_{irr} \\ B_z &= B_{reg} \sin(\ell - \ell_o) \sin(b - b_o) + B_{irr} \end{aligned} \qquad (2.14)$$

Let us examine the consequences of equations 2.14 more carefully. In the interesting case $b = b_o = 0$ then the field is in the plane, and equations 2.14 reduce to

$$\begin{aligned} B_{plane} &= B_{reg} \sin(\ell - \ell_o) + B_{irr} \\ B_z &= B_{irr} \end{aligned} \qquad (2.15)$$

i.e $Q(\ell)$ which is proportional to B^2 will show a double sine wave with a minimum value at $\ell = \ell_o, \ \ell_o + \pi$. The residue at these locations indicates

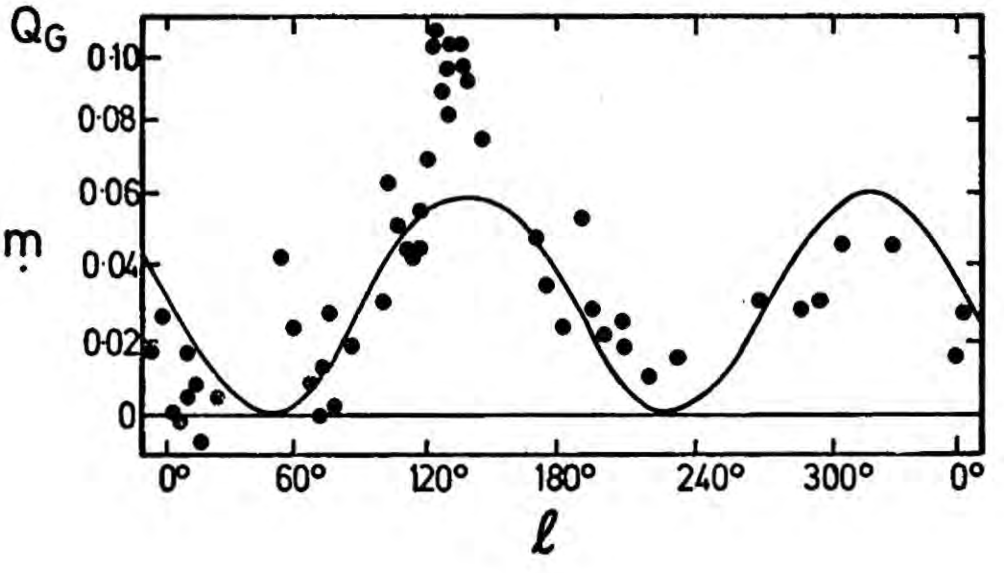

(a)

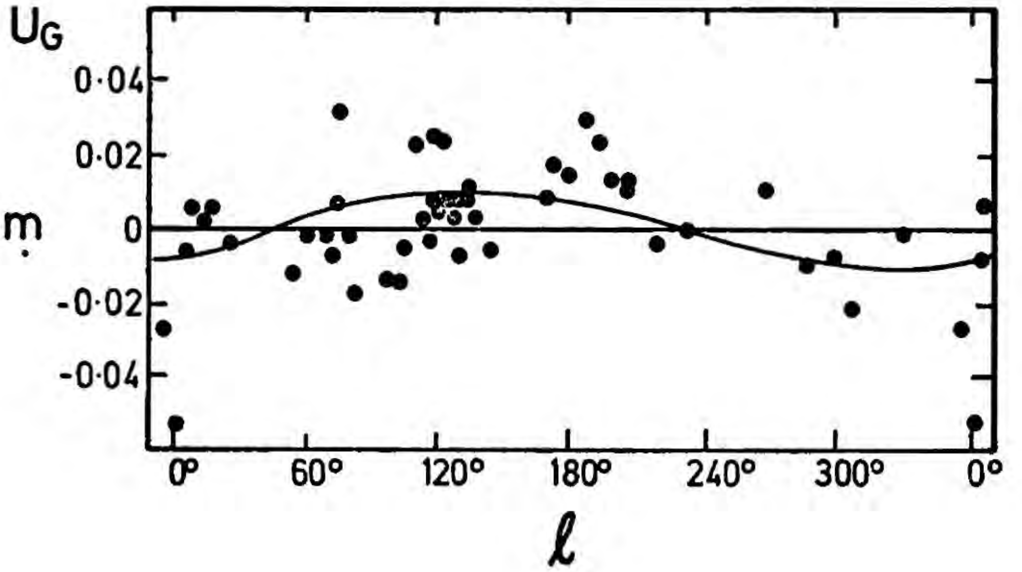

(b)

Figure 2.6 Variation of the Stokes parameters with galactic coordinates (according to Serkowski (1962))

(a) *The mean values of the Stokes parameter Q_G in intervals of galactic longitude ℓ^{II} chosen so that the numbers of stars in the interval is between 20 and 30. Only stars with $|b^{II}| < 3^{\circ}.0$ and more than 630 pc distant were used. The double sine wave is arbitrarily drawn with minima at $\ell^{II} \sim 50^{0}$ and 230^{0} (from Serkowski 1962).*

(b) *The mean values of the Stokes Parameter U_G for the same stars as those used in (a). The sine wave is arbitrarily drawn with minima at $\ell^{II} \sim 320^{0}$ (from Serkowski 1962).*

the size of B_{irr}, as does $U(\ell)$. If $B_{irr} = 0$ then $Q(\ell)$ at these minima will be identically zero and $U(\ell)$ will be zero everywhere. If however, the field is inclined at some angle $b_o \neq 0$ to the disk then from equations (2.14) we see that $U(\ell)$ will also show a sinusoidal variation, similar to $Q(\ell)$ and both Stokes' parameters will be a maximum when $\ell = \ell_o + \frac{\pi}{2}, \ell_o - \frac{\pi}{2}$. Therefore, by studying the variations of Q and U with galactic longitude it is in principle possible to deduce both the direction and inclination of the regular field and the magnitude of the irregular field. Such an analysis was carried out with a small fraction of the data now available by Serkowski (1962), who concluded that $\ell_o = 50^o$ and $b_o = 5^o$ (Figures 2.6). However, taking into account the standard deviations on his averages, which were extremely large, his plots really showed no effective variations with ℓ. Our diagrams (Fi 2.7 and 2.8) show a clear sinusoidal variation in Q, apart from the presence of two minima at $\ell < 90^o$, showing further evidence for possible anomalies in this direction. The minimum at $\ell = 225^o$ is better defined, and it is also interesting to note the unequal maxima at $\ell \sim 135^o$ and $\ell \sim 315^o$ (apparent also in Serkowski's diagram, figures 2.6). The error bars shown with each point are the standard errors on the mean bin Stokes parameter. Rather than using the minimum to determine the field direction from these plots the maximum should be used as they usually have better statistics associated with them. From these curves we therefore deduce that the field is directed to $\ell_o \sim 45^o$. (The solid curve in Serkowski's diagrams was arbitrarily drawn and ignores the unequal maxima we have just mentioned). There are two possible explanations of this feature; either the grain density is different in these two directions, or sizeable irregularities are present at $\ell \sim 315^o$,

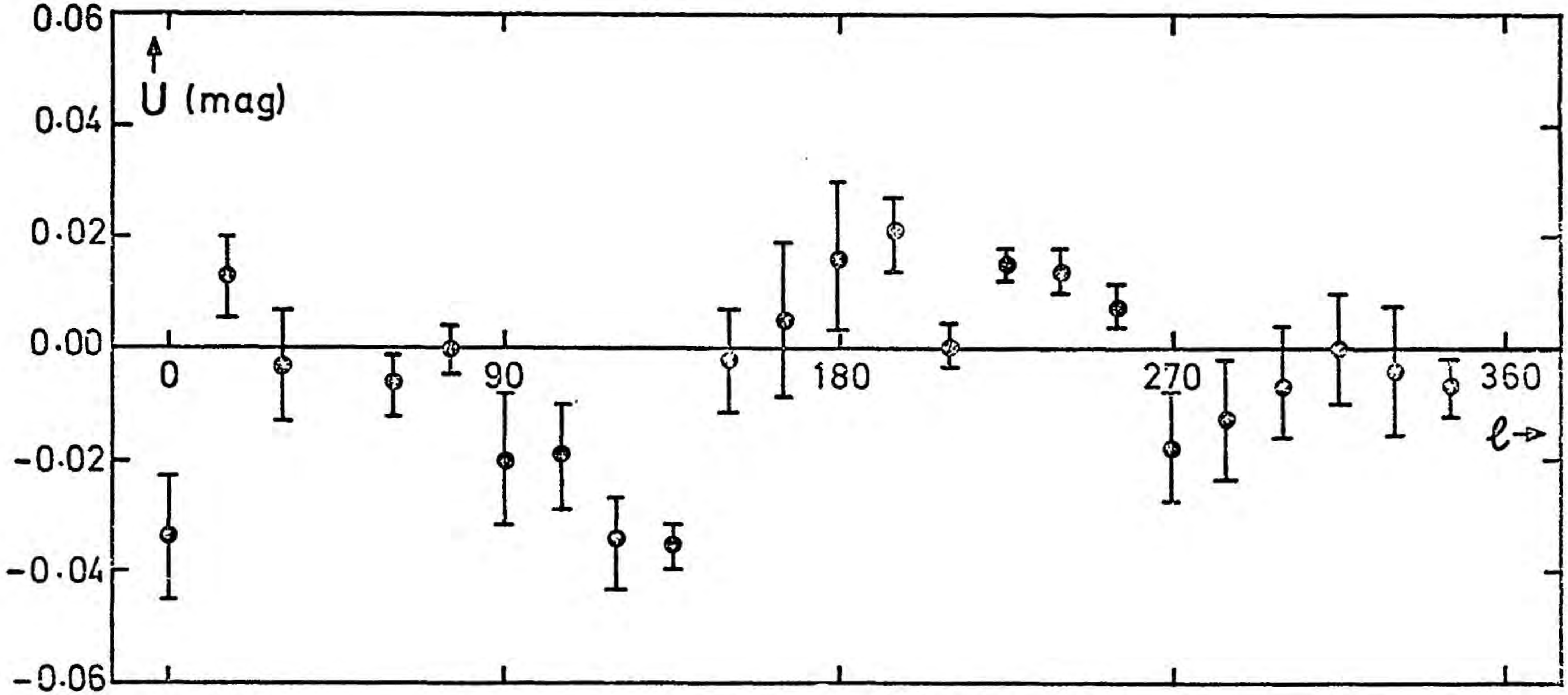

Figure 2.7 *Integrated Stokes parameter U versus galactic longitude for stars with $|b| \leq 15^{\circ}$ in the distance range 1500 - 2000 pc.*

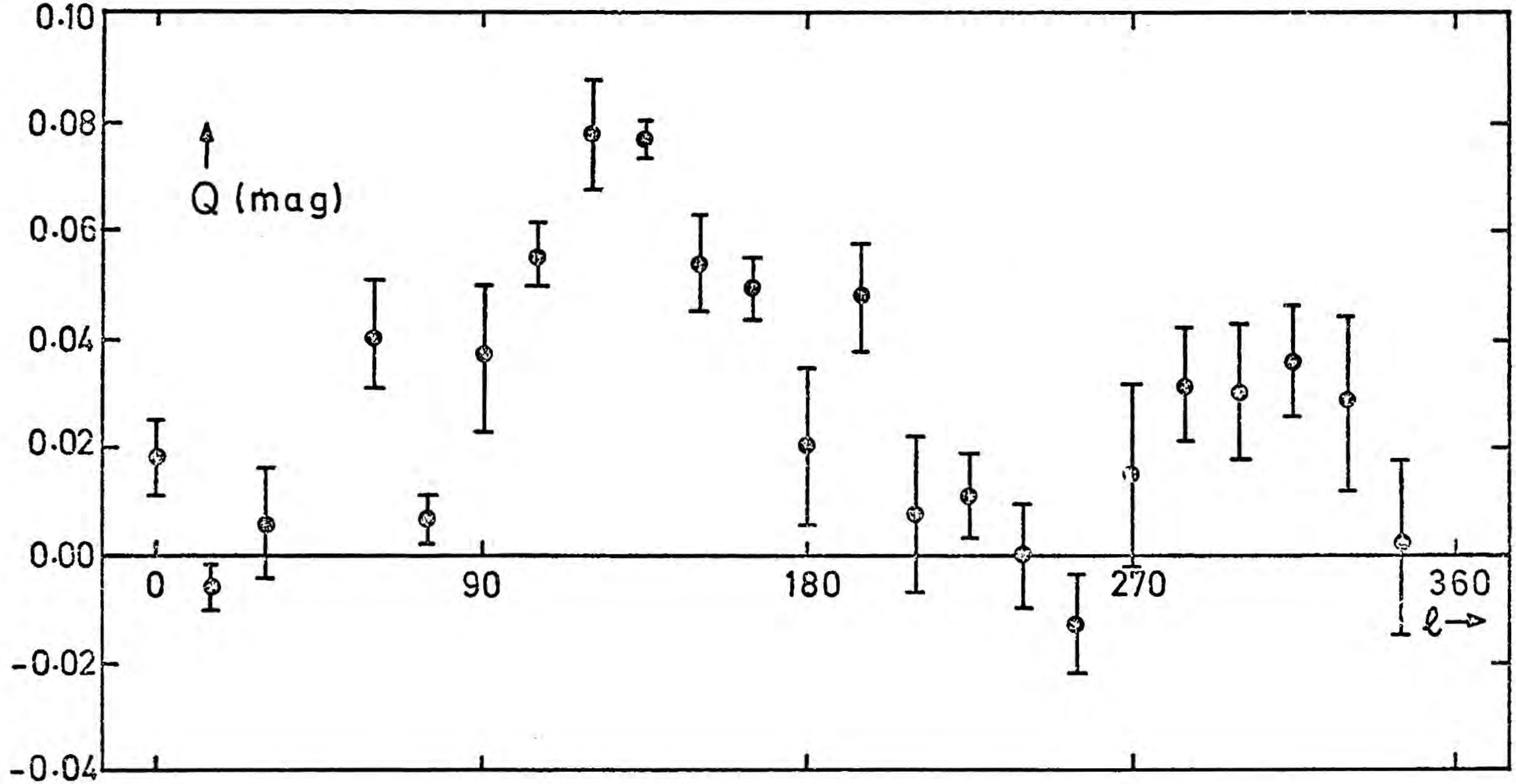

Figure 2.8 *Integrated Stokes parameter Q versus galactic longitude for stars with $|b| \leq 15^{o}$ in the distance range 1500-2000 pc.*

and on the basis of the present data it is not possible to decide between these two alternatives. A sinusoidal pattern is also evident in $U(\ell)$. The maximum in $|U(\ell)|$ agrees with that of $Q(\ell)$ at $\ell = 135^{\circ}$, but the pattern is not so well defined beyond $\ell = 180^{\circ}$ (Serkowski inexplicably draws a single sine wave, with a minimum at $\ell = 320^{\circ}$, through his data, Figure 2.6b). The existence of a sinusoidal pattern in $U(\ell)$ is consistent with either an inclined regular field (as indicated previously) or a large irregularity with its own field orientations at $\ell = 90 - 180^{\circ}$.

The residual in the sinusoidal curves is a measure of the irregular component, and from Figure 2.8 we estimate $B_{reg} \gtrsim 2\,B_{irr}$. This is independent of the possible inclination of the regular field, and agrees with the value suggested by Manchester (1974) on the basis of the pulsar data, and Smith and Wilkinson (1974) from the background radio data. If, however, the size of the irregularities is sufficiently small ($\lesssim 100$ pc) then most of the irregular contribution will cancel out along the line of sight, and thus even the value of $B_{irr} \sim 3\,B_{reg}$ found by Wright (1973) on the basis of the extra-galactic R.M.'s is not really exluded by this data.

Further information is contained in the development of $Q(\ell)$ and $U(\ell)$ with distance, as shown in Figures 2.9 and 2.10. For the regular field contribution we have $Q_{reg} \propto R$. If the number of irregularities along the line of sight, N, is large then the contribution from the irregular field $Q_{irr} \propto \sqrt{N}$, i.e $Q_{irr} \propto R^{\frac{1}{2}}$. Thus one expects the sinusoidal amplitude to decrease with decreasing distance quicker than the residual. Unfortunately the residuals represented at $\ell \sim 90^{\circ}$, 225° are too uncertain to fully justify this effect. The sinusoidal curve does however decrease, and in fact we

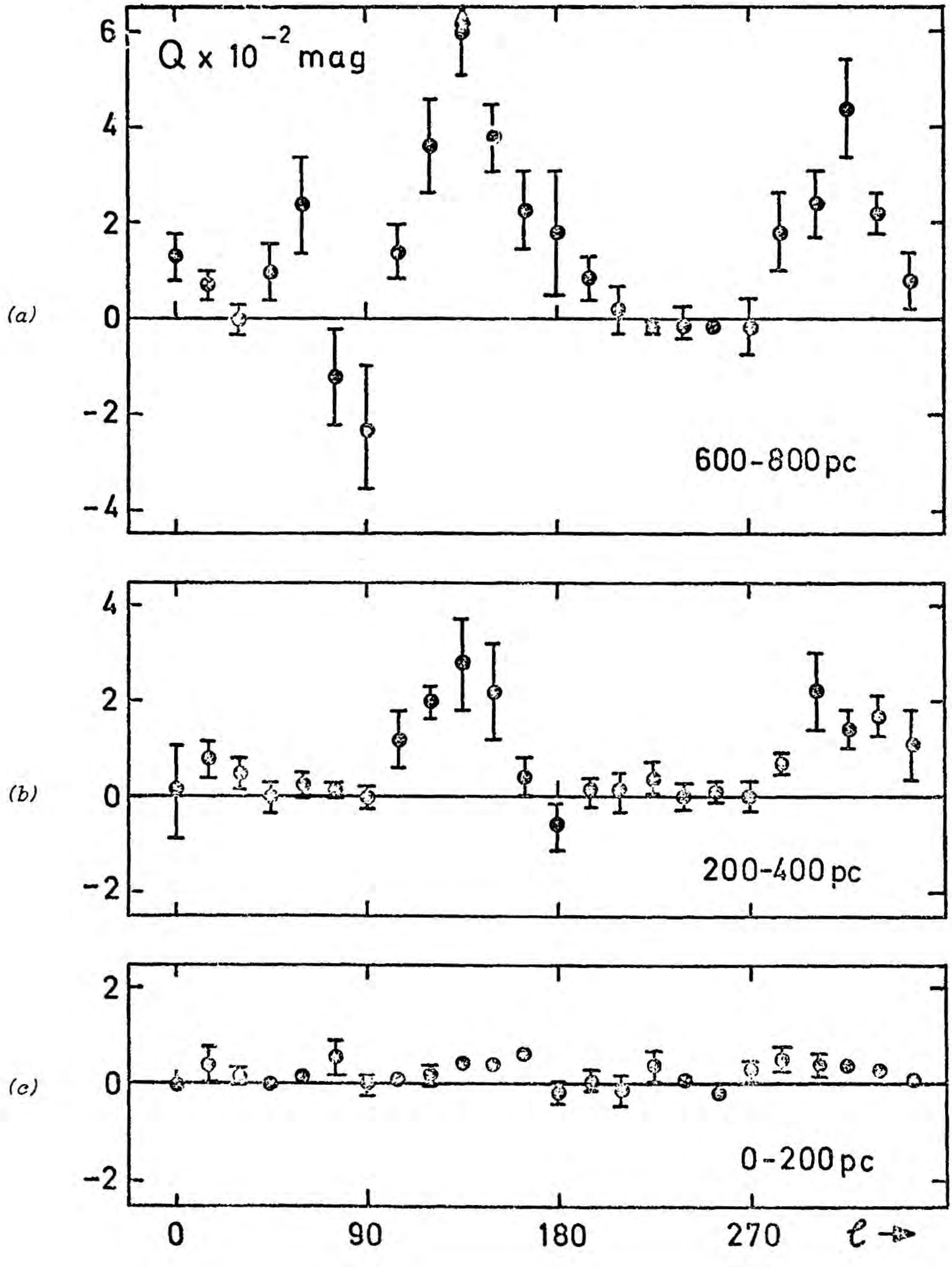

Figure 2.9 Development of Q(ℓ) with distance.

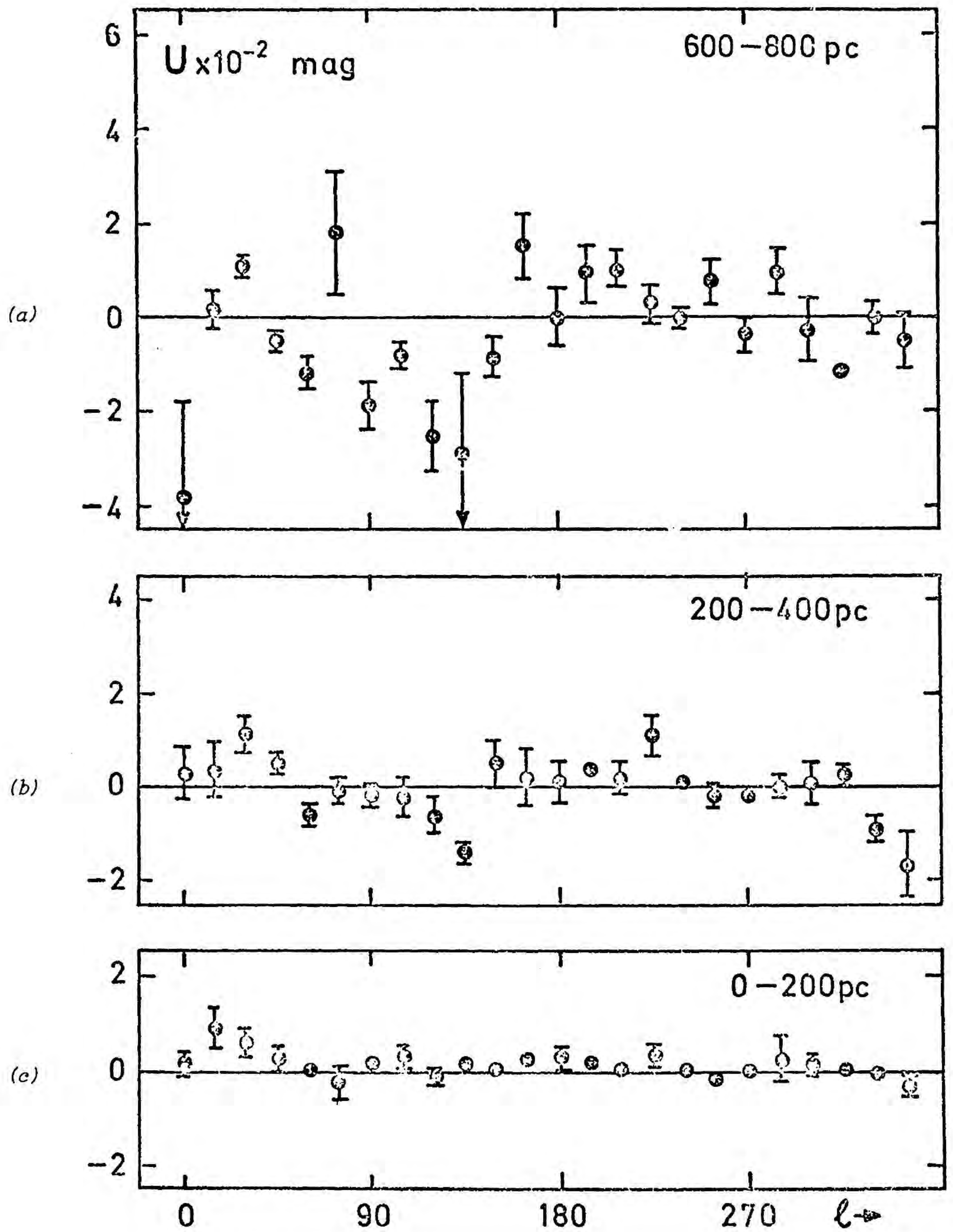

Figure 2.10 Development of U(ℓ) with distance.

note its total disappearance in Figure 2.9c, but many of these small polarizations are adversely affected by observational errors. Figure 2.10 shows a similar effect, further justifying the inclined field hypothesis.

Now in the case of a solely regular field, since $Q_{reg} \propto R$, the Stokes parameters should increase linearly with distance. Behr (1962) and Jokipii et al (1969) have reported this to be the case. However, Verschuur (1972), Drombovskii (1959) and Loden (1961) all state that in certain directions the degree of polarization increases steadily out to 1 kpc and then becomes saturated at greater distances. For each longitude interval we have traced the development of $Q(\ell)$ and $U(\ell)$ with distance. Figure 2.11 shows the development of Q and U for the $\ell = 135°$ direction, and this curve is typical of those for the other directions of ℓ. The error bars on these curves represent the bin standard deviations. These graphs quite clearly support Verschuur's claim that the polarization is predominantly produced within 1 kpc of the Sun, and saturates beyond this distance. Verschuur (1972) explains this saturation as a consequence of a "scale-length" of the irregularities, and indeed Osborne et al (1973) used curves such as Figure 2.11 to determine this quantity. Jokipii et al (1969) used the dispersions σ_Q and σ_U, based on 500 stars, for the same purpose. Our curves are based on much smaller tolerances in ℓ and distance, and yet we have statistics that are at worst 2-3 times as good as theirs, and generally 7-8 times as good. The dispersion on our Figures show no obvious correlation with distance, which is contrary to the conclusion of Jokipii et al, and moreover, we believe that they are too large to be used for this purpose. This criticism applies equally to the conclusions of Osborne et al. We re-examine the "scale-length" of the irregularities in section 2.7.

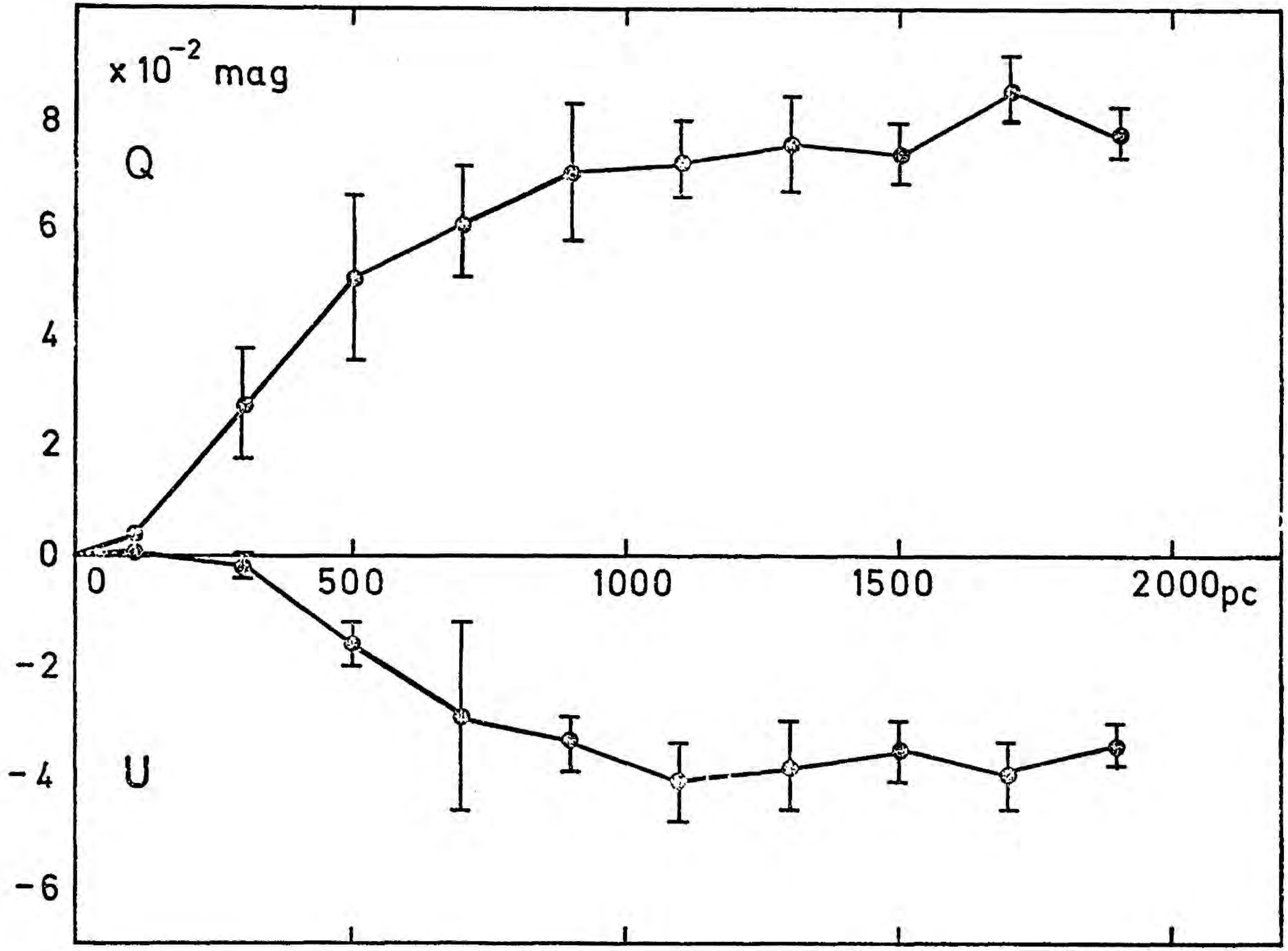

Figure 2.11 Integrated Stokes parameters Q and U versus distance for stars with $|b| \leq 15^{\circ}$ in the direction $\ell = 135^{\circ}$.

There is also a selection effect which might explain this behaviour. Supposing that Q and U increased linearly with distance, then extrapolating Figure 2.11 to 1500 pc we would observe $p = 0.^{m}15$. For a p/A_V ratio of $\lesssim 0.06$ (Schmidt-Kaler 1958) this gives an extinction of at least $2.^{m}5$. Thus even an O-star would appear fainter than $15.^{m}0$ at this distance. Quite naturally polarization measurements have been confined to the brightest stars. This suggests that only those stars which are not strongly dimmed by interstellar extinction have been observed. There is, therefore, a tendency for only stars with low polarization to have been observed. We have searched through our data in an attempt to find support for this selection effect, but the evidence is inconclusive either way. Of course we would hardly expect to find supporting evidence in data which is subject to the selection effect we are trying to detect. In order to investigate this effect we suggest that a new observational programme is required. The programme stars should be highly reddened O-stars. If our proposal is correct then these stars should have large polarizations $\gtrsim 0.^{m}12$. We appreciate the serious difficulties encountered in observing such faint stars, but the confirmation of the selection effect would be very important.

2.6 Incremental Polarization; The Magnetic Field and the Spiral Arms

The possibility of a selection effect with stars beyond $\sim$ 1 kpc makes comparison with spiral arm maps rather uncertain. For investigating such corrections we have constructed "incremental polarization" maps. This technique (first used by Fowler and Harwit 1974) makes use of the additive properties of the Stokes' parameters. The observed Stokes' parameters are the result of integration along the line of sight. The aim of the technique is to "differentiate" the Stokes' parameters and thus find the polarization contribution δp, at a given location (equation 2.12). As before the stars were binned in distance and longitude, and the incremental polarization calculated in the following manner. Suppose we have two adjacent distance bins i and $i+1$ at the same longitude. For each of these bins the mean Stokes' parameters $\bar{Q}_i$, $\bar{Q}_{i+1}$, $\bar{U}_i$, $\bar{U}_{i+1}$, are calculated and the means of the nearest bin $\bar{Q}_i$, $\bar{U}_i$, are subtracted from those of the more distant bin $\bar{Q}_{i+1}$, $\bar{U}_{i+1}$, to give the incremental Stokes' parameters

$$\begin{aligned} \delta Q &= \bar{Q}_{i+1} - \bar{Q}_i \\ \delta U &= \bar{U}_{i+1} - \bar{U}_i \end{aligned} \tag{2.16}$$

The incremental polarization δp and the intrinsic position angle $\delta\theta$ are then given by equations 2.13.

$$\begin{aligned} \delta p &= (\delta Q^2 + \delta U^2)^{\frac{1}{2}} \\ \delta\theta &= \tfrac{1}{2} \tan^{-1} (\delta U / \delta Q) \end{aligned} \tag{2.17}$$

We also calculate a root-mean-square uncertainty (R.M.S.) in the intrinsic polarization $<\Delta p>$ and the position angle $<\Delta\theta>$

$$<\Delta p> = \frac{1}{\delta p} [(\sigma_Q \, \delta Q)^2 + (\sigma_U \, \delta U)^2]^{\frac{1}{2}} \tag{2.18}$$

$$<\Delta\theta> = \frac{180}{4\pi \, \delta p^2} [(\sigma_Q \, \delta U)^2 + (\sigma_U \, \delta Q)^2]^{\frac{1}{2}} \tag{2.19}$$

where σ_Q and σ_U are the incremental standard deviations

$$\sigma_Q = (\delta Q_i^2 + \delta Q_{i+1}^2)^{\frac{1}{2}}$$
$$\sigma_U = (\delta U_i^2 + \delta U_{i+1}^2)^{\frac{1}{2}} \qquad (2.20)$$

and the δ_i^2's are the bin variances given by

$$\delta Q_i^2 = \overline{Q_i^2} - \bar{Q}_i^2$$
$$\delta U_i^2 = \overline{U_i^2} - \bar{U}_i^2 \qquad (2.21)$$

Fowler and Harwit presented several incremental polarization maps (their presentation is slightly different from that adopted here) for various galactic latitudes; their maps were based on 1732 stars. We have found the analysis is extremely sensitive to small fluctuations in the polarization, and particularly to distance errors. The problem is a classic one in astronomy; small bins lead to large statistical errors, whilst large bins contain stars that may be considerably far apart. At high latitudes ($|b| > 20^{\circ}$) we certainly feel there is little point in producing such maps. In these regions there are instances of very large polarizations as Fowler and Harwit noted, but these are isolated occurrences, based on very few observations. In fact 55% of all the data lies within $|b| < 15^{\circ}$, and beyond 500 pc there is virtually no data with $|b| > 15^{\circ}$. We have,therefore, restricted our analysis to stars below this latitude. For these stars we again binned the data in 15° longitude intervals, and originally in 50 pc distance elements. However, the uncertainties in δp and $\delta\theta$ where often large, particularly in distant bins, because of the paucity of data in some of the bins. This lack of data was characterised by the vectors in successive bins oscillating by 90° in position angle. This behaviour can be understood as being a result of subtracting a foreground polarization, Q_{for},

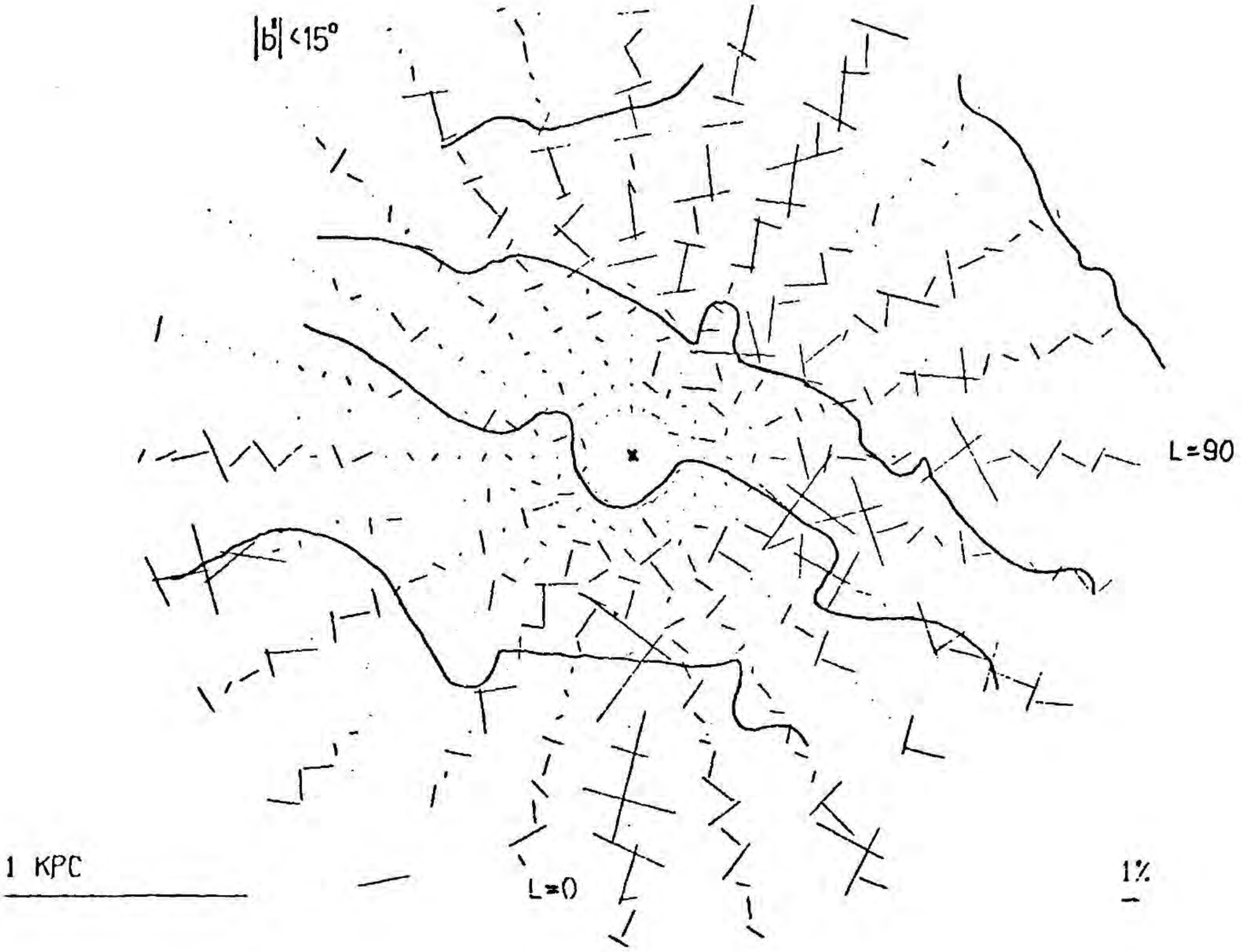

Figure 2.12 *Early incremental polarization map showing oscillating vectors.*

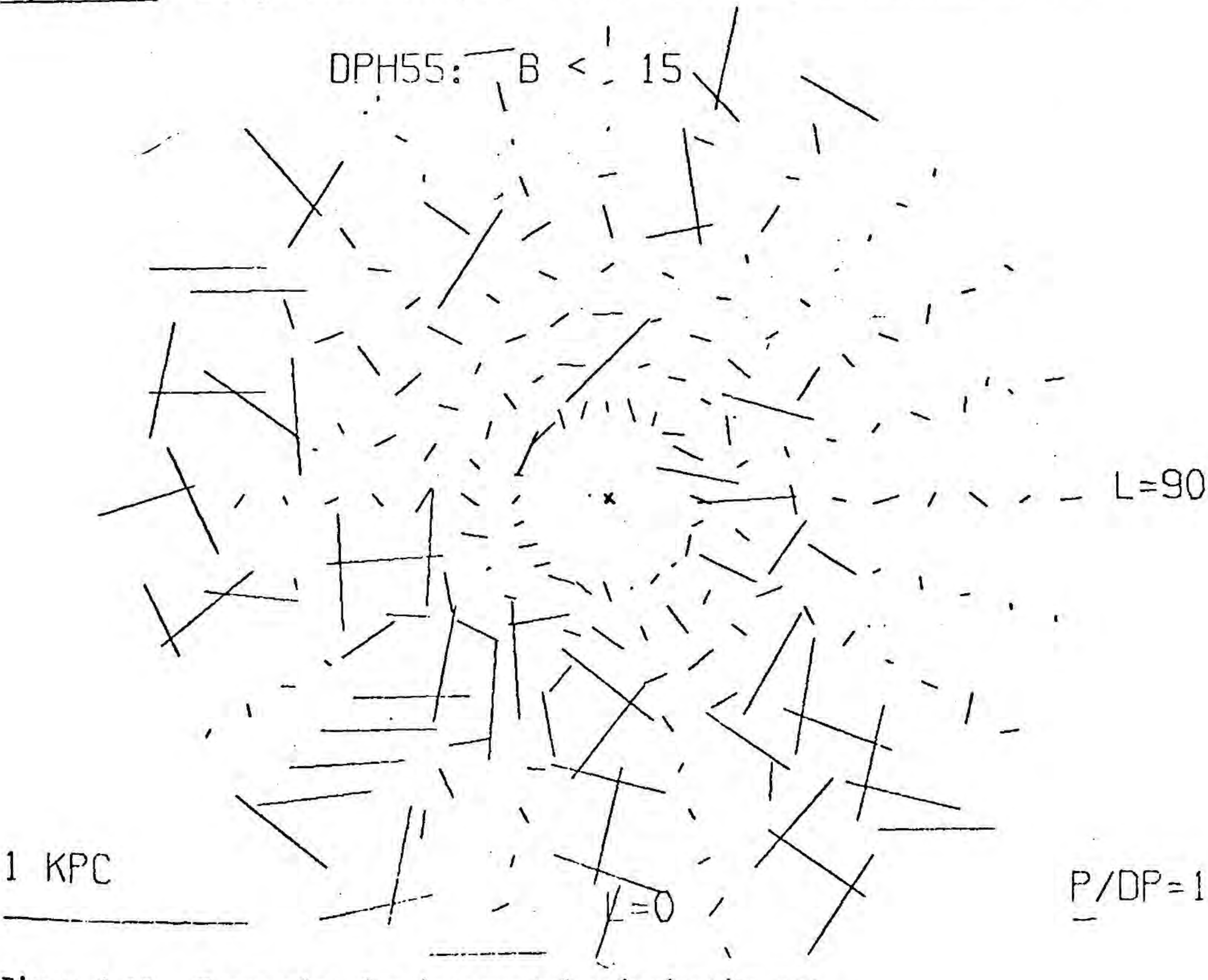

Figure 2.13 *Error plot for incremental polarization map.*

from a bin in which there is no data,then $Q_{bin} \sim 0$, so that the intrinsic polarization becomes $-Q_{for}$. At the next subtraction δQ becomes $+Q_{for}$ and so on. This effect is illustrated in Figure 2.12 which shows an early incremental map using too finer distance interval. The uncertainties in the intrinsic polarizations were in fact often greater than the intrinsic polarizations themselves, and the uncertainties in the position angles were sometimes $> 30^{o}$. In order to overcome this problem we found it necessary to have a bin size increasing with distance. By using plots of $\delta p / < \Delta p >$ and demanding that $| < \Delta \theta > | < 15^{o}$ and $\delta p / < \Delta p > \gtrsim 1$ we were able to optimise the increase in bin sizes. Figure 2.13 illustrates a typical error plot for a distance interval of 200 pc. Even though the distance interval between adjacent bins is not constant δQ and δU have been reduced to those corresponding to a fixed 200 pc increment. The incremental polarization maps are presented in two distance ranges, and the distance scale on both maps is nonlinear. Figure 2.14 presents the results beyond 250 pc with vectors at 250, 550, 1000, 1500, 2125 pc and Figure 2.15 is the map within 250 pc with vectors at 50, 112, 250 pc. Superimposed upon the former is a spiral arm map based on the positions of HII regions and young galactic clusters (Becker and Fenkart 1970) and those of X-ray sources (Schmidt-Kaler 1970). Also shown in Figures 2.16 and 2.17 are the 21 cm maps taken from Winnberg (1968) and Simonson (1970). The selection effect discussed earlier is immediately apparent in Figure 2.14. The polarizations are very large nearby, and virtually zero at 2 kpc. There seems no obvious variation between the arm and interarm regions which disagree with the conclusions of Lloyd and Harwit (1974). It is generally believed that the dust and the gas

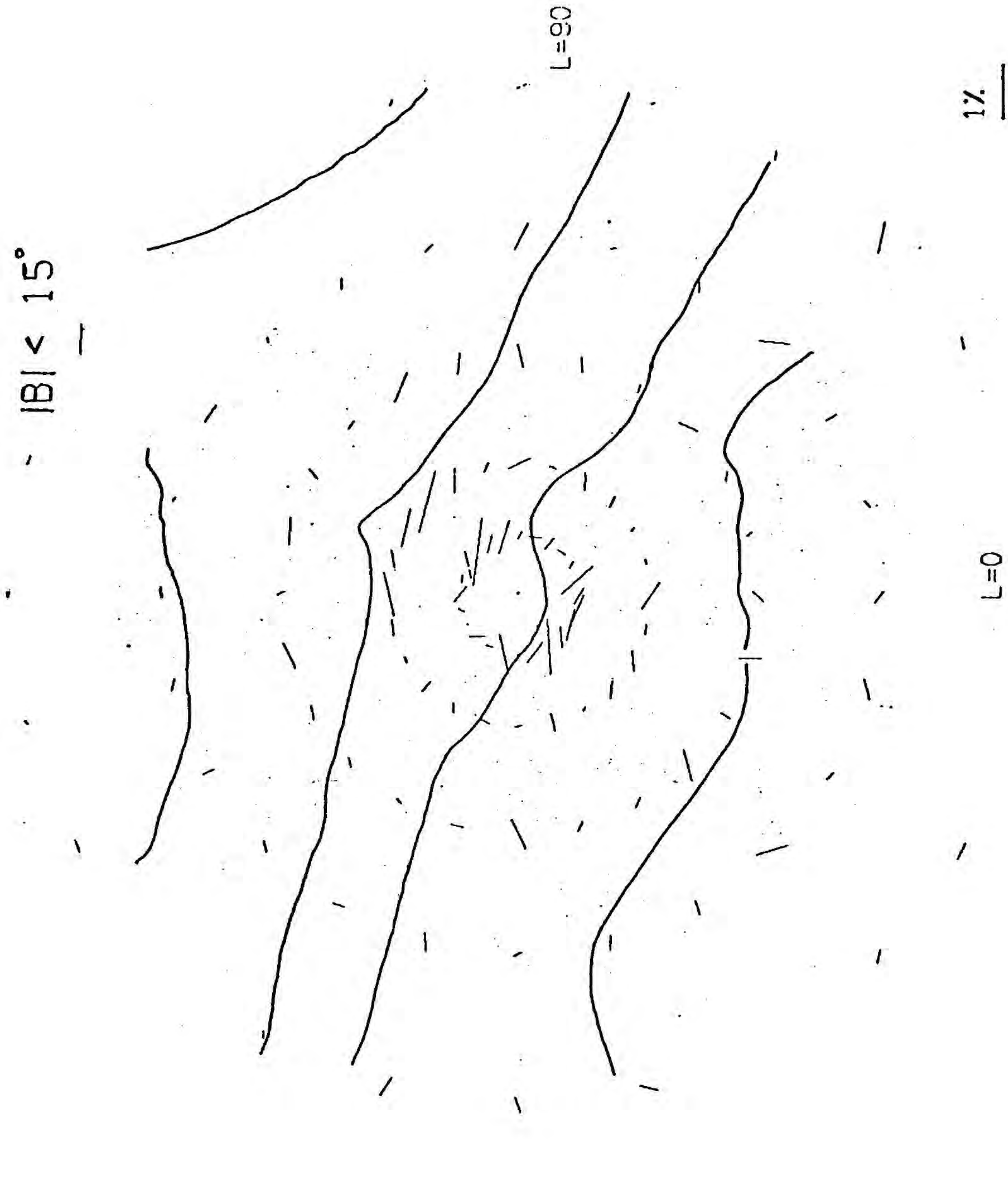

Figure 2.14 Incremental polarization map beyond 250 pc; the distance scale is non-linear with vectors at 250, 550, 1000, 1500 and 2125 pc.

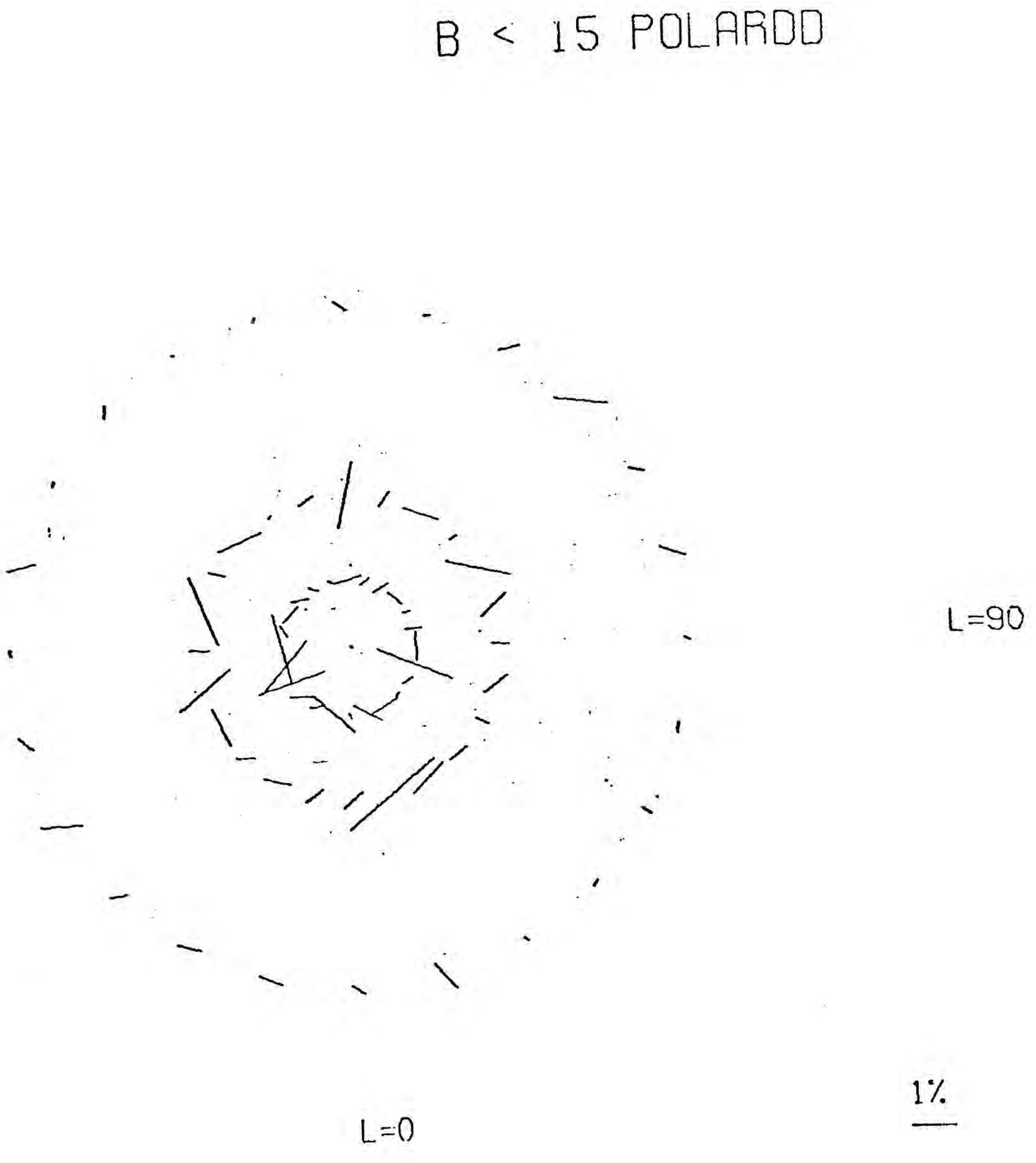

Figure 2.15 *Incremental polarization map within 250 pc; the distance scale is non-linear with vectors at 50, 112 and 250 pc.*

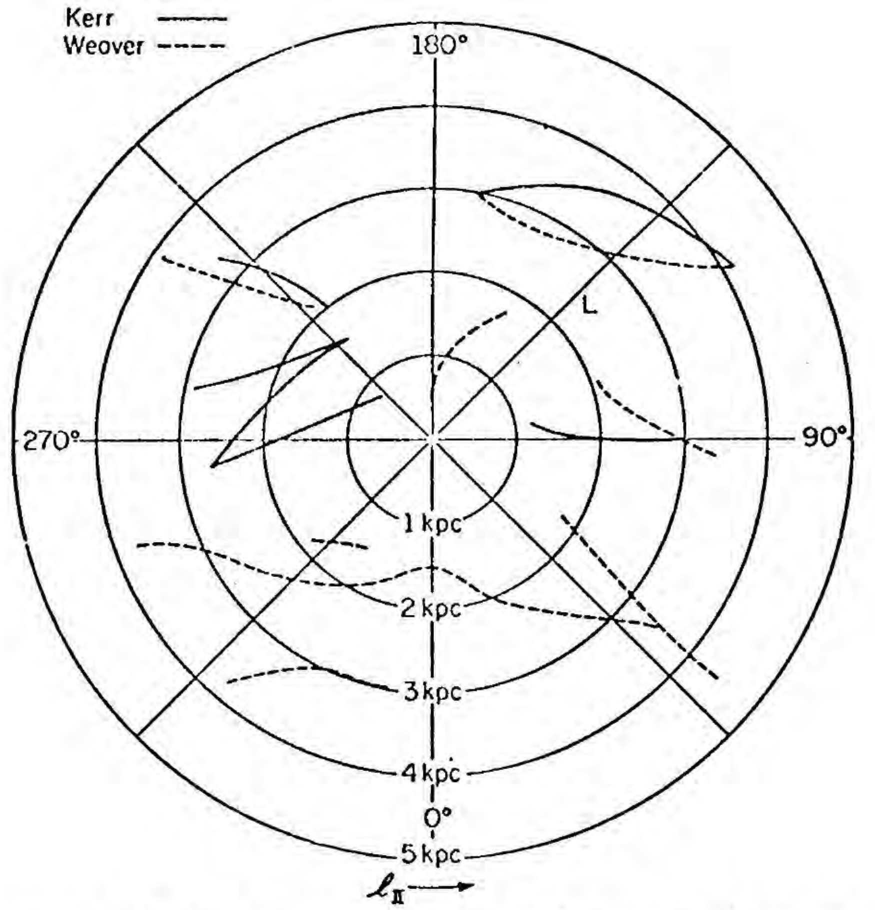

Figure 2.16 *Part of 21 cm map of Kerr and Weaver data as given in Simonson (1970).*

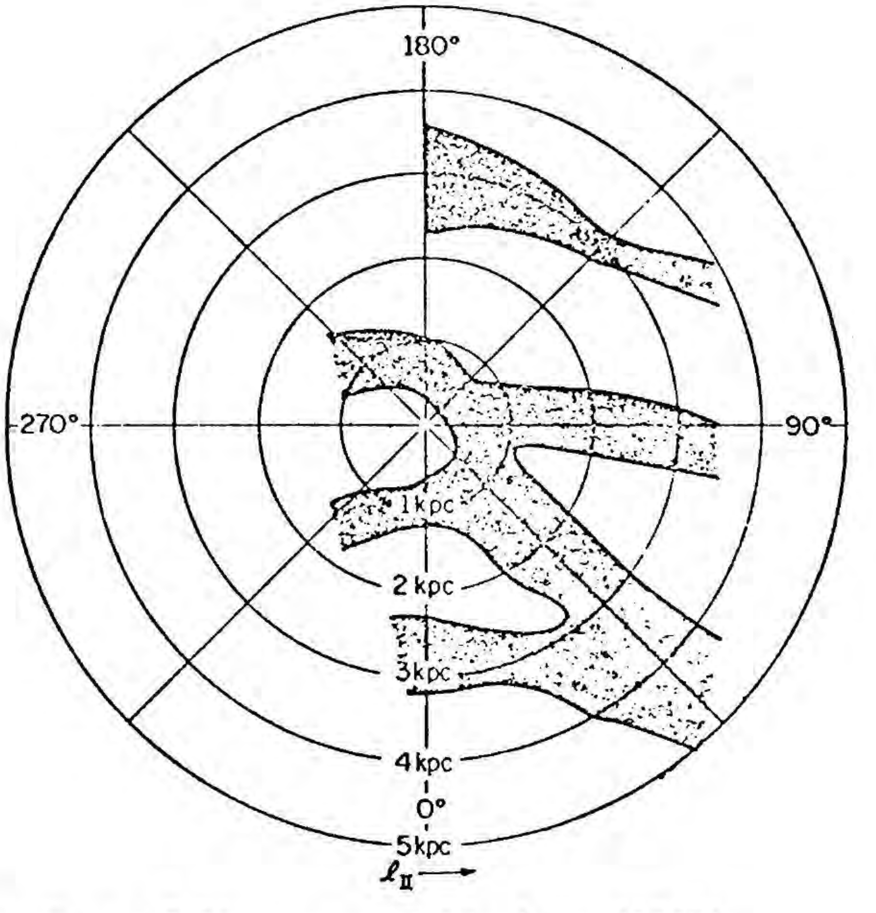

Figure 2.17 *Part of 21 cm map of Winnberg (1968).*

are correlated, in which case the polarization should fall away in the interarm regions. Clearly this is not the case, the present map being more consistent with the view of Gardener et al (1969) who suggest that the nearby polarization data is not related to the spiral structure. The most disappointing feature of these maps is the lack of systematic alignment in the directions orthogonal to the spiral arms, which would indicate that the magnetic field was indeed associated with the arms. Only at $\ell = 135^{\circ}$, and then only within 1 kpc is there any sign of order and this suggests the field runs towards $\ell = 45^{\circ}$. Even here the vectors in the Orion arm are almost identical to those in the interarm regions. Once again vectors with large inclinations are apparent everywhere, and it is particularly interesting to note the region of large inclination in the direction $\ell = 345^{\circ} - 45^{\circ}$, which is possibly the effect of the local spurs. In fact Uranova (1970) mentions a dust complex within 200 pc in that direction.

Several observers (e.g. Appenzeller 1968, Gardener et al 1969, Valleé and Kronberg 1975), have suggested that the polarization data is related to Gould's belt. In which case there should be regions of inclined vectors at $\ell = 112^{\circ}$ and 292° where this structure meets the galactic plane. On the evidence of these maps this is not justified by enhancement of the inclination at these locations.

The local map, Figure 2.15, further verifies the large increase in polarization nearby, and the vectors show little or no alignment which possibly reflects the large contribution of irregularities over such short distances. The inclination of the vectors nearby is even more pronounced than on the distant plots, lending further support to this idea. Realistically, however, we must remember that the uncertainties in δp and $\delta\theta$ are sometimes large, and some vectors are therefore not that reliable.

Shaijn (1955) and Verschuur (1970) have suggested that both dust clouds and gas clouds are elongated parallel to the magnetic field. However, Schoenberg (1964) has suggested that the dust clouds have random orientations and Hopper and Disney (1974) claim they are preferentially aligned in the galactic plane. If a correlation between the cloud orientations and the magnetic field exists it would give valuable information about local field irregularities and their relation to fluctuations in the interstellar medium. It is of course incorrect to compare the measured polarization directions with the cloud orientations as Verschuur has done, as these vectors are affected by intervening line of sight integration. The differentiating process of the incremental technique enables these effects to be removed. The magnetic field orientation at a given location can then be compared with the cloud orientation at the same location. The galactic coordinates, sizes and orientation of the clouds could be determined from the "Sky-Survey Plates" by using the COSMOS machine. Their distances would, however, have to be estimated from nearby stars and other well known features associated with the clouds. Even taking into account the uncertainty of these estimates and those of the intrinsic vectors the correlation is certainly worth investigating.

2.7 Irregularities in the Magnetic Field: A Correlation Analysis

The concept of an irregular magnetic field has already been mentioned in our previous discussion in order to explain the observed fluctuations of the polarization with position. Some attempt to quantify their strength, size and frequency has been made in sections 2.5 and 2.6 and we shall discuss those results shortly. Despite the simplicity and direct applicability of the previous methods they are, however, only useful for studying large scale features. The small-scale irregularities we have discussed are examined here using correlation techniques. The analysis to be described was carried out without distance binning, each star being treated as an individual datum point.

First we considered the autocorrelation of the observed Stokes' parameters along various directions. For given longitudes we calculated

$$C_Q(x_k) = \sum_i \sum_{j>i} Q_i Q_j \Big/ \sum_i \sum_{j>i} | Q_i Q_j | \tag{2.22}$$

where the summation is over pairs of stars for which the separations satisfy a binning interval $x_k < d_j - d_{j-1} \leq x_{k+1}$. Here we had better offer an explanation of our terminology as this might appear confusing in view of our previous statement that no distance binning was used. By "separation" we mean the distance between stars, that is to say two stars 50 pc apart have a separation of 50 pc regardless of whether their actual distances are 50 or 1000 pc. Thus each separation interval contains information taken from the complete range of star distances.

This analysis essentially checks the reality of the data since the additivity of the Stokes' parameter should lead to significant positive correlation. To help interpret the results, we have produced several "nonsense catalogues" (> 50 - 100, for statistical significance), which are arranged in the same form as the real data. A "nonsense catalogue" is a one-dimensional array of stars whose distances have been generated randomly in the range 0 - 2 kpc according to a $1/d^2$ fall-off. Increments δQ and δU were assigned randomly in the range $\pm 0.^m05$ $\pm 0.^m02$ respectively, and the total Stokes' parameters Q and U were found by addition. In such a catalogue, there is, of course, no distinction between Q and U; the purpose of generating both was only to see if the analysis is critically dependent on the size of the variations. The nonsense catalogues do not contain any regular component. The results of the integral autocorrelation are summarized in tables 2.5 and 2.6. Presented in these tables are the results for the real data and those for two typical nonsense catalogues for comparison purposes. Although the coefficients will normally be positive, negative values can occur because of the uneven distribution in distance. The larger separations are dominated by very distant (large Q_j) and local (random Q_i) data, which can lead to cases of anticorrelation. The real data shows an overwhelming preference for positive correlations, and like the nonsense catalogues, there is no unique trend with separation. It is interesting to note the remarkable correlations in Q for $\ell = 135^{\circ}$ and 319°. Indeed, the direction ℓ_o could be stimated from this alone, and also from the position of the anticorrelation in Q for $\ell = 45^{\circ}$ to 90° and for $\ell = 270^{\circ}$. Some proportion of the anticorrelation at large separations is inevitably due to the paucity of data in these regions. Nevertheless, the coefficients are in excellent agreement with the field geometry described previously.

The U coefficients show less agreement with the regular field structure. The values for $\ell = 135^{\circ}$ are again remarkably large, showing regular structure inclined to the disk; the effect is not observed at $\ell = 315^{\circ}$. The anticorrelations at $\ell = 225^{\circ}$ to 270° are not repeated at $\ell = 45^{\circ}$ to 90°. Perhaps the most important conclusion that can be drawn from the table concerns the relative values of the coefficients for the real and nonsense catalogues. The

Table 2.5

Correlation analysis of integrated Stokes' vector Q

$d_j - d_i$ (pc)	250	500	750	1000	1500
$l = 0^{o}$	0.31	0.58	0.66	0.24	-0.05
45	-0.03	0.46	0.05	-0.66	-0.41
90	-0.20	-0.06	0.38	-0.59	-0.69
135	0.99	0.99	0.99	0.99	0.99
180	0.35	0.04	0.34	0.06	-0.49
225	0.48	0.64	0.74	0.59	0.68
270	-0.26	-0.43	-0.52	-0.67	--0.22
315	0.82	0.92	0.96	0.95	0.93
Nonsense 1	0.97	0.90	0.88	0.92	0.74
Nonsense 2	0.77	0.48	0.26	0.51	0.58

Table 2.6

Correlation analysis of integrated Stokes' vector U

$d_j - d_i$ (pc)	250	500	750	1000	1500
$l = 0^{o}$	0.44	0.47	0.78	0.71	-0.25
45	0.60	0.50	0.47	0.42	0.11
90	0.85	0.53	0.37	0.64	0.22
135	0.96	0.95	0.91	0.94	0.57
180	0.00	0.19	0.49	0.01	0.14
225	-0.02	-0.02	0.04	0.15	0.71
270	0.32	-0.19	0.10	-0.33	0.07
315	0.31	-0.20	-0.49	0.05	0.13
Nonsense 1	0.62	0.69	0.61	0.44	0.09
Nonsense 2	0.91	0.84	0.93	0.93	0.97

real data is not arranged in one-dimension, there is an acceptance angle of 15° in ℓ and 30° in b. The latter constraint has virtually no effect beyond 500 pc, but the longitude angle implies a lateral displacement of $\pm$ 250 pc at 2 kpc. Thus stars that are totally uncorrelated could be brought together by this method. The coefficients in the real catalogue are, however, in many cases comparable to those in the idealized nonsense catalogues, suggesting that geometrical problems have had little effect.

We then examined the physically more interesting autocorrelation using δQ and δU

$$C_{\delta Q}(r) = \sum_i \sum_{j>i} \delta Q_i \ \delta Q_j \Big/ \sum_i \sum_{j>i} | \delta Q_i \ \delta Q_j |$$

where $\delta Q_i = (Q_{i+1} - Q_i) / (d_{i+1} - d_i)$

and r is given by

$$r = (d_{j+1} - d_j - d_{i+1} + d_i) / 2$$

i.e. the increments are normalized to a 1 pc interval. Again the same procedure was adopted for the nonsense catalogues. As expected, they gave $|C| \lesssim 0.2$ for all separations.

Some of the results for the catalogue are presented in Figures 2.18 and 2.19. Although the curves are very noisy it is evident that $C_{\delta Q} \approx 0$ for $\ell = 45^{\circ}$ and 225°, whereas there is a marked area of positive correlation for $r < 1$ kpc in the orthogonal directions $\ell = 135^{\circ}$, 315°. The results for $C_{\delta U}$ show similar though less prominent features. The erratic behaviour of the correlation curves tends to suggest that it is a consequence

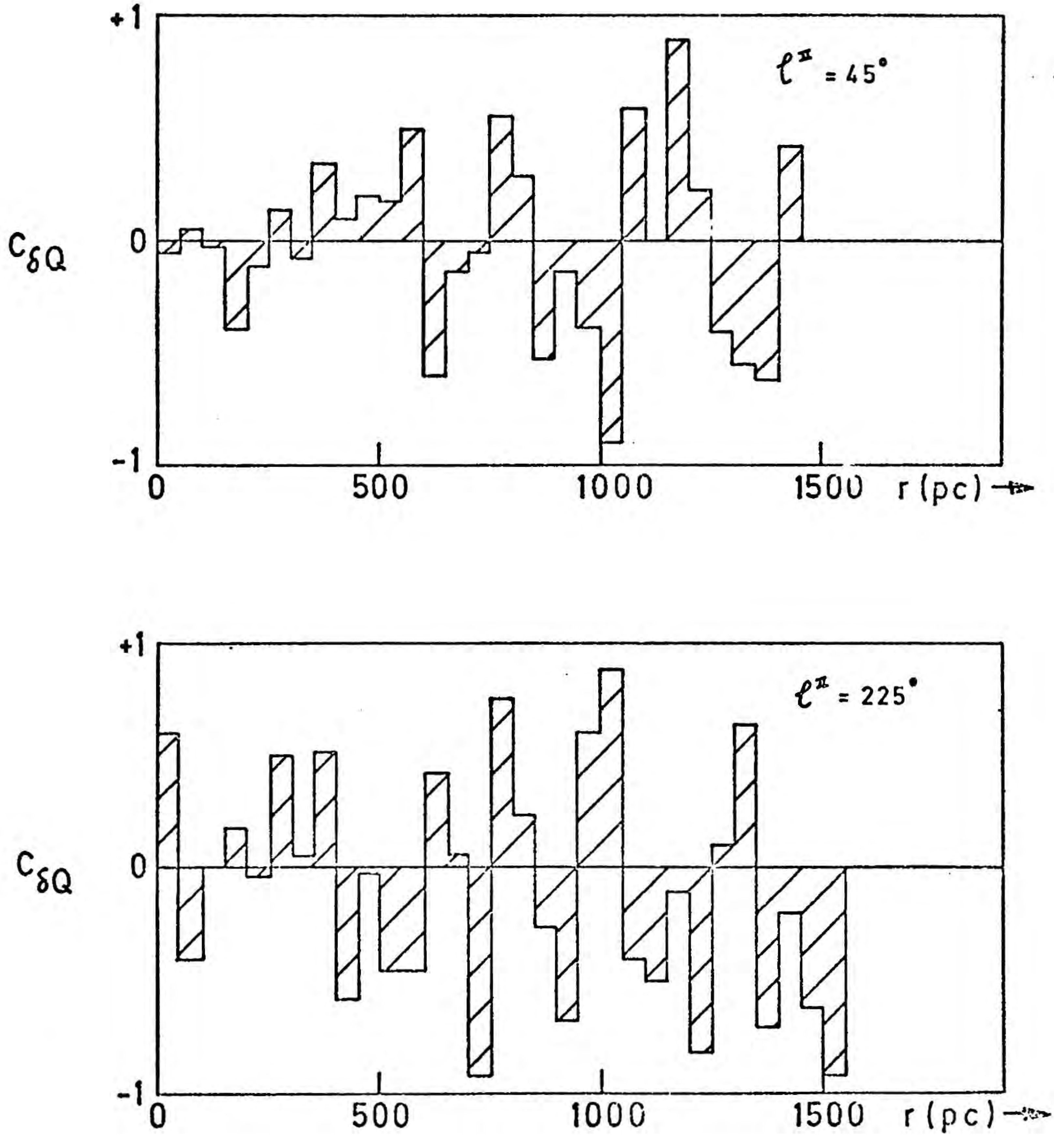

Figure 2.18 Correlation curves $C_{\delta Q}(r)$ for directions parallel to that of the regular field.

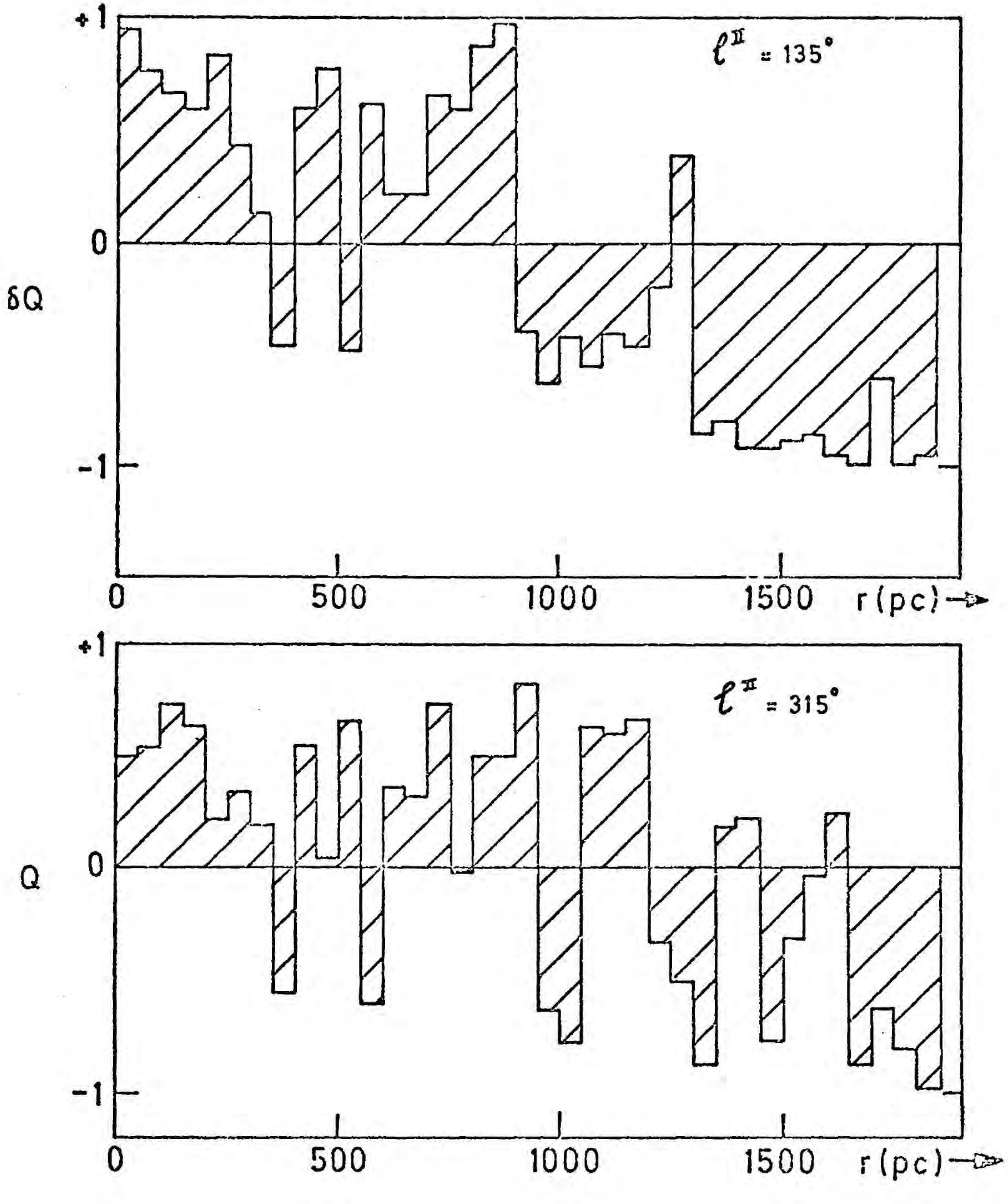

Figure 2.19 Correlation curves $C_{\delta Q}(r)$ for directions orthogonal to that of the regular field.

of relative distance errors, i.e. sudden negative correlations arise when the order of a pair of stars is reversed. The effect was quite obviously present in some of our early incremental polarization maps which had distance bins that were too small. The large scale coherence of 1 kpc at $\ell = \ell_o \pm \pi/2$ will of course not be prone to these smaller scale errors.

In order to help us interpret these results let us adopt a simple model for the irregular field. To do this we introduce the concept of a field "cell". A field "cell" is a region of space over which the irregular field may be considered uniform. The irregular field is then composed of many such cells, each of which has a field with a random orientation and magnitude. In this idealized situation the cell size is the size of the irregularities, but in reality the transitions between one field direction and another will not be sharp but will be a continuous process. In practical terms we therefore define the size of the irregularities in terms of a "correlation-length" or "scale-length", L, which is the distance that has to be travelled before the correlation function $C_{\delta Q}$ changes sign, i.e. the field changes direction by $\sim \frac{\pi}{2}$.

The directions $\ell = 135^o$ and 315^o are orthogonal to the regular field and thus this will produce the dominant contribution to the correlation curves in these directions. The simplest interpretation of the δQ coherence length on the scale of 1 kpc is that it is a consequence of a scale length for the regular field, that is, a change of direction every 1 kpc. However, it is most probable that it is a result of the saturation effect mentioned earlier, as although the method takes into account all pairs, the greatest contribution comes from those with a nearby member. The scale lengths observed in the polarization data do not, however, reflect the field scale alone as they will be a convolution of these scales with those of the dust. If the 1 kpc coherence length is a consequence of the saturation effect then it is most likely to reflect the scale of variation of the dust locally. Indeed Neckel (1966) has shown that the dust density falls sharply at 1 kpc in the range $\ell = 140^{\circ}$ to 160°, and the dominance of "nearby-pairs" could then account for the observed correlation behaviour.

The most important result however, is the lack of any coherence length at $\ell = 45^{\circ}$ and $\ell = 225^{\circ}$. Since this is roughly the direction of the regular field, one expects the scale length, L, to be that of the irregular field and the dust.

Jokipii and Parker (1969) obtained a value of between 100 and 300 pc from a small sample of optical data, and Jokipii and Lerche (1968) obtained a similar result, L $\sim$ 250 pc, from an analysis using extra-galactic rotation measure A more refined approach due to Jokipii et al (1969) used the variation of the variance on the polarization with distance to measure L. They showed that the variance was proportional to R^2 for distances less than L, and prportional to R for greater distances. Using the polarization data of Behr (1959) they apparently detected such an effect and attributed it to a scale length $\sim$ 150 pc. More recently Osborne et al (1973) used both optical and radio data to determine the scale length of the irregular field. Their treatment of the optical data was based on the development of the <u>median</u> polarization with distance using curves similar to those of Figures 2.11, and from the results of a least squares fit to these curves deduced a value for L consistent with that obtained by Jokipii et. al. We have already criticized some of these methods and the situation has also been commented on positively by Heiles (1974). The distance variations of the variance on our plots does not show the effect reported by Jokipii et al and we have also noted that we think that the variances are too large to set any faith by Osborne et al's analysis.

If the magnetic field is turbulence generated then this would certainly result in irregularities. Turbulent eddies would not be expected on a scale bigger than the thickness of the disk $\approx$ 250 pc and therefore, unless the irregularities are somehow anisotropic, e.g. stretched by differential rotation, we expect L to be less than the disk thickness. Scale sizes of this order are apparently required to account for the observed lifetimes (Jokipii and Parker 1969) of cosmic rays and to account for the anisotropies in their arrival directions if they are of galactic origin (Osborne et al 1974). Though this scale length is supported by the above analyses it is considerably larger than the observed sizes of gas clouds $\approx$ 70 pc (Kaplan 1966) and this has important consequences for the relation of the field and the gas in turbulent theories of the galactic field (Parker 1969a).

Our results show a definite absence of any structure on the scales discussed above. The situation is almost identical for adjacent longitudinal directions implying that this effect is not due to inaccurate or scarce data. Taken at face value the results imply $L \sim 50$ pc. We should remember that L reflects structure in both dust and field, though it has always been difficult to see very much correlation spatially between dust maps and polarization measurements. The concept of irregularities with one L value is in any case rather naive; it would be more realistic to invoke a spectrum of irregularities starting on the microscales observed from the angular correlations (Serkowski 1962, Krzeminski and Serkowski 1967) in clusters and associations, to structures of $\sim$ pc corresponding to dust clouds (Scheffler 1967). Even taking into account relative distance effects our results certainly prohibit the larger scale-lengths we have mentioned earlier.

2.8 Discussion and Conclusions

The inclined vectors in the region $\ell \sim 135^{o} \pm 30^{o}$ are evidently the result of a large scale structure. As we pointed out previously this is either a global feature, i.e. a regular field inclined to the disk, or a large cloud with its own systematic alignment. We have carefully checked for anomalies in this direction. The region has been studied extensively by several Northern hemisphere observers, particularly Hiltner (1959). Mathewson and Ford's (1970) plots show little evidence of this inclination, but Serkowski's analysis based solely on Hiltner's data confirms the presence of negative U vectors here. The most striking aspect of the inclination is the clear sinusoidal variation of U (1) in Figure 2.7 which makes it very difficult not to associate it with the regular field. We estimate that the inclination of the field is $\sim 15^{o}$. The inclination of the regular field has important implications for the origin of the field. There are currently two rival proposals for its origin. Parker (1971a) has proposed that the field results from regeneration of a "seed field" by random turbulence in the interstellar medium by the dynamo process. The regeneration process depends on the rapid coalescence of field lines and the rate of dissipation of the field from the surface of the disk by turbulent diffusion, together with alignment of the field in the azimuthal direction by differential galactic rotation (White 1976), however, Piddington (1972) has raised doubts about this process. Alternatively, the galactic magnetic field has a primordial origin (Zel'dovich 1964, Thorne 1967) and was compressed to reach its present strength during the formation of the galaxy. Parker (1971b) has objected to this on the grounds that turbulent diffusion would dissipate the primordial field within $\sim 10^8$ years, but Piddington (1972) disagreed with this conclusion. There are however, several major problems with the primordial field origin which arise as a direct consequence of the differential rotation of the galactic disk (Woltjer 1967). Continual winding of a field frozen in the galactic disk will steadily increase its strength and also creates field reversals. These problems can however, be overcome if the field is inclined to the disk (Piddington 1972). Until now there seems to have been little evidence for an inclined field, and the primordial field origin was therefore generally discounted. Clearly the model must now be reconsidered particularly since the observed inclination is so large.

We believe that the data cannot be explained by a simple longitudinal model with a unique direction. The evidence points to a local field running towards $\ell = 45^o$. This agrees with the direction of the spiral arm as indicated by stellar objects but does not agree with the arms as defined by the neutral Hydrogen data (Figure 2.16 and 2.17). The disagreement between the stellar and gaseous spiral arms is well known, but it is perhaps surprising that the magnetic field favours the former particularly in view of the "freezing" of the interstellar gas to the magnetic field lines. There are however, several problems associated with the direction $\ell = 45^o$ which are partly caused by poor statistics. Beyond 1 kpc there is evidence to suggest that the magnetic field runs towards $\ell = 75^{o}$. Actually a preliminary double longitudinal model (Waddington 1976) with equal fields directed towards $\ell = 35^{o}$ and $\ell = 70^{o}$ based on the possible bifurcation of the local spiral arm (Georgelin 1975) would provide better agreement with the observed variation of Q (ℓ, d). In the opposite direction the issue seems to be less confused and the field is more clearly defined and runs towards $\ell = 135^{o}$. We can find no evidence to support the idea of a field directed towards $\ell = 90^{o}$. We believe that the earlier suggestions that the field was directed towards $\ell = 90^{o}$ are the consequence of the prominent large irregularities in this direction. This would also explain the disagreement between the radio and optical data. There is no longer any reason to interpret the deviations from the longitudinal model in terms of a helical structure. At present we feel that $\ell = 45^{o} \pm 15^{o}$ is the best estimate for direction of the longitudinal field. The auto-correlation curves strongly prefer $\ell_{o} \approx 45^{o}$ to $\ell_{o} \approx 80^{o}$.

The polarization mainly increases within the first 1 kpc and beyond this distance it is more or less constant and this effect could be associated with the spiral arm. This saturation effect could equally well be due to irregularities and we have suggested that it could also be a consequence of an observational selection effect and have advocated a survey of the polarization of highly reddened stars be carried out to search for such an effect. The comparison with the spiral arm maps via the incremental polarization analysis has turned out to be disappointing. The large scatter in the intrinsic E-vectors, even with large bins, makes interpretations very difficult. There is an overall tendency for inclined vectors and we have suggested that it would be worth-while to compare their orientation with those of dust clouds. There is good evidence to suggest that there is also an irregular component to the galactic magnetic field, and we have suggested that this accounts for some of the disagreement between different analyses of the data. Turning to these irregularities we have investigated their characteristic size using a correlation/nonsense catalogue technique. In the directions $1 = 135$ and 315^{o} we find a coherence length ~ 1 kpc and suggest that this is a consequence of the saturation effect we have just discussed. In the direction of the regular field we cannot find any evidence to support the claims of previous workers that the irregular field has a coherence length ~ 150 pc. If the scale length of the irregular field were smaller than this then it would agree well with Michel and Yahil's (1973) proposal that the field had a filamentry structure. The filaments being the result of magnetic fields in stellar winds being stretched by the galactic differential rotation. This proposal is however, very speculative.

In some ways analyses of stellar polarization have perhaps been over confident. Despite observational care and increased precision, stellar distances are still too uncertain and they naturally affect attempts to find scale lengths. The correlation/nonsense catalogue approach is however, a very powerful tool for investigating such structure. But the approach we have used here is a very elementary one and it will be considerably refined in future work. At present we compare the real catalogue, supposedly largely determined by a <u>regular</u> field component, with nonsense catalogues which contain only <u>irregular</u> fields. Clearly the nonsense catalogue should also contain regular components. The effects of distance errors and variations in dust density should also be investigated and irregularities with a variety of sizes generated e.g. perhaps the irregularities could be considered as spherical with a given distribution of radii whose centres are randomly distributed in space and whose grain density fluctuates about some mean value. This would also enable the saturation effect to be investigated further. In order to be able to adopt this more realistic approach we must have a better idea about the regular field structure. We are pursuing this problem, initially close to the plane and later extending the method to higher altitudes, by detailed simulations of the polarization and pulsar rotation measures from various models, including the bi-longitudinal structure we have proposed. By comparing the results of these simulations within the observations in small areas of the sky it should then be possible to obtain a best fitting model by this method. The amount of work involved in both these extensions to our present work is very large and particularly consuming in terms of computer time and the results are hardly likely to be forthcoming.

REFERENCES

Ellis, R.S. and Axon, D.J.	1976	M.N.R.A.S. in press
Appenzeller, I	1966	Zeitschrift F. Ast., 64, p.296
	1968	Ap. J., 151, p.907
Axon, D.J. and Ellis, R.S.	1976	M.N.R.A.S. December 1976 in press
Becker, W. and Fenkhart, R.	1970	I.A.U. Symp. No. 38, p.205
Behr, A.	1959	Veroffenlichangen U. Sternwarte Gottingen, No. 126
Berkhuijsen, E.M., Haslam, C.T., Salter, C.J.	1971	Astron.and Astrophys. 14, p.252
Bingham, R.G. and Shakeshaft, J.R.	1967	M.N.R.A.S., 136, p.347
Blanco, V.M.	1956	Ap. J., 127, p.64
Blanco, V.M., Demers, S. Douglas, G.C. and Fitzgerald, M.P.	1968	Pub. U.S. Naval obs. 2nd Ser. Vol. 2
Brand, P.W.J.L. and Zealey, W.J.	1975	Astron. and Astrophys. 38, p.363
Blaauw, A.	1963	Basic Astronomical Data, Stars and Stellar Systems No. 3, p.383, C.U.P.
Burn, B.S.	1966	M.N.R.A.S., 133, p.67
Cahn, J.H. and Nosek, R.D.	1973	I.A.U. Symposium 52, p.237
Carrasco, L. Sirom, S.E. and Strom, K.M.	1973	Ap. J., 182, p.95
Chandrasekhar, S. and Fermi, E.	1953	Ap. J., 118, p.113.

Cugnon, P.	1971	Astron. and Astrophys., 12, p.398
Davis, L, Jr., and Berge, G. L.	1968	Nebulae and Interstellar Matter, Stars and Stellar Systems 7, p.755, C.U.P.
Davis, L. Jr., and Greenstein, J.L.	1951	Ap. J., 114, p.206
Davis, L., Jr.	1955	Vistas in Astronomy, 1, p.336 Pergamon Press, New York.
Davies, R.D., Booth, R.S. and Wilson, A.J.	1968	Nature, 220, p.1207
Davies, R.D.	1969	Nature, 223, p.355
Davies, J.G. et al	1968	Nature, 217, p.910
Drombrovskii, V.A.	1959	Vest Lennigr gos Univ. 19, p.315
Disney, M.J. and Hopper, P.B	1974	M.N.R.A.S., 168, p.639
Fowler, L.A. and Harwit, M	1974	M.N.R.A.S., 167, p.228
Galt, J.A. et al	1960	M.N.R.A.S., 120, p.87
Gardener, F.F., Morris, D and Whiteoak, J.B.	1969a	Australian Journal of Physics, 22, p.813
	1969b	ibid., 22, p.107
Ginsburg, V.L. and Syrovatski, S.I.	1964	Origin of Cosmic Rays, Pergamon Press, London.
	1965	A.Rev. Astron. and Astrophys., 3, p.297
Gold, T.	1952	M.N.R.A.S., 132, p.215
Gardener, F.F. and Davis, R.D.	1966	Aust. J. Phys., 19, p.119
Georgelin, Y.	1975	Thesis, University of Provence, France.

Gillett, F.C., Jones, T.W., Merrill, K.M. and Stein, W.A	1975	Astron. and Astrophys., 45, p.77
Harwit, M.	1970	Nature, 226, p.61
Hall, J.S.	1958	Pub. U.S. Naval Observatory 2nd Ser. Vol.17., No: VI
Hiltner, W.A.	1951	Ap. J., 114, p.241
	1954a	ibid. 120, p.41
	1954b	ibid. 120, p.454
	1956	Ap. J. Suppl., 2, p.381.
Hofflett, D.	1964	Yale Catalogue of Bright Stars (Yale University Press).
Hoyle, F. and Ireland, J.G.	1961	M.N.R.A.S., 122, p.35
Hornby, J.M.	1966	M.N.R.A.S., 133, p.213
Heiles, C.	1974	I.A.U. Symp., 60, p.13
Jones, R.V. and Spitzer, L. Jr.	1967	Ap. J., 147, p.943
Johnson, H.L. and Morgan, W.W.	1953	Ap. J., 117, p.313
Johnson, H.L. and Hiltner, W.A.	1956	Ap.J. 123, p.267
Johnson, H.L.	1957	Ap. J. 126, p.121
Johnson, H.L. and Iriarte	1958	Lowell Obs. Bull. 4, p.47
Johnson, H.L.	1963	Basic Astronomical Data, Stars and Stellar Systems, Vol. 3, p.204

Jokipii, J.R., Lerche,I. and Schommer, R.A.	1969	Ap.J., 157, L119
Jokipii, J.R. and Parker, E.N	1969	Ap. J. 155, p.799.
Jokipii, J.R. and Lerche, I.	1969	Ap. J., 157, p.1137
Kaplan, S.A.	1966	Interstellar Gas Dynamics (Pergamon Press, N.Y., p.109)
Klare, G., Neckel, Th. Schnuur, G.	1971	Astron. and Astrophys., 11, p.155.
Keenan, M.	1963	Basic Astronomical Data, Star and Stellar Systems. Vol. 3, p.78
Lodén, L.O.	1960	Stockholm Obs. Medd. No. 119
	1961a	Stockholm Obs. Ann., 21, No. 7
	1961b	ibid. 22, No. 1
Lodén, L.O.	1975	Private Communication
Lloyd, S. and Harwit, M.O.	1974	I.A.U. Symp. No. 12, p.203
Mills, B.Y.	1970	I.A.U. Symp. 38, p.178
Manchester, R.N.	1972	Ap. J.172, p.43
	1974	ibid., 188, p.637
Mestel, L.	1976	Personal Communication
Mathewson, D.S. and Ford, V.C.	1970	Mem. R. Ast. Soc. 74, p.139
Morgan, W.N., Johnson, H.L. and Harris, D.L.	1953	Ap. J. 117, p.92
Menodza, E.E.	1956	Ap. J. 123, p.54
Morgan, W.N., Keenan, M Kellman, H.	1943	An Atlas of Stellar Spectra, University of Chicago Press.

Martin, D.G.	1974	I.A.U. Symp. No. <u>52</u>, p.161
Morris, D. and Berge, G.L.	1964	A.J., <u>69</u>, p.641
Mathewson, D.S.	1968	Ap. J. (Lett), <u>153</u>, L47
Mathewson, D.S. and Nichol D.C.	1968	ibid. <u>154</u>, L11
Mathewson, D.S.	1969	Proc. Astr. Soc. Australia <u>1</u>, p.209
Michel, F.C. and Yahil, A.	1973	Ap.J. <u>174</u>, p.771.
Neckel, Th.	1968	Landerawerte Heidelberg-Kongistahl Veroffentlichungen No. 19
Neckel, Th.	1966	Z. Astrophys. <u>63</u>, p.221.
Oort, I.	1958	
Parker, E.N.	1969	Ap. J. <u>157</u>, p.1129
	1971a	ibid., <u>163</u>, p.255
	1971b	ibid., p.279
Piddington, J.H.	1972	Cosmic Electodynamics <u>3</u>, p.60.
Purcell, E.M.	1969	Physica, <u>41</u>, p.100
Purcell, E.M. and Spitzer, L., Jr.	1971	Ap. J. <u>167</u>, p.31
Prentice, A.J.R. and ter Haar D.	1969	M.N.R.A.S. <u>146</u>, p.423
Reinhardt, M.	1942	Astron. and Astrophys., <u>19</u>, p.104
Saltpeter, E.E. and Wickramasinghe, N.C.	1969	Nature, <u>222</u>, p.442
Serkowski, K.	1962	Advance in Astron. and Astrophys. <u>1</u>, p.304.

Smith, E., and Evan, P.	1956	Ap. J. 124, p. 23.
Schroeder, R.	1976	Astron and Astrophys. Suppl. 23, p.125
Sharpless, S.	1963	Stars and Stellar Systems 3, p.22
Serkowski, K. Mathewson, D.S and Ford, V.L.	1975	Ap. J. 196, p. 241.
Stebbin, J. Huffer, C.M.Whitford	1940	Ap. J. 91, p.20
Schmidt-Kaler, Th.	1965	Landott-Bornstein, Vol. 1. Astron. and Astrophys, Group 4, p. 30, ed. H.A. Voigtt, Springer-Verlagg, Berlin.
Stokes, R.A., Swedlun, J.B. Avery, R.W. Michalsky, J.J.	1974	Ap. J. 71, p.678
Spoelstra, T.A. Th.	1971	Astron. and Astrophys. 13, p.237
	1972a	Astron. and Astrophys. Suppl. 5, p.205.
	1972b	ibid.
	1972c	Astron. and Astrophys.
	1972d	Astron. and Astrophys. 21, p.61
Smith, F.G., Wilkinson, A.	1974	M.N.R.A.S., 167, p.593.
Osborne, J.L., Roberts, E. Wolfendale, A.W.	1973	J. Phys. A. Gen. 6, p.44
Schmidt-Kaler, Th.	1970	I.A.U. Symp. No: 38, p.284
Simonson, S.C.	1970	Astron.and Astrophys., 9, p.163.
Shaijn, G.A.	1955	Zu. 32, p.381.
Schoenberg, E.	1964	Veroff Sterm Munchen 5, No: 21
Serkowski, K	1968	Ap. J. 154, p.115
Serkowski, K., Krzeminski, W	1967	Ap. J. 147, p.988

Schmidt-Kaler, Th.	1958	Zeitschrift fur Astr. 46, p.145
Scheffler, H.	1967	Zeitschrift fur Astr. 65, p.60
Theilheim, K.O. and Langhoff, W.	1968	J.Phys.A. General 1, p.694.
Thorne, K.S.	1967	Ap. J. 148, p.51
Thielheim, K.O.	1975	Origin of Cosmic Rays (Ed. J.L. Osborne, A.W. Wolfendale) D. Reidel Publishing Co. Dordrecht, Holla
Uranova, T.A.	1970	I.A.U. Symp. 38, p.205
Vershuur, G.L.	1969a	Ap. J. 156, p.861.
	1969b	Nature, 223, p.140
	1969c	Ap. J. Sept., 1970
	1970a	I.A.U. Symp. No: 34, p.150
	1970b	Ap. J. 155, L155
Vallée, J.P., Kronberg, P.P.	1975	Astron. and Astrophys. 43, p.233
Vallée, J.P., Kronberg, P.P.	1975	Nature, 246, p.49
Woltjer, L.	1967	I.A.U. Symp. 31, p.479
Whiteoak, J.B.	1974	I.A.U. Symp. 60, p.137
Wright, W.E.	1975	Unpublished Thesis, Cal. Tech.
Weaver, H.F.	1970	I.A.U. Symp. 39, p.30
Winnberg,	1969	
White, M.	1976	Unpublished Thesis, University of Durham
Wickramasinghe, N.C.	1967	Interstellar Grains, Chapman and Hall, Lo
Zel'dovich, Ya. B.	1964	Soviet Phys. - JETP 21, p.656
Waddington, G.	1976	Private Communication
Bingham, R.G.	1967	M.N.R.A.S. 137, p.157.

PART II

CHAPTER 3

THE NEBULA POLARIMETER

3.1 The Designs and Techniques Used in Polarimetry

3.1.1 Photographic Polarimeters

Photographic detection provides the simplest method of satisfying the basic requirement of a polarimeter, namely that it should be possible to record the change in intensity of starlight as it is modulated by a rotatable analyser. To eliminate the influence of changing atmospheric extinction a complete measurement of the degree of polarization should be made on each photograph. Inspection of equation 1.1 shows that this condition is satisfied provided both the O and E intensities are recorded simultaneously on each plate. The early photographic polarimeters (e.g. Öhman 1939) used plane-parallel Iceland - Spar crystals as analysers. However this has the disadvantages that the O and E rays have different path lengths and hence focal lengths, and the E ray is distorted by astigmatism. A better approach is to replace the Calcite plate by a Wollaston or Rochon prism, in which both beams are transmitted and are distortion free.

If the direction of the polarization vector is known in advance, only one observation is required to deduce the total polarization. However, a complete determination of the magnitude and direction requires two independent measurements. The measuring technique normally employed is one originally suggested by Pickering (1873) and consists of making two observations of the star with the instrument at two different position angles 45° apart. If P_1 and P_2 are the observed polarizations in these two positions, then the true polarization, P, and the angle, θ, between the plane of vibration and the preferred analyser axis are given by

$$P = \left(P_1^2 + P_2^2\right)^{\frac{1}{2}}$$

$$\theta = \tfrac{1}{2} \tan^{-1}\left(\frac{P_2}{P_1}\right) \tag{3.1}$$

where P_1 and P_2 are given by equation (1.1). In order to calculate the image intensities each plate has to be calibrated by means of a standard wedge, as photographic emulsions do not show a linear response to increasing intensity. This is the most serious drawback of the technique. However there are several other lesser disadvantages such as adjacency, reciprocity failure, intermittency, scattering in the emulsion, to name but a few. Photoelectric detectors have a linear response, and suffer from none of these other disadvantages and have therefore effectively superseded photographic detectors. However, the important advantages associated with photographic plates namely, long integration times and therefore a fainter detection limit, and the storage of detailed information over large areas should not be forgotten.

<u>3.1.2 Photoelectric Polarimeters</u>

There are two main classes: single beam and double beam, depending on whether the analyser allows one or both of the orthogonal components to be measured. Three subdivisions are formed by the detection methods which are A.C., D.C. or "Differential"

The first "Single beam" polarimeter of the D.C. type was constructed

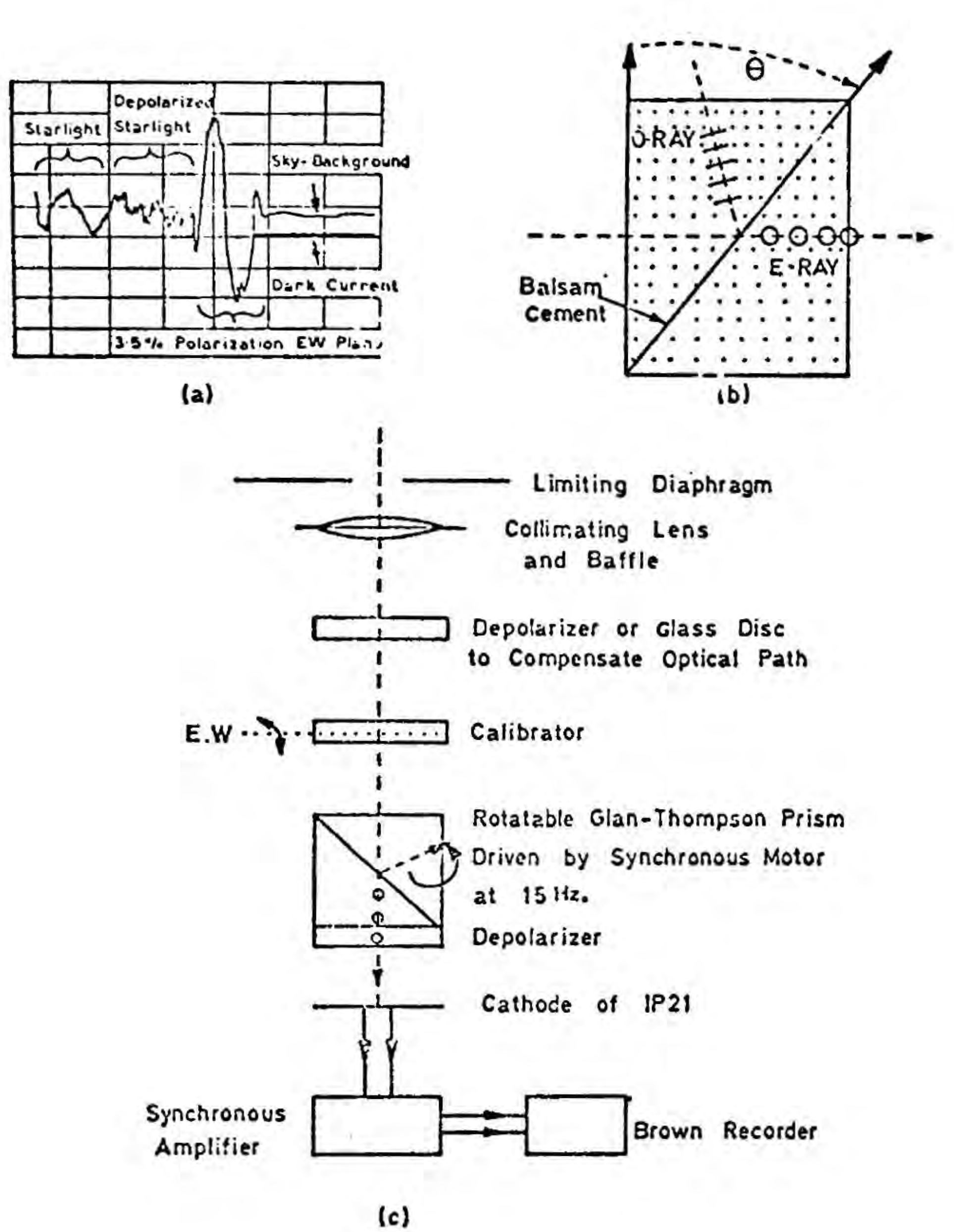

<u>*Figure 3.1*</u> *(a) Typical output from Brown recorder for a polarized star.*

(b) Details of action of Glan-Thompson prism. Typical value for Θ of 38°. Acceptance angle 7°.

(c) Schematic diagram of Hall's A.C. Polarimeter

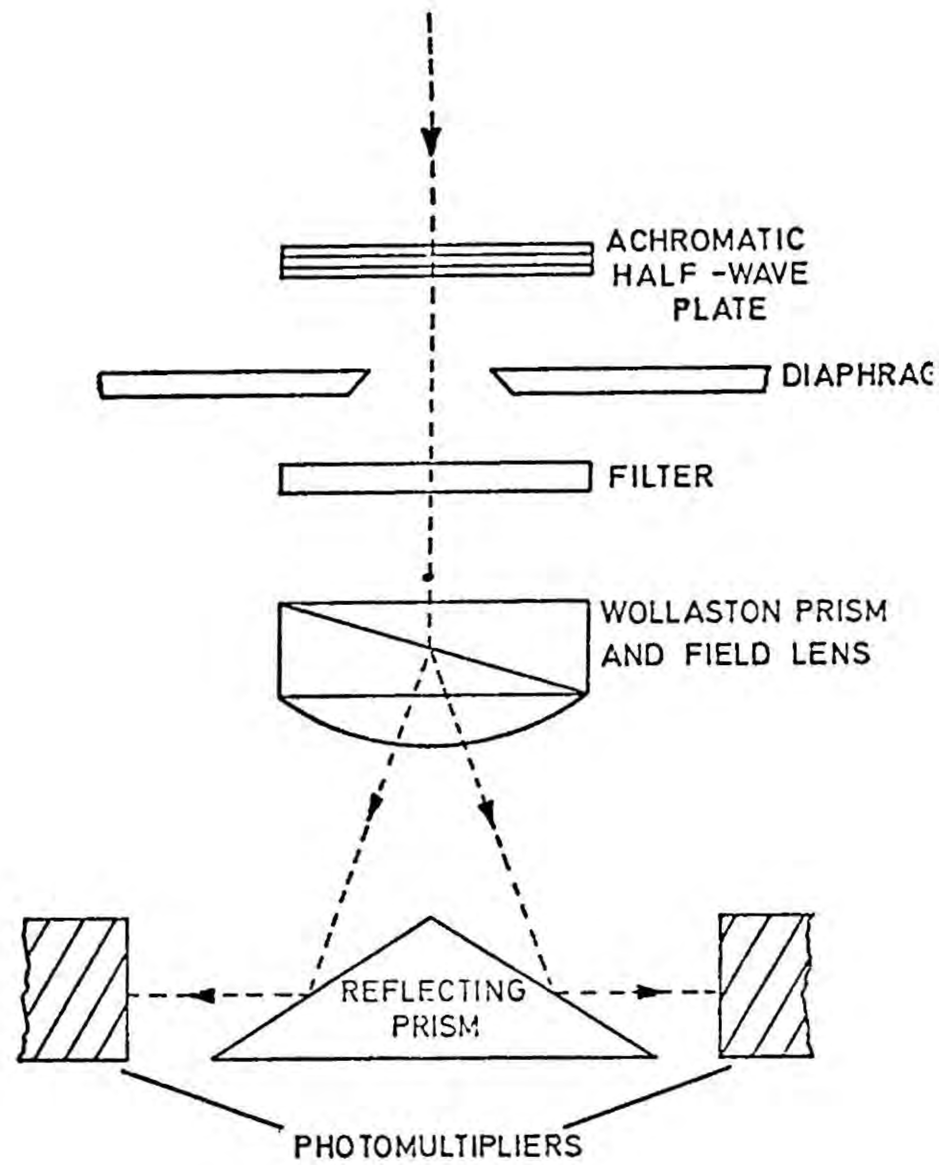

<u>*Figure 3.2*</u> *Schematic diagram of Appenzeller's half-wave plate polarimeter (after Appenzeller 1966).*

by Hiltner (1949, 1951). A polaroid sheet, whose preferred axis could be rotated to one of two positions 90° apart, was used as an analyser, and in addition to 90° rotation the assembly housing the polaroid could be rotated by any position angle. For a given position angle setting the intensity difference at two orientations of the polaroid is measured. Plots of the intensity differences against position angle give a double sine curve. The polarization parameters can then be determined from the position angle of the peak of the curve. The serious disadvantage of this method is that extinction changes between the observations will produce spurious polarization.

In A. C. polarimeters the analyser is made to rotate about the optical axis. An example of this type of polarimeter (Hall and Miksell 1950) is shown in Figure 3.1. The polarization is determined from the amplitude and phase of the alternating current-output from an RCS 1P21 photomultiplier tube after the light has passed through a Glan-Thompson prism rotating at a constant speed of 15 Hertz. If the star is polarized the resulting photocurrent varies as $\cos 2\phi$, where ϕ is the angle by which the prism has rotated beyond the position of maximum light transmission. A square wave frequency of 30 Hertz is generated with the aid of a phasing switched linked mechanically to the rotating prism, and mixed with the signal in a synchronous amplifier. The relative phase of the two waves is changed every two minutes and the D. C. output voltage of the amplifier goes through a cyclic change. This curve having a form similar to $\cos 2\phi$ is drawn on the recorder every two minutes. A Lyot depolarizer is then introduced depolarizing the starlight before it reaches the analyser. Any spurious effects present can then be detected as a deviation from the expected horizontal line. Finally a tilted glass plate is introduced between the depolarizer and the prism. The plate is at a fixed angle and therefore produces a known polarization (Lyot 1929). The spurious effects detected in the second measurement are subtracted from the first and third measurements and a comparison of these then gives the angle and degree of polarization from one setting of the instrument. Neither A. C. nor D. C. polarimeters are able to compensate for the effects of scintillation which is the main source of error for bright stars, but A. C. polarimeters are less susceptible to errors caused by changes of extinction because much shorter integration times are used. (Here a distinction is made between scintillation which is regarded as a short time-scale phenomena caused by turbulence, and "extinction" which is a phenomena caused by large scale atmospheric changes).

There are several important advantages gained by using a "double-beam" device, particularly if both beam intensities are measured simultaneously, as in "differential" polarimeters. The most apparent of these gains is that whereas in the single beam devices 50% of the light is discarded, all the light is used in a double-beam device, and for a given degree of required accuracy this results in shorter exposure times. Variations in atmospheric extinction and sky brightness are also eliminated. However, the major advantage of such a differential instrument is its ability to compensate for scintillation. Miksell, Hoag and Hall (1951) have shown the scintillation of two perpendicularly polarized components is almost exactly the same, and the ratio of the simultaneous intensities of these components is not affected by scintillation.

A Wollaston prism is used almost exclusively as the analyser in such devices. Figure 3. 2, illustrates a differential device due to Appenzeller (1967) but with an achromatic half-wave ($\lambda/2$) plate included (a half-wave plate rotates the plane of polarization through twice the angle of its rotation), so eliminating the need to turn the whole polarimeter on a bearing. The achromatic $\lambda/2$-plate is of the Pancharatnam (1955) type which is effective between 3500 A° and 6800 A°. The intensity of each beam is measured simultaneously at 16 positions of the $\lambda/2$-plate differing by 22.5°, thus enabling Pickering's method to be applied.

3.2 The Nebula Polarimeter

Of the polarimeters discussed above, the "double-beam" photoelectric devices are considered the most accurate, as they are able to measure polarizations smaller than 0.1%. However, the Spatial mapping of the polarization of faint extended objects requires an instrument which is not only capable of measuring the degree of polarization accurately, but which also has a high position resolution, and ideally, a wide field of view. If the positional accuracy is low then it is possible that during the course of a measurement, or series of measurements, different parts of the object would be sampled, thus inducing false polarization. A wide field of view enables as much of the object as possible to be measured, while at the same time allowing monitoring of the background illumination. With photoelectric polarimeters a "blind-offset" positioning has to be used, and it is not possible to achieve a precision better than 1%.

Photographic polarimeters offer very good positional resolution, but are notoriously inaccurate in their measurement of the degree of polarization, though these errors may well occur in the reduction (see Chapter 4.1).

Clearly a polarimeter designed specifically for extended object studies, which combines the best features of photographic and photoelectric devices is required. The instrument described below, which we called the "Nebula polarimeter", attempts to fulfil these requirements. It was designed by Dr. R.G. Bingham, Dr. S.M. Scarrott and the author, and is based on Öhman's (1939)

(a)

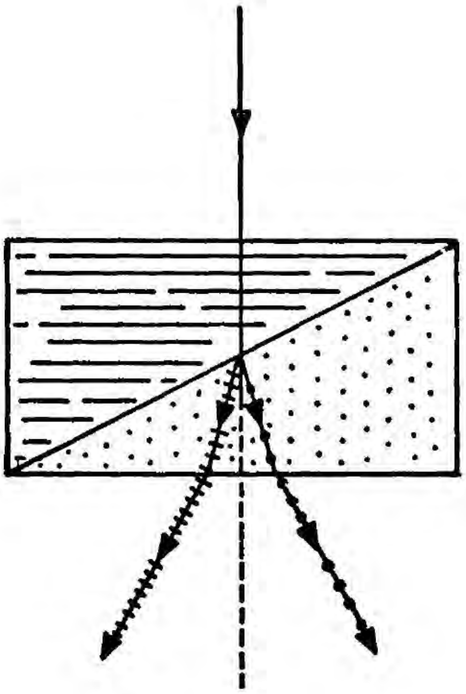

(b)

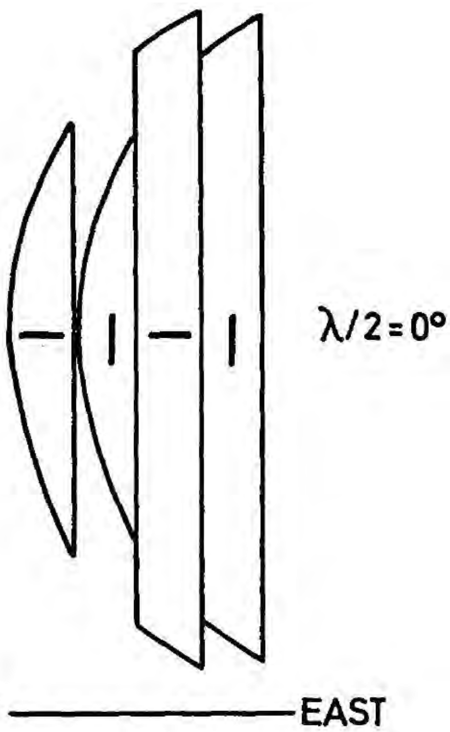

(the black lines represent the E-vectors)

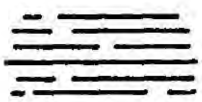 *optical axis horizontal in plane of paper*

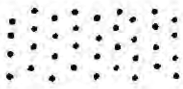 *optical axis into plane of paper*

 *E-vector in plane of paper*

 *E-vector into plane of paper*

Figure 3.3 (a) *Action of the Wollaston prism*

(b) *Resulting image produced in the Nebula Polarimeter* modification to Pickering's (1873) polagraph. The polarimeter has been designed so as to be as flexible as possible in its optical configuration, mechanica construction and detection system. In its current form the polarimeter is arranged primarily for use with electronographic recording devices (in particular Dr. McMullan's electronographic camera) and as such represents the first device of its kind, though it can be used with photographic plates, and indeed some trial measurements were made in this way.

The need for accurate mapping has demanded that the traditional method of plate reduction be abandoned in favour of "two-dimensional" digital processing (this is in itself a new step in polarimetry) details of which will be given in Chapter 4.

3.2.1 The Optical System

The Nebula polarimeter is a double beam instrument which uses a Wollaston prism analyser, whose action is illustrated in Figure 3.3. Since both the O and E rays are diverged equally they have the same focal plane and experience very similar losses due to absorption in the prism. (The advantage of a single focal plane is obvious for photographic or electronographic work). Two Quartz Wollaston prisms were purchased from the Bernard Haller company of Berlin with working surfaces of 2 and 4 sq. cm. respectively, both prisms having a nominal divergence of 1° in the visible part of the spectrum. The complete optical system is shown schematically in Figure 3.4 and was designed for use at the Cassegrain focus.

A "Grid" consisting of equal, alternating, opaque strips and gaps, Figure 3.5(a), is situated in the focal plane of the telescope, and blocks out exactly half the field of view, thus providing enough space for the resolution

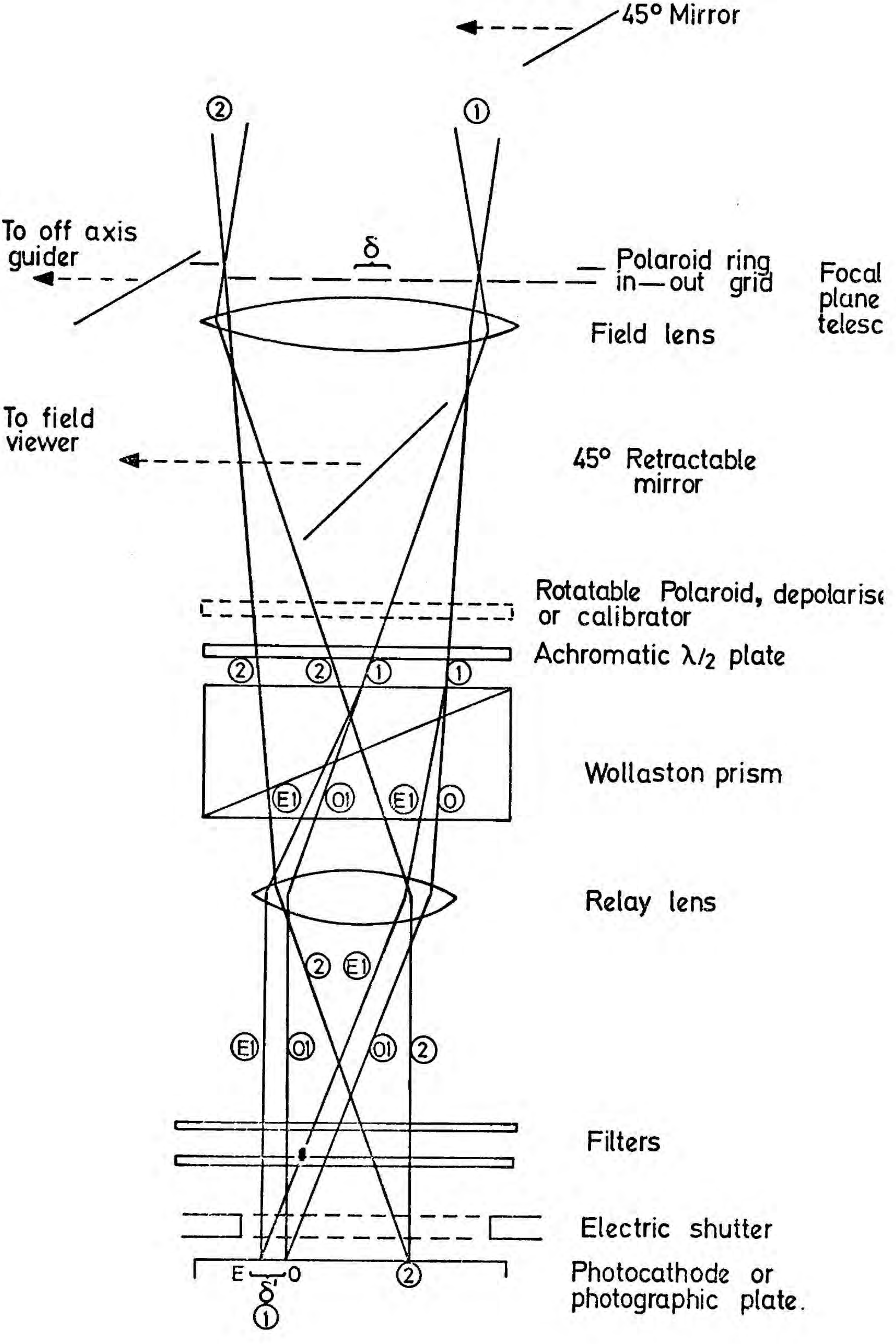

Figure 3.4 *Schematic diagram of the polarimeter optics.*

of each strip into orthogonal polarization forms in the final image, Figure 3.5(b). Each strip has a "knife-edge" with a rear surface chamfered at 45° to avoid unwanted reflections, and the positioning of the grid in the focal plane of the telescope prevents diffraction images being formed. Pospergelias (1965) has reported that metal diaphragms polarize light linearly by as much as 0.2% with the E-vector parallel to their edges. To avoid such "metal edge" affects the grid has been constructed of perspex (Figure 3.6). The grid can be moved in and out by exactly one strip width so that the other half of the field can be photographed. In addition to this motion the whole grid assembly can be pushed aside and replaced by a large circular diaphragm for standard star measurements Mounted on the periphery of the grid is a thin annulus of polaroid sheet which enables visual identification of each strip on the electronographic plate, and can also be used for calibration purposes.

Immediately behind the grid is a 55 mm diameter achromatic "Field-Lens", which is effectively in the focal plane of the telescope, and has a focal length of 180 mm. The field lens is the first component of an image reducing system and merely reduces the size of the "exit-pupil" of the telescope beam, allowing the image of the object to pass through the $\lambda/2$-plate and prism which are positioned at its focus. The second component of the reducing system, the "Relay Lens" is situated behind the prism and images the object onto the photocathode. The amount of magnification of the system is given by the ratio of the focal lengths of the relay and field lenses. The relay lens normally used has a diameter of 40 mm and a focal length of 50 mm. and therefore gives a demagnification of the order of 4:1. This gives an increase in speed of the same order, adequately compensating for the halving of intensity caused by the

(a)

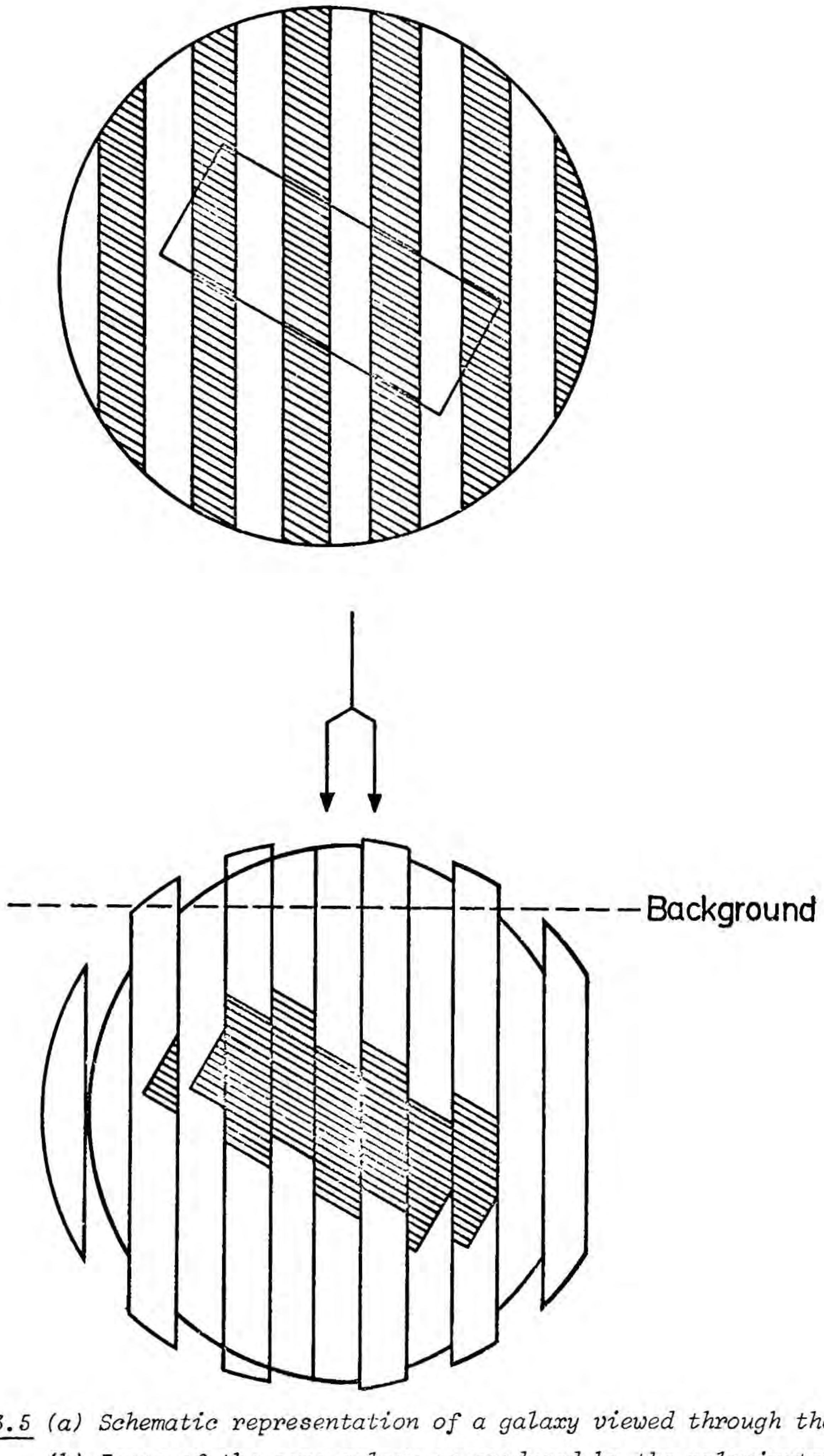

(b)

Figure 3.5 (a) Schematic representation of a galaxy viewed through the grids

(b) Image of the same galaxy as produced by the polarimeter. Alternate strips are in orthogonal polarizations whose direction depends on the position angle of the half-wave plate.

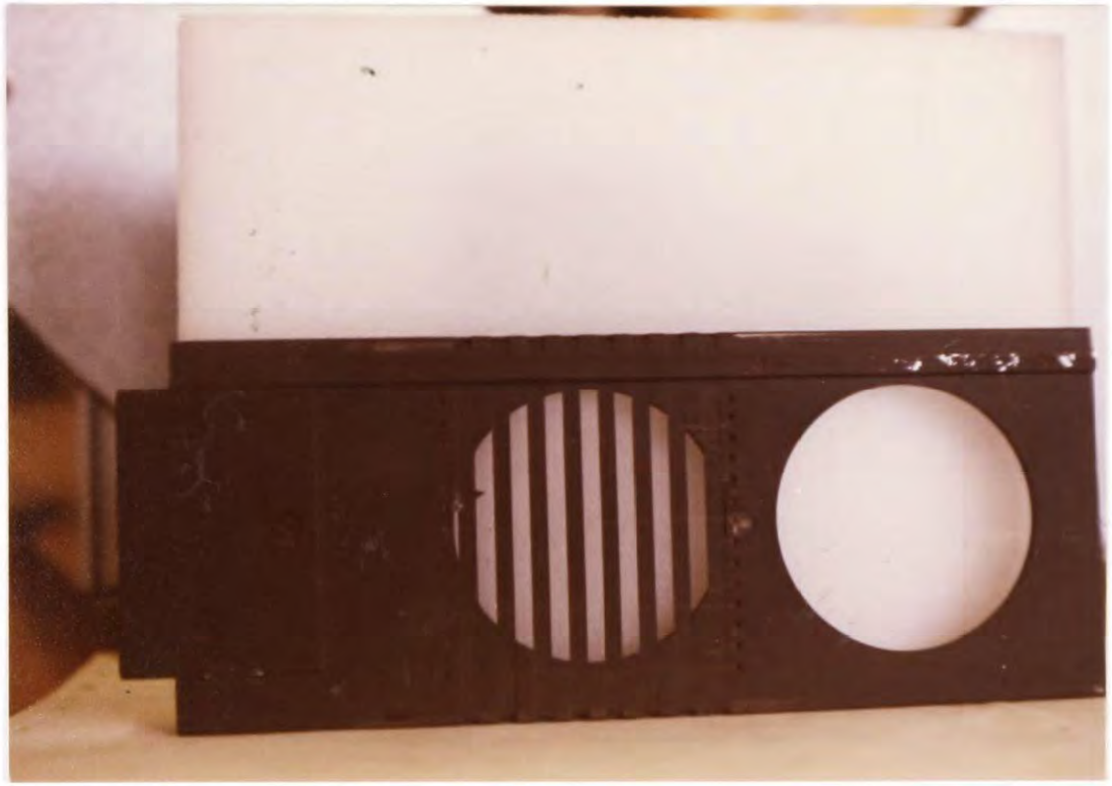

Figure 3.6 Photograph of the perspex grid assembly.

prism. A final image with a size of 1 sq. cm. is produced on the plate, and this is a convenient size for scanning with a densitometer. Flexibility in the choice of demagnification is achieved by having both lenses mounted in standard sized holders with a screw thread fitting. To minimize the effects of large scale variations in cathode sensitivity, non-uniformity of development and emulsion irregularities it is desirable that the O and E images of each gap be adjacent, Figure 3.3(b). For a given field lens there is one grid dimension for which the prism displaces each image by half a grid spacing $\delta'/2$ (δ' is the apparent grid size in the final image) one to the left and the other to the right when they are focussed onto the photographic plate or photocathode, producir a final image similar to Figure 3.5(b). For the case when both the O and E ray suffer equal divergence (Figure 3.7) simple geometry gives

$$\delta = 2f_F \tan \frac{\alpha}{2} \qquad (3.2)$$

where

δ = grid size

f_F = focal length of the field lens

α = angular divergence of the prism

The validity of the expression was ascertained for the real prism and each field lens by the use of a variable slit, and good agreement was obtained. For the optical configuration described above with δ = 3.142 mm.

Immediately in front of the grid assembly is a 45° mirror 10" x 8" (containing a 9 x 6 inches elliptical hole which allows light from the object to reach the grids) which is used to deflect unwanted light to an "off-axis-guider" so that the position of the polarimeter can be accurately maintained. The mirror is made of silvered perspex and although not of high optical

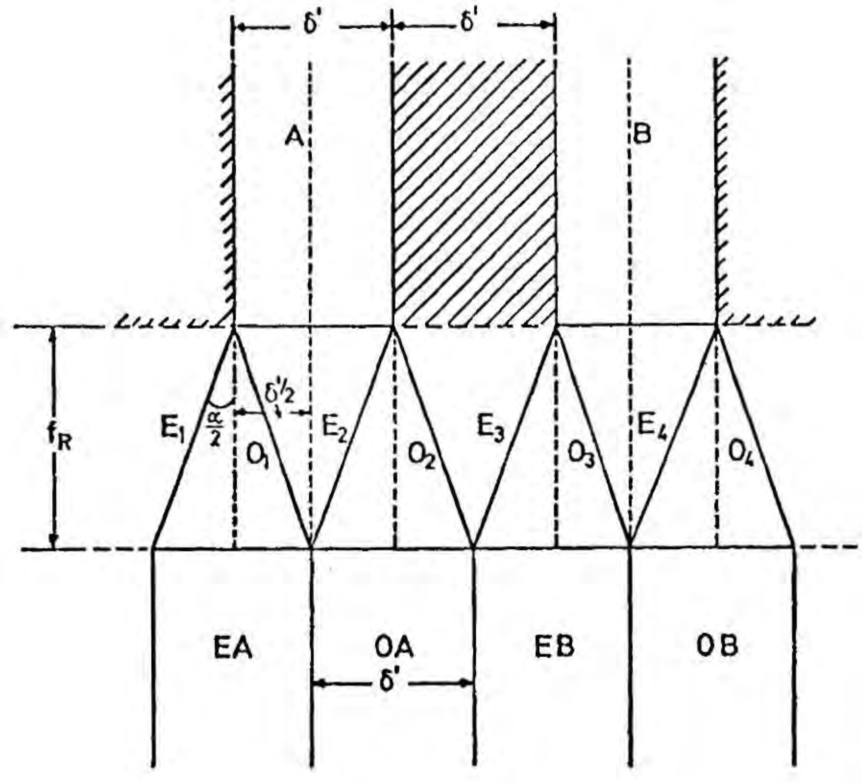

Figure 3.7 *Geometry used to calculate the grid spacing assuming equal divergence of the O and E rays.*

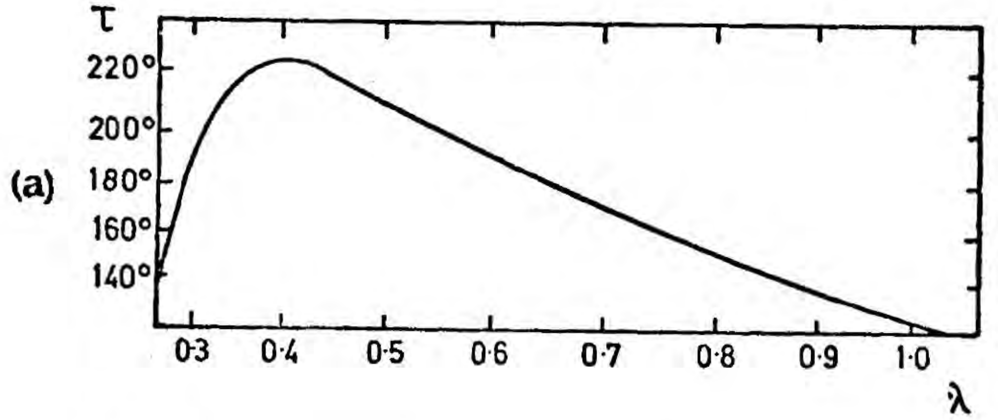

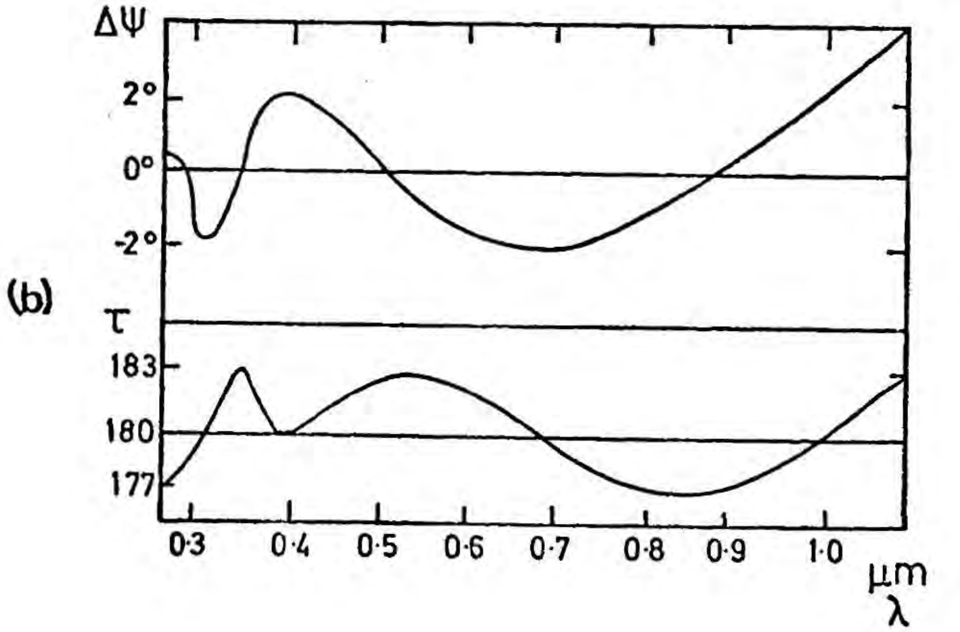

Figure 3.8 (a) *Wavelength dependence of the retardance of a half-wave plate made from magnesium fluoride and Quartz.*

(b) *Wavelength dependence of the position angle of the equivalent optical axis $\Delta\psi$ and the retardance τ of a Pancharatnam super achromatic half-wave plate of magnesium fluoride and Quartz (from Serkowski K, 1974).*

quality provides a good enough image for guiding purposes and has the advantages of being light (about 1/4 of the weight of a glass mirror), robust, and easily machineable.

A second 45^{o} perspex mirror can be introduced into the main beam just after the field lens, to allow light to be sent to a "Field-Viewer". The Field-Viewer is used for three purposes, the most important of which is the accurate alignment of the grids in a North-South direction. The method of doing this as follows: The polarimeter is mounted on the telescope Cassegrain turntable and a suitable star found, the telescope is moved in declination, i.e. the star is moved from North to South in the field of view, and the Cassegrain head carefully rotated until the star runs up and down the edge of a strip when viewed through the Field-Viewer. Since the grids are in one of the prisms preferred directions this establishes the zero of position angle as North and thus all measurements are reduced directly to the equatorial system. The Field-Viewer is also used in focussing the telescope by the "knife-edge" method, the grid proving the "knife-edge". Finally the Field-Viewer enables objects bright enough to be seen visually to be centred in the field of the polarimeter. When the field viewer is removed the beam of light continues through a "half-wave ($\lambda/2$) plate" in a rotable mounting which is designed to move in steps of $22\frac{1}{2}^{o}$ only. In its initial position (labelled 0^{o}) the $\lambda/2$-plate fast axis is aligned North to South. Since each plate records two orthogonal polarizations just two plates with the $\lambda/2$-plate in successive positions give a complete specification of the Stokes' parameters I, Q and U and hence P and θ. However, in order to account for the variation of the cathode sensitivity between the left and right strip and the different exposures of each plate, four plates are required. Further plates enable checks for consistency, and normally a series of eight are used for each half of the object under investigation.

Two different $\lambda/2$-plates have been used. In the April 1974 measurements $\lambda/2$-plate, purchased from Roffin Limited, and cut for 4500 A^o was used. This plate suffers from chromatic effects and large corrections have to be applied to the results even in the range $\pm$ 500 A^o from the working wavelength (see later). Because of this alarming behaviour an "Achromatic $\lambda/2$-plate" made of fused Magnesium fluoride and Quartz, 2 cm in diameter, with an angular acceptance of 8^o was purchased from the Bernard Haller company A comparison of this type of plate with a Pancharatnam plate (Figure 3.8) shows that over a wide range of wavelengths its constancy of retardance is somewhat inferior (but remember it has the advantage of having a constant optical axis direction). However, over the small range of wavelengths studied with the polarimeter (4000-6000 A^o) this is not the case. Measurements in the laboratory (Pallister 1974) have shown that in the B band (where the polarimeter is normally operated) the retardance of the plate is $180^o \pm 1^o$ and then falls to 169^o at 6000 A^o.

Following the $\lambda/2$-plate is the "prism" which is mounted in a holder which can be rotated through 180^o, thus allowing the two beams to be interchanged on the photocathode. Behind the prism is the relay lens which is in a movable tube thus enabling the object to be focussed on the photocathode via the filters which are situated after the relay lens (thus eliminating any possibility that they can induce artificial polarization into the system by strain birefringance. The focussing is usually accomplished by taking trial exposures of the dome wall with the relay lens at different positions, and adjusting its position until the outline of the grids is sharp. The filters used in the work described later were a Shott BG12 blue filter and a red absorbing BG38 filter which in combination restricted the pass band of the polarimeter to 4500 $\pm$ 500 A^{o}.

The polarimeter end plate incorporates an "electronic shutter" whose purpose is to protect the image tube photocathode. There are also facilities for the introduction of a polaroid, a depolarizer, or a calibrator, into the beam for test purposes in various positions in the polarimeter.

3.2.2 The Mechanical Construction of the Polarimeter

The instrument is based on a hollow one inch steel framework 570 x 380 x 410 mm in dimensions on which is fastened a high precision optical bench which defines the optical axis of the polarimeter. The optical bench carries the off-axis guider mirror, grid and field lens assembly and calibration components (Figure 3.9) and accurately aligns them in the horizontal plane, while at the same time allowing for several different lens systems to be used. The field lens position can be adjusted by means of the rack and pinnion on the optical bench and mounting, and the position set accurately with the vernier scale incorporated. The heights of the components are adjustable and are centred on that of the prism by means of locking collars.

The "front plate" of the polarimeter is 15 mm thick steel plate 510 mm in diameter, containing a hole 230 mm in diameter and numerous fastening holes so that the polarimeter can be attached to the telescope. The plate can be carefully adjusted so as to be orthogonal to the optical bench by means of several levelling screws. Similarly, the "Back-plate" carries the image-

(a)

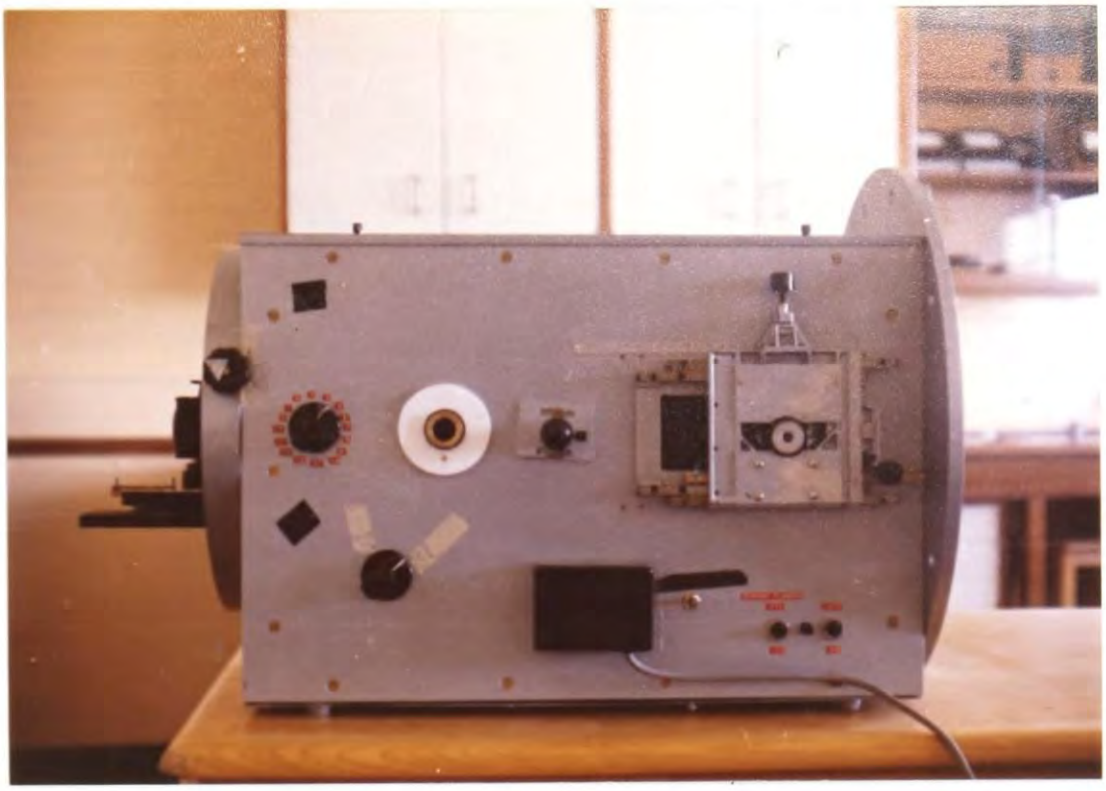

(b)

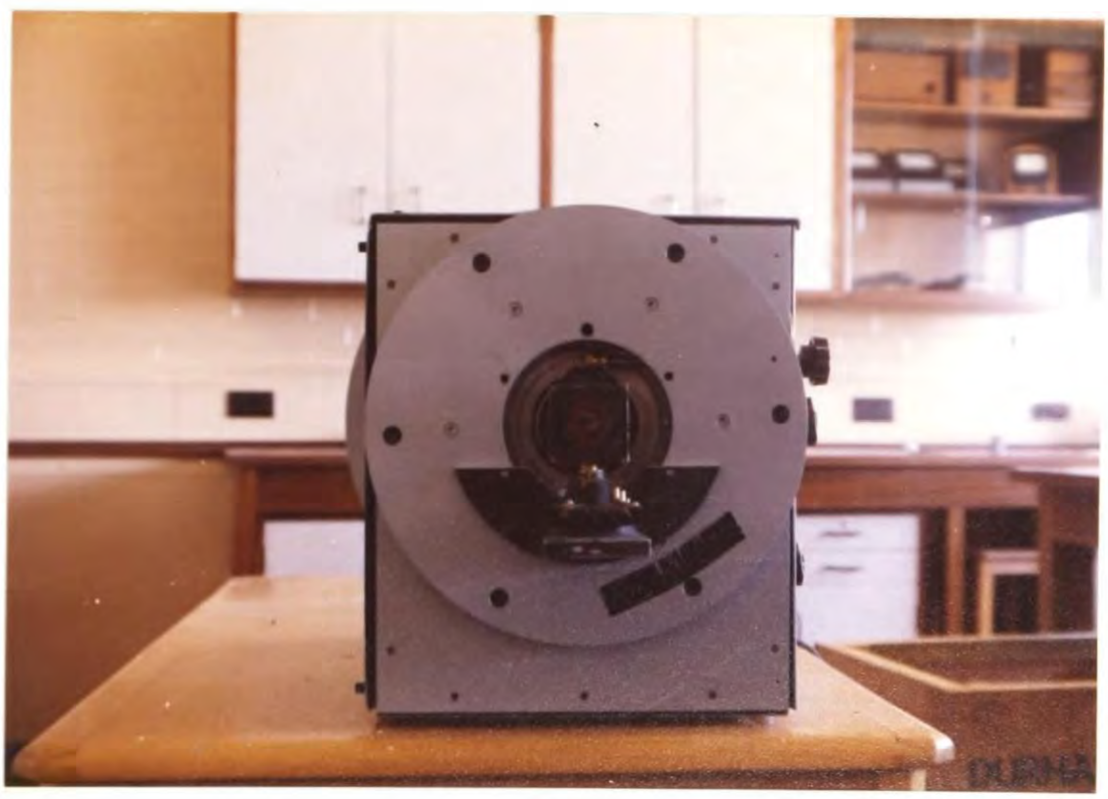

<u>Figure 3.9</u> *Construction of the Nebula polarimeter -*

(a) View from the side showing off-axis guider and control rods and gears.

(b) Rear view of polarimeter showing the arrangement for mounting plate holders for photographic work.

(c)

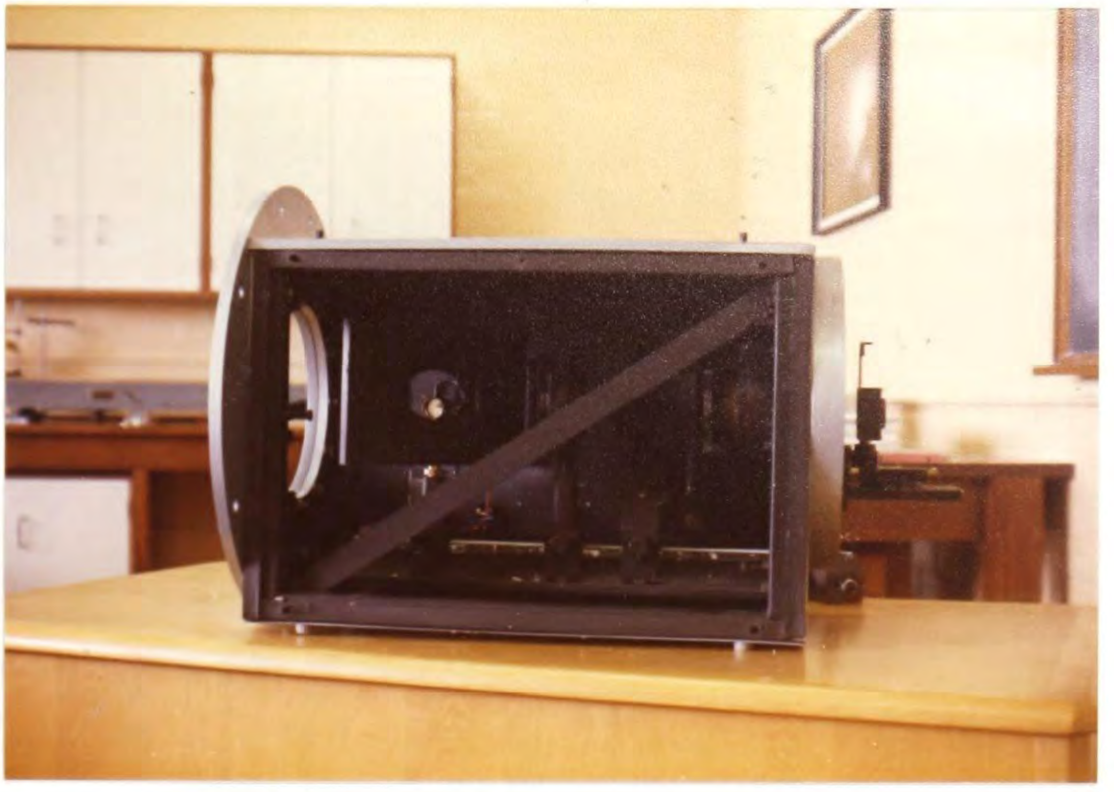

Figure 3.9 (c) View of the interior of the polarimeter

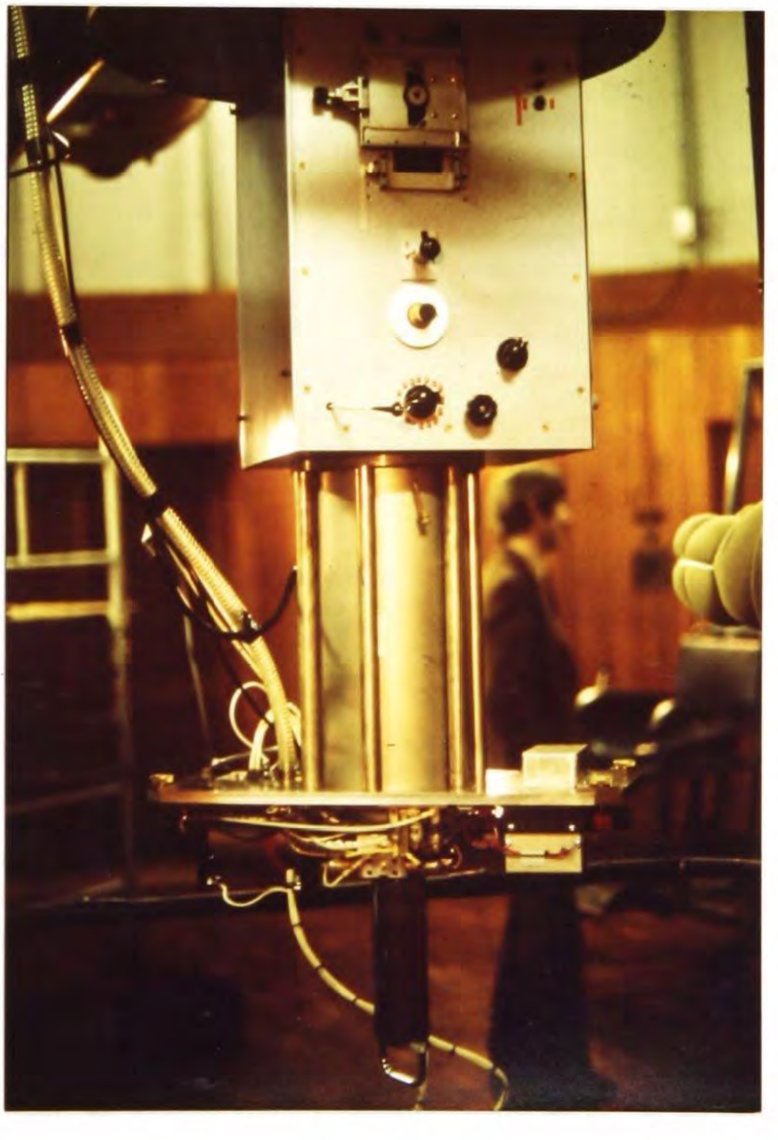

Figure 3.12 The polarimeter and the 4 cm McMullan camera mounted on the 36" telescope at R.G.O.

tube and can also be adjusted. The back-plate also carries on its inside the prism holder, the $\lambda/2$-plate mounting, the relay lens and the electronic shutter. In order to ensure that the polarimeter is light tight, the frame is lined with foam rubber and the inside of the walls blackened to avoid reflections. The top and one side of the polarimeter are readily removable for access and are flanged to add extra protection against light leakage. As many of the mountings as possible are made of light weight low expansion materials with matt finishes e.g. Tufnol.

The operation of the optical components (except for the rotation of the prism) can be done without opening the polarimeter, by means of various rod and gear systems. The $\lambda/2$-plate housing is "Click-Stopped" every $22\frac{1}{2}°$ and this prevents a rotation by any other angle being made. The off-axis guider incorporates two photo-diodes which can be made to blink on and off and illuminate the cross wires, making the guiding on faint stars far easier.

3.2.3 The Electronographic Camera

The electronographic process, that is the conversion of an optical image into an electron image, which is recorded on a nuclear emulsion has several advantages over conventional photography:

1. The detective quantum efficiency is high, approaching that of the photocathode, which can be as much as 20% c.f. Eastman II-ao quantum efficiency 1.5%. Which gives a considerable gain in speed $\sim$ 10-20 times that of Eastman II-ao baked. Consequantly, telescopes of moderate aperature may be used to reach

the same detection limit as attained by conventional photography with the largest instruments.

2. Since each electron entering the emulsion will leave a developable track there is no reciprocity failure, and the absence of the threshold effect means that the low intensity end of the characteristic curve can be utilized.

3. The process is linear, the density being proportional to exposure up to density $3\frac{1}{2}$ (Penny 1976), thus greatly simplifying the reduction process.

4. The storage capacity for the emulsion is very high. Much longer integration periods are possible, so that much fainter sources may be detected against the sky background.

5. The resolution exceeds that of normal photographic plates. The resolution of the McMullan tube is 50-100 ℓp/mm c.f. Eastman II-ao $\sim$ 30 ℓp/mm.

Although the process is simple in principle, there are several technical problems which have to be overcome in the construction of an operable camera. The presence of the highly reactive alkali metals in the photocathode means that even minute amounts of contaminant can severely damage or destroy it. Decker (1969) has investigated such processes and found that of the common residual gases water vapour, carbon dioxide, and oxygen are the most active. A partial pressure of only 5×10^{-8} torr of water vapour will cause serious losses in sensitivity in a few hours.

Since the main source of this "poisoning" is the nuclear emulsion a method of protecting the cathode has to be found if it is to be a practicable detector. The problem is made more complicated by the need to remove the emulsion for development, and substitute a fresh emulsion prior to the next exposure without damaging the cathode.

Other serious problems are the suppression of electronic background in the presence of stray cathode material on the walls of the tube, and gaseous emission from the cathode, both of which can severely depress the signal to noise ratio.

Several electronographic cameras which overcome these problems have been built. One such device, designed by Dr. McMullan and his associates at the Royal Greenwich Observatory (R. G. O.) is used in conjunction with the Nebula polarimeter, and at present forms its principle detector. A brief description of the construction and operation of the "McMullan tube" will be given below, for a more detailed discussion reference should be made to the designer's own publications (McMullan 1969, 1971, 1972, McMullan et al 1972, 1974). A cross-section of the tube is shown in Figure 3. 10. The tube envelope is of fused silicate 130 mm in diameter with a 40 mm photocathode formed directly on the faceplate. The high tube vacuum is maintained by an ion appenda pump. The electrode assembly is made up of Titanium annuli spaced by Soda-lime glass cylinders, 10 mm long, which form closing surfaces of uniform poten gradient between the electrodes. The whole structure is fused together with solder glass. Metal Oxide-glaze resistors (30 x 100 M Ω) forming the potential divider are mounted directly on the electrode structure.

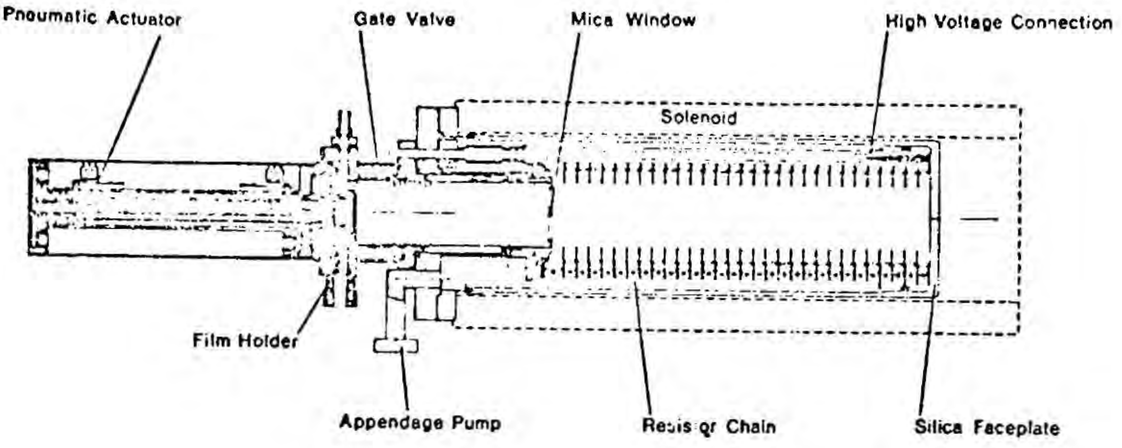

Figure 3.10 *Cross-section of the 4 cm Electronographic camera (from McMullan et al, 1972).*

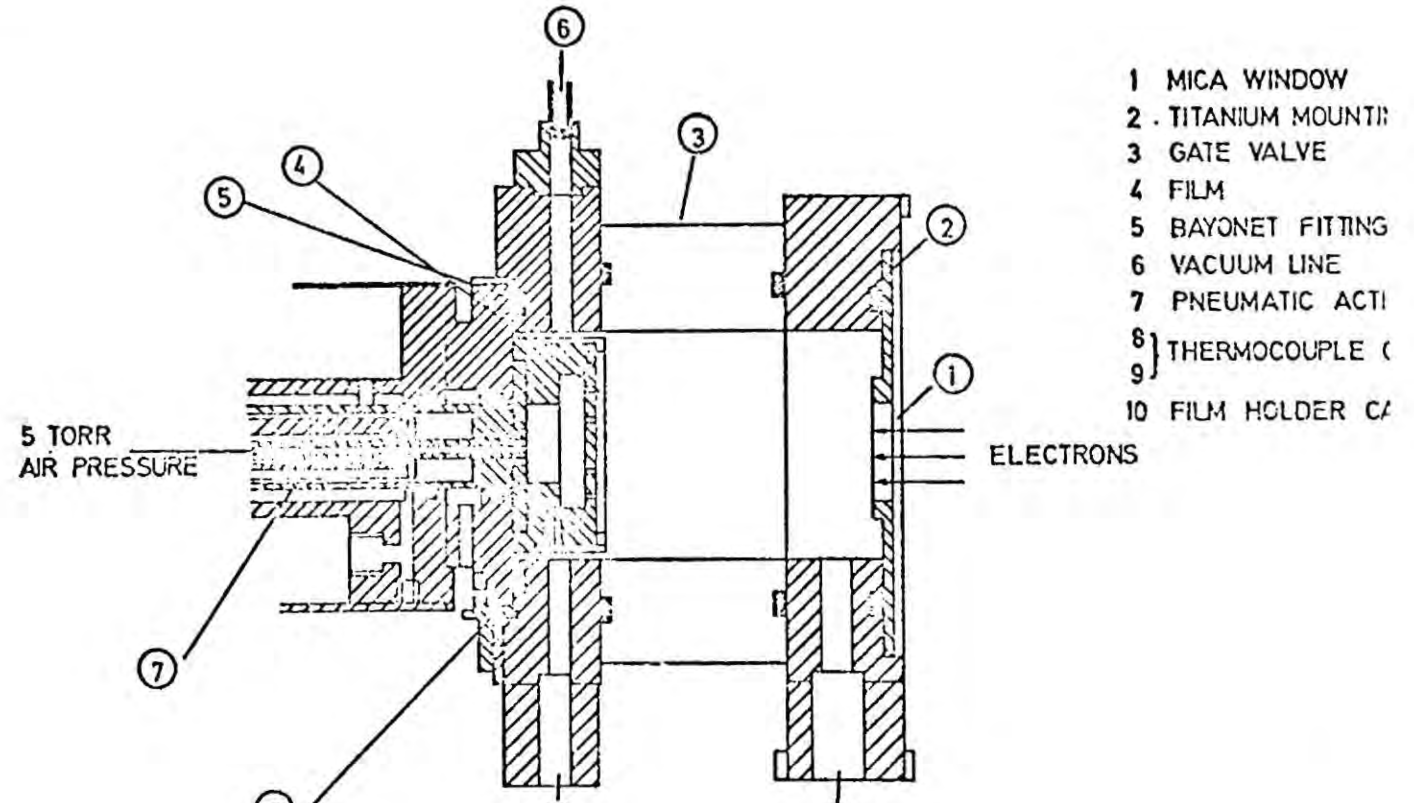

Figure 3.11 *Output end of the McMullan camera (from McMullan et al 1972).*

A 40 kV supply to the photocathode and potential divider is connected by bringing the high voltage cable through a glass tube. The insulation is provided by the Silicon envelope.

A Lenard Window is incorporated in the tube and forms a vacuum tight barrier between the nuclear emulsion and the photocathode, but is permiable to high velocity electrons. The window is made of Mica 40 mm in diameter and 4μm thick and is stretched tight and sealed to a Titanium mount with solder glass. The use of this type of window in an electronographic camera was pioneered by McGee in the spectracon (McGee et al 1969). The window in the spectracon is designed to withstand atmospheric pressure and is limited in size to 20 mm. The McMullan tube with window of 40 mm diameter would certainly not withstand atmospheric pressure and it is necessary to keep the output side of the window at a pressure of one Torr or less by means of a sorption pump. A vacuum lock is provided through which the nuclear emulsion can be inserted. Since the air pressure is low the Mica window presents an almost plane surface to the emulsion, which is of great value as very close contact between the two is required if good resolution is to be obtained (the electrons are scattered by the Mica into a cone of half-angle about 45° so that the radius of the disk of confusion produced by scattering is of the same order as the gap between the window and the emulsion). Figure 3.11 shows the output end of the tube, 1 is the Mica window on its Titanium mounting, 2, 3 is the gate valve, 4 is the film mounted on the holder and is held in place by a cap 10. The holder is inserted into the bayonet fitting 5 of the vacuum lock assembly. The nuclear emulsion on melinex (50 μm thick) is brought up to the Mica by the pneumatic activiator 7 through the gate valve which acts as a vacuum lock. The valve is opened only when the pressure on the film side has been reduced to below one Torr. When the film has been moved up to the window the space behind the film is pressurized with air at about 5 Torr, thus pressing the emulsion into contact with the taut Mica-window. The whole process is carried out by an automatic electro-pneumatic control system and the vacuum is monitored by thermocouple gauges 8 and 9. The whole process can be completed in almost a minute.

The tube uses magnetic focussing which is accomplished by acclerating the electrons in the presence of a coaxial magnetic field (of several hundred Gauss). The electrons are focussed at a plane which is advantageous for recording on emulsion. The whole tube is bolted to the back flange of the Solenoid which is contained in a thick μ-metal shield and the whole camera is attached to the polarimeter backplate by means of the Solenoid (Figure 3.12). The emulsions used with the camera are Ilford G5 and L4. Electronographic recordings on the very fine grained L4 emulsion appear to be unspectacular because their information content, present at modest densities but high signal to noise ratio, is not visually resolvable. Exposures with both G5 and L4 have shown that for equal exposure times L4 plates, though appearing under-exposed, show far more detail when examined with a microdensitometer (Penny 1976), and with their high storage capacity allow full advantage of the electronographic process to be taken. However, the course grained G5 still gives a gain in speed compared to exposures on II-ao photographic plates and has the advantage of linearity. A typical polarimeter electronograph on G5 emulsion is shown in (Figure 3.13) and the majority of the results presented

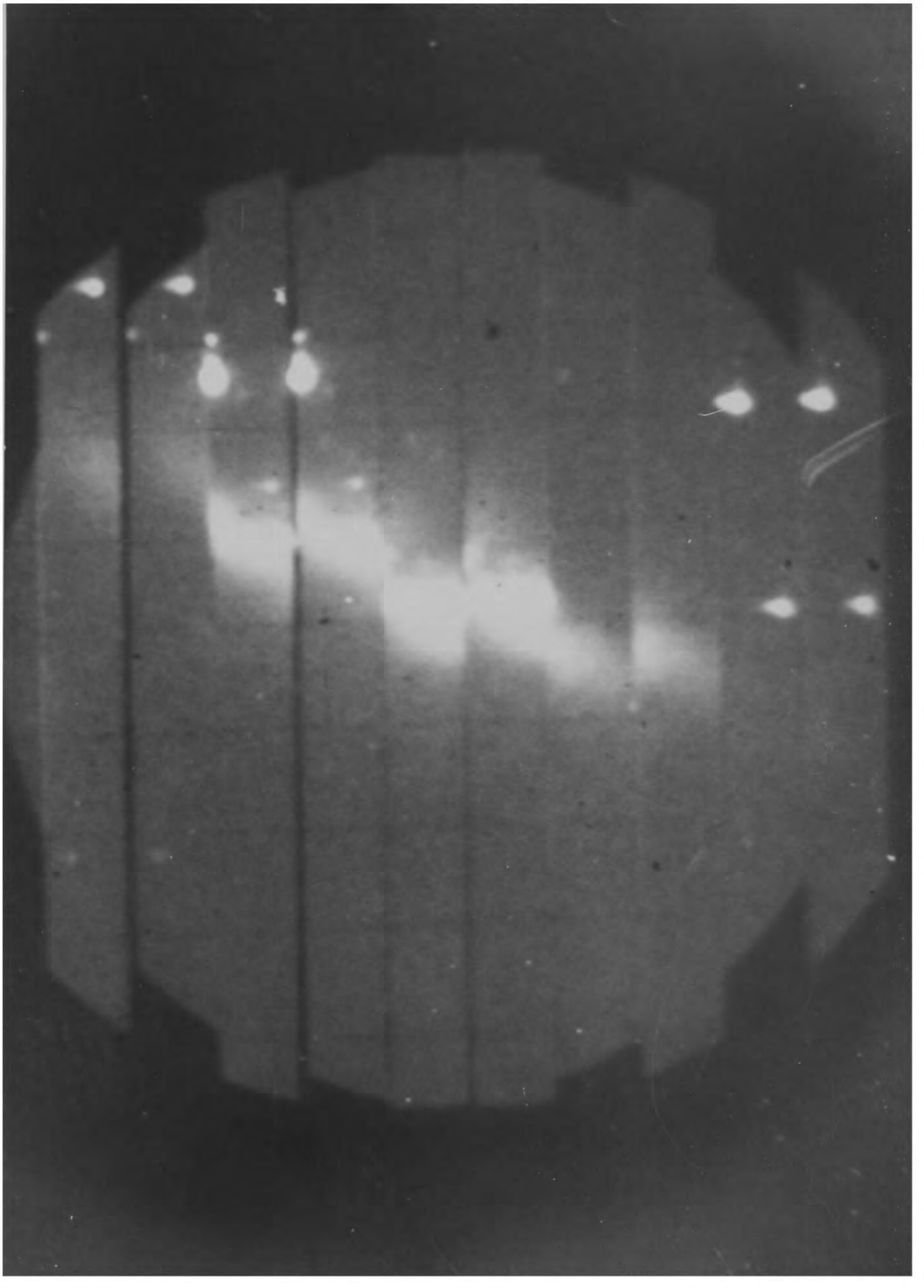

Figure 3.13 A polarimeter electronograph.

later were obtained using this emulsion, mainly because at the time the measurements were made the advantages of L4 emulsion were not known. The actual size of the image on the plate is 1 cm. The outline of the grids is clearly visible on the plate and so are several stars and the galaxy M82. Gaps and overlaps between the strips are apparent and these are due to the imperfect milling of the grid assembly. As we shall see later this overlapping will be put to good use during the analysis of the plates (Chapter 4).

3.3 The Theory of the Polarimeter

Consider a beam of light of intensity I consisting of a linearly polarized component of intensity I_p, whose E-vector makes an angle θ with North (measured North to South through West, i.e. anticlockwise from North) and therefore a preferred prism direction, and an unpolarized component of intensity $(I - I_p)$.

Now the component of the E-vector parallel to the reference direction $(\theta = 0^{o})$ from the polarized light in this direction will be $I_p \cos^2\theta$. So a detector sensitive only to this plane of polarization will register an intensity

$$I_1 = I_p \cos^2\theta + (I - I_p)/2 = I/2 + I_p/2 \cos 2\theta \tag{3.3}$$

as the unpolarized light will be divided equally between $\theta = 0^{o}$ and $\theta = 90^{o}$. Similarly for the plane of polarization at 90^{o} to the first

$$\begin{aligned} I_2 &= I_p \sin^2\theta + (I - I_p)/2 \\ &= I/2 - I_p/2 \cos 2\theta \end{aligned} \tag{3.4}$$

The first Stokes' parameter I is given by

$$\hat{I} = I_1 + I_2 = I \tag{3.5}$$

and is just the total intensity I.

The second Stokes' parameter Q is

$$Q = I_1 - I_2 = I_p \cos 2\theta \tag{3.6}$$

If we adopt the same procedure for a new pair of axes rotated through 45^o we find

$$\begin{aligned} I_3 &= e_1[I_p \cos^2(\theta - 45) + (I - I_p)/2] \\ &= e_1[I/2 + I_p/2 \sin 2\theta] \end{aligned} \tag{3.7}$$

This is equivalent to a rotation of the $\lambda/2$-plate by $22\frac{1}{2}^o$, and similarly

$$I_4 = e_1[I/2 - I_p/2 \sin 2\theta] \tag{3.8}$$

where e_1 is a factor due to the different exposure of the second plate (only two components can be recorded on each plate) and can be used to normalize the plates

$$e_1 = (I_1 + I_2)/(I_3 + I_4) \tag{3.9}$$

by defining the third Stokes' parameter U to be

$$U = (I_3 - I_4) \frac{(I_1 + I_2)}{(I_3 + I_4)} = I_p \sin 2\theta \tag{3.10}$$

The position angle of the E-vector θ is then given by

$$\theta = \tfrac{1}{2} \tan^{-1} U/Q \tag{3.11}$$

where the quadrant for θ can be established from the signs of U and Q as indicated in table 3.1, and the degree of polarization P is given by

$$P = I_p/I = \frac{(U^2 + Q^2)^{\frac{1}{2}}}{I} \qquad (3.12)$$

The fourth Stokes' parameter V, which gives a measure of the circular polarization is set to zero as our system cannot measure it (V is in practice always very small). The value of the additive nature of the Stokes' parameters has already been described in section 1.2 and this important property will be used extensively in the removal of foreground and instrumental polarization. The four values I_1, I_2, I_3, I_4 are of course the intensities read of a pair of plates with the polarimeter. From equations (3.3 - 3.12) it is obvious that two further rotations of the $\lambda/2$-plate by $22\frac{1}{2}^{o}$ leads to a second set of four intensities I_5, I_6, I_7, I_8. Clearly

$$I_5 = I_2$$
$$I_6 = I_1$$
$$I_7 = I_4$$
$$I_8 = I_3$$

if there is a variation in the photocathode response between the left and right strips these equalities will not be satisfied. By sacrificing the independence of the two sets of data we can allow for this effect. If we call the response of the right-hand strip at some point 1 and that of the left-hand strip at the corresponding point f (Figure 3.14) then the values of I_2, I_4, I_6, I_8 will be overestimated by this factor f. The eight intensities are now

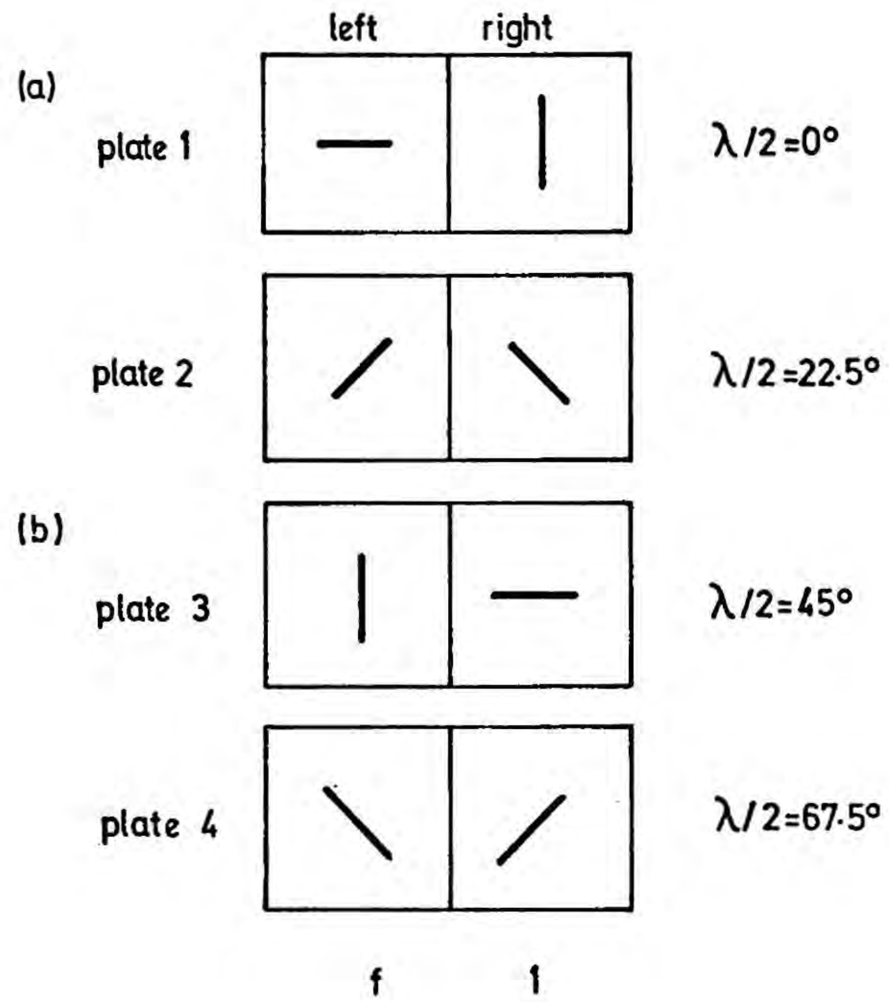

Figure 3.14 *The use of the f-factors in correcting for the effects of the variation of the cathode sensitivity; by combining two pairs of observations. The direction of the E-vector recorded at each $\frac{\lambda}{2}$-plate setting is shown by the black line.*

$$
\begin{aligned}
I_1 &= \quad [\, I/2 + I_p/2 \ \cos 2\theta \,] \\
I_2 &= \quad f\, [\, I/2 - I_p/2 \cos 2\theta \,] \\
I_3 &= e_1 [\, I/2 + I_p/2 \sin 2\theta \,] \\
I_4 &= e_1 f [\, I/2 - I_p/2 \sin 2\theta \,] \\
I_5 &= e_2\, I_2/f \\
I_6 &= e_2 I_1\, f \\
I_7 &= e_3 I_4/f \\
I_8 &= e_3 f\, I_3
\end{aligned}
\tag{3.13}
$$

where e_1 to e_3 are the relative exposures of each plate, Hence

$$\frac{I_7}{I_8} = \frac{I_4}{f^2 I_3} \tag{3.14}$$

giving a first estimate of f

$$f_2 = \left(\frac{I_4 I_8}{I_3 I_7} \right)^{\frac{1}{2}} \tag{3.15}$$

Similarly

$$\frac{I_5}{I_6} = \frac{I_2}{f^2 I_1} \tag{3.16}$$

giving a second estimate of f

$$f_1 = \left(\frac{I_6 \ I_2}{I_5 \ I_1} \right)^{\frac{1}{2}} \tag{3.17}$$

and hence the variation of the photocathode response at each point may be calculated. We apply a correction to the measured Stokes' parameters by forming the mean-value of the f-factors

$$< f > = (f_1 + f_2)/2 \tag{3.18}$$

and modifying equations (3. 5-3. 11) by dividing each occurrence of an even numbered intensity by $< f >$. Hence

$$\begin{aligned} I &= (I_1 + I_2/< f >) \\ Q &= (I_1 - I_2/< f >) \\ U &= \frac{(I_3 - I_4/< f >)(I_1 + I_2/< f >)}{(I_3 + I_4/< f >)} \end{aligned} \tag{3.19}$$

with these new definitions of the Stokes' parameter equations (3.5 - 3. 11) appear unchanged. The equations 3.19 will now give a polarization map from each pair of plates corrected for the photocathode sensitivity and any variations in response of the tube to orthogonal polarization will also have been removed.

The final map is obtained by forming the average of the Stokes' parameters. A similar set of parameters I', Q', U', f_1', f_2', e_1', e_2', e_3', are obtained for the other half of the galaxy. Since it is impossible to determine e_1/e_1' to e_3/e_3' without extra information the Stokes' parameter I cannot be compared between strips exposed in the grid IN and grid OUT positions. Theoretically f_1 and f_2 should be identical and so should the two sets of corrected Stokes' parameters. Similarly the exposure factors e_1 to e_3 should be constant over the whole plate. The observed distributions of these e- and f-factors also provides an important estimate of the internal accuracy of our measurements. The practical application of this theory to the reduction of the polarimeter electronographs is described in some detail in chapter 4.

3.4 Discussion of Systematic Errors

3.4.1 The Problem of Foreground Illumination

When the "Sky background" is not completely black there is a high probability that it will also be polarized. The effect will be small for bright objects, but could be a serious source of error for faint objects.

The choice of site is important as terrestial illumination will be highly nonuniform. From this aspect the Herstmonceux site appears far from ideal because of its proximity to several large conurbations. However, we have not detected any positional dependence in the background intensity and polarization which might be ascribed to this source.

Illumination by moonlight or twilight will certainly mean that the background will be polarized. Considerable importance must therefore be attached to having "dark-time" for polarimetry, particularly for extended object studies where the increase in the background intensity greatly hampers observation of regions with low surface luminosity. Because of the limited amount of dark time available "grey-time" was also utilized in this project, but observations were only made when the moon was below or close to the horizon.

In order to avoid the possible effects of sunlight Rayleigh scattered from below the horizon the hour before sunrise and after sunset was not used. One of the most important features of the Nebula polarimeter is its wide field of view which enables the night sky to be monitored on the same exposure as the object being studied. By adjusting the instruments lens system a sufficient object free area can be made available on the electronograph so that the background Stokes' parameters can be determined. Details of the calculation and subtraction of the background are given in Chapter 4.

3.4.2 Errors Introduced by the Telescope

The optical components of a telescope can introduce polarization or have a depolarizing action. Since these effects occur before the analyser the measured polarization will not be the true polarization. Unfortunately these effects can occur in all types of telescope. In refractors the objectives can introduce circular or elliptical polarization, as glass under strain exhibits birefringance. The phase difference, τ, introduced between the two polarized components is

$$\frac{\tau}{2\pi} = \frac{\delta}{\lambda} \tag{3.20}$$

where δ is the relative retardation given by

$$\delta = |n_o - n_e| \, d \tag{3.21}$$

where d is the thickness of the objective (typically a few inches) and $|n_o - n_e|$ is the difference between the O and E refractive indices ($\sim 4 \times 10^{-7}$). If the objective gives rise to relative retardation of only $\lambda/16$ the observed linear polarization will only be 93% of the true value (Serkowski 1960), since the stress on the objective changes with the orientation of the telescope and the necessary corrections are often very complicated.

In the case of reflectors the non-uniformity of the Aluminium surface often results in both the primary and secondary mirrors having numerous irregular shaped polarizing patches, each of which introduces a polarized component which may have one of many different planes of vibration. Furthermore the degree of polarization introduced by these patches is usually highly colour dependent and this can cause severe problems when the wavelength dependence of polarization is being investigated, (e.g. Behr (1960) found that observations of different coloured stars made with the McDonald 36 inch reflector needed differing amounts of correction).

A further complication is introduced because these effects varying strongly with the age of the Aluminium layer. Treanor (1962) and Theissen and Broglia (1959) have reported negligible instrumental polarization with freshly aluminized mirrors, but high instrumental polarization, accompanied by large changes of phase angle (greater than 5^{o}) in localized regions of badly weathered mirrors. In early photographic trials of the polarimeter we experienced difficulties with the 36 inch Yapp telescope at R.G.O., but these were mainly concerned with reflection losses due to poor state of the mirror. However, before the observations reported in this thesis were made both the primary and secondary mirrors were freshly aluminized. Linear polarization can be produced by freshly aluminized mirrors if the Aluminium is put on at angles which differ greatly from normal incidence (Reiner 1957) but this problem did not occur with the Yapp mirrors.

Our decision to design our instrument for use at the Cassegrain focus was not only influenced by telescope payload requirement but by the possible difficulty in correcting for the instrumental effects of refracting telescopes. Mostobservers have made their observations at the Cassegrain focus and in fact the only serious attempt to measure polarization on a Newtonian reflector by Van P. Smith (1955, 1956) ran into serious problems because of the polarization introduced during the reflection from the optical flat.

Special rotatable relescopes have been built so that telescopic polarization effects can be eliminated by combining two observations of each object obtained with the telescope in two positions 90^{o} apart. By observing "standard stars" which have already been observed with a rotatable telescope it is possible to determine, and hence remove, the instrumental polarization induced in a non-rotatable telescope, and it is this method we have used in our work. Using data from Axon and Ellis (1976) we have compiled a list of polarized and unpolarized standard stars for this purpose (tables 3.3 and 3.4). The results of the standard star measurements are described in Chapter 5.

3.4.3 Errors Intrinsic to the Polarimeter

If plane polarized light is not incident perpendicular to a photosensitive surface the output signal will depend on the direction of the E-vector with respect to the surface (Clancy 1952, Figure 3.15). In the case of a double beam instrument such as the Nebula polarimeter, where the planes of polarization are fixed, any difference in the response of the photocathode to orthogonal polarization forms can be removed by interchanging the O and E rays and combining the measurements. The Wollaston prism mounting was in fact designed so that this can easily be accomplished, and the choice of a small divergence prism keeps the angle of incidence nearly orthogonal to the photocathode.

A second and more conspicuous source of error is caused by the non-uniformity of the photocathode sensitivity. Measurements by Serkowski and Chojnacki (1969) have shown that the sensitivity at different points on the surface of a photomultiplier tube cathode may change by at least a factor of two (Figure 3.16). However, the photocathode of the McMullan camera is far more uniform than this, mainly because of the great care taken in its production. Measurements by Penny (1976) have shown that the sensitivity varies by no more than $\pm$ 10%, which agrees well with our own measurements. By combining measurements made with the $\lambda/2$-plate in four successive positions $22\frac{1}{2}^{\circ}$ apart w

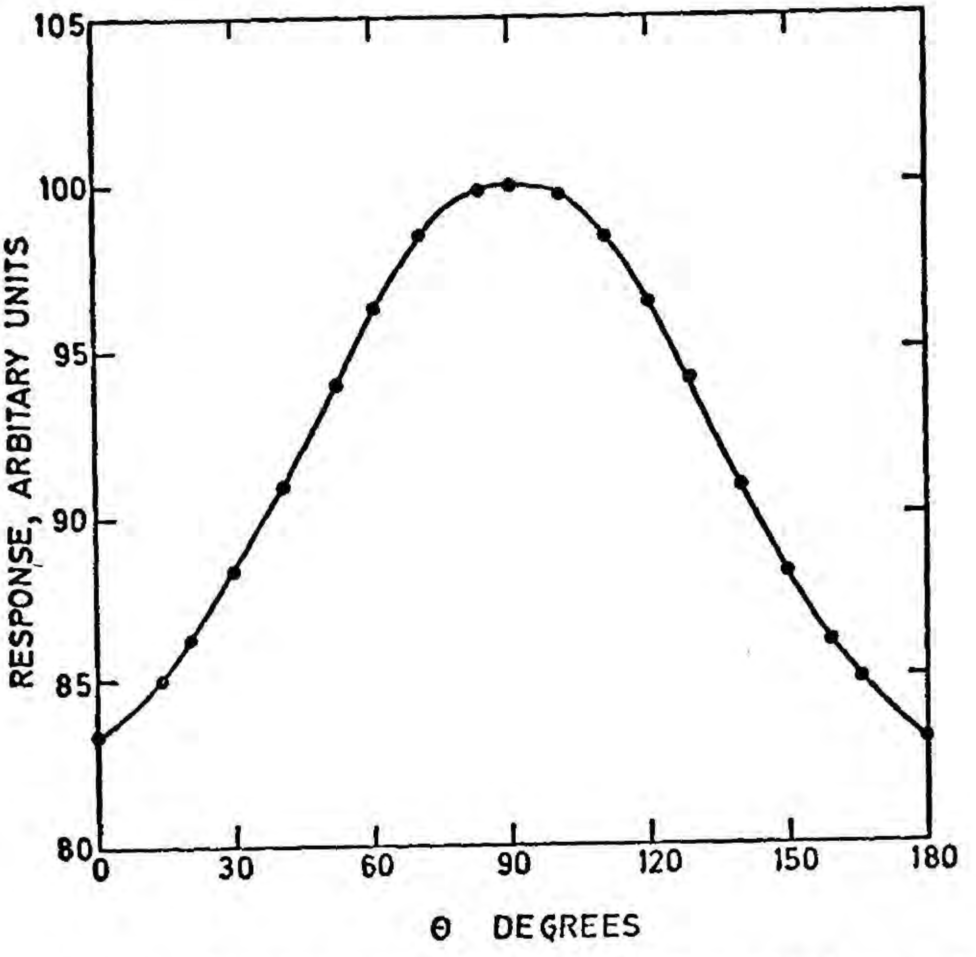

Figure 3.15 *Response of RCS 931-A photomultiplier tube as a function of the angle Θ which the E-vector of the incident light makes with the longitudinal axis of the tube (Clancy 1952).*

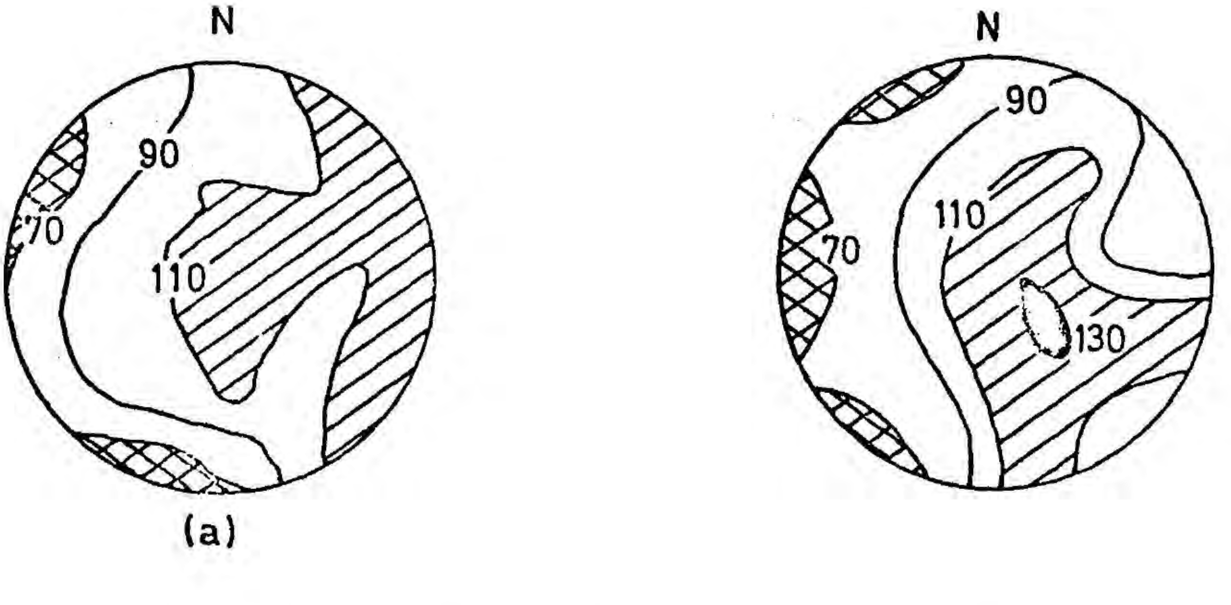

Figure 3.16 *The distribution of sensitivity on the photo-cathode of two EMI 6256 photomultipliers (a) and (b) (from Serkowski & Chojnacki 1969).*

have shown in section 3.4 that it is possible to measure the point to point variations of the photocathode sensitivity directly from the polarization measurements, and to correct them for this effect. This correction procedure also removes any dependence of cathode response to the orthogonal polarization forms. The rotation of the Wollaston prism can be used to check these corrections and we shall describe shortly a third method of measuring the cathode sensitivity directly using what we term "Cloth" exposures (Chapter 5).

We now turn our attention to possible errors caused by defects in the optical components of the polarimeter. We have already commented on the behaviour of the chromatic $\lambda/2$-plate purchased from Rofin Limited. Most of the observations reported later were obtained using this $\lambda/2$-plate, and its deviation from $\lambda/2$-behaviour will be a serious source of error. In order to remove its depolarizing effects complicated and lengthly corrections are required and these are described in Chapter 5. This $\lambda/2$-plate was later replaced by an achromatic $\lambda/2$-plate, thus overcoming the problem, but even with the achromatic $\lambda/2$-plate care must be taken to ensure that the angle of incidence of the converging telescope beam is not more the $\pm\ 12^o$ otherwise deviations from achromaticity occur Some of the trial observations made using this $\lambda/2$-plate are also reported in Chapter 5. Care must also be taken in aligning the $\lambda/2$-plate fast axis with a preferred prism direction in the "zero position" of the $\lambda/2$-plate, as otherwise the observed position angles will be incorrect. Errors of this sort can of course be corrected for by observing standard stars, or by using the "cloth" exposure described in Chapter 5. In practice, the method of alignment described in Chapter 5 proved so satisfactory that the observed position angles did not need correcting.

Of equal importance are possible errors due to the Wollaston prism. If the prism divergence varies with wavelength, light of different colours, from different parts of the object, will be focussed at the same location, inevitably causing a depolarization. To make sure this was not occurring the prism divergence was measured at several wavelengths (Chapter 5.) Another problem that has been encountered by previous observers using a Wollaston prism as analyser (e.g. Loden 1961) is a dependence of the observed polarization with the position in the field of view. Laboratory and telescope tests have shown no such "field effects" with our instrument (Chapter 5).

Multiple reflections from the many optical surfaces in the polarimeter could present a problem, though they appear to be small. Only when a Laser beam was shone into the polarimeter could we detect these multiple reflections. Before the instrument was mounted on the telescope we aligned the optical components relative to the optical axis of the polarimeter so that the multiple Laser beam images disappeared.

Finally one point of technique. In many older polarimeters measurements with a depolarizer of tilted plate calibrator in the beam were used for calibration. This practice is however very unreliable, and usually unnecessary. Therefore we have generally avoided using this method. Occasionally we have however taken exposures of standard stars with a Lyot (1928) type depolarizer in the beam for comparison purposes.

3.5 The Observing Procedure

The observing procedure adopted with the Nebula polarimeter is as follows:

1. The image tube performance is checked by running through its

operational cycle with a dummy film and the operation of the electronic shutter checked to ensure that there is no danger of burning out the photocathode, and the image tube allowed to stabilize for one hour.

2. The electronic shutter is closed to protect the image tube and the telescope mirror uncovered and the focus of the telescope checked in the manner described previously.

3. The North-South alignment of the grids is checked, also as described previously.

4. "Standard star measurements" are made. One polarized standard and one unpolarized standard by running through steps (5) and (6).

5. The object is located in the grids and a suitable guide star chosen and the $\lambda/2$-plate moved to 0° and the emulsion exposed.

6. The $\lambda/2$-plate is moved through $22\frac{1}{2}^{\circ}$ and another exposure taken, and this process is repeated four times.

7. The standard star measurements are then repeated as in (4)

8. The grid assembly is moved by one grid spacing so that the other half of the object is in the field of view and the $\lambda/2$-plate is returned to the zero position, and an exposure taken.

9. Step (6) is repeated.

10. The standard star measurements are repeated.

11. Occasionally various other exposures are taken. The prism is sometimes rotated by 180^{o} thus swopping the O and E images on the photocathode and providing a check on the removal of the cathode sensitivity. Exposures of standard stars and extended objects are taken with a depolarizer inserted. The telescope aperture is covered with a white cloth, which acts as a diffuser and calibration exposures of the dome wall taken with and without a polaroid at a known position angle.

3.6 The Observations

The observations reported in this thesis were made using the 36" reflector at the R.G.O, Herstmonceux during two periods in 1974. During the period March to June 1974 observation of the galaxy M82 were made using the chromatic $\lambda/2$-plate. We shall identify each of these plates by their exposure numbers, which are as listed in table 3.2. Further observations were made in October to November 1974 with the achromatic $\lambda/2$-plate and the 4 cm prism. These consisted mainly of standard star and Cloth exposures for test purposes. Some Cloth exposures with the chromatic $\lambda/2$-plate were also made. Again these observations are itemised in table 3.4. After exposure the electronographs were processed in a standard manner. Each electronograph was developed within half an hour of exposure in ID19 at 20 ± 1°C for five minutes using both nitrogen bubble bursts, with a fixed burst and interval duration of eight seconds, and hand agitation. The electronographs were then rinsed for 30 seconds in an acetic acid stop bath and fixed for twice the clearing time (eight minutes) in Hypam and hardener. They were then washed for one hour in deionized water, bathed in wetting agent for two minutes and allowed to dry.

Table 3.2

List of the Observations

a) Old $\lambda/2$ Plate

Plate Numbers	Object	$\lambda/2$ - plate orientation	Grids In/Out	Comments
9		0		
10	M 82	+ $22\frac{1}{2}$	IN	G5 emulsion
11		+ 45		
12		+ $67\frac{1}{2}$		
13		+ 0		
14	M 82	+ $22\frac{1}{2}$	OUT	G5 emulsion
15		+ 45		
16		+ $67\frac{1}{2}$		
19		+ 0		
20	M 82	+ $22\frac{1}{2}$	OUT	G5 emulsion prism rotated by 180°
30		+ 0		
31	M 82	+ $22\frac{1}{2}$	OUT	G5 emulsion
32		+ 45		covered by glue deposits
36		+ $67\frac{1}{2}$		
44-51	Cloth	8 positions		No polaroid G5
52-55	Cloth	4 positions		Polaroid at 45° G5
56-59	Cloth	4 positions		Polaroid at $22\frac{1}{2}^{\circ}$ G5
110-119	ρ cas	8 positions		
122-129	ρ cas	8 positions		Depolarized
131-135	μ cas	4 positions		

Table 3.2 (cont)

b) New λ/2 plate

Plate Numbers	Object	λ/2 - plate orientation	Comments
71-74	μ cos	4 positions	L4 emulsion, defocus
77-85	Cloth	8 positions	Polaroid 0^{o}
86-86	Cloth	4 positions	Polaroid 45^{o}
90-93	Cloth	4 positions	Polaroid $22\frac{1}{2}^{o}$
	9 GAM	4 positions	
	HD 122945	4 positions	
	HD 155528	4 positions	
	HD 80083	4 positions	
	ρ cos	4 positions	Defocused

TABLE 3.1

POSITION ANGLE ANALYSIS

θ	U	Q	Tan 2θ
0 - 45	+	+	+
45 - 90	+	-	-
90 - 135	-	-	+
135 - 180	-	+	-

UNPOLARIZED STANDARDS

NEARBY STARS

HD	BD	α (1960) H M	δ (1960)	m_v	Spectral type (mK)	r(pc)	Source	P (mags)	θ°
6582	μ CAS	1 05.6	+ 54° 31'	5.1	G5V	7	BEHR	0.002	24
19373	Σ Per	3 06.2	+ 49 28	4.0	GOV	12	BEHR	0.000	27
34411	λ Aur	5 16.3	+ 40 04	4.7	GOIV	15	BEHR	0.001	142
39587	ψ' Ori	5 92.1	+ 20 17	4.4	GOV	10	BEHR	0.001	112
82885	11 Lmi	9 33.4	+ 36 01	5.4	G8IV-V	9	BEHR	0.001	58
90839	36 Uma	10 28.1	+ 56 11	4.8	F8V	12	BEHR	0.000	153
109358	β Cun	12 31.9	+ 41 34	4.3	GOV	9	BEHR	0.000	92
110897	10 Cun	12 43.2	+ 39 29	5.9	GOV	15	BEHR	0.001	158
114710	β Com	13 10.0	+ 28 02	4.3	GOV	8	BEHR	0.001	60
126660	θ B oo	14 23.8	+ 52 02	4.1	F7V	19	BEHR	0.001	70
188512	β Aql	19 53.3	+ 6 18	3.7	G8IV	14	HALL BEHR	0.000 0.000	- 100
210027	i peg	22 05.2	+ 25 09	3.8	F5V	14	BEHR	0.001	111

TABLE 3.3

TABLE 3.3 (CONTINUED)

B) MORE DISTANT STARS

N_o	HD	B D	α (1960) H	α (1960) M	δ (1960)	m_v	Spectral type (mK)	r (pc)	Source	P (mags)	θ°
13	7927	ø CAS	1	17.5	+58° 01'	5.0	FOIa	1500	Behr	0.069	94
									Hall	0.070	96
									Hiltner	0.074	93
									Serkowski (4350 A°)	0.069	95
14	2129	2H CAM	3	25.8	+59 48	4.2	B9Ia	850	Behr	0.074	115
									Hall	0.072	115
									Hiltner	0.072	117
15	23572	+23° 524 #	3	44.2	+23 30	8.1	AOV	130	Behr	0.043	28
									Hall	0.047	28
									Serkowski (4350 A°)	0.049	30
									(5550 A°)	0.050	28
16	43384	9 CAM	6	14.4	+23 45	6.3	B31a	1700	Behr	0.066	172
									Hall	0.058	168
									Serkowski (4350 A°)	0.068	173
									Hiltner	0.062	170
17	84567	-29 7758	9	43.6	-30 01	6.5	B2		Hall	0.019	80
									Smith	0.020	77
18	154445		17	03.5	-0 50	5.6	BIV	400	Hall	0.072	88
									Smith	0.077	88

TABLE 3.4

POLARIZED STANDARDS

No	HD	BD	α (1960) H	M	δ (1960)		m_v	Spectral type (mK)	r(pc)	Source	P (Mags)	θ°
1	160529		17	39.3	-30°	29'	6.7	A2Ia	1200	Hall	0.164	20.6
										Hiltner	0.150	20.0
										Smith	0.156	18
2	164852		18	20.7	+20	50	5.1	B4	400	Behr	0.020	171
										Hall	0.021	176
										Hiltner	0.018	178
3	183143		19	25.7	+18	12	6.9	B7Ia	1200	Behr	0.126	178
										Hall	0.143	179
										Hiltner	0.130	179
										Smith	0.147	0
4	198478	55 Cyg	20	47.6	+45	58	4.8	B3Ia	950	Behr	0.062	2
										Hall	0.068	4
										Hiltner	0.061	5
5	209481	14 Cep	22	007	+57	48	5.6	09V	600	Behr	0.035	67
										Hall	0.043	72
6	224014	p Cas	23	52.4	+57	17	4.1	F8Ia	1100	Behr	0.027	55
										Hall	0.029	50
										Hiltner	0.030	51
7	134320	46 Boo	15	07	+26	23	6.73	KO		Behr	0.0138	
8	156110		17	12	+45	24	7.3	B3		Hiltner	0.016	

REFERENCES

Appenzeller, I.	1967	Pub. A.S.P. p 136.
Axon, D.J. and Ellis, R.S.	1976	M.N.R.A.S. in press
Behr, A.	1960	Lowell Obs. Bull. No. 4, p 292
Clancy	1952	J. Opt. Soc. Am. 42, p 357
Decker, R.W.	1969	Advances in Electronics and Electron Physics, Volume 28A, p 364
Hall, J.S. and Miksell, A.M.	1950	Pub. U.S. Naval Obs. 17, No: 93.
Hiltner, W.A.	1949	Ap. J., 109, p 471
	1951	Ap. J., 114, p 241
Loden, L.O.	1961	Stockholm Obs. Ann. Vol. 21, 7
Lyot, B.	1928	Ann. de Observatoire Astron. Phys. de Paris (Meudon) Torni i Fasc. 1-2, 8, p 102.
Lyot, B.	1929	Ann. de l'obs. de Meudon, 8, p 21.
Miksell, A.M., Hall, J.S. and Hoag, A.A.	1951	J. Opt. Soc. Am. 41, p689
McMullan, D.	1972	Proceeding ESO/CERN conference on instrumentation for large telescopes. Geneva May 1972, 433-445.
McMullan, D.	1969	Observatory 91, p. 199
McMullan, D., Hartley, K.F.	1974	Conference on Electronography and its applications to Astronomy, McDonald Observatory.
McMullan, D., Powell, J.R. Curtis, N.A.	1972	Advances in Electronics and Electron Physics Volume 33.

McGee, J.D., McMullan , D	1969	Advances in Electronics and Electron Physics 28A p61-180.
Ohman, Y.	1939	M.N.R.A.S., 78, p 553
Pickering	1873	American Academy of Arts and Science 1 IX, 1
Pancharatnam, S.	1955	Proc. Indian Acad. Sie (Ser.A), 41, p 130.
Pospergelias, M.	1967	Astron. Zh. 42, p 398
Pallister, S.W.	1974	Private communication
Penny, A.	1976	Ph.D. Thesis, University of Sussex.
Reiner, L.	1957	Optick, 14, p83.
Serkowski, K. and Chojnacki, W.	1969	Astron. and Astrophys., 1, p 442.
Serkowski, K.	1960	Lowell Obs. Bull. No. 4, p296
Van P. Smith, E.	1955	Ph.D. Thesis Harvard.
Smith, Van P.E.	1956	Ap. J. 124, p43
Treanor, P.J.	1962	Astronomical Techniques (Ed. W.A. Hiltner), C.U.P. Chap. II.
Theissen, G. and Broglia, P.	1959	Z. Astrophys. 48, p 81.
Serkowski, K.	1974	Planets, Stars and Nebulae studied with photopolarimetry, T. Gehrels (Ed) U. of Arizona Press.

CHAPTER 4

THE DIGITAL ANALYSIS OF POLARIZATION

4.1 The Problems Associated with Analogue Reduction Techniques

The quantitative analysis of photographic images using a microdensitometer needs little or no introduction. Even though the density is normally displayed graphically high precision is possible in one-dimensional applications such as spectroscopy. In contrast two-dimensional projects such as ours are notoriously difficult and time consuming. We shall describe the standard approach to this sort of problem as the "analogue method". Figure 4.1(a) shows a schematic representation of a polarimeter electronograph, defined on an XY coordinate system, and illustrates this method. Quite simply the two-dimensional analysis is accomplished by making successive traces covering the complete Y extent of the plate at the X locations X_1, X_2, X_3, ... X_N.

A preliminary analysis of the M82 polarization data was conducted in this manner. A 186-point analysis of the plates 30, 31, 32, 33 (White 1974) using the Joyce-Loebel automatic microdensitometer at the Royal Greenwich Observatory, operating in a manual mode, and an independent 192-point analysis of plates 13, 14, 15, 16 using the analogue microdensitometer of the Applied Physics Department of the University of Durham were made using a slit of 100μ square, and similar reduction procedures.

In order to determine the polarization at a given location in the galaxy we see, referring to chapter 3.4, that the O and E intensities of that point on each

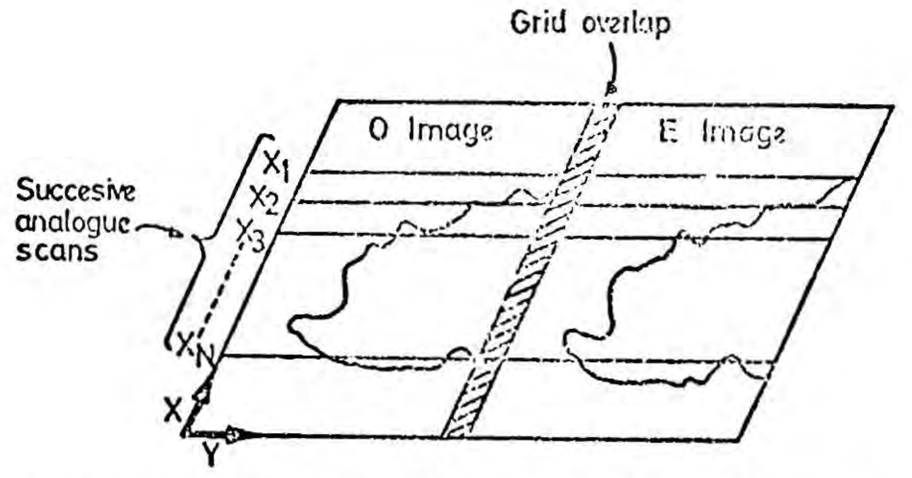

Figure 4.1(a) The analogue method of plate analysis. Successive traces in the Y direction made at locations X_1, X_2, X_3 .... X_N until the whole plate has been covered.

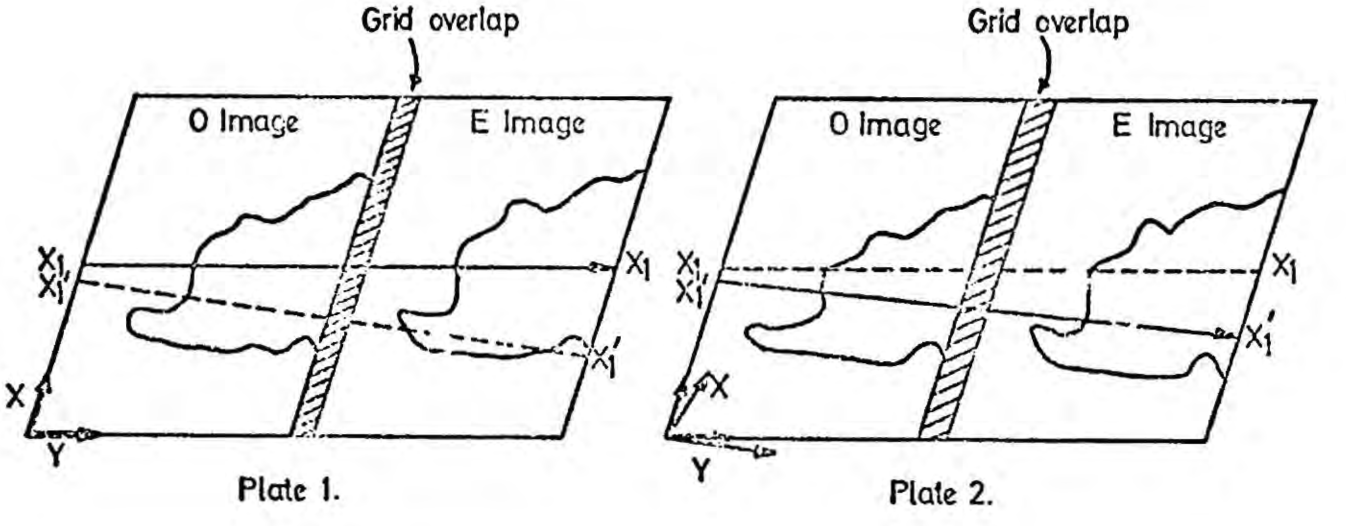

Figure 4.1 (b) Example of misregistered images. A trace on the second plate, at supposedly the same position X_1 as on the first plate, is in fact made at position X_1', and at an angle to the X_1 direction.

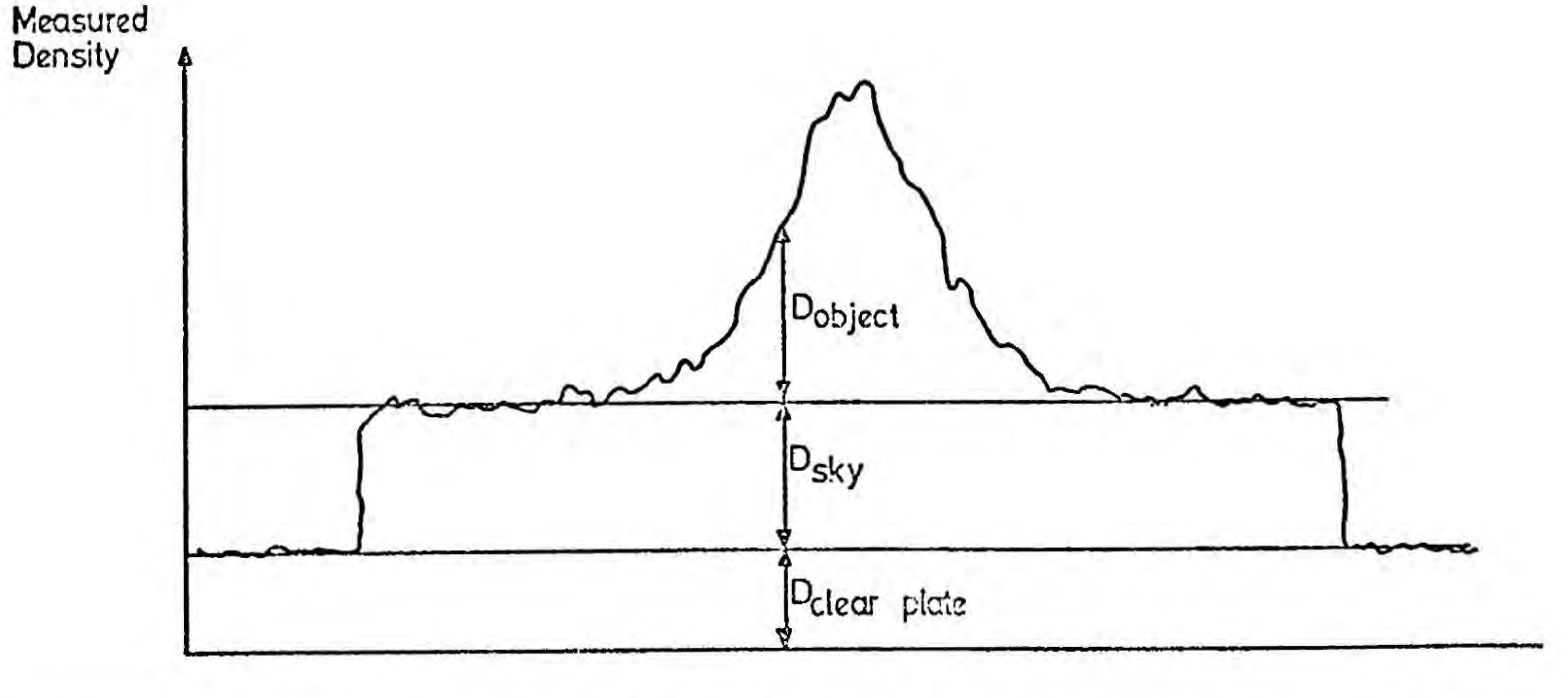

Figure 4.2 A representation of the composition of the measured density on the electronographs.

of four successive plates have to be determined and combined. However, the density at a given point on the plate is not only due to the light from the galaxy (Figure 4.2). Firstly, there is a residual plate noise on the "clear" or unexposed plate which is due to the background noise in the electronographic camera, and contributions from the emulsion itself, which produces a density D_{clear}. Secondly, there will be a contribution from the night sky, D_{sky}, so that the total density on the plate will be

$$D_{total} = D_{galaxy} + D_{sky} + D_{clear} \tag{4.1}$$

Before we can calculate the Stokes' parameters we must estimate and subtract D_{clear} on each trace. A region of clear plate was measured at either end of a trace, and D_{clear} estimated at intervening points by linear interpolation. The remaining density

$$D_{obs} = D_{galaxy} + D_{sky} \tag{4.2}$$

reduces directly to intensity as the electronographic processes is linear, and we may calculate the Stoke parameters I_{obs}, Q_{obs}, U_{obs} immediately using the theory of chapter 3.4. These Stoke's parameters contain contributions from the galaxy and the sky, but because of their additive properties (chapter 1.2) the galaxy Stoke's parameters I_{gal}, Q_{gal}, U_{gal} can be obtained simply by subtracting those due to the sky I_{sky}, Q_{sky}, U_{sky}; which were determined for each pair of strips from traces taken far away from the galaxy.

$$\begin{aligned} I_{gal} &= I_{obs} - I_{sky} \\ Q_{gal} &= Q_{obs} - Q_{sky} \\ U_{gal} &= U_{obs} - U_{sky} \end{aligned} \tag{4.3}$$

In principle then the analogue method appears to be straightforward, but a number of practical problems exist, the most serious of which is that of "image-registration". This is the process of matching the information from the same location in several corresponding images. In our case we not only have to match the O and E images on each plate but also have to identify the same points on four separate plates. The problems arise because of the very small information scale of our electronographs, and astronomical photographs in general. The size of the information scale is generally limited by the size of the "seeing disc" (particularly so with modern emulsions which have a very fine grain size ~ few microns) and this is typically of the order of a few tens of microns, and in our case is ~ $125\,\mu$.

Even though most microdensitometers incorporate vernier scales on their plate carriages, and systems for viewing magnified images of the plate, it is not possible to set the microdensitometer slit to an accuracy of $125\,\mu$. Consequently a trace intended for a particular place on the plate will often be made at a slightly different location; figure 4.1(b) illustrates the consequence of this misplacement. Plate 1 has been traced along the direction (X_1, X_1) but because of errors in setting the microdensitometer slit, including a misorientation, plate 2 has been traced not only at a slightly different position but at an angle to (X_1, X_1) along (X_1', X_1'). Entirely different parts of the galaxy have been measured on the two plates, and on plate 2 O and E images from different places have been used. The result of this misregistration will inevitably be spurious polarization and erronious position angles. Clearly the more plates that have to be combined into one measurement the more serious the problem becomes. A second source of image misregistration arises when the density at the Y locations of corresponding traces is determined, as the Y positions can only be read to a limited accuracy of ~ ½ a division. Attempts to make estimates to smaller scales than this are necessarily very subjective. This same problem affects the density determination from the traces and is particularly important near the sky background level, as after subtraction small changes in density lead to large polarization changes.

Defects on the plates such as scratches, emulsion flaws and blobs of dirt are also a very real problem. If they are not identified and separated from "real features" this will result in spurious polarizations. This is far from easy in practice, and proved extremely difficult on plates 30 to 33 which were covered by deposits of glue, caused by the developer, attacking the adhesive used to mount the emulsion.

The problem of orientating the plates was partially overcome by using the grid overlaps on the electronographs in a manner analogous to the way the grids were aligned North to South (Chapter 3.3). By traversing the plate in the X-direction, and using the image magnification and viewing system of the microdensitometer, it was possible to ensure that the beam scanned down a grid overlap along the whole length of the plate. This ensured that successive plates were oriented to within 3° of each other.

The 192-point analysis was accomplished by making traces in 20 X locations separated by 500μ and measuring three points, separated by $300\,\mu$, on each strip. This is in fact a rather coarse sampling of the data on the plate. Assuming an information scale of $125\,\mu$ it represents only 1/15 of the information present. Clearly the full potential of the Nebula polarimeter is not being realized with this method. However, even though we regard this number of points as insufficient, the time required to conduct the analysis, over 350 hours, prohibits a more extensive mapping using this method. Furthermore, even though great care was taken throughout the analysis, gross errors of frightening proportions were present in the results. As an illustration of the seriousness of these discrepancies we have presented a typical sample of 24 points taken from one strip on plates 13, 14, 15, 16 in table 4.1. After the Stoke's parameters from each pair of plates have been corrected for the variations of the photocathode sensitivity, and the differing exposure times, they should be identical. Clearly this is not the case. The polarization on the two sets of plates can differ by as much as a factor of 3 and the angles by more than 90°. We estimate the mean errors to be ± 10% for the polarization and ± 20° in the position angles. These errors are so large that the results are virtually meaningless. Some insight into the cause of these large discrepancies is reached by examining the f-factors. Figure 4.3 shows the f1-factor (see chapter 3.3) for the plates 13, 14, 15, 16. Theoretically this quantity should be unity, but we have already pointed out that in practice the cathode sensitivity varies by ± 10%. The f-factors might therefore be expected to have a distribution with mean 1.0, and a range from 0.90 to 1.10. If we examine Figure 4.3 we see f-factors uniformly distributed over the range 0.5 to 1.5 implying sensitivity variations of 300%. The f2-factor is very similar, but more alarmingly the difference between these two estimates shows a similar form indicating large disagreements. If the plates have been misregistered then the combination of images from different locations in the galaxy will produce just this effect, and we suggest that this is indeed the situation. This has interesting implications for previous photographic polarization measurements, which as we have already commented are generally

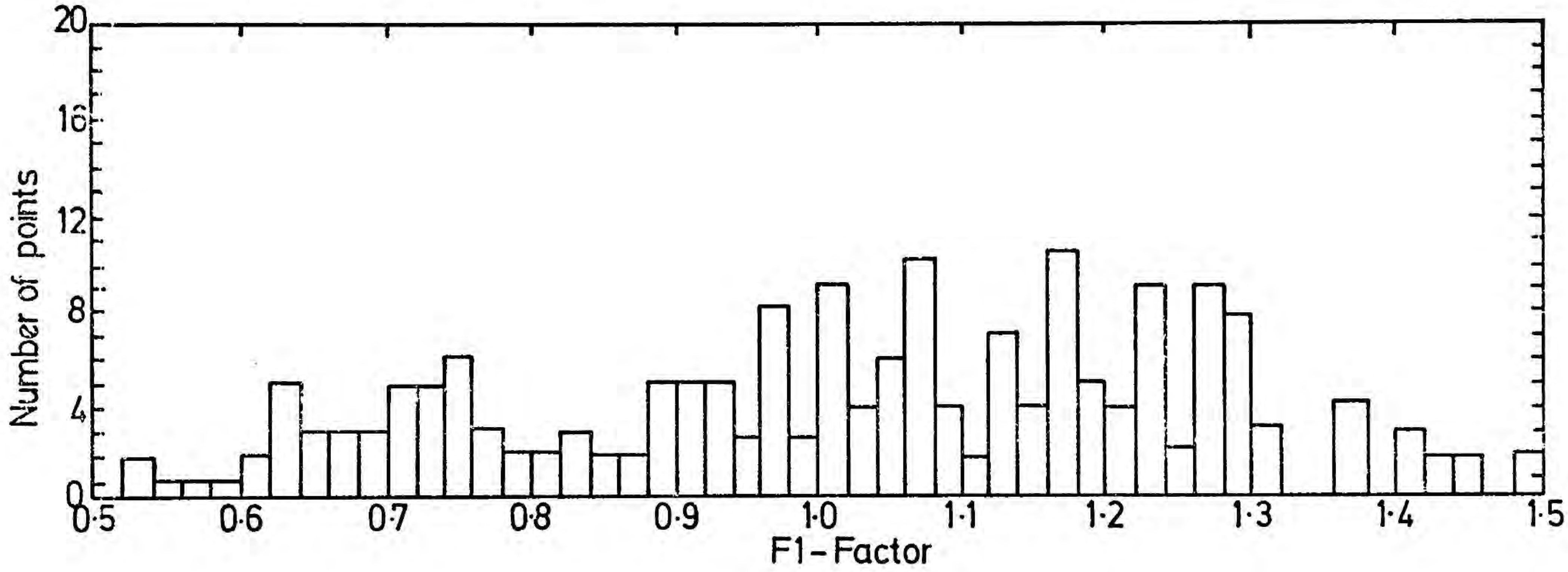

Figure 4.3 *Histogram of F1-factor from 186 point analogue analysis of plates 13, 14, 15, 16.*

Table 4.1

The Discrepancies in the Analogue Results

Location (arbitrary units)		Plates 13/14		Plates 15/16	
x	y	p%	θ°	p%	θ°
234	79.3	4.3	161	7.7	162
234	86.5	44.2	142	98.1	5
234	93.7	3.4	162	17.2	137
234	100.9	2.3	160	13.4	139
234	108.1	2.2	142	3.9	164
234	115.3	8.3	96	9.2	20
234	122.5	22.6	118	16.0	50
234	338.8	12.7	64	14.2	45
234	346.0	15.6	166	12.1	159
234	253.3	7.7	90	15.1	7
234	360.4	6.7	77	14.8	158
234	367.0	4.3	116	3.7	38
234	374.9	2.3	146	2.2	98
234	382.1	2.9	109	3.8	57

regarded as inaccurate. On the basis of the above results we suggest that these inaccuracies are a consequence of analogue reduction procedures and are not intrinsic to the measurement.

Fortunately recent developments in microdensitometer and computer technology have now made the digital processing of photographic images a viable proposition. The new generation of fast microdensitometers, such as the PDS machine, can scan automatically in a two-dimensional mode. Small measuring apertures and position increments can be used, and each scan has a positional accuracy $\sim \pm\ 0.2\,\mu$ (Van Alter and Auer 1975). The vast amount of data produced in a digital analysis has deterred most astronomers from applying the technique. However, with the advent of large computers the data processing is now possible. We shall show that with the application of digital reduction methods electronographic polarization measurements become a powerful rival of photoelectric measurements, and we shall illustrate our discussion with examples taken from our analysis of the M82 polarization data. Since plates 30 to 33 were covered with dirt blobs and scratches, and plate 32 had also been misguided, they were not used in the digital polarization analysis. The plates 9, 10, 11, 12 were analysed and combined with plates 13, 14, 15, 16 to provide a complete polarization map of the galaxy.

4.2 The Production of a Digital Picture

A region 1.03 cm x 1.03 cm containing the image on each electronograph was scanned with the Royal Greenwich Observatory PDS microdensitometer using a $25\,\mu$ square aperture and a step spacing of $25\ \mu$. The plates were aligned on the plate carriage in the manner outlined previously.

A raster scan pattern in which successive scans were in opposite directions was used, even though this meant alternate scans had to be inverted before the analysis, as this scanning mode was the most efficient timewise.

We shall describe the end product of the digitization process as a "Digital Picture". This is an array of real numbers $A(i, j)$ where each A_{ij} is called a digital picture element of "pixel" and measures the density at the location (i, j) in the array (Figure 4.4). The i index is for the rows, and the j index for the columns, and they are an ordered set of integers which correspond to successive 25μ microdensitometer steps Δx , Δy, where the X direction is parallel to the strips (Declination) and the Y direction is orthogonal to the strips (R.A. Direction). The digital picture produced from our electronographs has dimensions 512 x 512 and therefore contains 262, 144 pixels. The values of A_{ij} are the densities in each of the corresponding 25μ x 25μ areas on the electronograph (Figure 4.4) and are measured on a density scale running from 0 to 1024, in integer increments, which we shall refer to as the "grey-scale". Since the electronograph density is linearly related to the intensity the grey-scale is in fact a direct measure of the incident intensity.

There are two things which are immediately apparent about our digital picture. The most obvious of which is that whereas the density on the electronograph was a continuous function, the density in the digital picture is a discrete function which is only defined at grid points. The first reason for digitizing the electronographs on a scale considerably smaller than that of the seeing disc arises as a direct consequence of this. We will see shortly that several of the operations involved in analysing the pictures require an estimation of the grey-value at non-grid points, and by adopting as fine a grid as possible we can obtain more reliable estimates of these values (this will be of particular importance in the registration of the images). The second reason is that by adopting a small pixel size we are able to isolate small fluctuations in the emulsion and photocathode and then ignore these "bad-points" when summing the pixels to form a "cell" or area which corresponds to the size of the "seeing-disc". The use of a larger pixel would result in the measured density being contaminated by these bad points. A related point is that the density gradients on the electronographs could be so steep that with a large pixel size the measured density would not reflect the true average density in the pixel, because of lag in the microdensitometer response. Here we should point out that the digitization scheme adopted in this analysis is not the best from this point of view. A better approach would be to use a "jigsaw" scheme in which the step size was half the aperture size. However, a complex "unscrambling" process is then required to reconstruct the individual pixels, and the amount of computer time this requires effectively prohibits the use of the scheme.

The second point concerning our digital picture is that because the PDS grey-scale only has a limited range, i.e. 0 to 1024, this sets an ultimate limit on the accuracy to which we can determine the polarization of 0.1%. In practice the grey-value at a given point is subject to an uncertainty of greater than one grey-scale increment, and repeated scans of the same region would seem to indicate an uncertainty of ± 5 increments (Pilkington 1975), implying an accuracy limit of 0.5%. Each of our digital pictures was subsequently stored on a random access magnetic disc, and analysed using an IBM 370 computer, at the University of Durham, which uses an interactive operating system. The suite of programmes that were written to perform the analysis described below made extensive use of this particular aspect of the computers operating system. From the programmers point of view the analysis has now become a problem in handling several two subscript array. The limited range of the grey-scale values enabled us to store each pixel as half a computer word (Integer *2), thus halving the storage and core requirements of each array. Even with a machine as large as the IBM 370 we would not have been able to read a complete matrix into core without doing this. For most of the analysis the data remained in Integer *2 format, but where floating point format was required, to avoid rounding errors in numerical operations, each array was read into core in small sections and converted as required. Needless to say, this sort of involved input/output manipulation considerably increases the complexity of the programmes, and the amount of computer time required for the analysis. Mindful of these "housekeeping" problems we will not dwell on them further.

The analysis of the polarization data involves the following steps:

1. Feature extraction: the measurement of the positions in the matrix of stars, grid overlaps and gaps, scratches and dirt blobs, etc.

2. Image Registration: the matching of a set of four pictures, and the matching of the O and E strips.

3. The Summation of the individual pixels into seeing disc cells of dimensions 5 x 5, the subtraction of the clear plate background and calculation of the e- and f-factors for each cell.

4. The rejection of bad points and the calculation of the Stoke's parameters corrected for the variations of exposure and cathode sensitivity.

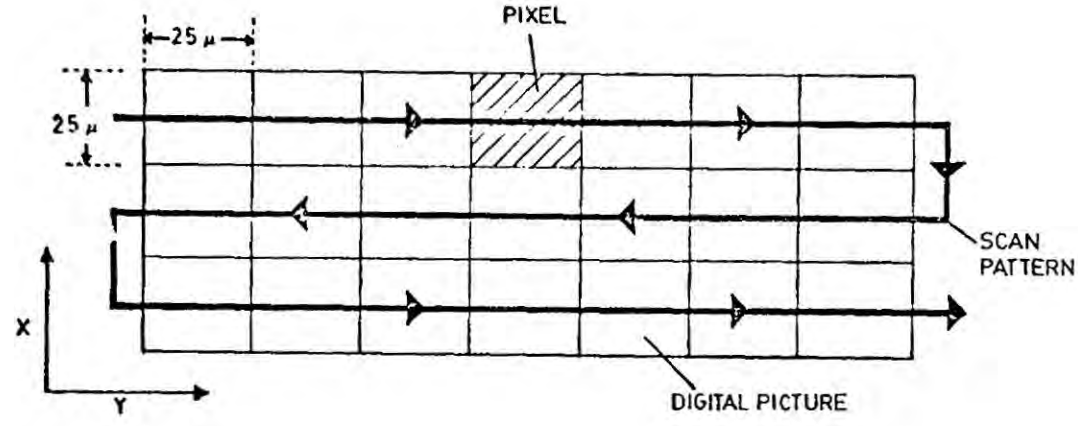

Figure 4.4 *The production of a Digital Picture*

(a)

(b)

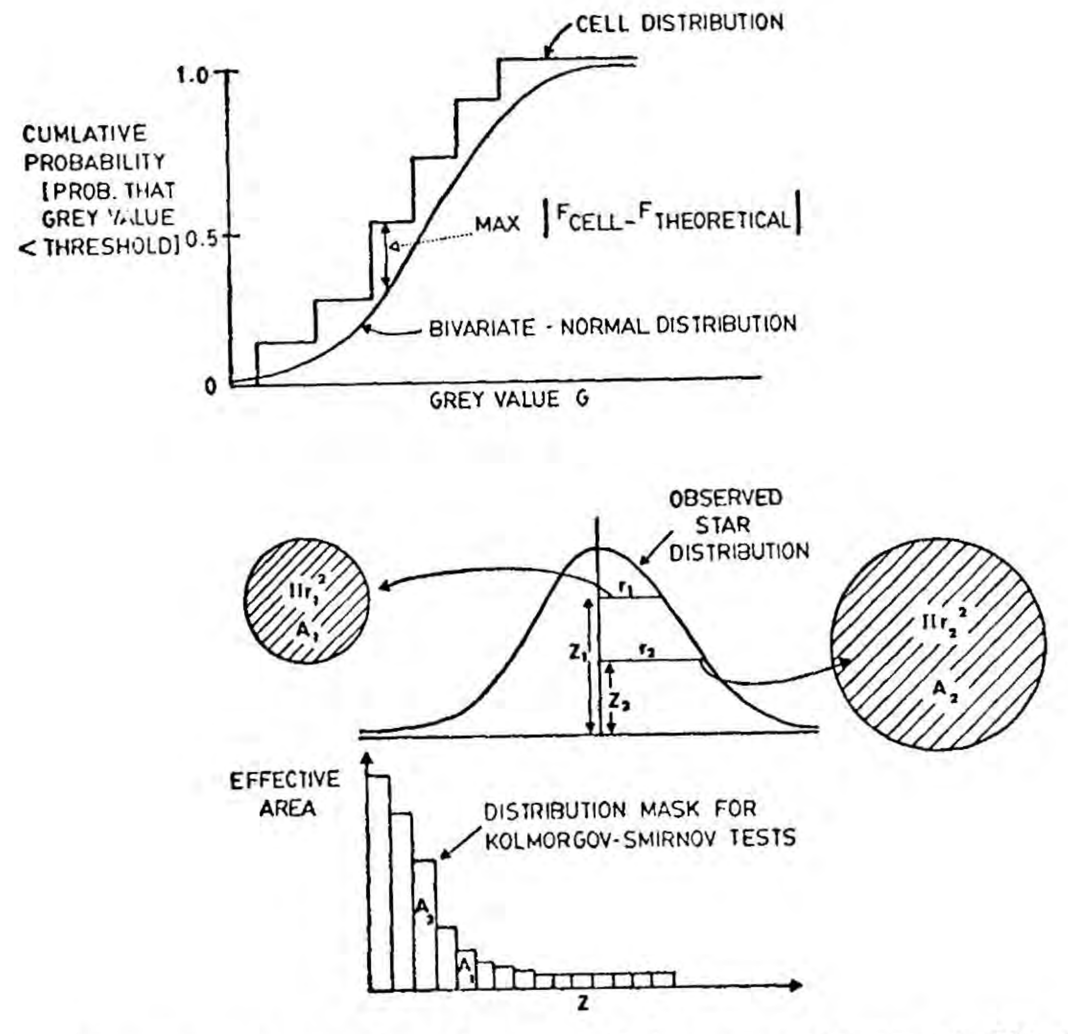

Figure 4.5 (a) *The Kolmorgov-Smirnov goodness of fit test*

(b) *Proposed method for producing a more realistic star density function.*

5. The Subtraction of the sky background and the transformation of the polarization map into the equitorial coordinate system.

We will deal with each of these steps in turn.

4.3 Feature Extraction

Before we can analyse the polarization data we need to determine the positions of various features in our digital pictures. Firstly, we must know the location and the width of each O and E strip in pixel units as ultimately the Stoke's parameters will be calculated for 5 x 5 pixel cells, which correspond to the size of the seeing disc. It is particularly important that the dimensions of the grid gaps and overlap are measured, because pixels from these regions do not contain polarization information and must not be included in any of the cells. (As we shall see the overlaps and gaps are easily distinguishable, and thus provide a convenient means of determining the dimensions and locations of each O and E strip.) Secondly, the positions of the stars in the picture have to be located as we shall be using these not only for astronometric purposes but also in the image registration.

Thirdly, scratches and glue or dirt blobs have to be located. All real features will be "paired" in the picture, so the location of flaws basically involves searching for unpaired objects in the matrix.

In the early stage of the project attempts were made to carry out these identifications and locations automatically. Stars were assumed to have bivariate-Gaussian density distributions

$$\rho(x,y) = \frac{1}{2\pi\sigma_x\sigma_y} \exp\left(-\left[(x-\bar{x})^2/\sigma_x^{\,2} + (y-\bar{y})^2/\sigma_y^{\,2}\right]\right) \quad (4.4)$$

where $\bar{x}$, $\bar{y}$, σ_x, σ_y are the means and standard deviations respectively in the X and Y directions. For an object to be recognized as a star we required that its size was greater than 4 x 4 pixels and that it had an average density greater than a preset threshold level. The method of detection was to sweep through the picture, incrementing by two units the i and j locations of a search cell at each sweep, until the whole picture had been covered. Initially a cell size of 20 x 20 pixels was adopted and the process repeated with the cell size diminishing by two units until the minimum size of 4 x 4 pixels had been reached. The threshold level was then reduced and the process continued until a threshold level of three times the clear plate background had been reached. Because of the vast amounts of computer time this required, our experiments were carried out on a small portion of a picture known to contain a star image. The size of the current search cell determined $\bar{x}$, $\bar{y}$ and σ_x, σ_y as the centre of the cell and 1/3 the cell width respectively. Using these parameters the culmative bivariate normal distribution, F_{theory}, was calculated using equation 4.4, and compared with the observed the culmative frequency distribution, F_{obs}, in the cell using the Kolmogorov-Smirnov two sample test (Kraft and Van Eaden 1968). This test yields a measure of the goodness-of-fit (illustrated in Figure 4.5(a)) from the quantity α, which is the maximum difference between the two distributions

$$\alpha = \text{Max} \left| F_{obs} - F_{theory} \right| \tag{4.5}$$

A confidence coefficient was obtained from $n\alpha$, where n is the total cell density, and if this was less than 80% the cell was not accepted as a star. The results obtained using this search mode were very disappointing for several reasons. Firstly, actual star distributions are not two dimensional Gaussian distributions. Bright stars have pronounced Platykurtic distributions because their central regions are "burnt out", and faint stars have Leptokurtic profiles as only the central regions of the seeing disc have been recorded. Secondly, no account of plate noise or varying background was made and this will certainly have to be introduced if a meaningful fit is to be reached. Probably the best method of overcoming these two problems would be the use of empirical star profiles. The simplest technique would be to trace the area enclosed by successive density contours in the star and use these to form a masking function as illustrated in Figure 4.5(b). A third complaint against the procedure is that vast amounts of computer time are required to completely analyse a plate (somewhere in excess of thirty minutes).

We also experimented with the automatic straight edge detector suggested by Rosenfield and Lillas (1970) as a means of locating the grid overlaps and gaps. This was slightly more successful than the star finding algorithm, but both algorithms obviously required considerable refinement before they could be relied on. Since a very simple and fast alternative was available we regretfully abandoned them. Hopefully they will be resurrected and refined in later work.

Now let us turn to the method of feature detection we actually adopted. Basically we found a method of reconstructing a real picture from our digital picture and then carefully examined it by eye. We achieved this by using a contouring programme which produced a series of isophote maps of each picture with differing contour intervals. The interactive operating system of the computer was ideal for this sort of approach, particularly as cathode-ray graphic units (V.D.U's) were available on which the isophote maps could be plotted at high speed. The first stage in the

ISOPHOTE MAP OF PLATE APR74F10

CONTOUR INTERVAL IS 30., NUMBERS SCALED BY 1.

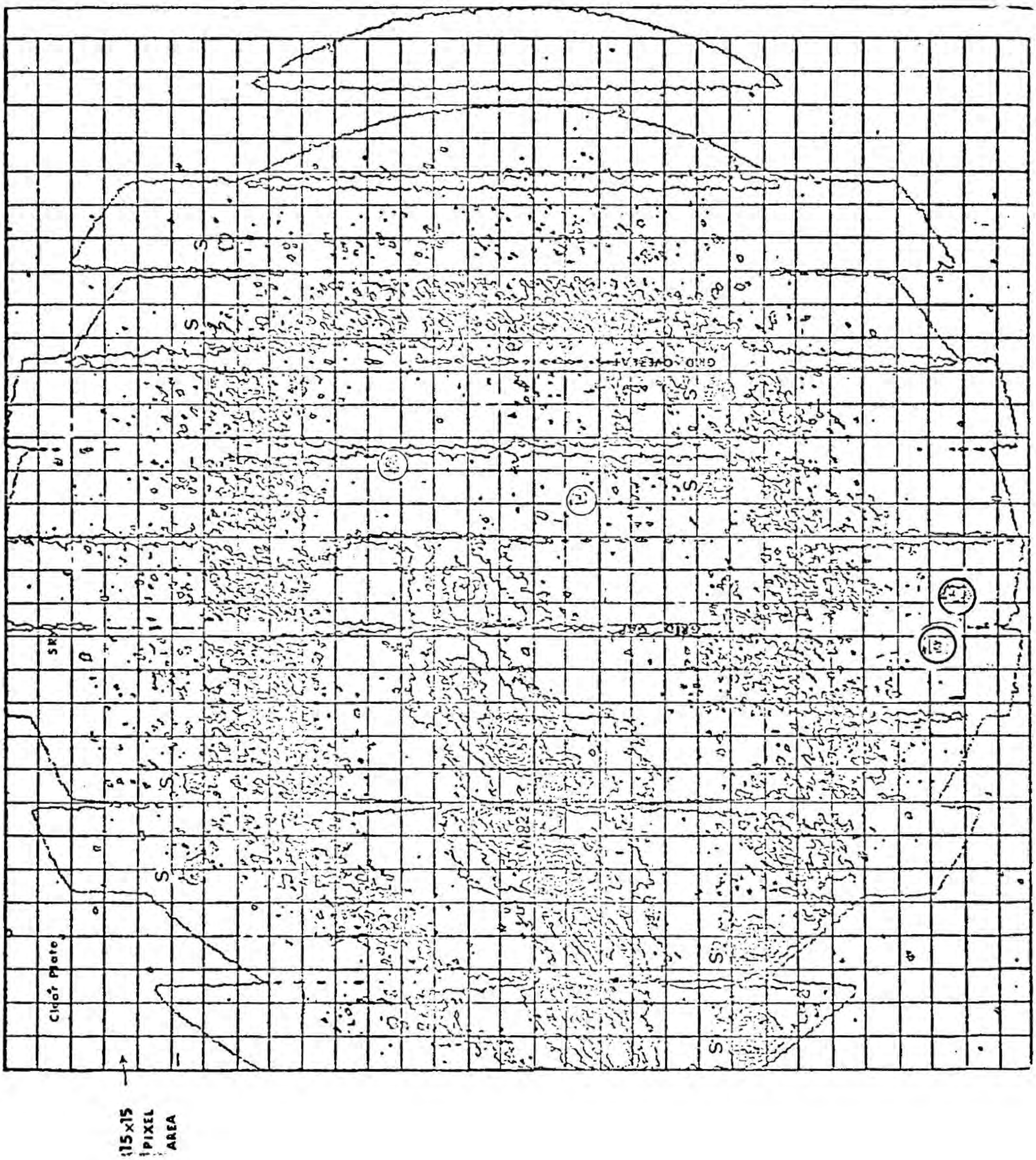

Figure 4.6 Isophote map of an M82 electronograph.

processes was to make an isophote map of the whole plate using a course contour interval. A trial contour interval was specified to the programme and plotting commenced. If this interval was not satisfactory the plot could be interrupted and restarted with a different interval, and so on until a convenient interval had been found. Generally a contour interval between 30 and 80 grey-scale divisions was found to be satisfactory for this initial mapping. Figure 4.6 shows such an isophote map for one of the M 82 digital pictures, and was made using a contour interval of 30 grey-scale divisions. The isophote map uses data from alternate rows and columns in the matrix and is superimposed on a grid, each of whose divisions represents 15 pixel units, which is used for measuring the positions of features. The outline of the grids is clearly visible on the plot and so are the grid overlaps and gaps. Star images are also very prominent. There are four stars altogether and there are therefore eight star images visible in the picture, and these are marked with the letter S. The bright central regions of M82 are well defined on the left-hand side of the plot. Numerous "un-paired" features are apparent and some of these are caused by polarization effects and others are image flaws. Those that have been positively identified as flaws are marked with a ring. From this preliminary mapping the positions of all the visible features were recorded. The contouring was then repeated using various density thresholds and a much finer contour interval so that less prominent features could be located. Generally the digital pictures were examined using threshold levels differing by 100 grey-scale divisions and a contour interval of five grey-values. Once a feature, such as a star, had been located recourse was made to the raw digital picture. The contour feature was located in the numerical display and its position and dimensions determined to within a few pixels.

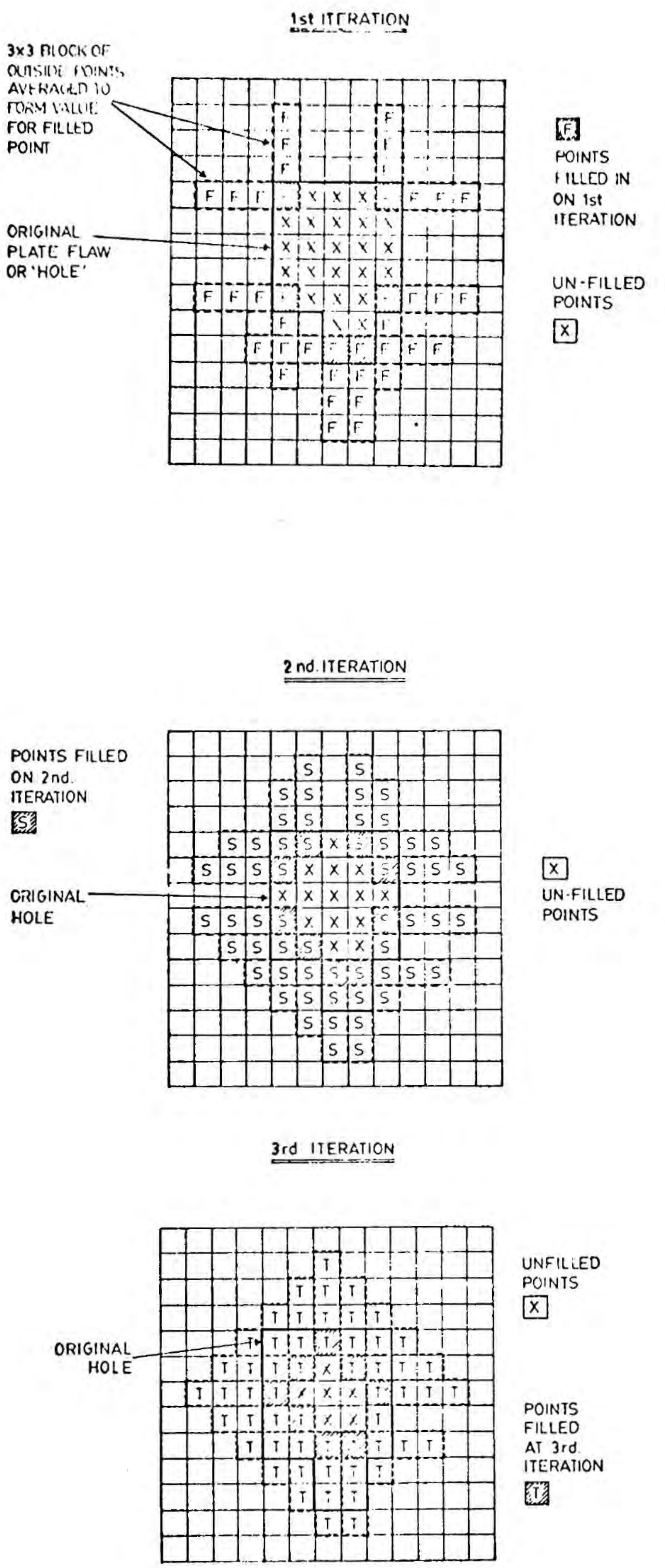

(a)

(b)

(c)

Figure 4.7 *The moving averages interpolation scheme*

Grid overlaps and gaps have a typical size of 8 to 10 pixels, and their locations were determined to within 1 or 2 pixels. The typical width of a grid is 45 pixel units. An area 30 x 30 pixels surrounding each star image was identified and its coordinates recorded. In order to decide whether a feature was a flaw or not we cross-correlated the contour maps, the digital listings and prints taken from the original electronographic plates. Only features which could be identified on the original electronographs were accepted as flaws. After identification of the flaws the digital pictures had to be "cleaned" so that the flaws did not produce spurious polarization changes. The values of pixels in flaw areas were replaced by values interpolated from the surrounding "good" region using a moving - averages interpolation scheme (Figure 4.7). Starting at the periphery of a flaw the value of any pixel having two or more "good" neighbours was replaced by an average value of its three adjacent good enighbours on each side. At the end of the first iteration (Figure 4.7a) only the corners of the flaw had therefore been replaced by interpolated valued. Before the start of the second iteration the position of the flaw was updated so that these points now became "good" points. The procedure therefore propagates inwards at each iteration until the whole flaw has been replaced by interpolated values.

Having removed the large flaws the next step was to register the pictures.

4.4 The Method of Image Registration

If we could find a system of reference points, or Fiducial marks, with known locations and separations on each electronographic plate, we could use these to register the images. A system of Fiducial crosses, fixed in the

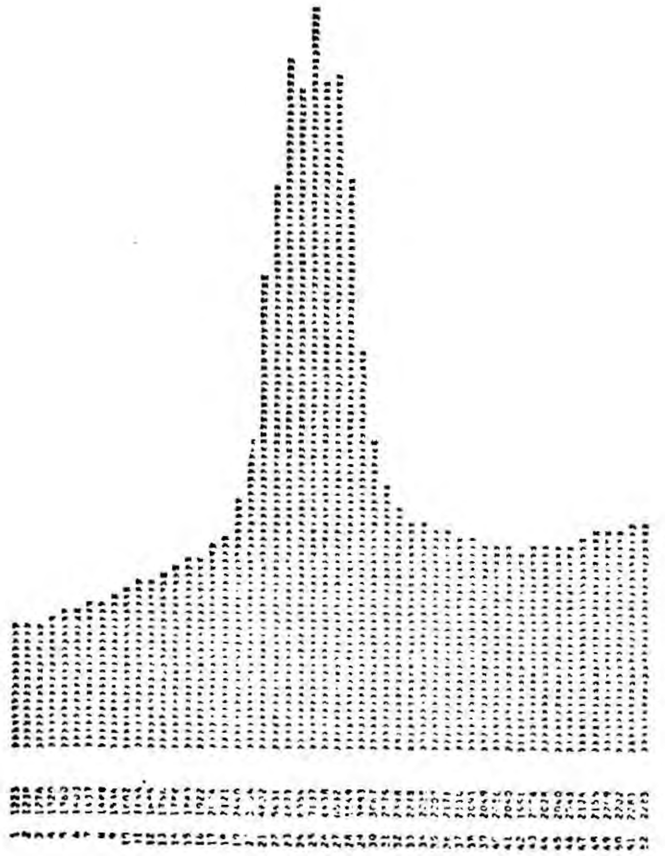

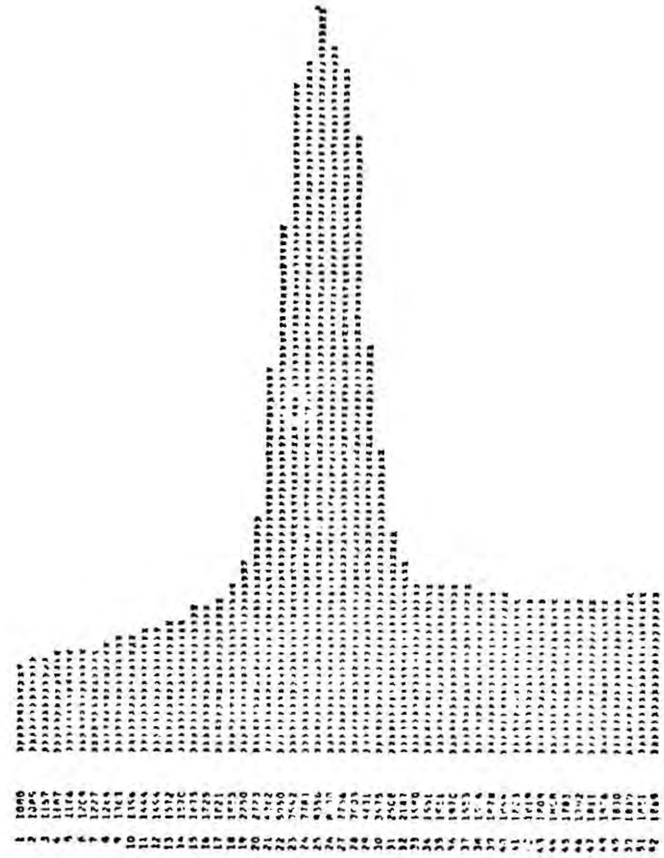

es 4.9 (a) *X-profile of star showing variable background* (b) *Y-profile of star showing variable background*

(a)

INITIAL GEUSSES FOR STAR POSITIONS
91 106 87 104 1
SUBSET CHOSEN FOR STAR

1	59	63	68	69	68	71	72	75	68	74	75	75	75	70	68	72	66	70
2	60	65	69	70	73	74	72	75	72	75	76	75	79	75	70	73	65	72
3	67	69	73	73	75	76	74	78	81	80	80	80	76	74	74	71	69	75
4	66	74	72	71	73	80	77	81	92	89	88	90	80	76	74	72	69	73
5	57	67	70	70	72	87	95	103	113	109	106	104	91	79	72	70	71	71
6	59	65	73	73	73	94	114	137	139	137	131	115	96	84	76	68	65	72
7	65	67	72	77	83	106	129	141	165	146	150	132	105	92	85	74	68	74
8	64	69	69	75	94	105	142	172	193	163	164	156	119	104	94	81	72	75
9	64	68	73	78	93	104	127	156	177	177	165	149	133	150	102	86	76	75
10	64	64	75	76	89	98	110	124	145	151	149	131	124	145	102	85	79	74
11	63	63	72	72	79	88	97	103	112	115	116	112	104	101	92	81	76	73
12	62	65	68	69	74	74	88	94	85	56	93	95	92	85	83	80	77	73
13	64	63	68	72	73	77	79	83	83	87	81	79	79	80	77	80	76	75
14	68	65	73	72	72	76	75	75	77	77	74	73	71	74	72	76	74	77
15	66	67	68	73	69	72	73	75	75	73	61	54	69	69	70	71	75	78
16	62	69	66	69	88	71	74	75	74	66	42	43	70	69	71	72	73	75

BACKGROUND SUBRACTION USING SIMPLE AVERAGE
BACKGROUND= 69NUMBER OF POINTS USED IN ESTIMATE 64

(b)

1	0	0	0	0	0	2	3	6	0	5	6	6	6	1	0	1	3	1
2	0	0	0	1	4	5	3	6	3	6	7	6	10	6	1	4	0	3
3	0	0	4	4	8	7	5	9	12	11	11	11	7	5	5	2	0	6
4	0	5	3	2	4	11	8	12	23	20	19	21	11	7	5	3	0	4
5	0	0	1	1	3	16	26	34	44	40	37	35	22	10	3	1	2	2
6	0	0	4	4	4	25	45	68	70	68	62	46	27	15	7	0	0	3
7	0	0	3	8	14	37	60	92	54	57	81	63	36	23	16	5	0	5
8	0	0	0	10	25	40	73	103	124	114	95	87	50	35	25	12	3	6
9	0	0	4	9	24	35	50	87	108	108	96	80	64	81	33	17	7	6
10	0	0	6	7	20	29	41	57	76	82	50	62	95	76	33	16	10	5
11	0	0	3	3	10	17	28	34	43	46	47	43	35	32	23	12	7	4
12	0	0	0	0	5	5	17	25	20	27	24	26	23	16	14	11	8	4
13	0	0	0	1	4	8	10	14	14	16	17	10	10	11	8	11	7	6
14	0	0	4	3	3	3	6	6	8	8	5	4	2	5	3	7	5	8
15	0	0	0	4	0	3	4	6	4	4	0	0	0	0	1	2	6	9
16	0	0	0	0	0	2	5	6	5	0	0	0	1	0	2	3	4	6

Figures 4.8 (a) *Star subset with underlying background*

(b) *Subtraction of constant background from the subset.*

polarimeter field of view and associated with each grid space, would enable the O and E images of each space to be registered. However, such a system would not be a satisfactory means of registering successive plates, as even using the same guide star the galaxy cannot be reproducibly positioned in the field of view of the polarimeter from night to night. We catually require a Fiducial system which is fixed on the sky and is relatively polarization independent. The field stars provide just such a reference system. However, their radii are $\sim 125\mu$, and before we can use them as a reference system we must be able to find a more accurate defintiion of their positions. This we did by computing the centroid of each star image, there being at least eight star images per picture. Using the measurements made from the isophote maps, initial guesses for the locations of each star isolated a subset, B(i, j) of the digital picture A(i, j), containing the star and points in the surrounding background area. The density at each point in the star also contains a contribution from the underlying background (Figure 4.8a). If the background is uniform then the centroid of the subset B(i, j), $(\bar{x}, \bar{y})$ will be the centroid of the star $(\bar{x}_s, \bar{y}_s)$, but if it varies the subset centroid will not be the stars. Before calculating the centroid of the subset B(i, j) we therefore subtracted the background density. We determined the shape of the background from cross-sections in the X and Y directions. For each row we calculated a sum density $D_i = \Sigma_j B(i, j)$, which we plotted to give an effective X profile (Figure 4.9a), and similarly we calculated and plotted the quantity $D_j = \Sigma_i B(i, j)$ for the columns to give a Y profile (Figure 4.9b). In most cases the background was flat but, as a precautionary measure we then subtracted a constant background density determined from the average of the peripheral points of the subset (Figure 4.8b). In the

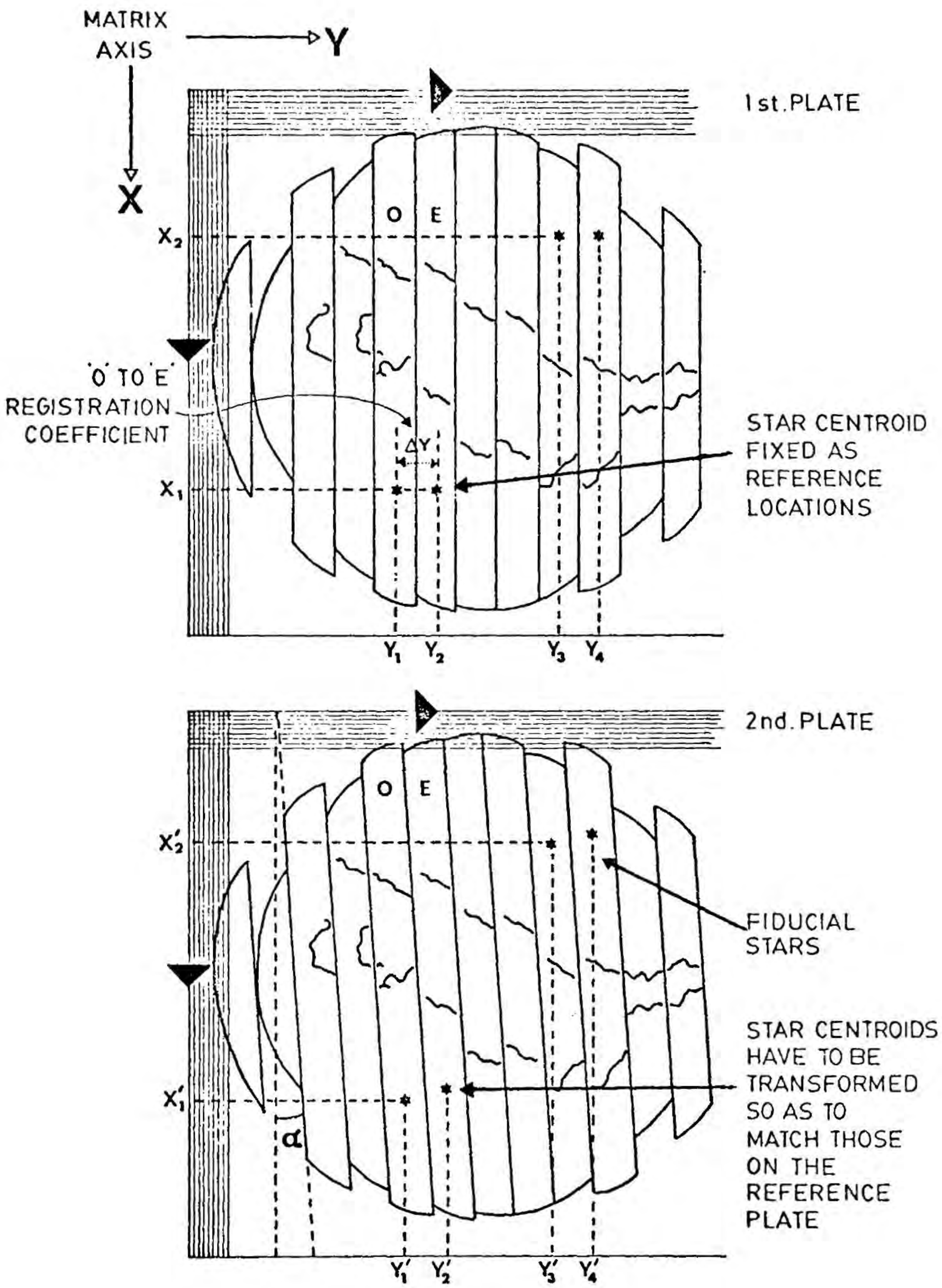

Figure 4.10 *The registration of the electronographs*

cases when the background varied with position (Figures 4.9) we employed the moving averages interpolation scheme described previously to estimate the background at points inside the star, and then did a point-by-point subtraction. The centroid of the subset $(\bar{x}, \bar{y})$ was then found by forming means of the x_i and y_i coordinates weighted by their mean density. So the X coordinates $\bar{x}$ was computed by forming a weighted mean for each column $\bar{x}_j$

$$\bar{x}_j = \Sigma_i \; B(i, j) \cdot x_i / D_i \tag{4.6}$$

and $\bar{x}$ was then found from

$$\bar{x} = \Sigma_j \; \bar{x}_j \cdot D_j / \Sigma_j D_j \tag{4.7}$$

and $\bar{y}$ was calculated in a similar manner. Each centroid coordinate was determined to better than 0.2 of an increment (4μ). The centroids of the first digital picture of a set of four provided a set of reference points, to which the corresponding centroid on the second, third and fourth pictures had to be mapped by the transformation. In general these transformations involved translations and rotations for the x and y coordinates (Figure 4.10) and were different for each picture. For an individual centroid with coordinates (x_i, y_i) in the reference picture, and coordinates (x_i', y_i') in a second picture the transformation will be

$$x_i' = y_i \sin \alpha + x_i \cos \alpha + x_o \tag{4.8}$$

$$x_i' = y_i \cos \alpha' - x_i \sin \alpha' + y_o$$

where α, α', x_o, y_o are the rotation and translation coefficients for the X and Y directions respectively. For computational reasons we have written equation 4.8 as the transformation which maps the reference picture XY to the second picture X'Y'.

If we apply equation 4.8 to each star centroid in a pair of pictures, we find that we are unable to determine unique values for the parameters α, α', x_o, y_o such that all the centroids are transformed to exactly the desired positions. This may be due to a variety of reasons, e.g. plate noise or image distortion. In order to find a transformation applicable to the whole picture we therefore adopted an optimization procedure to determine the values of α, α', x_o, y_o which give the best fit for all the centroids in the picture pair. To do this we rewrote equation 4.8 to give the difference between the reference position and the corresponding transformed position for each centroid ΔF_i and ΔG_i in the X and Y directions respectively

$$\begin{aligned} \Delta F_i &= y_i \sin \alpha + x_i \cos \alpha + x_o - x_i' \\ \Delta G_i &= y_i \cos \alpha' - x_i \sin \alpha' + y_o - y_i' \end{aligned} \tag{4.9}$$

The best values for α, α', x_o, y_o were then found by minimizing the total - sum - of squares over the whole picture ΔG_y, ΔF_x given by

$$\begin{aligned} \Delta F_x &= \min \left| \sum_i \Delta F_i^2 (\alpha, x_o) \right| \\ \Delta G_y &= \min \left| \sum_i \Delta G_i^2 (\alpha', y_o) \right| \end{aligned} \tag{4.10}$$

An iterative algorithm due to Powell (1964) was used to perform the optimization. The trial values for the transformation parameters were refined until a convergence criterion, that the total sum of squares had changed by less than 1/10,000 between iterations, had been reached. After convergence the differences for individual stars ΔF_i, ΔG_i were always less the 0.1

increments and in most cases better than 0.01 increments, implying a picture to picture registration of 2μ.

Our aim was then to transform the picture X' Y' so that each of the lattice points in the transformed picture X Y corresponded to the lattice point at that same location in the reference picture. The transformation equation 4.8 gives the location (x_i', y_j') of each of these lattice points (i, j) in the original X' Y' picture. To transform X' Y' we therefore had to determine the grey-value at the point (x_i', y_j') for every lattice point (i, j) in the new picture. However, if we implement equation 4.8 we find that the points (x_i', y_i') are not necessarily lattice point in the X' Y' picture. If we try and overcome this problem by moving to the nearest X' Y' lattice point (i', j') some of the (i', j') points will contribute several times to the transformed picture, and others will not contribute at all. To make the transformation work we therefore need to interpolate the grey-values at the locations (x_i', y_j') from the (i', j') lattice points in the X' Y' picture.

The simplest, and computationally cheapest, interpolation rule is to use a weighted distance estimate of the grey-value at (x_i', y_j') from the four nearest (i', j') neighbours. If we rewrite (x_i', y_j') as $(i'_1 + \alpha_1\ j_1' + \beta)$ where i_1' and j_1' are integers, and α and β are non-negative fractions, then the grey-values $B(i, j)$ to be ascribed to the point (i, j) in the transformed picture is allocated from those of the nearest neighbours in the original picture $A(i', j')$ as follows

$$B(i, j) = (1-\alpha)(1-\beta)\,A(i_1'\ j_1') + \alpha(1-\beta)\,A(i_2', j_2') + (1-\alpha)\beta\,A(i_1'\ j_2') + \alpha\beta A(i_2', j_2') \tag{4.11}$$

This sort of linear interpolation scheme is unfortunately rather poor in regions of steep density gradients and is adversely affected by local noise, and "bad-points" in the nearest neighbour. Since the determination of the densities at the new lattice points is the most crucial part of the registration we adopted a more elaborate interpolation scheme in order to estimate them more accurately. The method we adopted was based on fitting a smooth piecewise bivariate spline function in X and Y to the density $A(x'_i, y'_j)$ at the X' Y' lattice points (Hayes 1972, Akima 1974a, b). Each interpolation polynomial was applicable to a X' Y' rectangle bounded by four grid points $x' = x'_i$, $x' = x'_{i+1}$, $y' = y'_j$, $y' = y'_{j+1}$ and approximates $A(x'_i, y'_j)$ as a bicubic spline

$$B(i, j) = A(x'_i, y'_j) = \sum_{\delta=0}^{3} \sum_{\varepsilon=0}^{3} x'^{\delta} y'^{\varepsilon} \tag{4.12}$$

where the points (i', j'), $(i'_1\ j' + 1)$, $(i' + 1, j')$, $(i' + 1, j' + 1)$ are the four nearest lattice points to the desired point. The calculation of the interpolation polynomial involves the evaluation of the partial derivatives $\partial A/\partial X'$, $\partial A/\partial Y'$, $\partial^2 A/\partial x' \partial y'$ at each data point, and the scheme not only matches the function $A(x', y')$ but also its first order derivatives. The calculation of the partial derivatives was carried out using 13 data points centered on the nearest data point to the interpolation point, and consisting of two data points on each side of it in the X' and Y' directions, and one data point in each diagonal direction. By using such a large number of "local points" we overcome the problem of adjacent "bad-points". The partial derivatives are calculated as weighted means of the divided differences $\delta y'_{i'j'}$, $\delta x'_{i'j'}$, $\delta xy_{i'j'}$

$$\begin{aligned} \delta y'_{i'j'} &= A(i', j'+1) - A(i', j') \Big/ (y'_{i'+1} - y'_{i'}) \\ \delta x'_{i'j'} &= A(i'+1, j') - A(i', j') \Big/ (x'_{i'+1} - x'_{i}) \\ \delta x'y'_{i'j'} &= (\delta x'_{i', j'+1} - \delta x'_{i', j'}) \Big/ (y'_{j'+1} - y'_{j'}) \end{aligned} \tag{4.13}$$

for the rectangle containing the point to be interpolated. For example the partial derivatives at the point (x'_3, y'_3) are

$$\frac{\delta A}{\delta x'}_{33} = (w'_{x2}\ \delta x'_{23} + w'_{x3}\ \delta x_{33}) / (w'_{x2} + w'_{x3})$$

$$\frac{\delta A}{\delta y'}_{33} = (w'_{y2}\ \delta y'_{22} + w'_{y3}\ \delta y'_{33}) / (w'_{y2} + w'_{y3}) \tag{4.14}$$

$$\frac{\delta^2 A}{\delta x'\delta y'}_{33} = [w_{x2}\ (w_{y2}\delta x'y'_{22} + w_{y3}\delta x'y'_{23}) + w_{x3}\ (w_{y2}\delta x'y'_{32} + w_{y3}\delta x'y'_{33})] / [(w_{x2} + wx_3)\ (w_{y2} + w_{y3})]$$

where the w's are the weight functions

$$w_{x2} = |x_{43} - x_{33}|$$

$$w_{x3} = |x_{23} - x_{13}| \tag{4.15}$$

$$w_{y2} = |y_{34} - y_{33}|$$

$$w_{y3} = |y_{32} - y_{31}|$$

Further details of the calculations are given by Akima (1974a, b). Needless to say the interpolation of ~ 250,000 per transform is a non-trivial operation. As a check on the accuracy of the transformation we redetermined the coordinates of the star centroids on the transformed pictures and compared them with the centroids on the reference picture. The agreement was excellent in all cases the coordinates agreed to better than 0.2 of an increment (4μ), and for the brighter stars was considerably better than this (< 0.09 increments).

Comparing these figures with those achieved with the analogue procedure we see that the digital method has produced a significantly improved registration.

The registration of corresponding O and E strips only involves translations which are determined purely by the polarimeter optics, and will be the same for all pictures. Each pair of strips does however have a different set of translations coefficients, because of the varying widths of the grid gaps and overlaps. Once again the star centroids were used to determine the required translation coefficients, Δx, Δy, which are given by the difference between the X and Y coordinates of the O and E centroids on each pair of strips

$$\begin{aligned} \Delta x &= \bar{x}_O - \bar{x}_E \\ \Delta y &= \bar{y}_O - \bar{y}_E \end{aligned} \tag{4.16}$$

Unfortunately not all of the strip-pairs, in a given picture, contained stars. However, since the position of M82 in the field of view was different in some of the pictures, a complete set of translation coefficients could be obtained. When several pictures included stars in a particular strip-pair this enabled us to check on the accuracy of the transformation. The Δx coefficients showed no correlation from picture to picture, or even in the same picture, for individual strip-pairs. They were always between 0.1 and 0.5 increments, the large values occurring for faint stars. We ascribe these fluctuations to the uncertainties in the x centroid location, and using only the brighter stars we obtain an accuracy for the registration of 0.2 increments. Under the assumption that these variations are noise generated we did not apply a Δx correction but combined the O and E intensities according to their i

Table 4.2

Summary of registration coefficients for each strip pair

Strip No:	ΔY Registration coefficient Plate number													$\bar{y}$
	9	10	11	12	13	14	15	16	18	30	31	32	33	
											42.6	43.0	43.3	
1/2	43.1	43.0	43.0	43.2					43.0					43.0 ± 0.3
											43.1	42.7	43.4	
3/4	43.5	43.4	43.3	43.5					43.4					43.4 ± 0.2
5/6					46.8	47.0	46.8	46.6						46.8 ± 0.2
									44.3	44.8	44.9	44.9		
7/8	45.4	45.0	44.9	45.5	44.8	44.9	45.4	44.8					45.3	45.1 ± 0.4
									45.5	45.5	45.1	45.3		
									45.8	45.2	45.0	45.2		
9/10	45.9	45.5	46.3	46.5									45.5	45.6 ± 0.4
									45.6	45.3	45.5	45.1		

coordinate in the matrix.

The Δy coefficients for each strip-pair are summarized in table 4.2. Though there is some scatter between estimates from individual pictures, and again the faint stars are responsible, the agreement is on the whole good, and they are certainly more consistent than the Δx coefficients. The mean translation coefficient (table 4.2) for each strip-pair was calculated and used to register those O and E images in all of the pictures.

4.4 Seeing-disc cells: The subtraction of the clear plate background

Each O-strip was subdivided into an integral number of seeing-disc cells of dimensions 5 x 5 pixels, and the total cell density found by summation. Since the PDS machine can only record densities up to a maximum grey-value of 1024 all higher densities will not be assigned the correct grey-value. In the brighter regions of M82 this effect will mask any polarization present resulting in artificially low polarizations. In order to allow for this we tested the value of each pixel and rejected all those with a grey-value greater than 1000. If the number of rejected pixels in the cell exceeded five the whole cell was discarded, if less than five pixels had been rejected the true 5 x 5 cell density was calculated as a weighted average of the recorded density. This procedure also allowed for the possibility that high-density pixels could occur in an otherwise low-density cell because of emulsion or cathode defects.

The E-strip location corresponding to each O-cell pixel was calculated from equation 4.16 using the translation coefficients of table 4.2. The density at each of these locations was determined using the bivariate interpolation scheme described previously, and the total density in the 5 x 5 E-cell corresponding to each O-cell was calculated using the procedure

Figures 4.11 *Composite scatter plots of the clear plate density with position.*

The plotting symbols used correspond to the number of points at each location according to the following scale:

Symbol	*No. of points*
1 to 9	*1 to 9*
A to Z	*10 to 35*
+	*greater than 35*

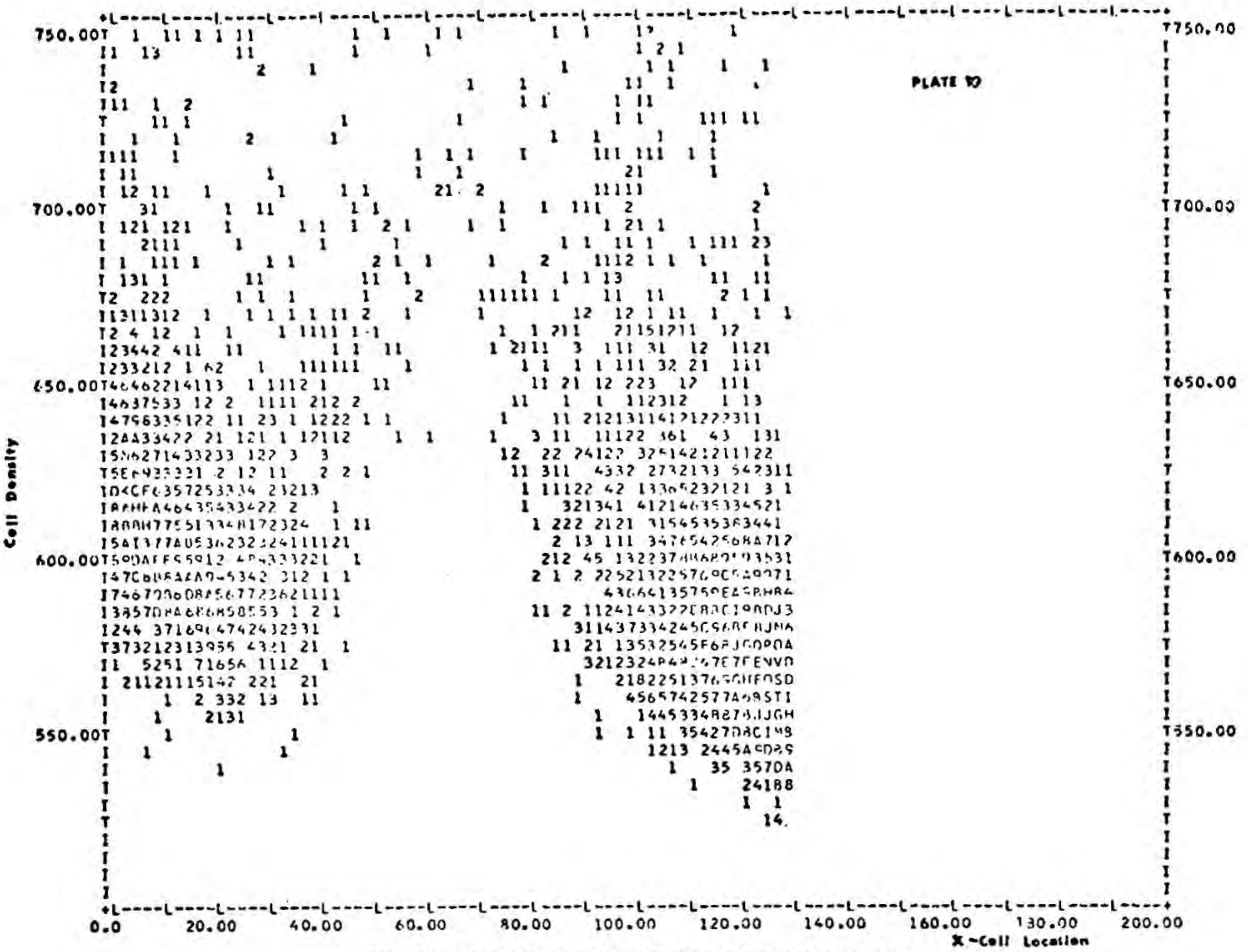

THE VARIATION OF THE CLEAR PLATE DENSITY WITH X

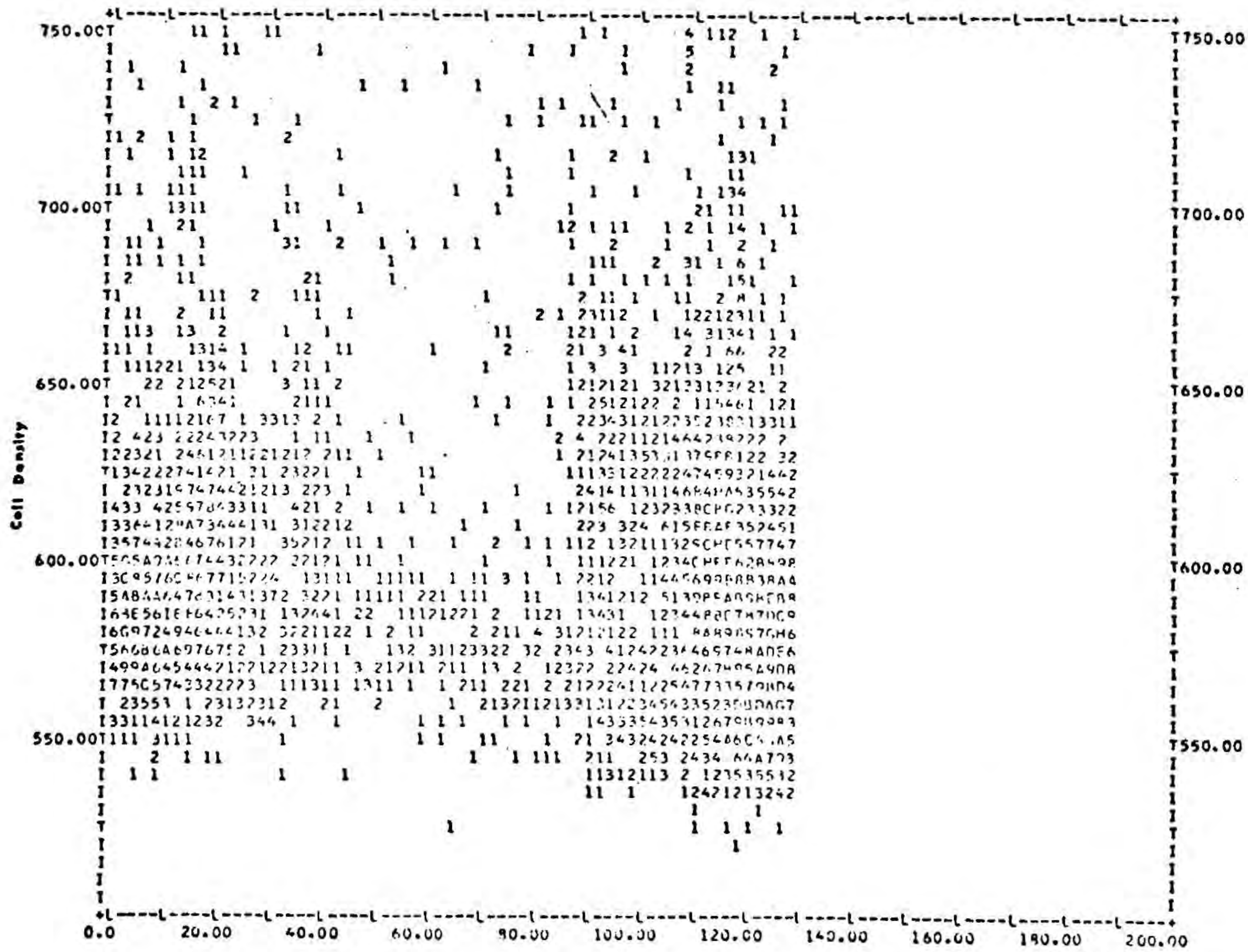

THE VARIATION OF THE CLEAR PLATE DENSITY WITH Y described above. Each O and E cell pair was assigned an X and a Y coordinate given by the centre of the O-cell. In each clear plate region we summed the pixels into cells of dimensions 4 x 4 and calculated the mean pixel value for each of these curves. The possibility of a positional dependence in the clear plate background was investigated by examining the variations in the cell density along rows in X and Y at different plate locations, and by calculating and plotting the density centroid of each row and column. Though considerable variations in the plate background were observed, no systematic XY dependence (e.g. due to drift in the microdensitometer zero-point) was detectable above the one sigma level (± 5 grey-values). Composite scatter plots in the X and Y directions for plate 14 are shown in Figure 4.11. Though the individual plots are far easier to interpret, these plots nevertheless show the random variations in clear plate density that we have been describing. These are probably due to a combination of factors such as emulsion noise, cathode defects and non-uniform development.

The mean clear plate density, D_{clear}, was calculated from the average 4 x 4 cell density by scaling. Figure 4.12 shows plots of the distributions of the 4 x 4 cell densities for plates 13, 14, 15, 16 (the plots for plates 9 to 12 are very similar. See Figures 4.17). Taking the full-width half-max (FWHM) of these distributions as an estimate of the variability of the cell density we obtain values of between 5 and 10%, which can be accounted for by the probable measuring error of the PDS machine (Chapter 4.2) at these densities. The mean values of D_{clear} for these plates were subtracted point-by-point from the O and E cell densities in the appropriate plate. From our previous discussion of the linearity of the electronographic process we

Figures 4.12 *Clear plate density distributions from plates 13 to 16*

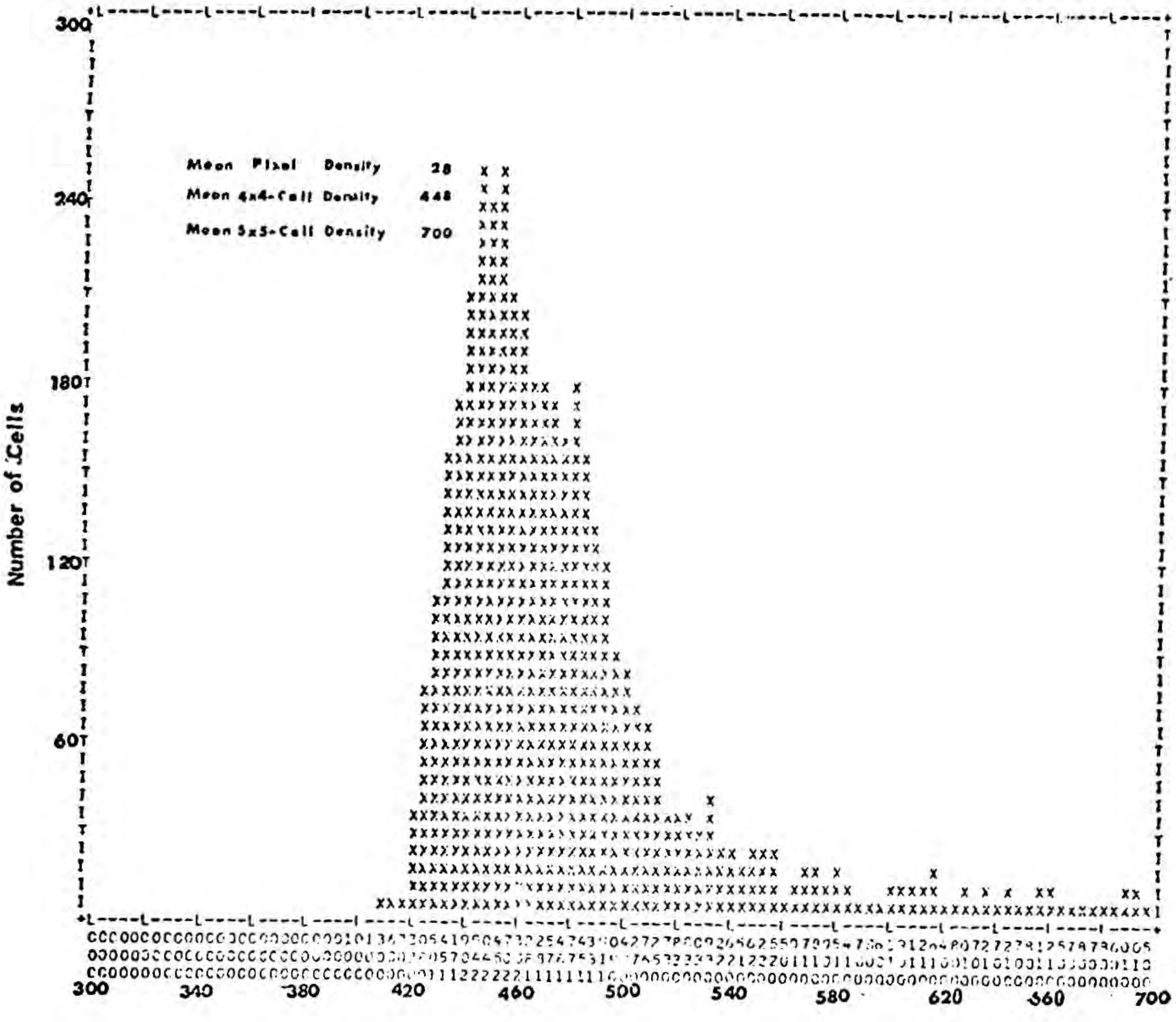

Clear Plate Density No 16

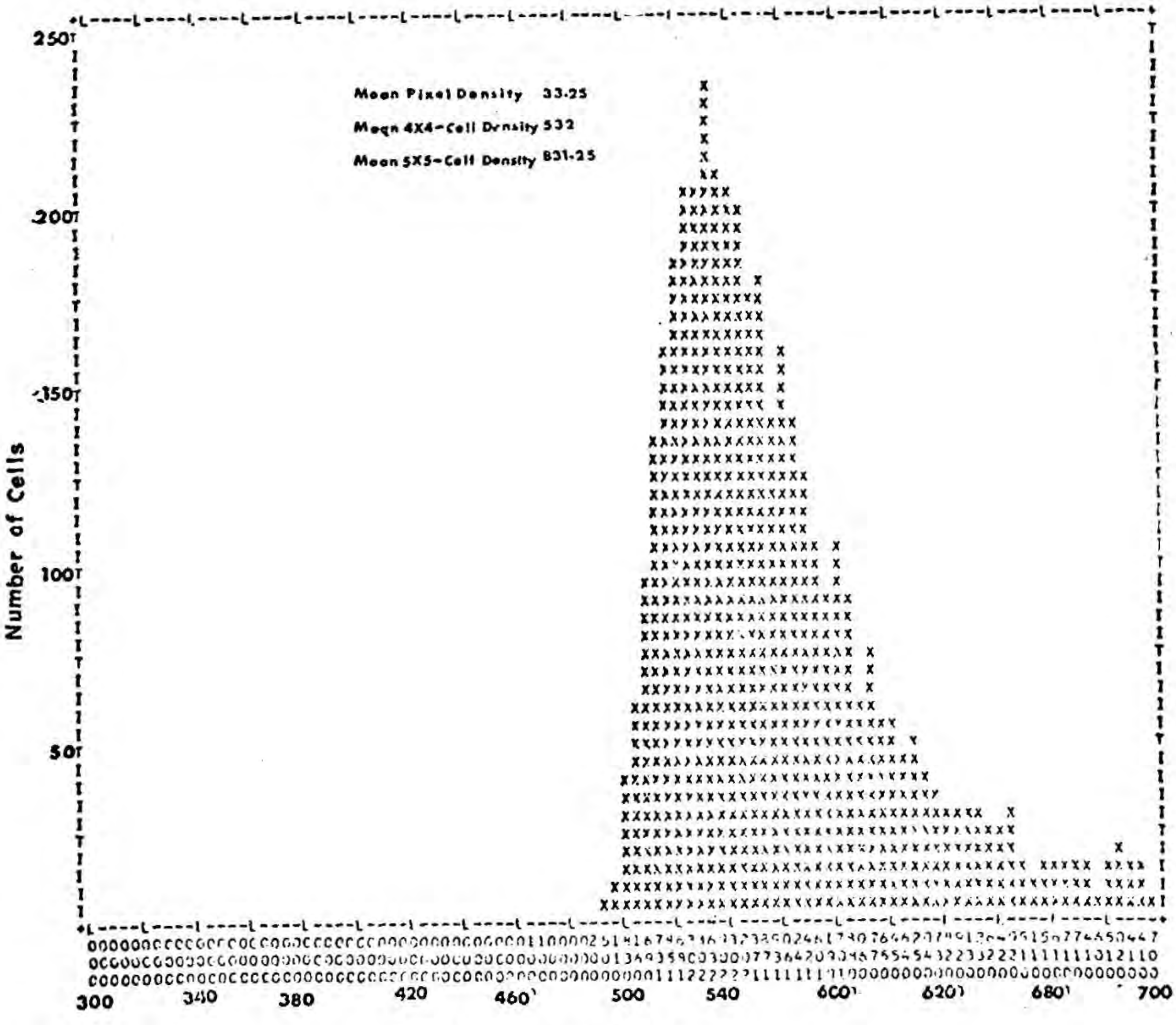

Clear Plate Density No 13

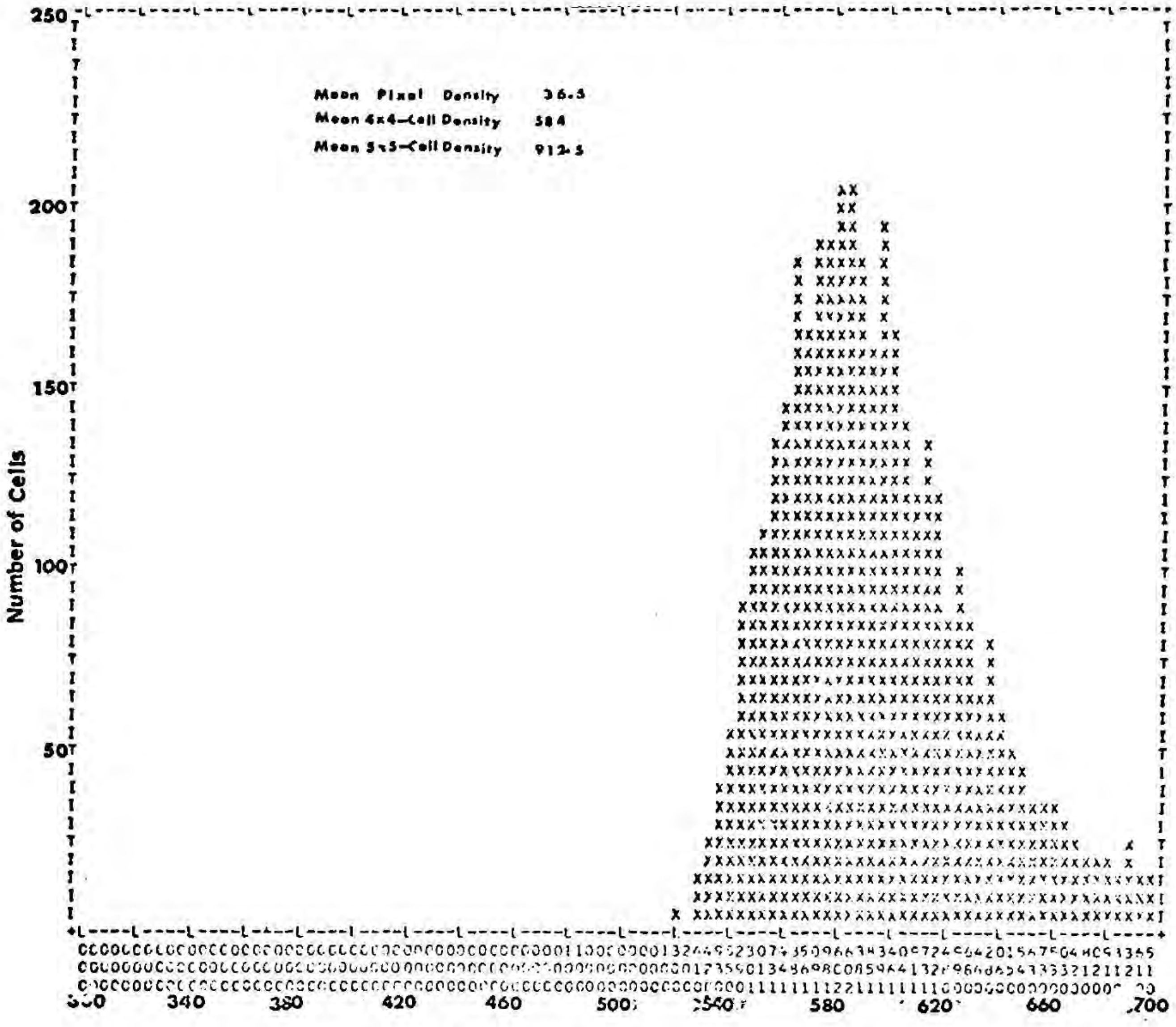

Clear Plate Density No 14

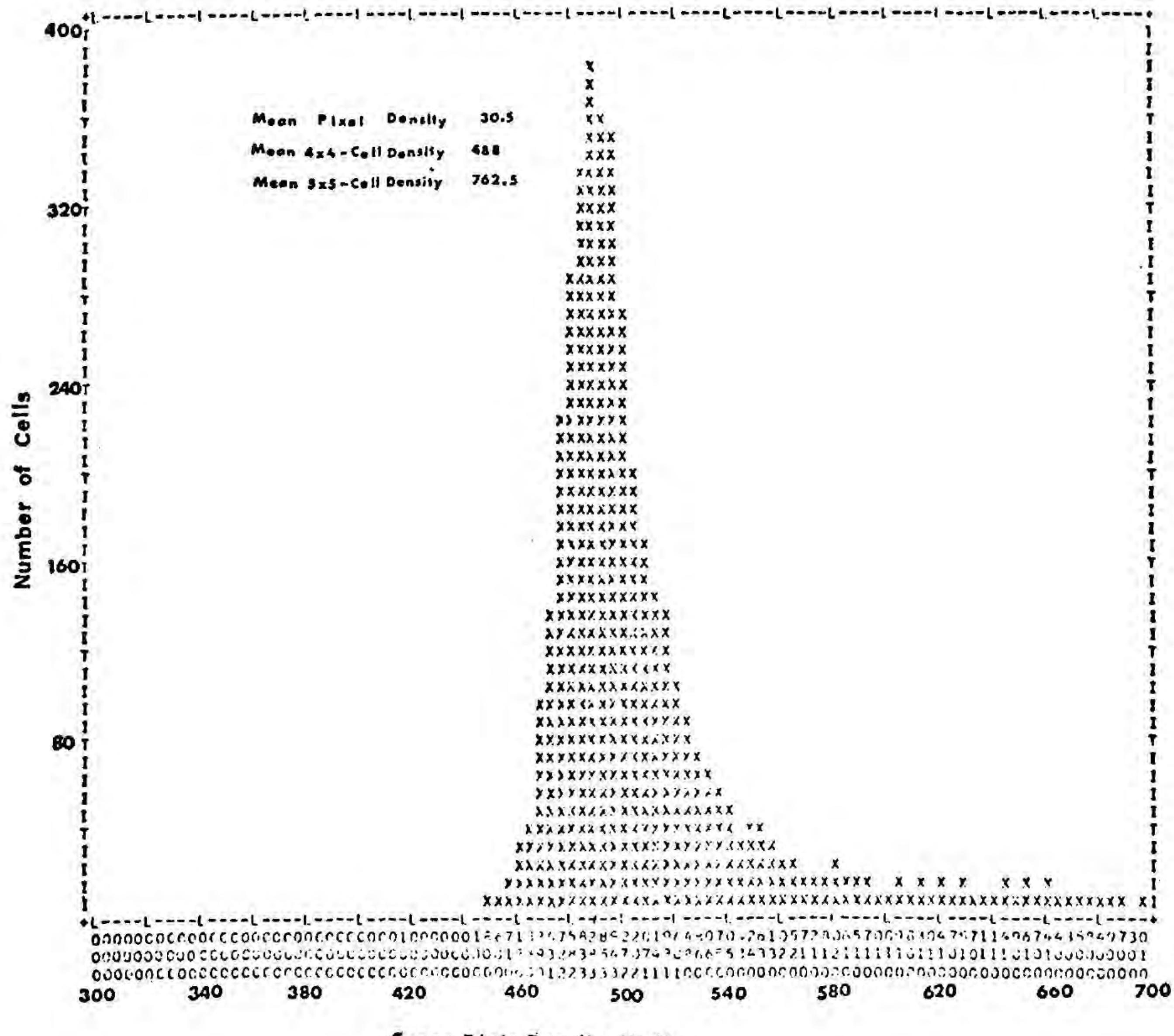

Clear Plate Density No 15

see that we are now in a position to apply the theory developed in Chapter 3.3 to calculate the Stoke's parameters from the remaining cell densities D_{obs}

4.5 The f-factors, e-factors and Stoke's Parameters

Before calculating the Stoke's parameters we must apply corrections for the variation of the cathode sensitivity and the differing exposures of each plate. As we showed in Chapter 3.3 the f-factors defined by equations 3.16 and 3.18 enable us to measure and correct for the sensitivity difference between each O and E locations. Since the sensitivity variations also affect the computed e-factors, which measure the relative exposure of each plate (Chapter 3.3), we started by calculating the f-factors for each half of the galaxy. Figure 4.13 shows the f-factors from plates 13 to 16, and again virtually identical distributions were obtained from the other half of the galaxy. The mean values of both the f_1 and f_2 factors are 1.01, which disagrees only slightly (1%) from the theoretical mean of 1.0 and possibly reflects a polarization dependence in the response. The observed distributions are in excellent agreement with those expected from our previous discussions: virtually all the points lie in the range 0.9 to 1.10 ($\pm 10\%$ cf Penny 1976) and 90% of the f-values between 0.96 and 1.06, implying sensitivity changes of only $\pm 5\%$. Penny's (1976) measurements refer to the whole 4 sq. cm area of the photocathode, whereas ours are confined to an area of only 1 sq. cm. The smaller sensitivity variations indicated here reflect the greater uniformity of the photocathode over small areas. It is instructive to compare Figures 4.13 and Figure 4.3 which shows a typical f-factor distribution from the analogue analysis. The remarkable improvement in the apparent uniformity

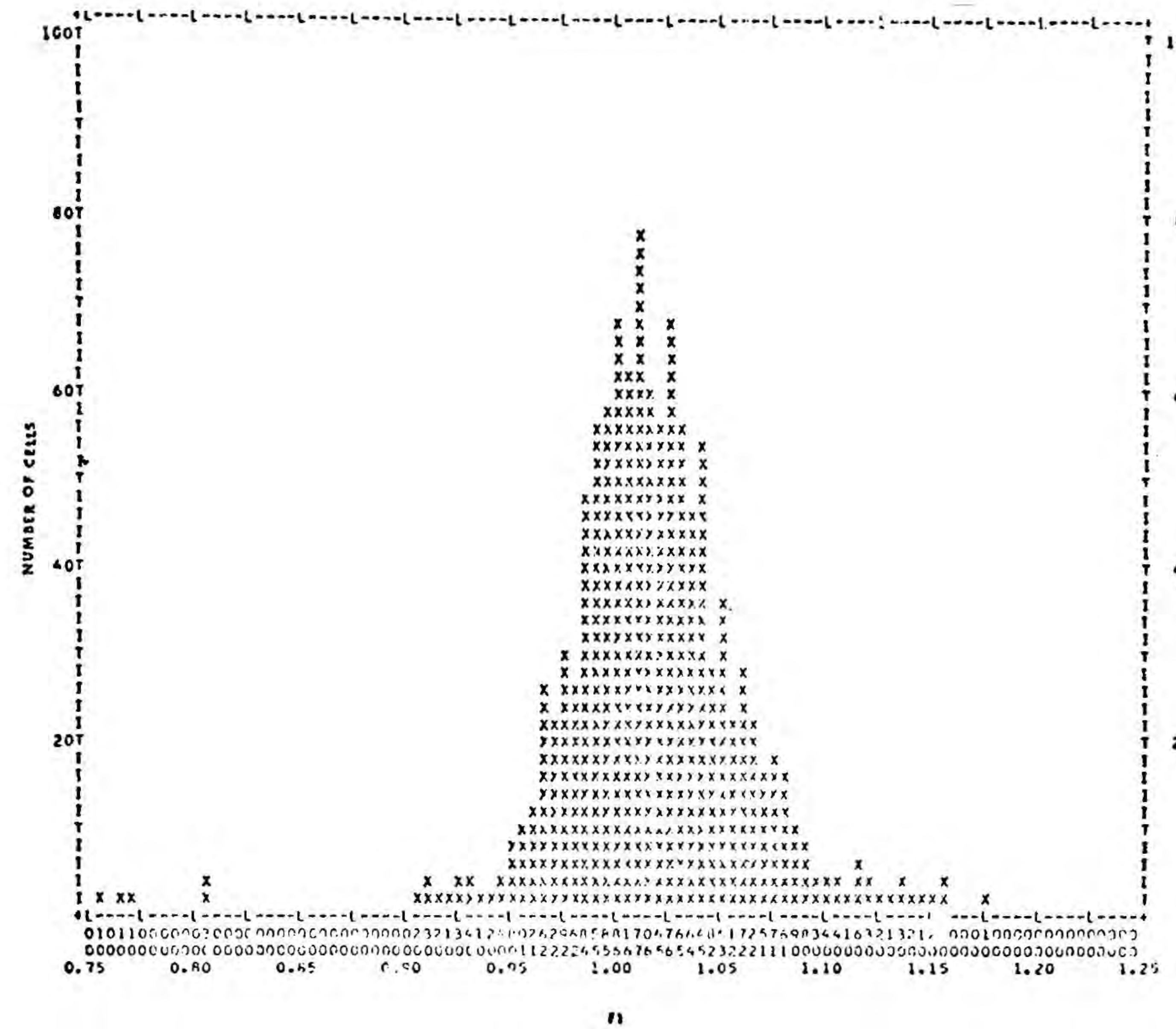

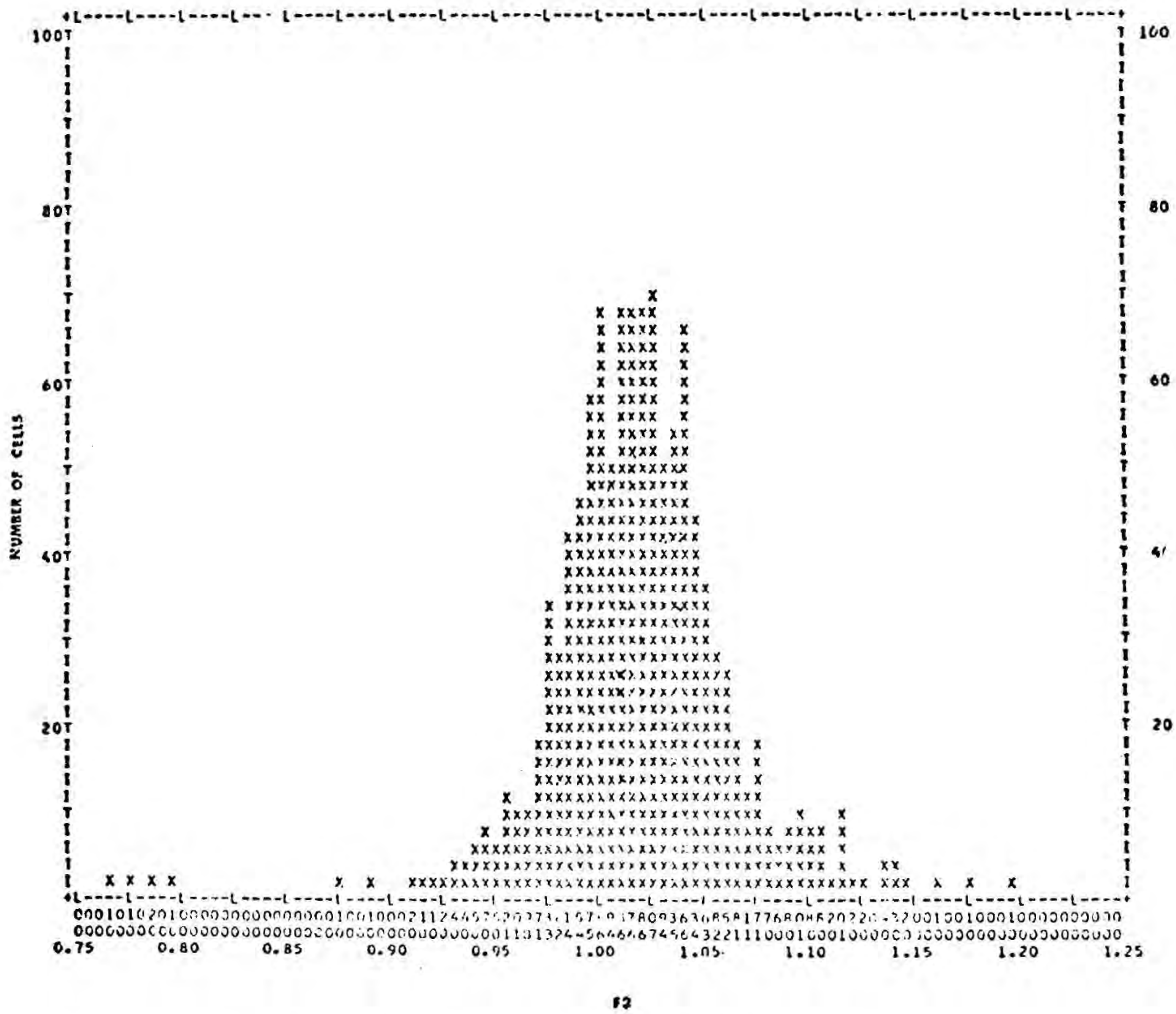

Figure 4.13 *f-factor distributions from plates 13 to 16*

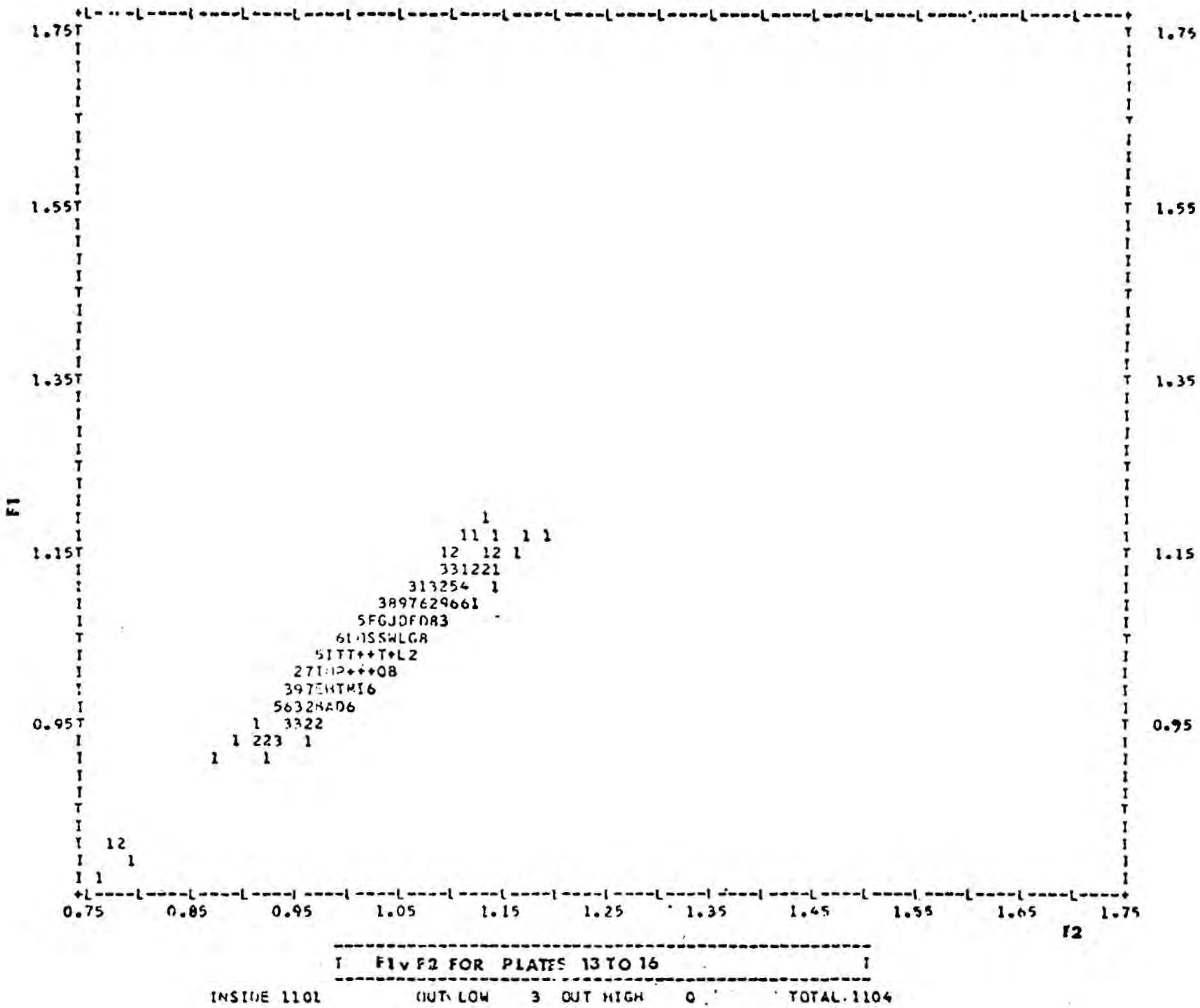

Figure 4.14 Correlation plot of the f-factors from plates 13 to 16. The nomenclature is as in figure 4.11.

of the photocathode shown by the digital f-factor distributions is directly attributable to the improved image registration and analysis procedure.

Since f_1 and f_2 are independent estimates of the cathode sensitivity at each point, the difference between them will provide a measure of our internal accuracy, and a criterion for rejecting suspect measurements. In the ideal case we would expect a correlation plot of f_1 and f_2 to produce a straight line with gradient one passing through the origin. For the real data the presence of any systematic effect would be shown by a correlation curve with a different gradient or a non-zero intercept, and the scatter of the points also provides a measure of the degree of agreement between f_1 and f_2 and hence our internal accuracy. Figure 4.14 shows the correlation plot for plates 13 to 16; the least squares regression line to these data has a gradient of 1 ± 0.03, thus providing an excellent fit. Furthermore the f-factors all lie within ± 0.025 of this line implying a consistency comparable to that indicated from the width of individual f-factor distributions, and probably implies that this is a noise limit figure. Combining the information from the f-factor plots we were able to form two criteria for rejecting "bad-points" Firstly, we demanded that each acceptable point had f-factors lying between 0.96 and 1.06 and secondly, that the difference between the two f-factors was no greater than 0.05. In the approach adopted here we used f-factors computed for each cell and contamination of the total cell f-factors by individual pixels could cause a higher rejection rate than necessary. A better approach would be to compute "f-factor maps" from the individual pixels and apply the rejection criteria during the cell construction stage, as we did with the saturation test. This refined approach demands large amounts of storage as two 512 x 512 f-factor arrays had to be stored simultaneously with the

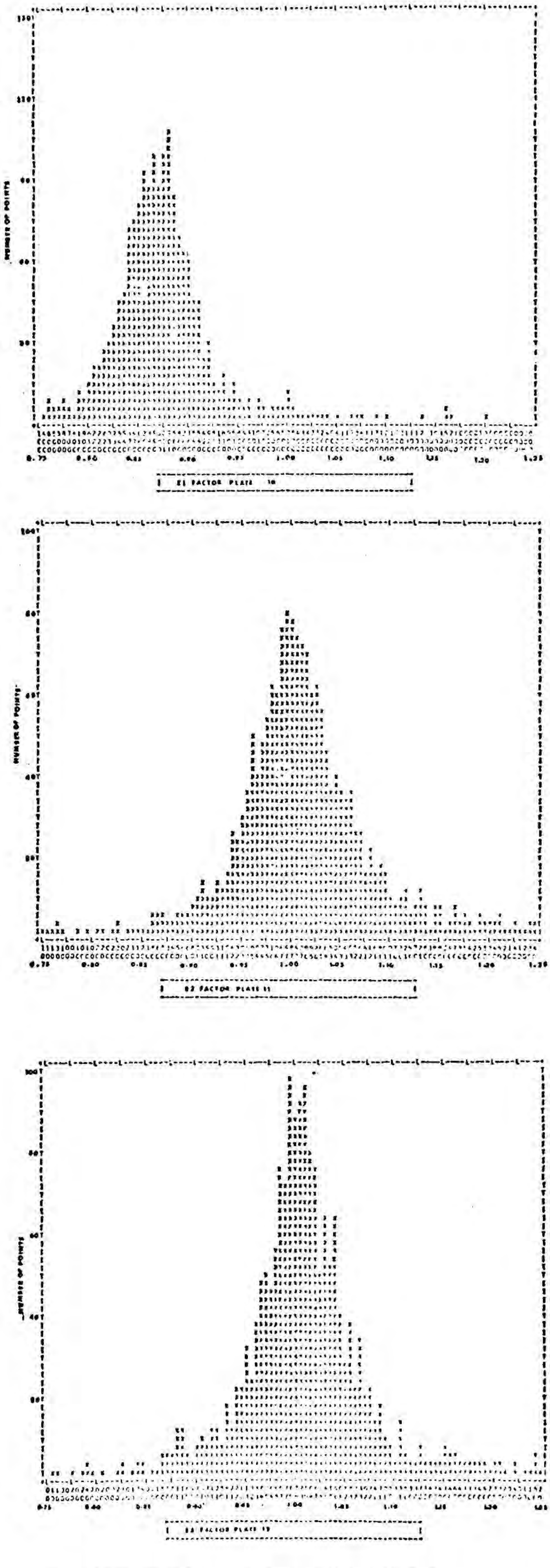

Figure 4.15 Three typical e-factor distributions.

four real pictures, and the complicated series of "table-lookups" required would be expensive in computer time. The inadequacy of the present data does not justify the use of this method. The e-factors for each plate, defined by equations of the form of equation 3.9, were calculated and modified, to correct for cathode sensitivity variations, by dividing even-numbered cell intensities by the mean cell f-factor, $< f >$. Typical e-factor distributions are shown in Figure 4.15. Since the e-factors measure the relative exposure of each plate, a unique value for each plate would be expected in the ideal case. In practice the e-factors, as with the f-factors, will have a distribution whose widths will provide a measure of our internal accuracy. The observed distributions have typical FWHM's of 0.10 (c.f. f-factors) and have a very similar form to those of the f-factors except that they have more prominent tails. The origin of these tails appears to be the "bad-points", as they virtually disappear when the f-factor test is applied. Examination of scatter plots of the e-factor values against position do not reveal any systematic dependance on location (Figure 4.16). There is, however, a tendency for an increase in the spread of the distribution towards the periphery, which can be accounted for by the less precise registration of the plates far away from the Fiducial stars.

Two estimates of the Stoke's parameters Q_{obs} and U_{obs} can be obtained for each half of the galaxy by applying equations 3.19 to each pair of plates; however, because of the e-factor normalization, only one estimate of the total intensity I_{obs} is obtained. The use of the f-factors means that the two sets of Q and U values are not strictly independent; nevertheless the difference between the estimates provides an important gauge of our internal accuracy. These Stokes' parameters do not however measure the polarization

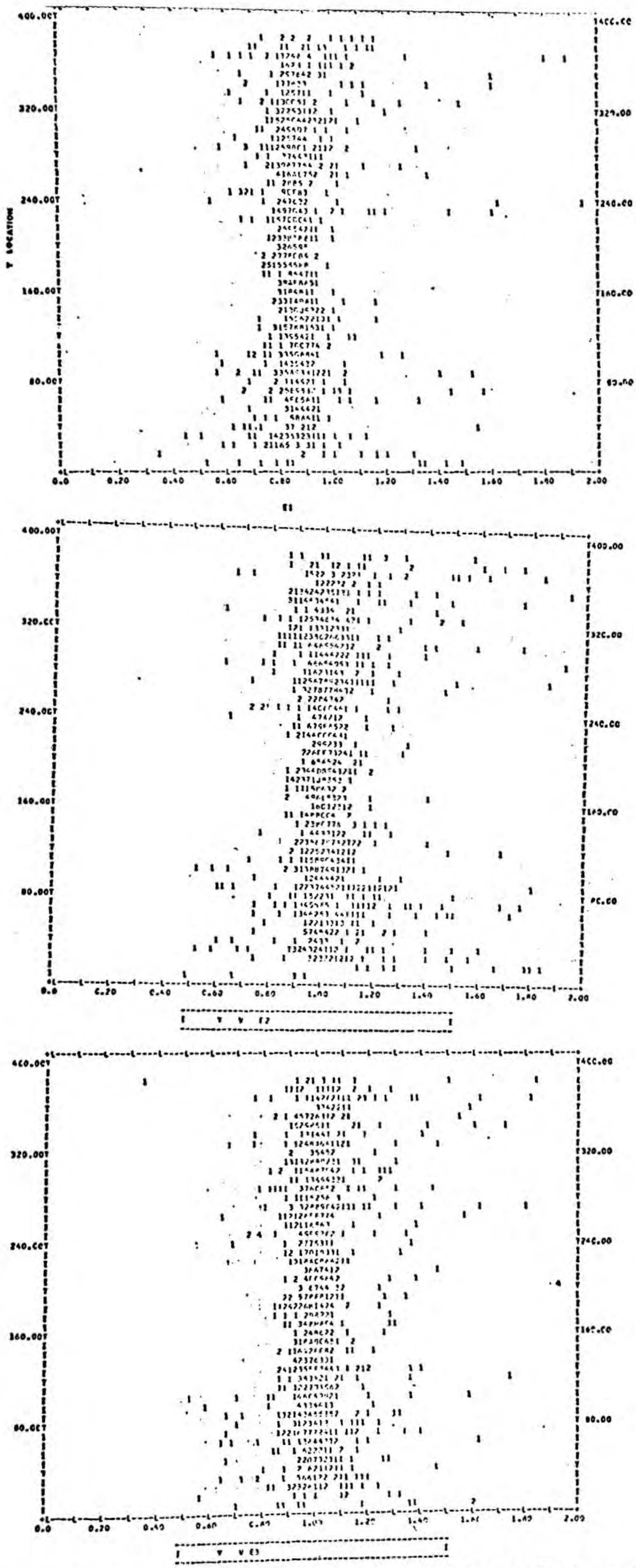

Figure 4.16 Scatter plots of the e-factor values against position. The nomenclature is as in figure 4.11.

of the galaxy as the polarization and intensity of the night sky has to be subtracted.

4.6 The Subtraction of the Sky Background

As in section 4.1 we used the average values of I_{obs}, Q_{obs}, U_{obs} in galaxy-free areas of the plates to determine the Sky Stoke's parameters. I_{sky} was measured separately for each half of the galaxy using the average of the exposure-corrected intensities from all four plates. Q_{sky} and U_{sky} were determined independently for each pair of plates. A point-by-point subtraction of I_{sky}, Q_{sky} and U_{sky} was then made, leaving the Stoke's parameters of the galaxy. In Figures 4.17 a comparison of the relative intensities of the sky and clear plate in 4 x 4 pixel areas on plates 9 to 12 is made. (The measured Sky intensities have been scaled down to give the equivalent 4 x 4 cell values so that a direct comparison can be made.) I_{sky} is $\sim 3 I_{clear}$ and a significant proportion of I_{obs}. Such a large Sky background not only makes it difficult to determine the polarizations in the fainter regions of M82 but also introduces large uncertainties as they are very sensitive to changes in the adopted value of I_{sky}. In the present work we only measured the polarization in locations for which $I_{gal} / I_{sky} \geq 0.1$, but even with this modest target the final polarization map contains obvious noise dominated regions and isolated examples of uncertain vectors (Figure 4.19). With the data obtained from a darker site during "dark-time" the methods developed here should work satisfactorily down to $I_{gal} / I_{sky} \gtrsim 0.05$ or even $I_{gal} / I_{sky} \gtrsim 0.01$, but in order to achieve comparable success with the present data highly sophisticated Fourier techniques are required, and the quality of the data does not justify the approach.

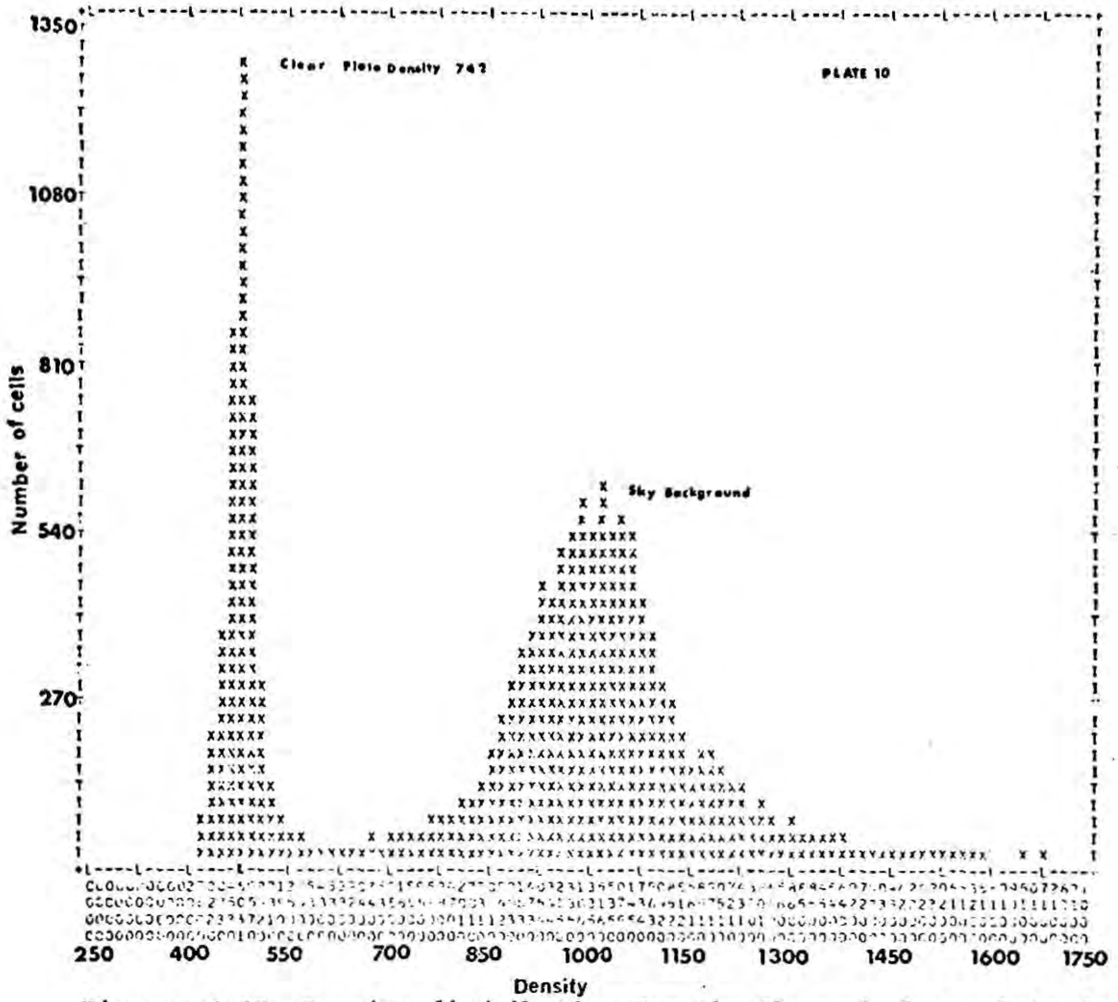

Figures 4.17 Density distribution for the Sky and clear plate from plates 9 to 12.

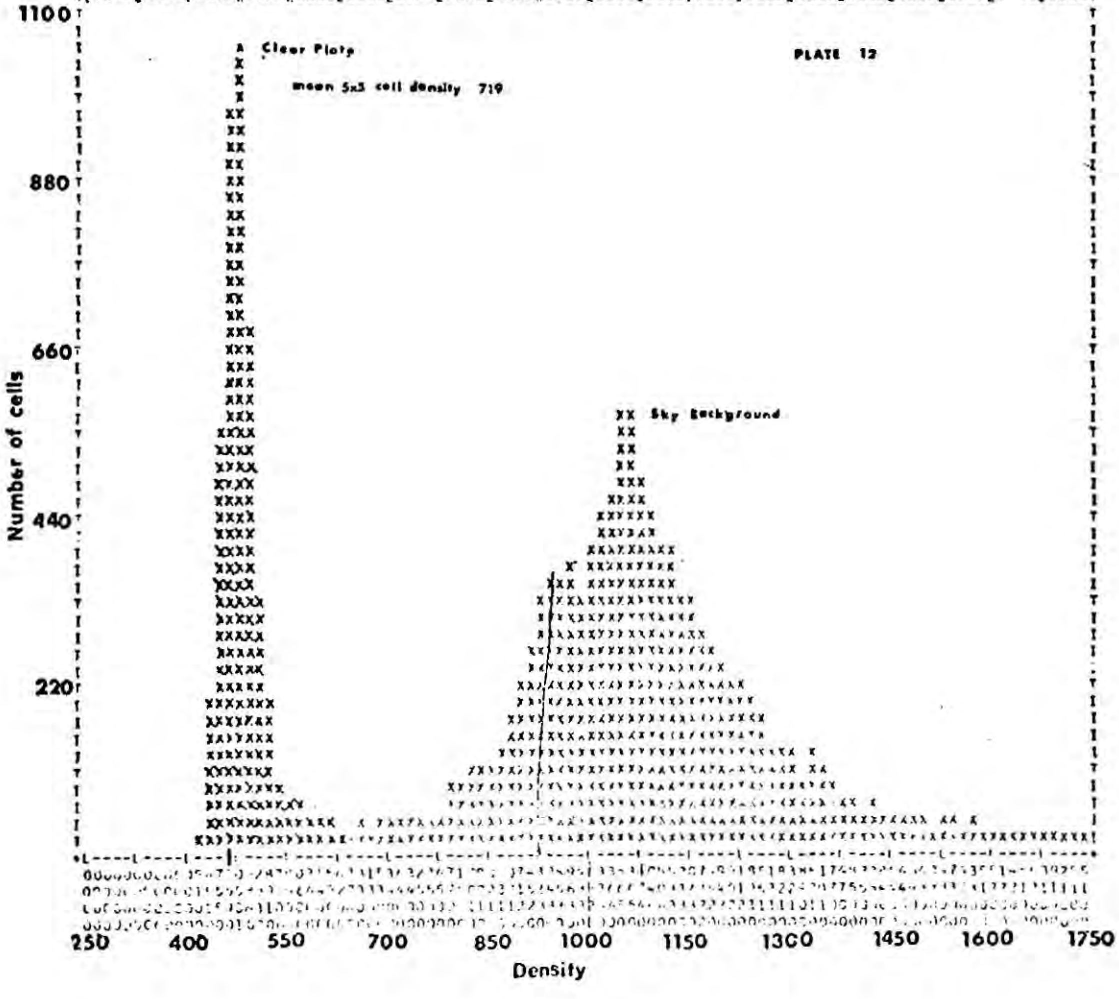

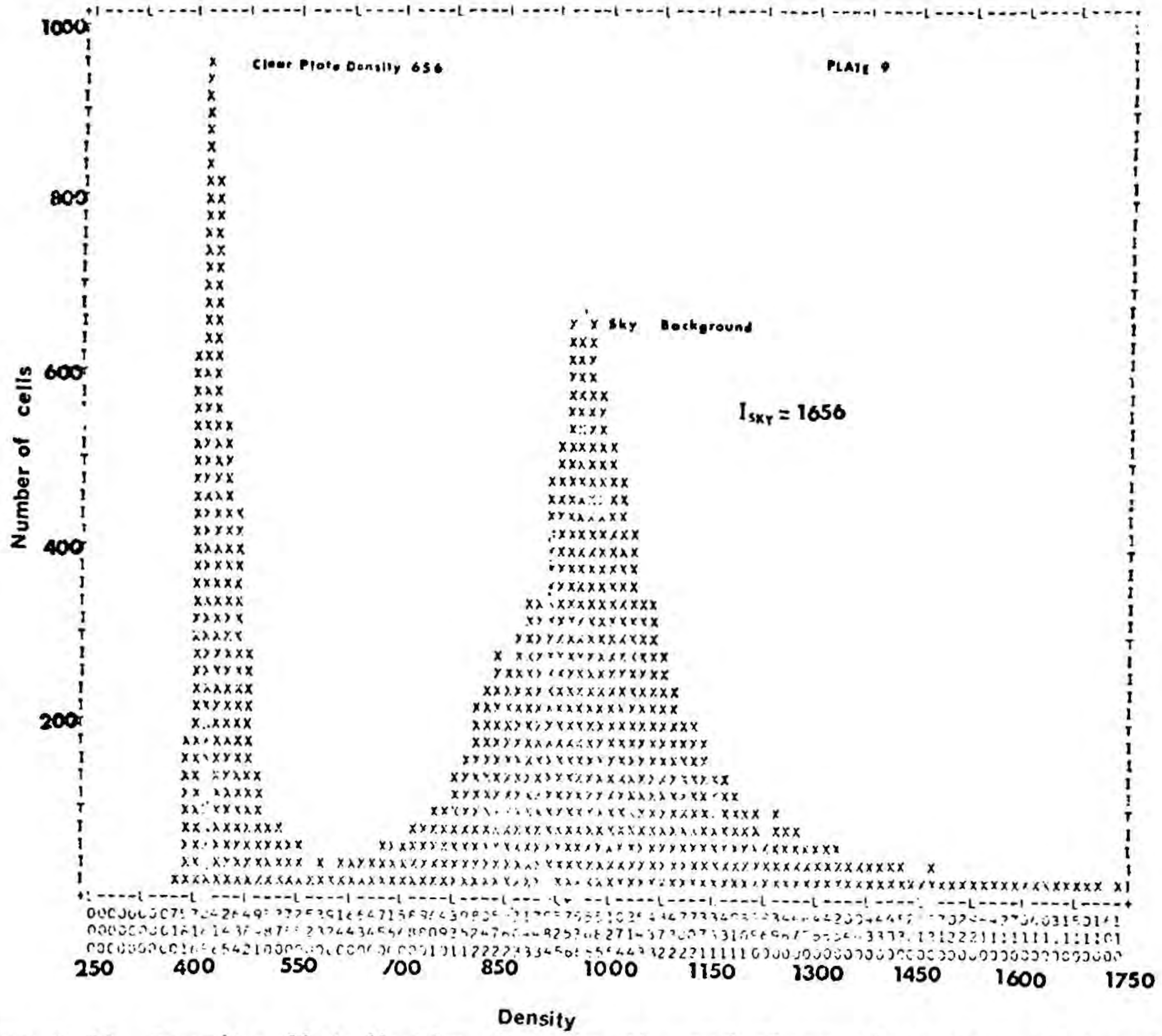

Figures 4.17 Density distribution for the Sky and clear plate from plates 9-12

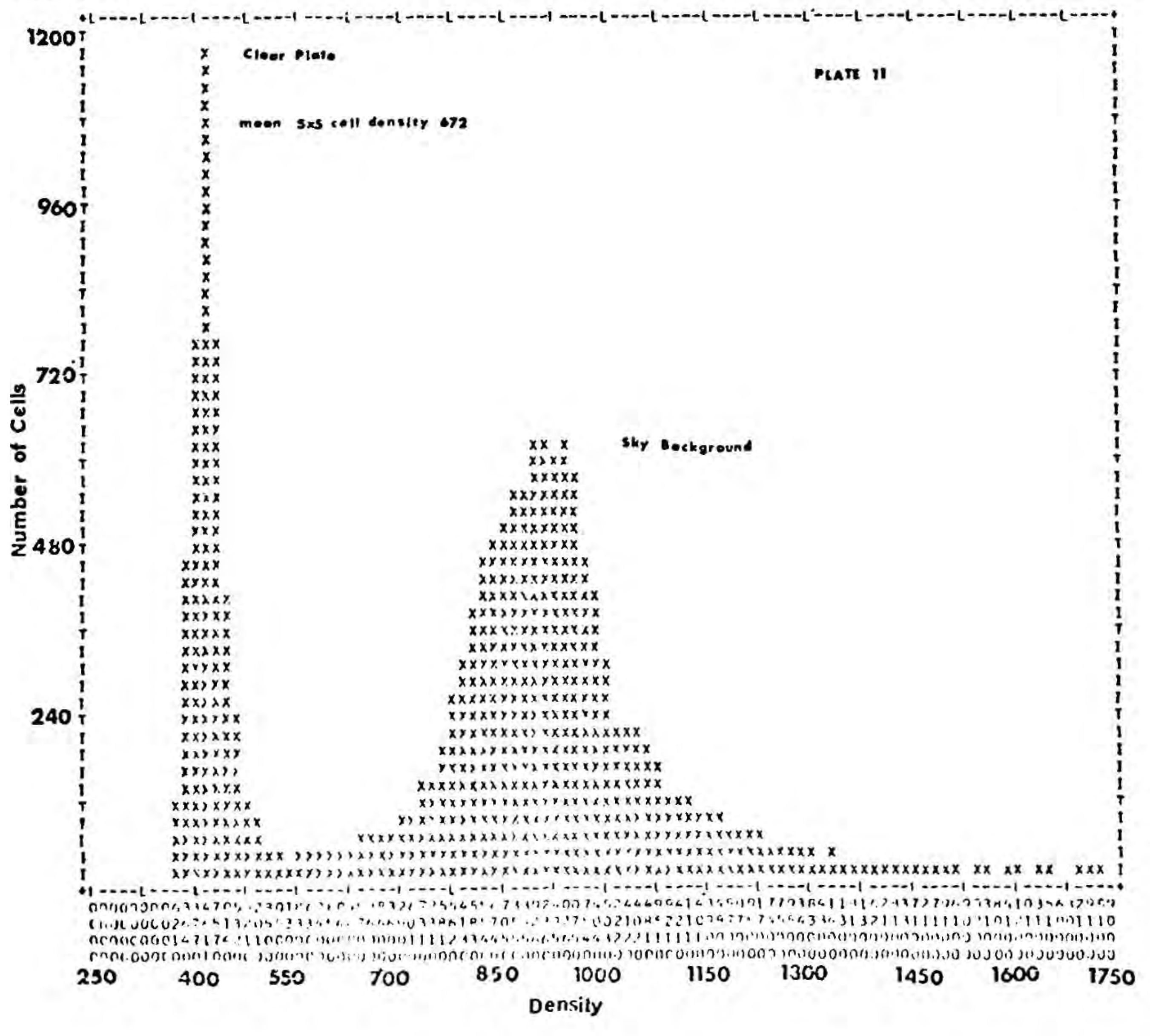

After the sky subtraction, the two estimates of Q_{gal} and U_{gal} for each location were averaged, and the polarization of the galaxy, and its position angle, computed according to equations 3.11 and 3.12. In order to estimate the accuracy of our results we also calculated the polarizations P1 and P2 and the position angles ANG1 and ANG2 from the two estimates separately, and examined the differences (P1 - P2) and (ANG1 - ANG2). The resulting distributions for both halves of the galaxy are shown in Figures 4.18. The uncertainties for plates 9 to 12 are 3% for the (P1-P2) plot and 6° for the (ANG1 - ANG2) plot whereas the corresponding uncertainties for plates 13 to 16 are only 1% and 4° respectively. These results illustrate the critical nature of the picture registration; plates 9 to 12 contain fewer Fiducial stars than plates 13 to 16 and are consequently less precisely registered, so producing larger errors. On the basis of these data we rejected all polarization measurements for which $|ANG1 - ANG2| > 15°$ or $|P1 - P2| > 8\%$. Approximately 10% of the data points were discarded, mainly towards the edges of the strips where some contamination from the overlaps had occurred.

An important refinement to the Sky subtraction method would be the inclusion of a correction for the differing cathode sensitivities at the Sky and galaxy locations. As the f-factors only measure the sensitivity difference between corresponding locations, this would require the use of a cathode sensitivity map, produced by the "cloth-method" described in Chapter 5, which provides a measure of the sensitivity difference, h, between points on the same strip. The sensitivity map has to be registered with the galaxy electronographs, and this could be accomplished with the optimization routine described previously, using "dead-points" on the photocathode as Fiducial marks.

Figures 4.18

(a) *Plot of the difference between the two estimates of the polarization for plates 13 to 16*

(b) *Corresponding plot to (a) for plates 9 to 12*

(c) *Plot of the difference between the two estimates of the position angle for plates 13 to 16*

(d) *Corresponding plot to (c) for plates 9 to 12*

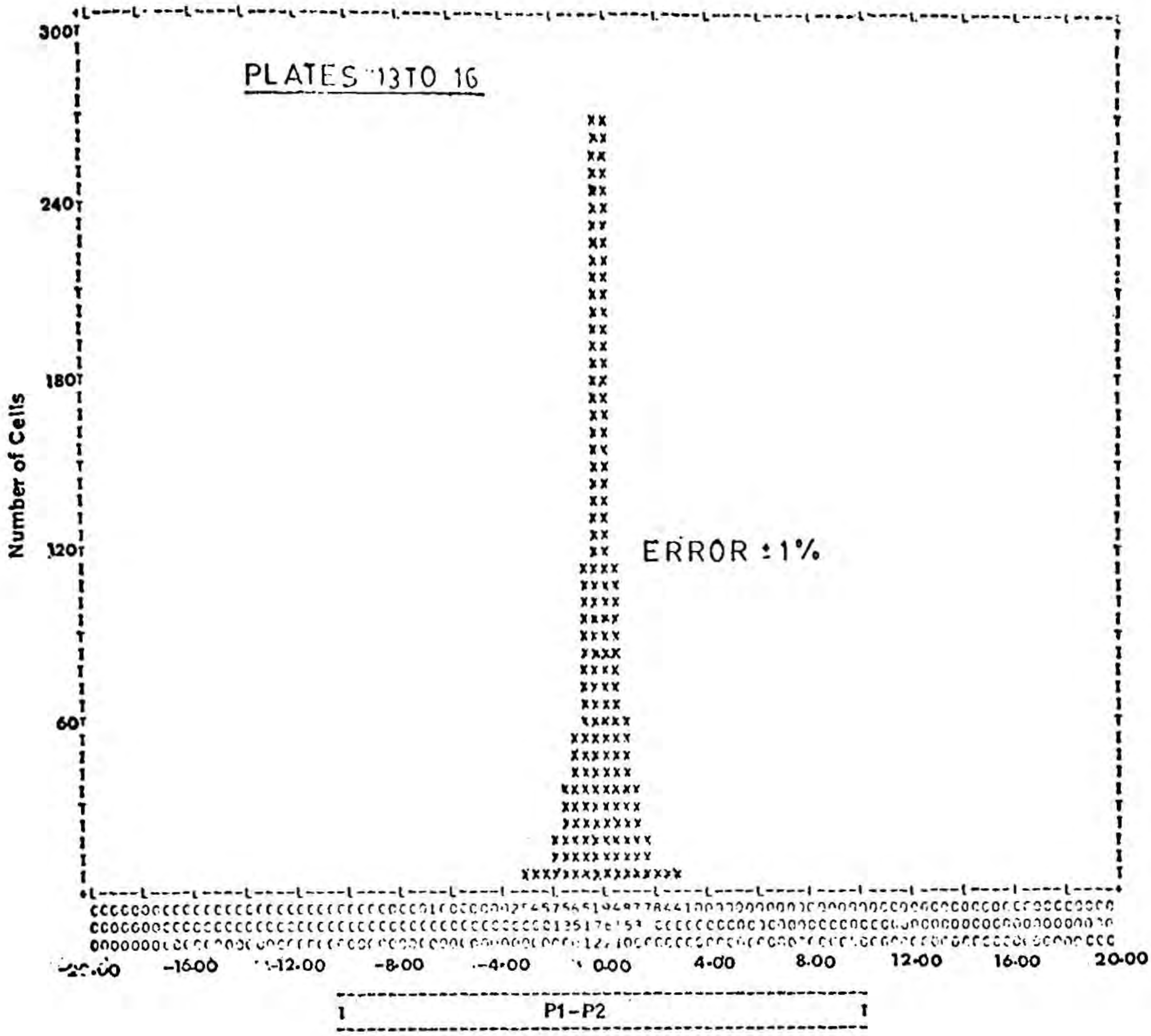
PLATES 13 TO 16
ERROR ±1%
Number of Cells
300
240
180
120
60
-20.00
-16.00
-12.00
-8.00
-4.00
0.00
4.00
8.00
12.00
16.00
20.00
P1-P2

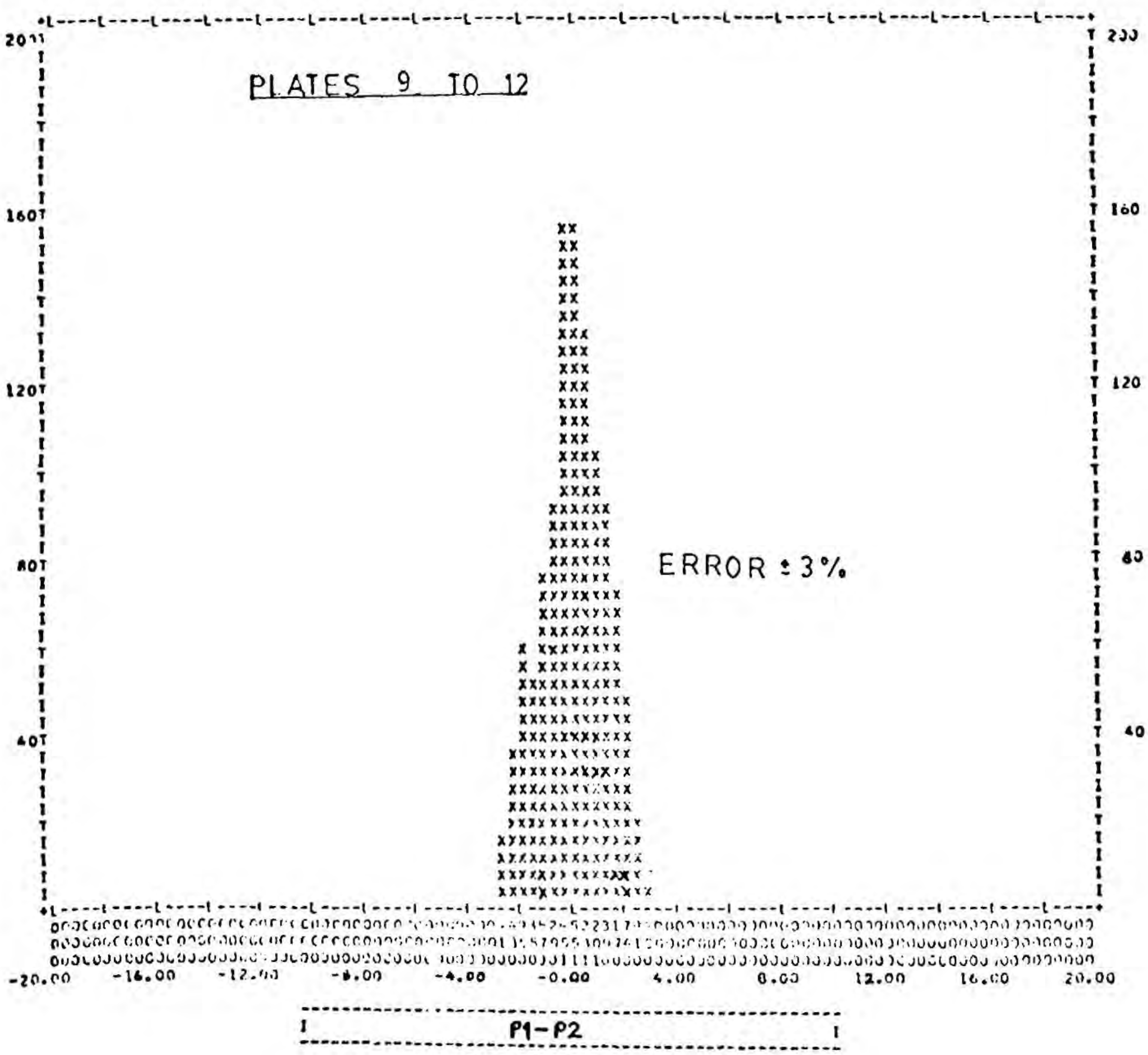
PLATES 9 TO 12
ERROR ±3%
200
160
120
80
40
-20.00
-16.00
-12.00
-8.00
-4.00
-0.00
4.00
8.00
12.00
16.00
20.00
P1-P2

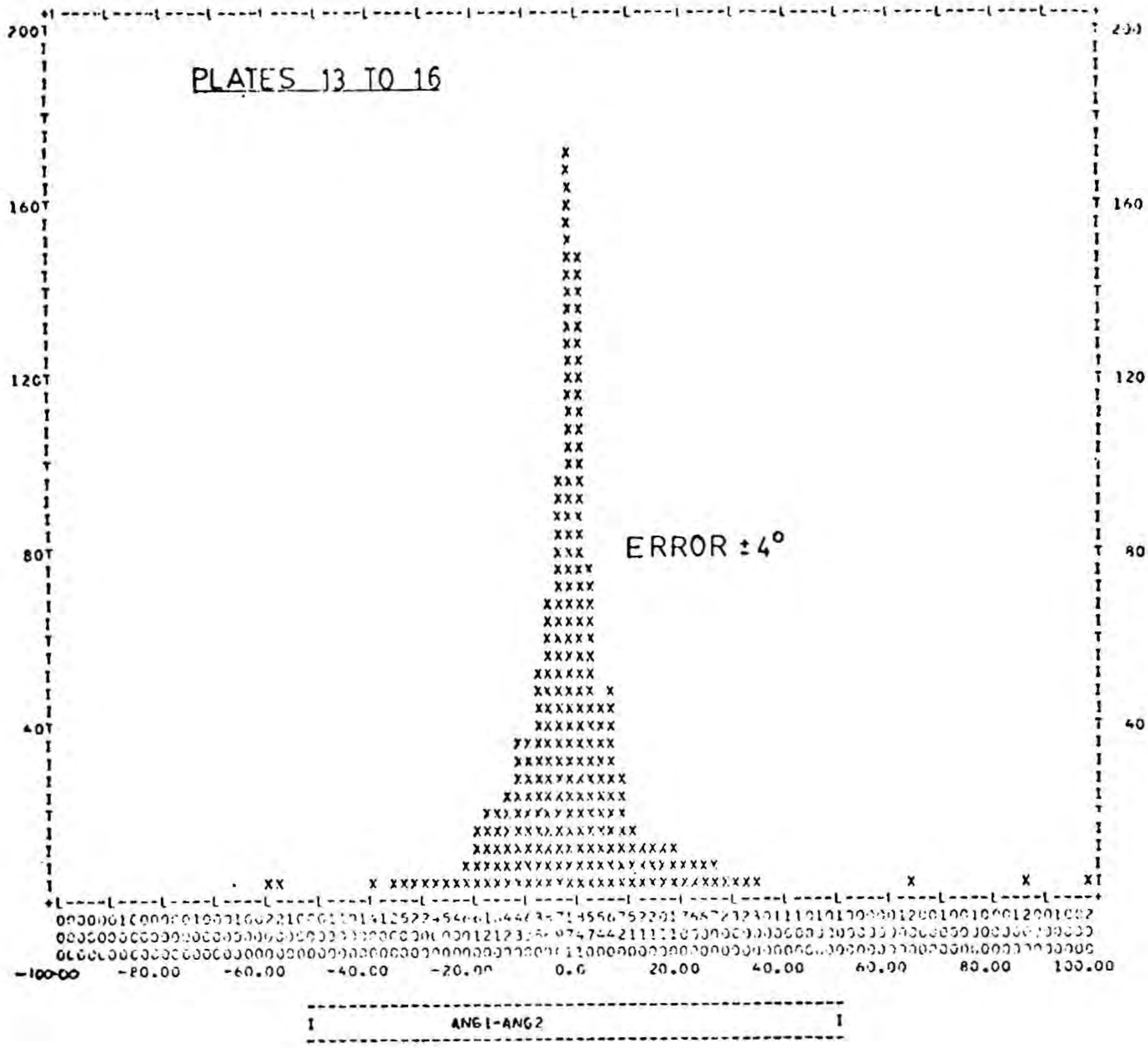
PLATES 13 TO 16
ERROR ±4°
200
160
120
80
40
-100.00
-80.00
-60.00
-40.00
-20.00
0.0
20.00
40.00
60.00
80.00
100.00
ANG1-ANG2

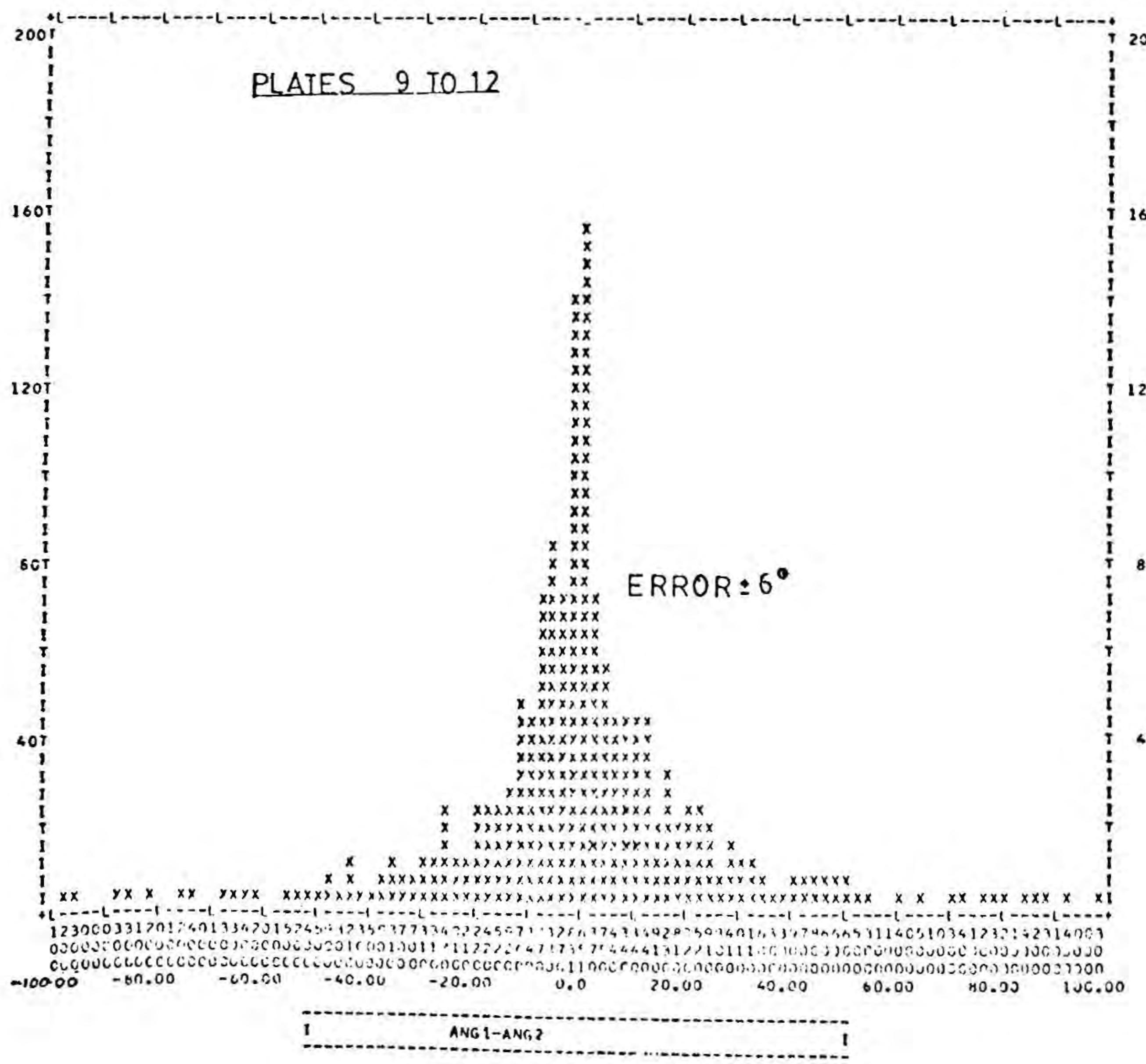
PLATES 9 TO 12
ERROR ±6°
200
160
120
80
40
-100.00
-80.00
-60.00
-40.00
-20.00
0.0
20.00
40.00
60.00
80.00
100.00
ANG1-ANG2

The average of each Sky Stoke's parameters $\bar{S}$ would then be computed for each strip according to equation 4.17.

$$\bar{S} = \frac{< \sum_i \sum_j h_{ij} S_{ij} >}{< \sum_i \sum_j h_{ij} >} \tag{4.17}$$

where S_{ij} is the Stoke's parameter from an individual cell and h_{ij} is the cathode sensitivity at that point. By weighting, $\bar{S}$ by the average h-value for the Sky cells, and the Stoke's parameter of any point in the galaxy by its measured h-value, sensitivity variations could then be taken into account during the Sky subtraction. We were unable to apply this correction to the present data as the photocathode used for the observations was unfortunately destroyed before it could be properly mapped. However, since the sensitivity variations are only ~ 5% this will only produce an appreciable error for faint points, and even for these measurements this error will be dominated by those from other sources (see below).

Using the coordinates of the centroids of the stars and their known R.A. and Dec we combined the two halves of the galaxy and transformed the complete map into the equatorial coordinate system. The least-squares optimization procedure described previously was used for this operation, with the transformation equation 4.18

$$\begin{aligned} F_i &= a_o + a_1 y_i + a_2 x_i + a_3 y_i^2 - (R.A)_i \\ b_i &= b_o + b_1 x_i + b_2 y_i + b_3 x_i^2 - (Dec)_i \end{aligned} \tag{4.18}$$

Figure 4.19 The uncorrected polarization map of M82.

The terms in x^2 and y^2 provide for possible distortion in the pictures. In practice both these terms and those in a_2 and b_2 are negligible, and convergence with a remarkable residual sum-of-squares of less than 1×10^{-24} could be obtained with a simple linear fit in each direction. The completed polarization map of M82 is shown in Figure 4.19. The polarization notation is as used elsewhere in the thesis, with the polarization at each location being as indicated on the accompanying scale. The map has been plotted with South at the top and the R.A. and Dec axes are marked in arbitrary units. Normally at this stage of the analysis reference would be made to the standard star data and corrections for instrumental polarization and the "zero-point" error in the position angles applied. There were however two important instrumental effects (described in Chapter 3) present when these observations were made which will cause large errors, and which the normal Sky subtraction method does not take into account. Firstly there was the depolarization caused by the chromatic behaviour of the $\lambda/2$-plate, and secondly there was the vignetting introduced by the use of the 2 cm prism. The laboratory determination of the corrections for these effects, and their application to the polarization is described in Chapter 5. We also present the results from other laboratory measurements, and the Standard Star and cloth measurements made at the telescope, together with a discussion of the instrumental and interstellar polarization corrections obtained from these data.

REFERENCES

Akima, H.	1972a	C.A.C.M. 17, p.18.
Akima, H.	1972b	ibid 17, p.26
Hayes, J.G.	1970	Approximations to Functions and Data, Athelone Press.
Kraft, C.A. and Van Eaden, C.	1968	A Nonparametric Introduction to Statistics. McMillan Press.
Pilkington, J.	1975	Private communication
Powell, M.J.D.	1964	Comp. J. 7, p.195.
Van Aulter, W.F. and Auer, L.H.		Proceedings of the Conference on Image Processing Techniques in Astronomy, Utrecht, 1975. Astrophysics and Space Science Library, No: 54, D. Reidel Publishers.
Rosenfield and Lillas	1970	Picture Processing and Psychopictorics, Academic Press.
White, C.	1974	Private communication.

CHAPTER 5

POLARIZATION RESULTS AND CORRECTIONS

5.1 Laboratory Measurements

5.1.1 The Polarimeter Transmission Characteristics

The polarimeter transmission characteristics were measured using a UNICAM SP80 absorption spectrometer, and are shown in Figures 5.1 and 5.2. The absorption losses in the multicomponent Nikon relay lens are large (Figure 5.1a), and the performance of the polarimeter could be improved considerably if this were replaced by a specially designed lens. The transmission curve for the Blue-transmitting BG12 filter is compared with that of an ideal Johnson-B filter in Figure 5.1b. There is a dip in the transmission window at 5500 A°, and the appearance of a second window beyond 7000A°, necessitating the use of the red absorbing BG38 filter (Figure 5.1C). The $\lambda/2$-plate (Figures 5.1d and e) shows a slight decrease in transmission towards the blue end of the spectrum. The total transmission function of the polarimeter is obtained by convolving these curves, as shown in Figure 5.2. The actual working transmission characteristics of the instrument at the telescope will also depend on the spectral variation of the detective quantum efficiency of the McMullan camera (Figure 5.3, McMullan 1975), and its effect on the transmission function is shown in Figure 5.2. The inclusion of sheet polaroids for test measurements will have a more pronounced effect (Figure 5.2) as they have strong wavelength dependent transmission functions (Figure 5.4), and this must be taken into account when attempting to verify the $\lambda/2$-plate

(a)

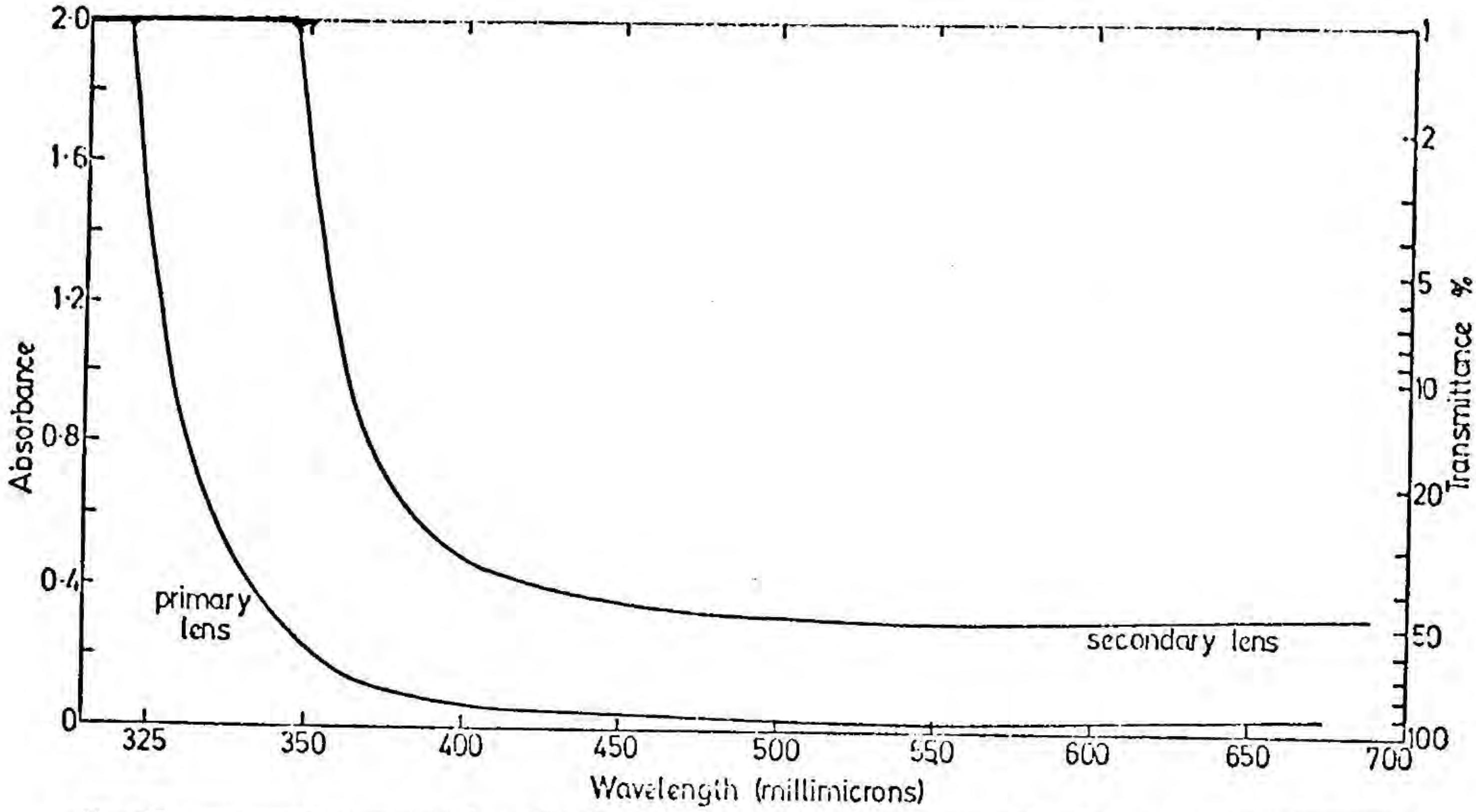
2·0
1·6
1·2
0·8
0·4
0
Absorbance
primary
lens
secondary lens
325
350
400
450
500
550
600
650
700
Wavelength (millimicrons)
1
2
5
10
20
50
100
Transmittance %

(b)

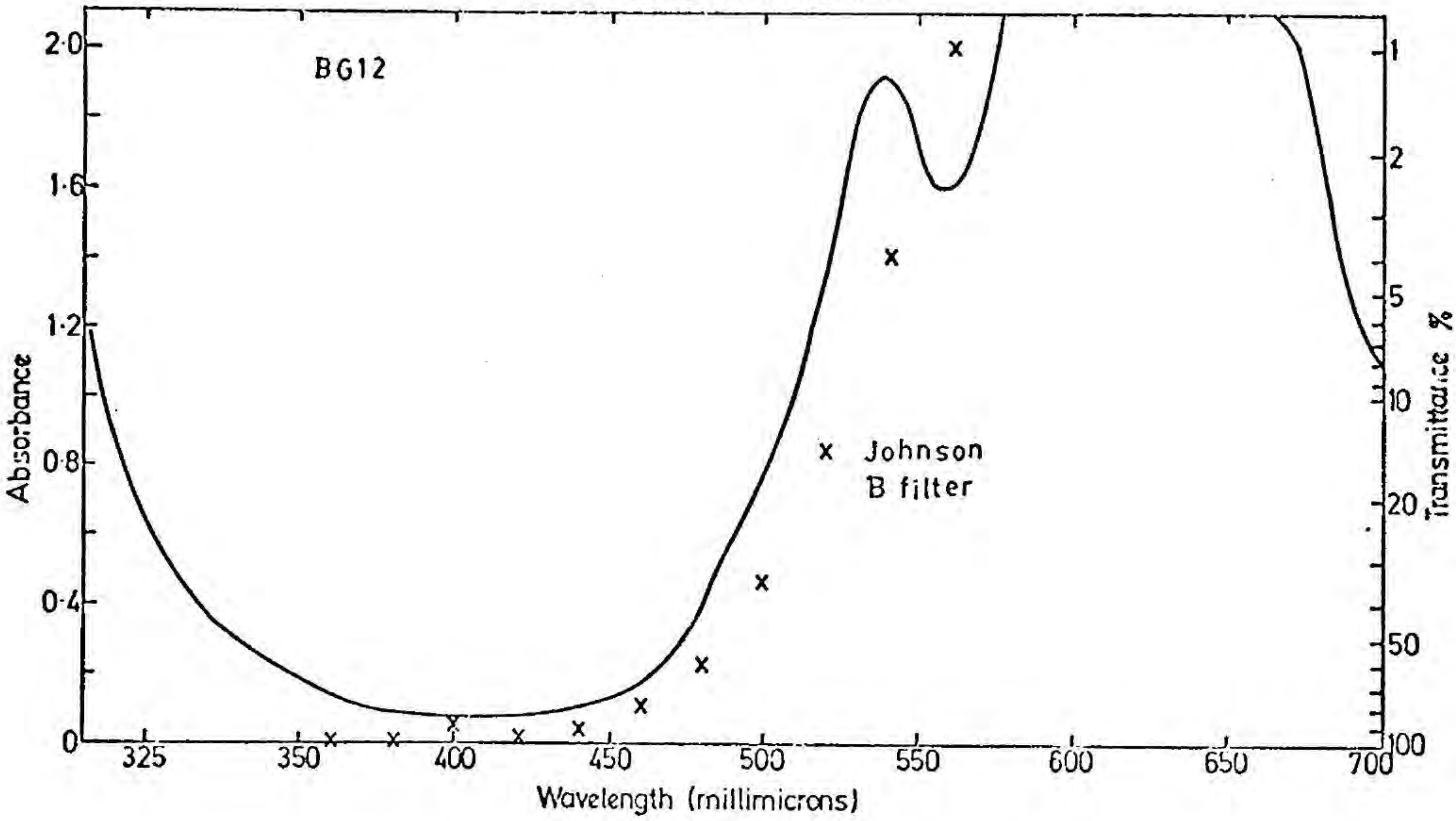
2·0
1·6
1·2
0·8
0·4
0
Absorbance
BG12
x Johnson
B filter
325
350
400
450
500
550
600
650
700
Wavelength (millimicrons)
1
2
5
10
20
50
100
Transmittance %

(c)

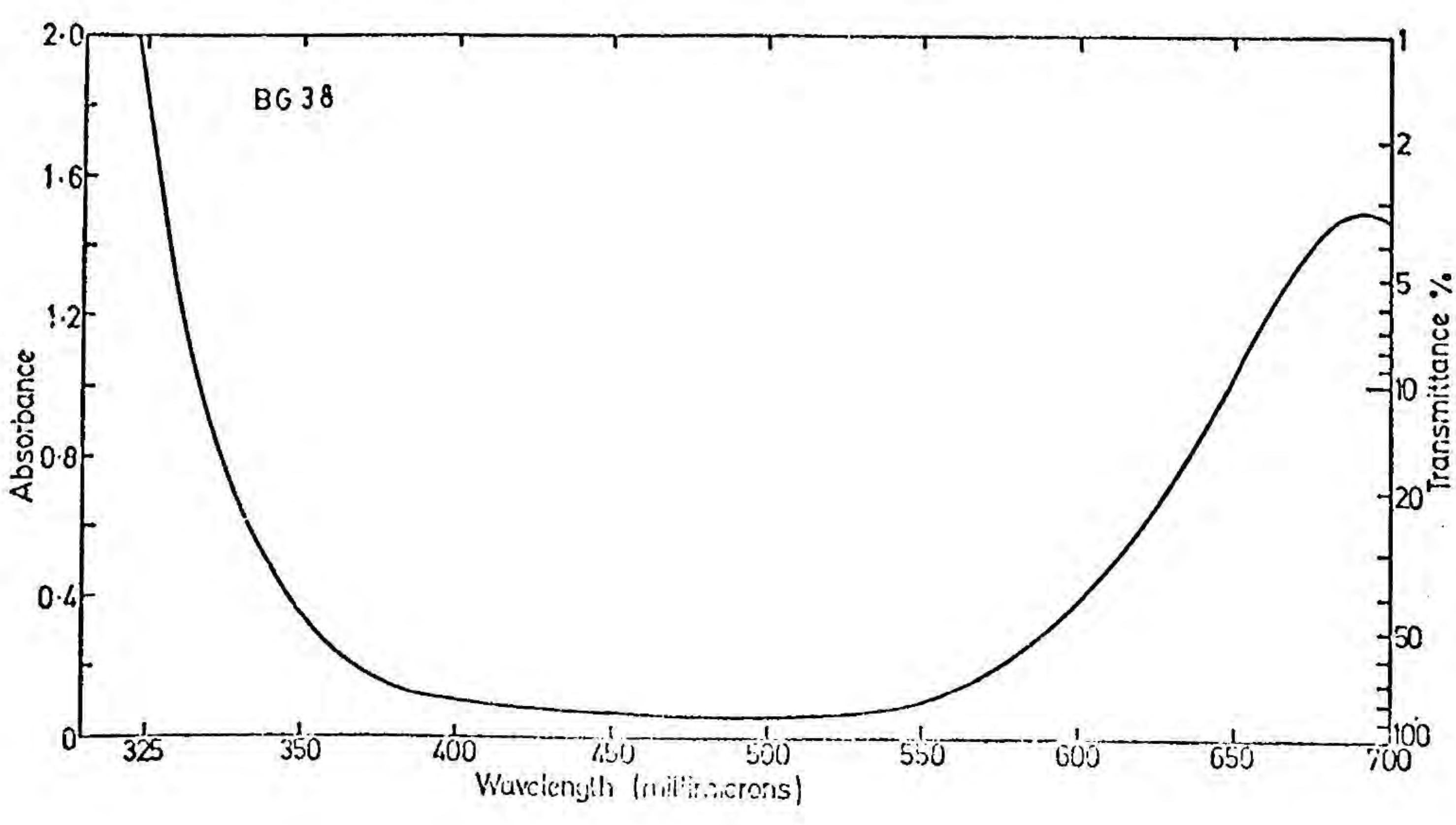
2·0
1·6
1·2
0·8
0·4
0
Absorbance
BG 38
325
350
400
450
500
550
600
650
700
1
2
5
10
20
50
100
Transmittance %

(d)

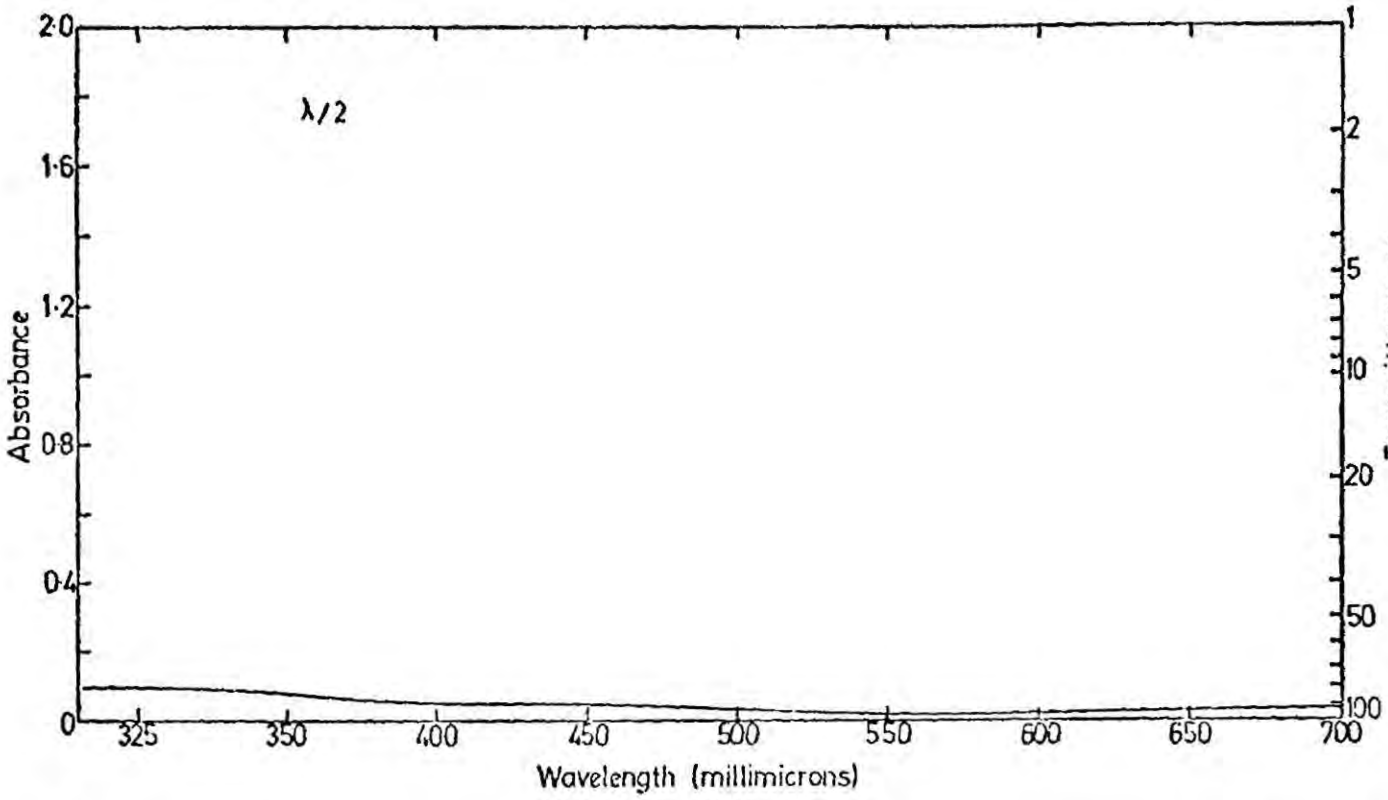

(e)

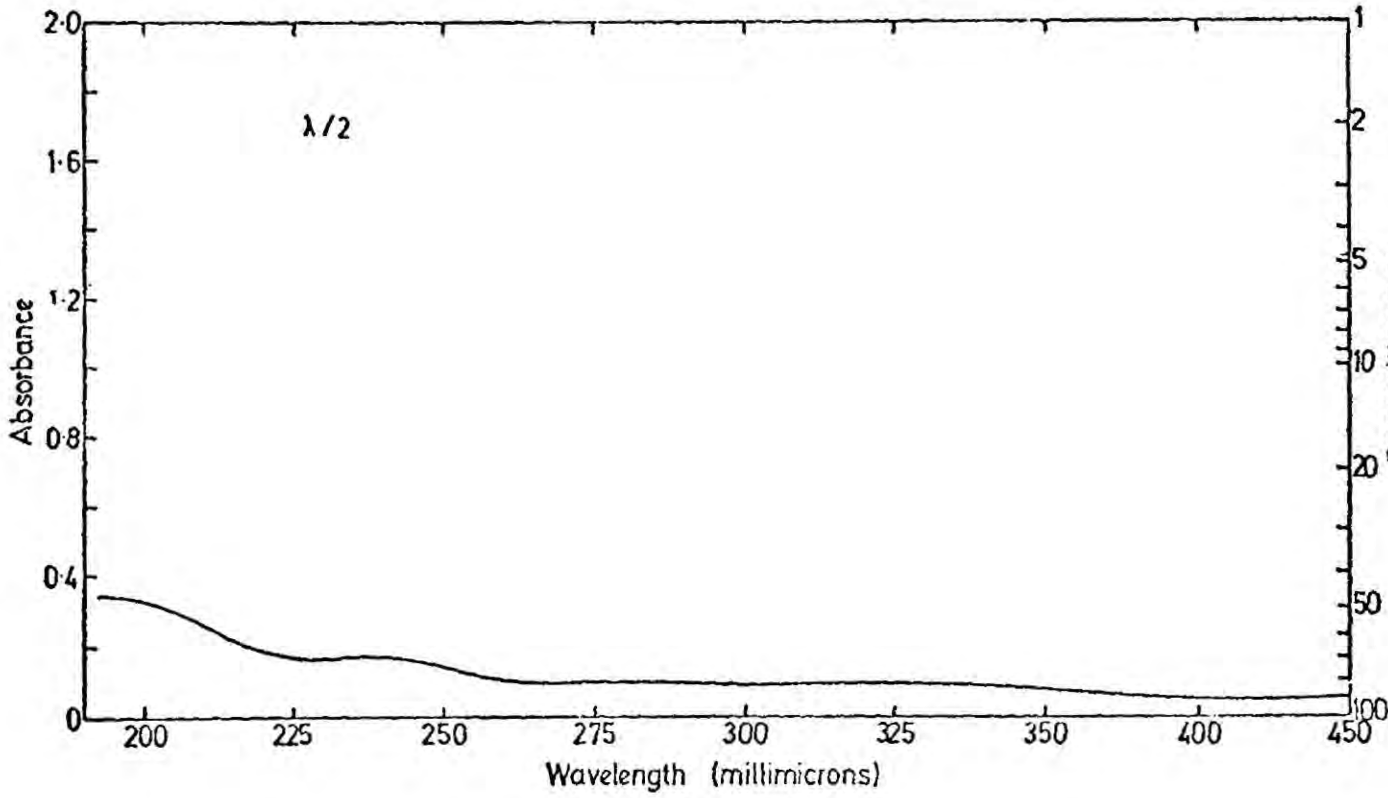

Figure 5.1 *The transmission of the optical components of the polarimeter*

(a) The lenses

(b) The BG 12 filter

(c) The BG 38 filter

(d) and (e) The chromatic λ/2 plate

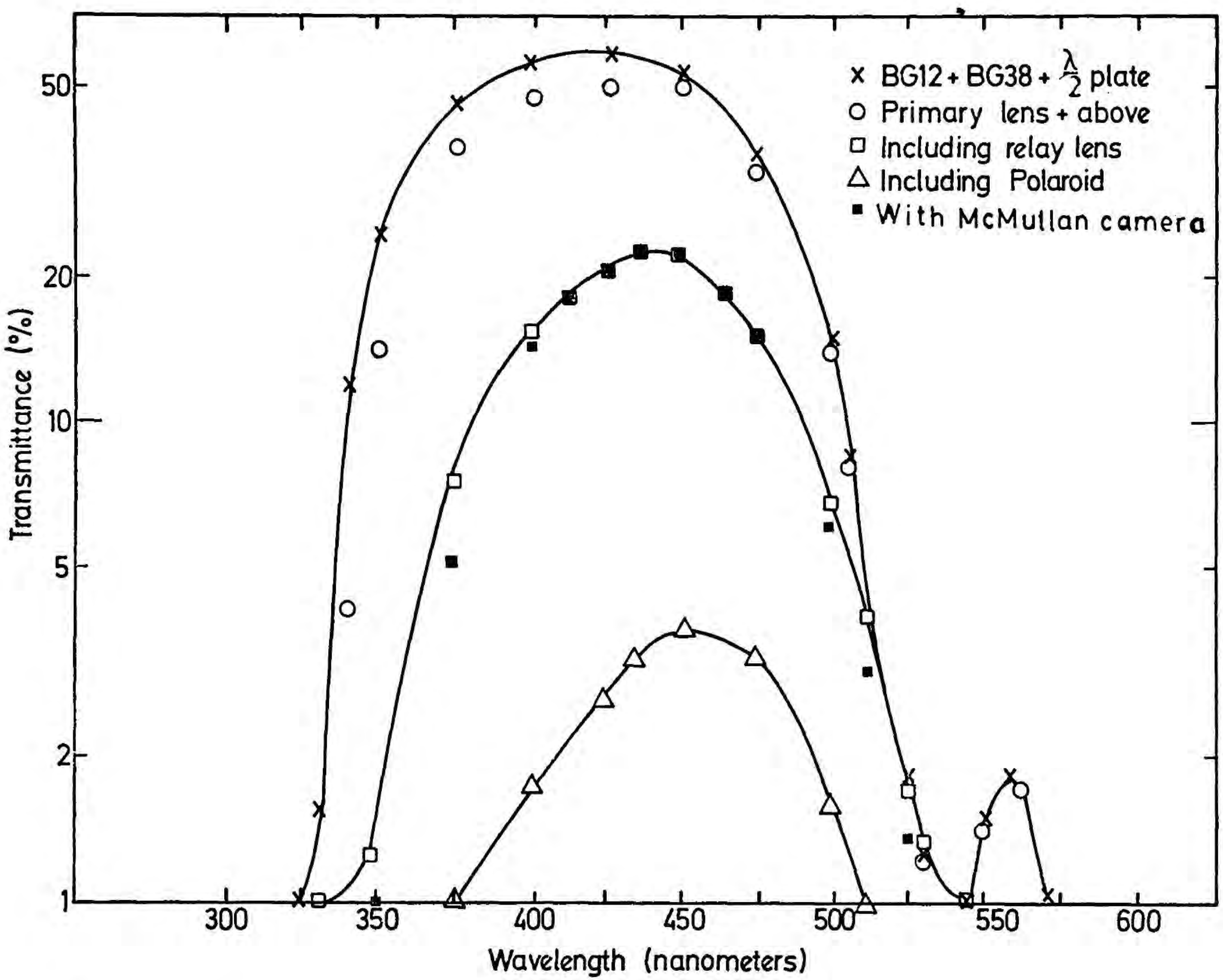

Figure 5.2 *The polarimeter transmission characteristics*

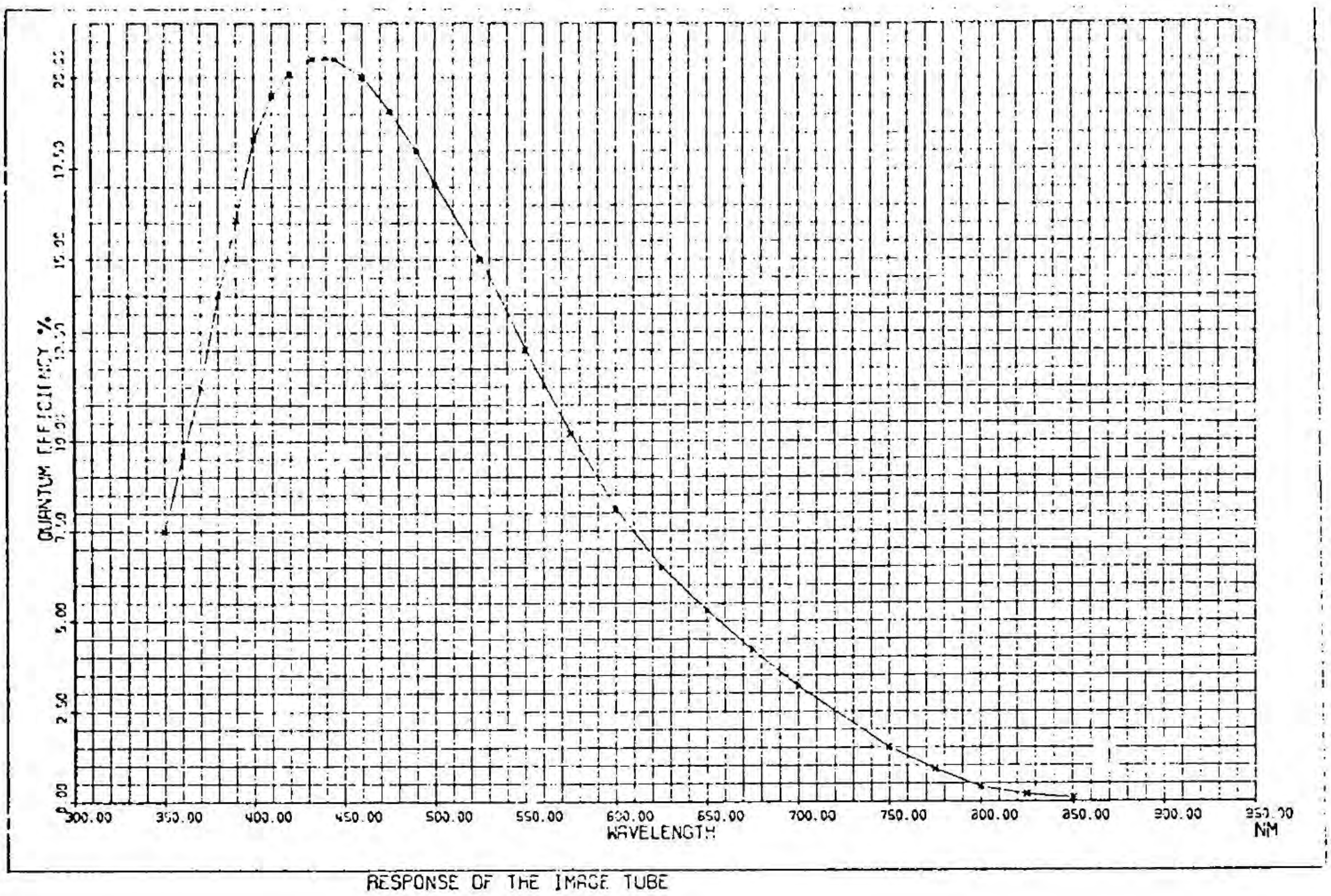

Figure 5.3 *Spectral variation of the McMullan Camera quantum efficiency (McMullan 1975)*

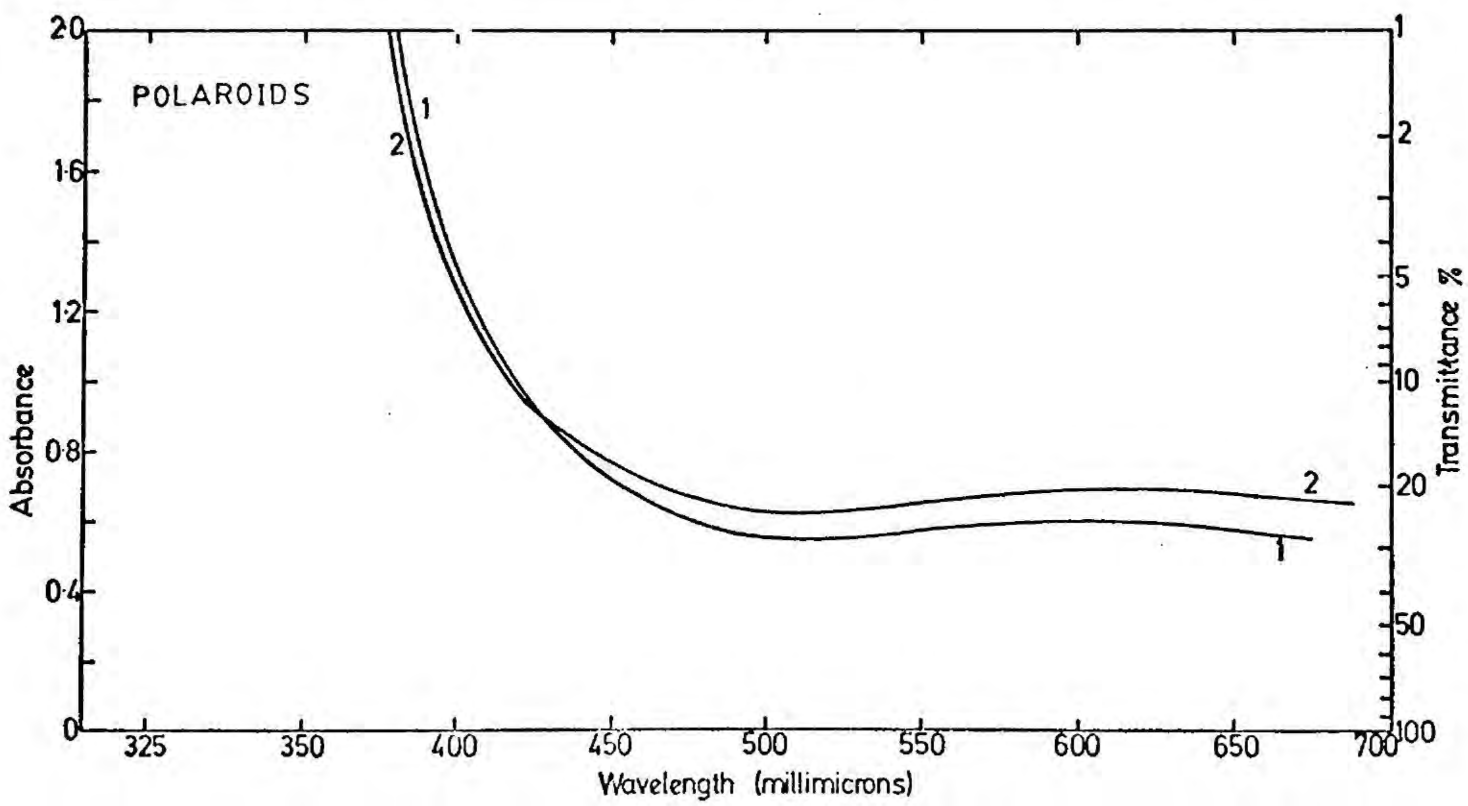

Figure 5.4 *Transmission of the polaroids*

corrections empirically.

5.1.2 The angular divergence and polarizing efficiency of the Wollaston prism.

The angular divergences of the O and E rays were measured at several wavelengths in the operating range of the polarimeter and both were found to be 0.5 ± 0.05°. A more accurate measurement using a lazer showed that the O and E rays suffered slightly different deviations of 0.492 ± 0.003° and 0.522 ± 0.003° respectively, giving a total divergence of 1.016 ± 0.003° which agrees well with the nominal divergence of 1°. The polarizing efficiency of the Wollaston prism was measured using the experimental configuration of Figure 5.6. The transmission with the polaroids in the crossed position was found to be immeasurably small showing that the light was polarized to greater than 99.9 %.

5.1.3 The Behaviour of the Chromatic λ/2-plate.

The phase-difference δ, introduced between the O and E components of a beam of light by a retarder of thickness d, at a wavelength λ is

$$\delta = \frac{2\pi}{\lambda} d|n_o - n_e| \tag{5.1}$$

where $|n_o - n_e|$ is the modulus of the difference in the refractive indices of the crystal for the O and E components respectively. Obviously for a monochromatic light source such a retarder will yield a unique phase difference δ_o, and the wave-plate used in the polarimeter was cleaved so as to be half-wave at 4400 A°. If, however, the incident light comprises of a range of wavelengths each will experience a different retardation, and the observations made with the B-filter will suffer from just this sort of chromatic effect (Figure 5.5).

(a)

(b)

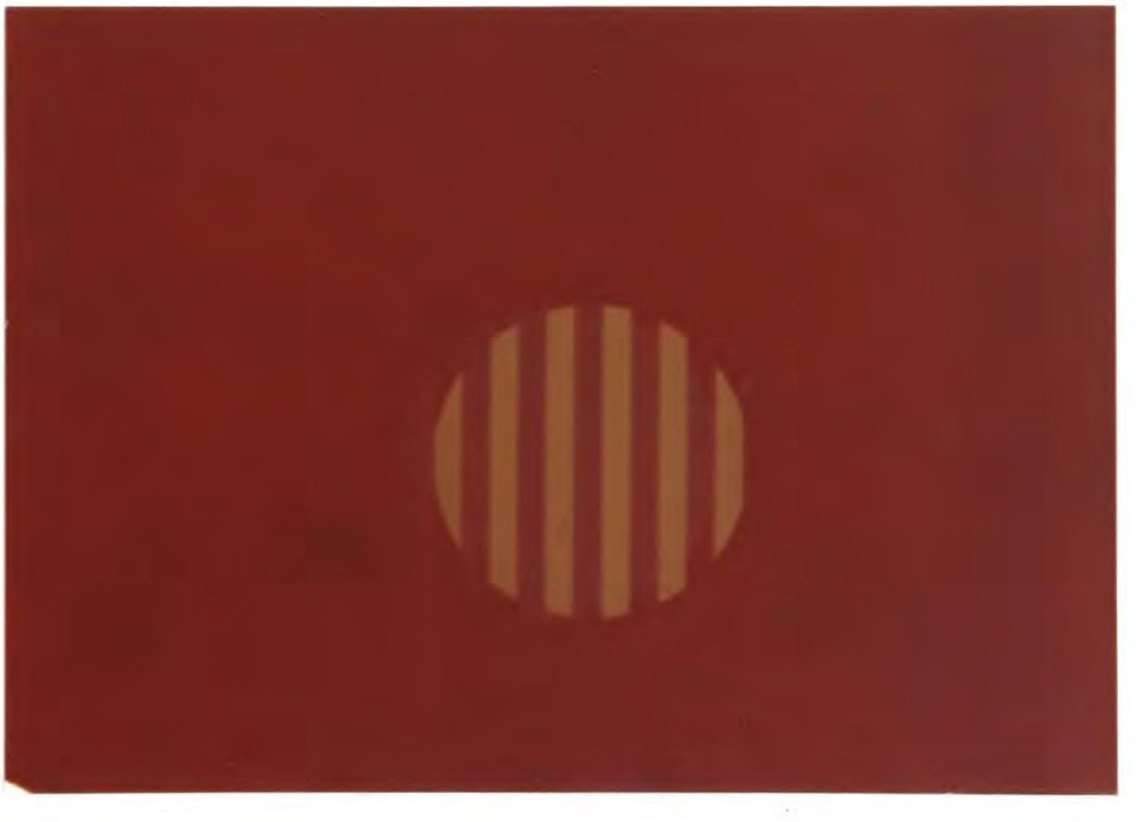

<u>Figure 5.5</u> *Chromatic effects with the $\lambda/2$ plate*

(a) $\lambda/2$-plate orientation 0^{o}, polaroid 0^{o}

(b) $\lambda/2$-plate orientation $22\frac{1}{2}^{o}$, polaroid 0^{o}

(c) $\lambda/2$-plate orientation 45^{o}, polaroid 0^{o}

(d) $\lambda/2$-plate orientation $67\frac{1}{2}^{o}$, polaroid 0^{o}

(c)

(d)

Figure 5.5 (continued)

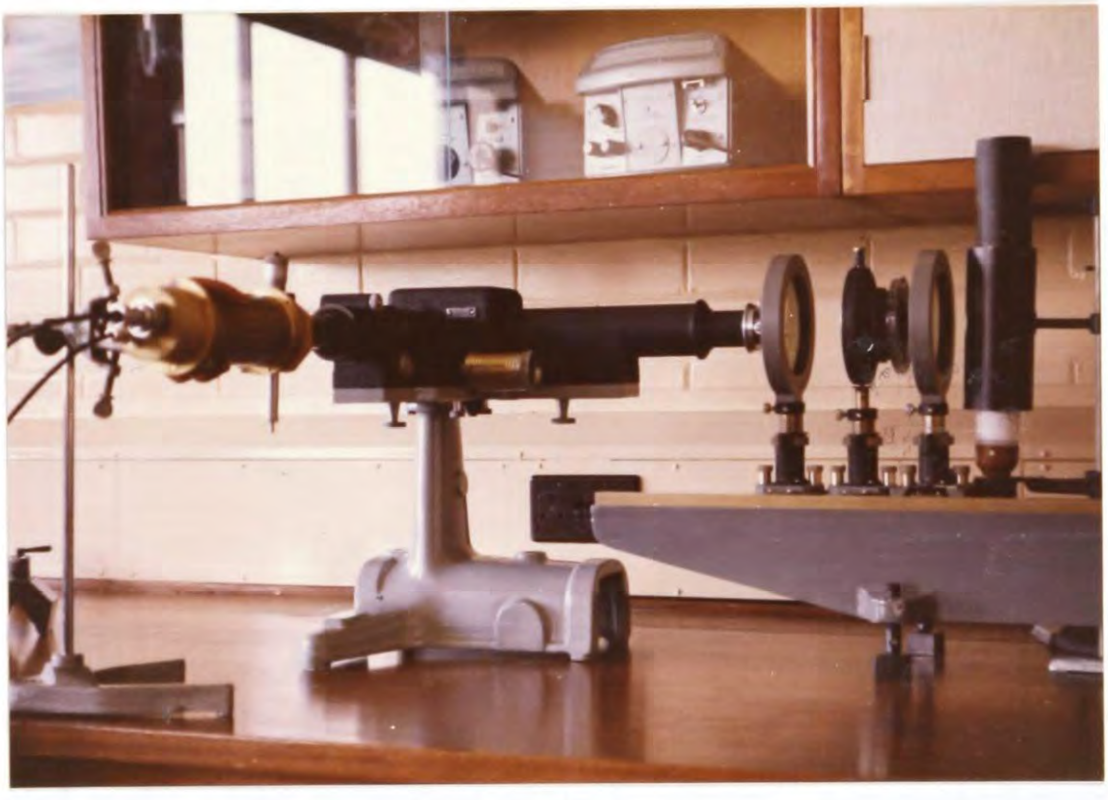

Figure 5.6 The Experimental configuration used to measure $\delta(\lambda)$

As a consequence the incident light will be depolarized by the $\lambda/2$-plate; the linearly polarized light is converted into elliptically polarized light of decreasing ellipticity as the wavelength of the light moves away from 4400 A°. In practice the problem is made more acute because the absolute phase-difference introduced by a retarder is seldom δ_o, but some multiple of it, such that the relative phase-difference between the two components is δ_o (this enables a thicker plate to be cleaved). Clearly as the plate thickness is increased so the variation of δ with wavelength becomes more rapid.

Large errors will be inherent in our polarization measurements as we have assumed that we have an achromatic $\lambda/2$-plate. The measurement of the true wavelength variation of δ, and the calculation and application of corrections for this effect is therefore of considerably importance.

The Measurement of the Spectral Variation of δ.

The experimental configuration shown in Figure 5.6 was used to determine the phase-difference introduced by the $\lambda/2$-plate at several wavelengths. A rotatable polaroid provides a linearly polarized beam, at a known azimuthal angle, which is incident on the $\lambda/2$-plate. A second rotatable polaroid situated behind the $\lambda/2$-plate acts as an analyzer. The light then enters a constant-dispersion spectrometer, whose eye-piece has been replaced by a slit, thus forming a monochromater, enabling individual spectral lines to be isolated. A photomultiplier tube, with an orthogonally mounted cathode, connected to a laboratory photometer measures the intensity of the light leaving the exit slit of the monochromater. By using several different discharge lamps a whole series of lines are made available for the determination of δ. With the $\lambda/2$-plate removed the photometer was calibrated in units of intensity using the law of the Malus. Plots of the photometer reading against $\cos^2 \theta$, where θ is the angle between the axes of the two polaroids, proved to be linear (Figure 5.7). In order to ensure that the photomultiplier tube output did not depend on the azimuthal angle of the incident polarized light the measurements were repeated with the analyzer at different angles. Such an effect, if present, was undetectable. To produce an unpolarized light source we introduced a sheet of greaseproof paper, pressed between glass plates, between the lamp and the polarizer. The greaseproof paper screen operates by transillumination and reduces a 100% polarized beam to an emergent beam with only 0.5 - 1% polarization. Since ordinary discharge lamps only exhibit polarizations $\sim$ 0.5%. (Worthing 1926, Billings 1951) the emergent beam will be unpolarized to an accuracy of 0.005%. Uniform illumination was produced by using a sheet of pearl-white perspex as a diffuser.

The fast axis of the $\lambda/2$-plate was determined by inserting it between crossed polaroids and rotating it in the azimuthal direction until perfect extinction of the Hgλ 4358 line was observed without the need to rotate the analyzer. The $\lambda/2$-plate was then rotated by 180° in the polar direction and the analyzer angle altered until extinction was again obtained. The difference between the two analyzer settings gives twice the setting error of the fast axis, which can then be adjusted and the measurements repeated until the 180° polar rotation does not necessitate a realignment of the analyzer.

The fast axis of the $\lambda/2$-plate was then orientated at angles of $\pm 22\frac{1}{2}°$, $\pm 45°$, $\pm 67\frac{1}{2}°$, $\pm 40°$ relative to the polarizers preferred direction (negative angles measured clockwise), and for each position the maximum intensity I_{max}, and the position angle θ of the analyzer at which it occurred, together with the minimum intensity were recorded, at which orientations the

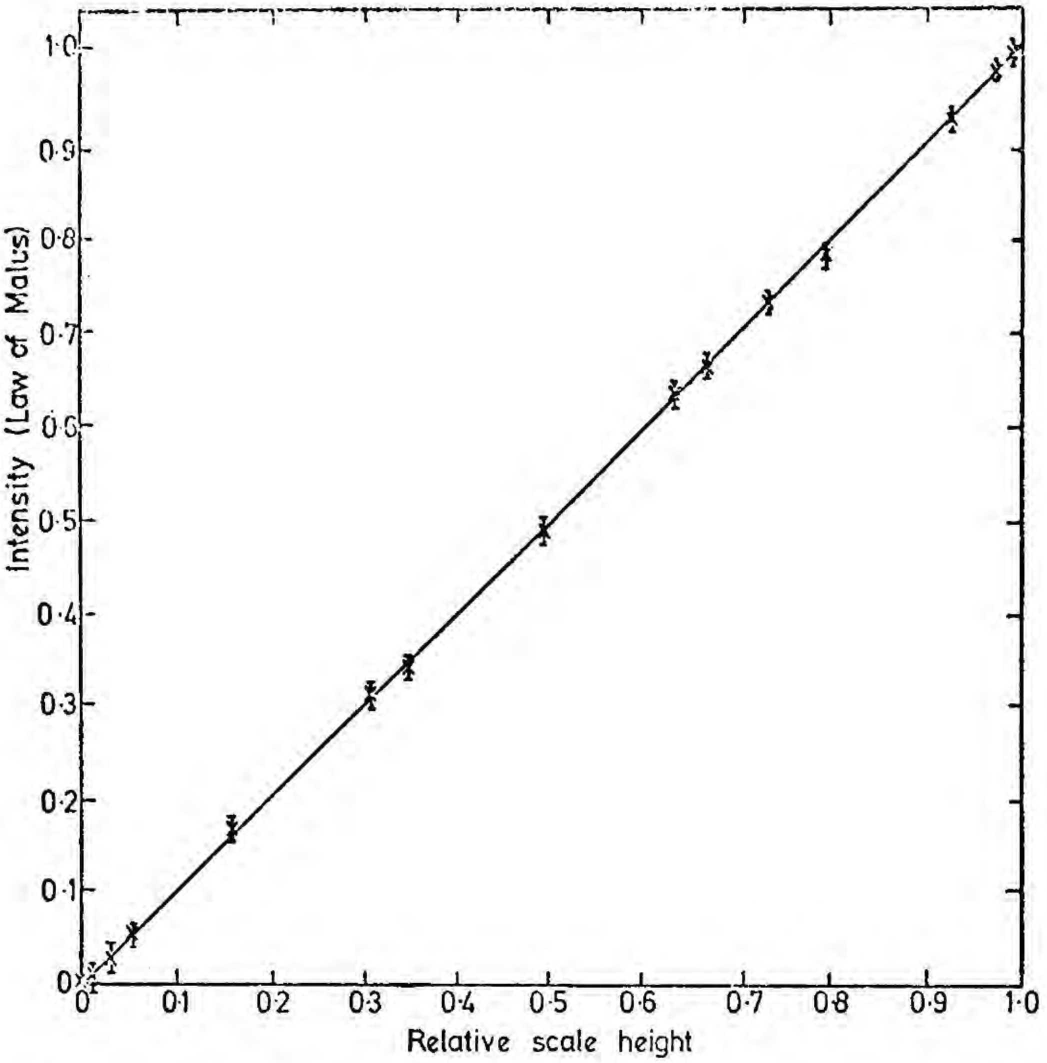

Figure 5.7 Calibration of the laboratory photometer intensity scale

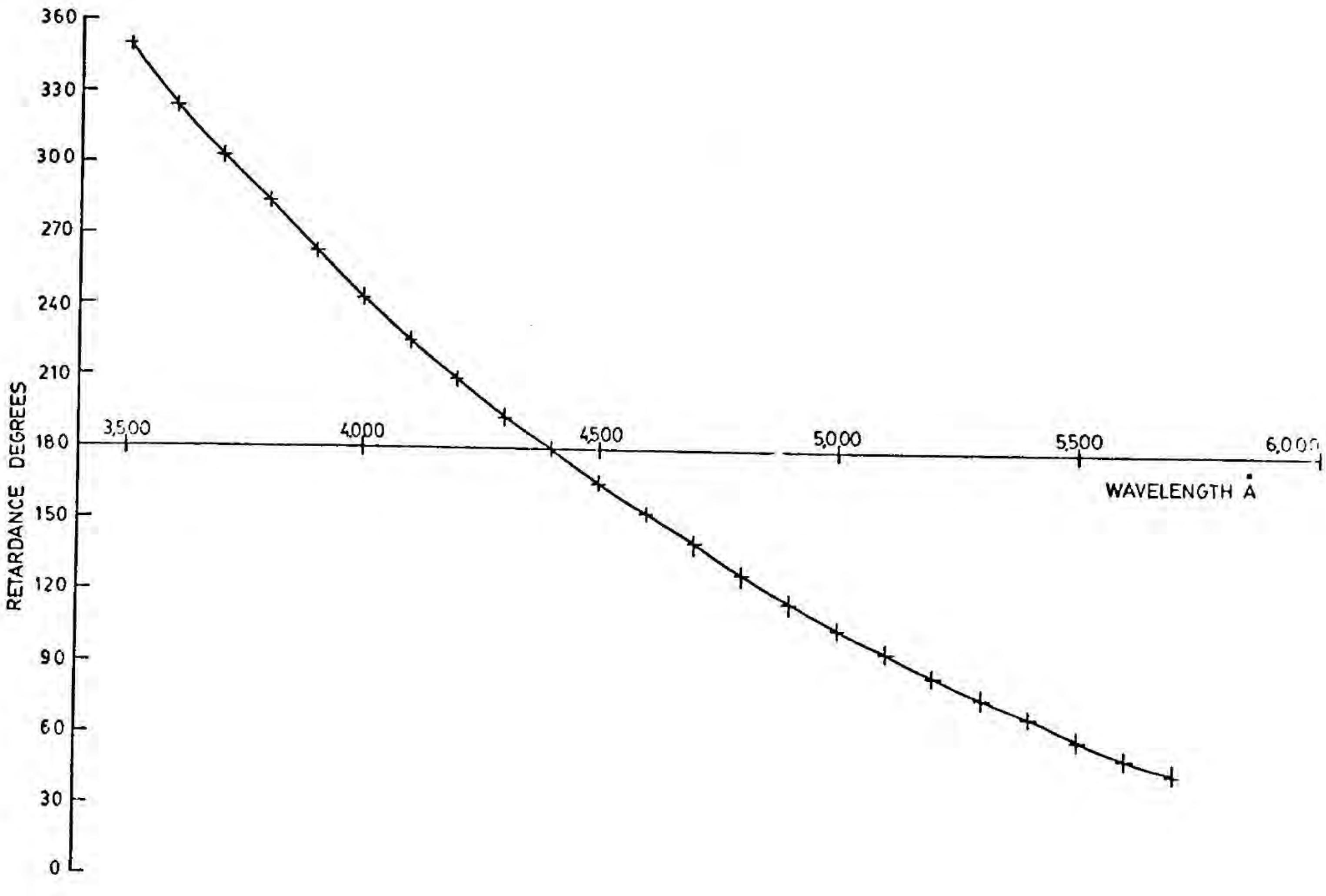

Figure 5.8 Wavelength variation of the retardance of a wave-plate of thickness 7.00355 × 10^5Å

analyzer preferred direction is parallel to the major and minor axes of the outgoing elliptically polarized light respectively.

The azimuthal angle of the ellipse major axes, ϕ is related to the angle of the incoming light, θ, relative to the plate-fast axis, and the phase-difference δ of the plate by (Appendix I)

$$\tan 2\phi = \tan 2\theta \cos \delta \tag{5.2}$$

Inspection of equation 5.2 shows that when $\theta = 45°$, ϕ will always be $\pm 45°$ unless $\delta = \pm \pi/2$ whence it is indeterminate (i.e. a $\lambda/4$-plate producing circularly polarized light). The ratio of I_{min} to I_{max} is given by (Appendix I)

$$\frac{I_{min}(\lambda)}{I_{max}(\lambda)} = \frac{\epsilon - \cos \delta(\lambda)}{\epsilon + \cos \delta(\lambda)} \tag{5.3}$$

where $\epsilon = \sin 2\phi / \sin 2\theta$, and in particular when $\theta = 45°$ and $\phi = 45°$ equation 5.3 reduces to

$$\frac{I_{min}(\lambda)}{I_{max}(\lambda)} = \frac{1 - \cos \delta(\lambda)}{1 + \cos \delta(\lambda)} \tag{5.4}$$

Thus $\delta(\lambda)$ can be determined directly from the measurements of I_{max} and I_{min} when the $\lambda/2$-plate is orientated at $\pm 45°$. The phase-differences determined in this manner were compared with those calculated from equation 5.1 for increasing thickness nd of the plate where nd is an odd multiple of $\lambda_o/2 = 2.3345 \times 10^5$ A°. Good agreement between the observed and calculated spectral variation of $\delta(\lambda)$ was obtained only when

$$nd = 3\lambda_o/2 = 7.0035 \times 10^5 \text{ A°}$$

A comparison between the experimental and theoretical values of $\delta(\lambda)$ is given in table 5.1 and the wavelength variation of δ for the adopted plate

TABLE 5.1

Variation of the $\lambda/2$-plate phase difference with wavelength

Wavelength A°	Observed $\delta°$	Theoretical $\delta°$
4077	236 ± 5	229.3
4358	194.7 ± 5	186.3
4678	152 ± 5	143.6
4800	130 ± 5	129.4
4916	122.0 ± 5	116.6
5085	105 ± 5	98.7
5460	92.0 ± 5	63.2
5790	65 ± 5	37.1
5892	43 ± 5	29.8

thickness of $3\lambda_0/2$, as calculated from equation 5.1, is shown in Figure 5.8. The large discrepancies for the wavelengths $\lambda5460$, $\lambda5790$ arise because of the difficulty in measuring I_{max}, I_{min} and ϕ for a nearly circularly polarized beam. As we suggested previously the observed deviations of $\delta(\lambda)$ from π are large, but fortunately, as we will see shortly, the contribution of each $\delta(\lambda)$ decreases as we move away from the central wavelength because of the polarimeter transmission characteristics. The ratio of I_{min}/I_{max} for other plate orientations was also calculated using equations 5.2 and 5.3 and compared with the measured ratio. Agreement to within $\pm$ 10% was obtained except when the light was nearly circularly polarized when large discrepancies were again evident.

Using these data and the transmission curves of section 5.1 we are now able to calculate corrections for the behaviour of the $\lambda/2$-plate. Since we know that δ_o should be π at 4400 A° we will adopt the theoretical retardance of Figure 5.8 as true values for the $\lambda/2$-plate, rather than the experimental values, in the correction calculations.

The Use of the Mueller Algebra to Calculate the Corrections for the Chromatic Behaviour of the $\lambda/2$-plate

Our aim in this section is to calculate the true Stoke's parameters $\{I, Q, U, V\}$ of the light from M82 given the measured Stoke's parameters $\{I_M, Q_M, U_M, V_M\}$ which are distorted by their passage through the chromatic half-wave plate. In order to solve the problem we will in fact consider the inverse situation, and calculate the effect of the $\lambda/2$-plate on an arbitrarily polarized beam $\{I, Q, U, V\}$. We may express this problem in mathematical terms by

$$[S_e] = [M_c] \cdot [S_i] \qquad (5.4)$$

where $[S_e]$ is $\{I', Q', U', V'\}$, the Stoke's vector of the emergent light, $[S_i]$ is $\{I, Q, U, V\}$, the Stoke's vector of the incoming light, and $[M_c]$ is the Mueller matrix that represents the retarder. The important properties of the Stoke's vectors that led to the concept of the Mueller algebra have already been introduced in Chapter 1; each of the Mueller matrices is a 4 x 4 matrix, which describes the orientation of the device and its action on the incoming light, and the normal rules of matrix algebra govern their use. For a more detailed discussion of the Mueller algebra the reader is referred to Shurcliff (1964). Writing the equation 5.4 in its explicit form we have

$$\begin{bmatrix} I' \\ Q' \\ U' \\ V' \end{bmatrix} = \begin{bmatrix} m_{11} & m_{12} & m_{13} & m_{14} \\ m_{21} & m_{22} & m_{23} & m_{24} \\ m_{31} & m_{32} & m_{33} & m_{34} \\ m_{41} & m_{42} & m_{43} & m_{44} \end{bmatrix} \cdot \begin{bmatrix} I \\ Q \\ U \\ V \end{bmatrix} \tag{5.5}$$

and applying the laws of matrix multiplication we obtain

$$\begin{bmatrix} I' \\ Q' \\ U' \\ V' \end{bmatrix} = \begin{bmatrix} m_{11}I + m_{12}Q + m_{13}U + m_{14}V \\ m_{21}I + m_{22}Q + m_{23}U + m_{24}V \\ m_{31}I + m_{32}Q + m_{33}U + m_{34}V \\ m_{41}I + m_{42}Q + m_{43}U + m_{44}V \end{bmatrix} \tag{5.6}$$

The existence of a linear transformation between the incident and emergent Stoke's parameters simplifies the problem to the determination of the individual elements m_{ij} of $[M_c]$. In our case each m_{ij} will be wavelength dependent which complicates matters, but fortunately as we will see most of them are in fact zero. In order to solve the problem we make the following simplifying assumptions:

(i) The half-wave plate is an ideal homogeneous linear retarder

(ii) Dispersion does not occur during the passage of the light through the $\lambda/2$-plate.

(iii) Absorption and scattering in the $\lambda/2$-plate are negligible.

(iv) Since we are interested in determining corrections for Q' and U' only, and because the Nebula polarimeter does not measure V, we set $V' = V = O$ (V' and V are in any case small and at the very worst this assumption will only introduce second order errors).

(v) Further to assumption (iv) as we do not have any information on the wavelength variation of the polarization of the light across the pass-band of the polarimeter we will assume that all incident wavelengths are identically partially lineary polarized.

(vi) The power distribution with wavelength of the incoming light, which determines the contribution of the polarization at each wavelength to the measured polarization, is given by the transmission function of the polarimeter (section 5.1). (To be completely rigorous, we should also consider the spectrum of the incoming light but this is not known for the galaxy).

The Mueller matrix of an ideal homogeneous retarder, with retardance δ, whose fast axis is at an arbitrary orientation θ is given by Shurcliff (1964a), (the lengthy derivation of this result is given by Gerrard and Birch 1975)

$$[M_c] = \begin{bmatrix} 1 & 0 & 0 & 0 \\ 0 & D^2-E^2+G^2 & 2DE & -2EG \\ 0 & 2DE & -D^2+E^2+G^2 & 2DG \\ 0 & 2EG & -2DG & G^2-1 \end{bmatrix} \quad (5.7)$$

where
$$D = Q_c \sin \tfrac{1}{2}\delta$$
$$E = U_c \sin \tfrac{1}{2}\delta$$
$$G = \cos \tfrac{1}{2}\delta$$

and Q_c and U_c are the second and third Stoke's parameters of the normalized fast eigenvector of the retarder. The eigenvector is that form of polarized light which is conserved during the passage through the retarder, in this case, linearly polarized light at an arbitrary orientation. The required values of the parameters (Shurcliff 1964b) are

$$\begin{aligned} Q_C &= \cos 2\theta \\ U_C &= \sin 2\theta \end{aligned} \qquad (5.8)$$

whence $[M_c]$ becomes

$$\begin{bmatrix} 1 & 0 & 0 & 0 \\ 0 & \cos 4\theta \sin^2 \tfrac{1}{2}\delta + \cos^2 \tfrac{1}{2}\delta & \sin^2 \tfrac{1}{2}\delta \sin 4\theta & \sin\delta \sin 2\theta \\ 0 & \sin 4\theta \sin^2 \tfrac{1}{2}\delta & \cos^2 \tfrac{1}{2}\delta - \sin^2 \tfrac{1}{2}\delta \cos 4\theta & \sin\delta \cos 2\theta \\ 0 & \sin\delta \sin 2\theta & -\sin\delta \cos 2\theta & \cos\delta \end{bmatrix} \qquad (5.9)$$

The retardance of the chromatic $\lambda/2$-plate is wavelength dependent and so a different solution to equation 5.5 will be obtained at each wavelength. Since $V' = V = O$, the solutions of equations 5.5 for any wavelength λ are

$$\begin{aligned} I_\lambda' &= I_\lambda \\ Q_\lambda' &= \tfrac{1}{2}[Q\{\cos 4\theta(1-\cos\delta_\lambda) + (1+\cos\delta_\lambda)\} + \\ &\quad U\{\sin 4\theta\,(1-\cos\delta_\lambda)\}] \\ U_\lambda' &= \tfrac{1}{2}[Q\{\sin 4\theta(1-\cos\delta_\lambda)\} + U\{(1+\cos\delta_\lambda) - \\ &\quad \cos 4\theta(1-\cos\delta_\lambda)\}] \end{aligned} \qquad (5.10)$$

where λ subscripts have been introduced to denote wavelength dependent quantities. The relative contribution of the intensity of any wavelength, ω_λ, to the total intensity transmitted by polarimeter, is given by

$$\omega_\lambda = \frac{t_\lambda}{T} = \frac{t_\lambda}{\int t_\lambda \, d\lambda} \qquad (5.11)$$

where t_λ is the measured transmission of the polarimeter at the wavelength λ and T is the total power transmitted by the polarimeter.

Utilizing the additivity of the Stoke's parameters.the total emergent Stoke's parameters I', Q' and V' are given by the integrals over wavelength of I'_λ, Q'_λ and U'_λ

$$I' = I$$

$$Q' = \tfrac{1}{2} Q \int \omega_\lambda . \{\cos 4\theta(1-\cos\delta_\lambda) + (1-\cos\delta_\lambda)\} d\lambda + \tfrac{1}{2} U \int \omega_\lambda . \{\sin 4\theta(1-\cos\delta_\lambda)\} d\lambda$$

$$(5.12)$$

$$U' = \tfrac{1}{2} Q \int \omega_\lambda . \{\sin 4\theta(1-\cos\delta_\lambda)\} d\lambda + \tfrac{1}{2} U \int \omega_\lambda . \{(1+\cos\delta_\lambda) - \cos 4\theta(1-\cos\delta_\lambda)\} d\lambda$$

where the integrals are taken over the band pass of the polarimeter. In practice we only sample the transmission function and the retardance at a discrete number of wavelengths and we therefore replace the integrations by summations. Hence equation 5.12 becomes

$$I' = I$$

$$Q' = \tfrac{1}{2} Q \sum_\lambda \omega_\lambda . \{\cos 4\theta(1-\cos\delta_\lambda) + (1+\cos\delta_\lambda)\} + \tfrac{1}{2} U \sum_\lambda \omega_\lambda . \sin 4\theta(1-\cos\delta_\lambda)\}$$

$$U' = \tfrac{1}{2} Q \sum_\lambda \omega_\lambda . \{\sin 4\theta(1-\cos\delta_\lambda)\} + \tfrac{1}{2} U \sum_\lambda w_\lambda . \{(1+\cos\delta_\lambda) - \cos 4\theta(1-\cos\delta_\lambda)\}$$

$$(5.13)$$

The required relationship between $\{I_M, Q_M, U_M, O\}$ and $\{I, Q, U, O\}$ is obtained by considering the effect of the Wollaston prism on $\{I', Q', U', O\}$ The prism preferred axes are fixed at position angles of 0° and 90° respectively and so we in fact only measure the Stoke's parameters I' and Q' of equations 5.13 giving the results

$$I_M = I$$

$$\begin{Bmatrix} Q_M \\ U_M \end{Bmatrix}_\theta = \tfrac{1}{2} Q_\lambda \sum_\lambda \omega_\lambda . \{\cos 4\theta (1-\cos\delta_\lambda) + (1+\cos\delta_\lambda)\} + \tfrac{1}{2} U \sum_\lambda \omega_\lambda . \{\sin 4\theta (1-\cos\delta_\lambda)\}$$

(5.14)

where it follows from Chapter 3.3 that Q_M is measured when $\theta = 0^\circ$ or 45° and U_M is measured when $\theta = 22\tfrac{1}{2}^\circ$ or $67\tfrac{1}{2}^\circ$. Evaluating equation 5.14 for each orientation of the $\lambda/2$-plate and using the notation of Chapter 3.3 we obtain the working equations

$$
\begin{aligned}
& I_M = I \\
\theta = 0^\circ \quad & Q_{M1} = Q \\
\theta = 22\tfrac{1}{2} \quad & U_{M1} = \tfrac{1}{2} Q \sum_\lambda \omega_\lambda . (1+\cos\delta_\lambda) + \tfrac{1}{2} U \sum_\lambda \omega_\lambda . (1-\cos\delta_\lambda) \qquad (5.15) \\
\theta = 45^\circ \quad & Q_{M2} = - Q \sum_\lambda \omega_\lambda . \cos\delta_\lambda \\
\theta = 67\tfrac{1}{2} \quad & U_{M2} = \tfrac{1}{2} U \sum_\lambda \omega_\lambda . (1-\cos\delta_\lambda) - \tfrac{1}{2} Q \sum_\lambda \omega_\lambda . (1+\cos\delta_\lambda)
\end{aligned}
$$

where the signs of Q_2 and U_2 have been changed so as to be consistent with the convention used in Chapter 3.3. Using the transmission and retardance data of Figures 5.2 and 5.8 we evaluated ω_λ and δ_λ at 22-points, separated by 10A° intervals, covering the band pass of the polarimeter, and thus calculated the summation terms of equations 5.15.

For an achromatic $\lambda/2$-plate $\delta_\lambda = 180^\circ \; \forall \lambda$ and so equations 5.15 reduce to the expected results

$$I_M = I, \quad Q_1 = Q, \quad U_1 = U \ , \quad Q_2 = Q, \quad U_2 = U$$

where we have dropped the M subscripts for the Stoke's parameters Q and U. The solutions of equation 5.15 for the chromatic $\lambda/2$-plate are

$$\begin{aligned} I_M &= I \\ Q_1 &= Q \\ U_1 &= 0.8514\,U + 0.1486Q & \text{(without} \qquad (5.16) \\ Q_2 &= 0.7029\,Q & \text{polaroid)} \\ U_2 &= 0.8514\,U - 0.1486\,Q \end{aligned}$$

When a polaroid is used with the polarimeter for calibration measurements the values of ω_λ are altered and so we obtain a second set of solutions

$$\begin{aligned} I_M &= I \\ Q_1 &= Q \\ U_1 &= 0.878U + 0.122\,Q \qquad (5.17) \\ Q_2 &= 0.756\,Q \\ U_2 &= 0.878\,U - 0.122\,Q \end{aligned}$$

and these are the required correction equations for the depolarization introduced by the $\lambda/2$-plate. Examining these two sets of solutions we see that when the chromatic $\lambda/2$-plate is in the 0° position the true Q value is measured, (as expected), but when the $\lambda/2$-plate is at the 45° position the measured Q is only 70% of the true value. With the inclusion of the polaroid the polarimeter bandpass becomes narrower and so the contributions from the δ_λ which deviate furthest from 180° diminish, thus the degree of depolarization is smaller and 75% of the true Q value is measured at the 45° position. The effect of the chromatic behaviour of the $\lambda/2$-plate is more complex for the measured U_1 and U_2 values as these are not just depolarized measurements of U but also contaminated by a contribution from Q, which has the considerable consequence that the U corrections depend on the measured Q values.

An experimental verification of the correction equations 5.17 was carried out photographically using a sheet polaroid to provide a 100% polarized beam at a known position angle. Each exposure was calibrated by means of a standard density wedge, and, since accurate image registration was not necessary, an analogue analysis method was used. Examples of the density traces obtained for a variety of polaroid/$\lambda/2$-plate orientations are shown in Figures 5.9. The experimental results are compared with the true Stoke's parameters, and those obtained by depolarizing them according to equations 5.17, in table 5.2. Because of the limited accuracy of graphical output the experimental errors range from ± 0.5 to 3.0% depending on the density of the exposure. The agreement between the measured and corrected Stoke's parameters is however very good except for a few measurements made with the $\lambda/2$-plate at the 22½° orientation .

In deriving the equations 5.16 and 5.17 we have not taken into account the f-factors used with the real polarization data, and we must now consider what effect the chromatic $\lambda/2$-plate has on these quantities, as they may also require correcting. Following the theory given in Chapter 3.3, but replacing I_1 to I_8 by the intensities I'_1 to I'_8 that would be measured when the chromatic $\lambda/2$-plate is used (determined from equations 5.16), we find that

(a)

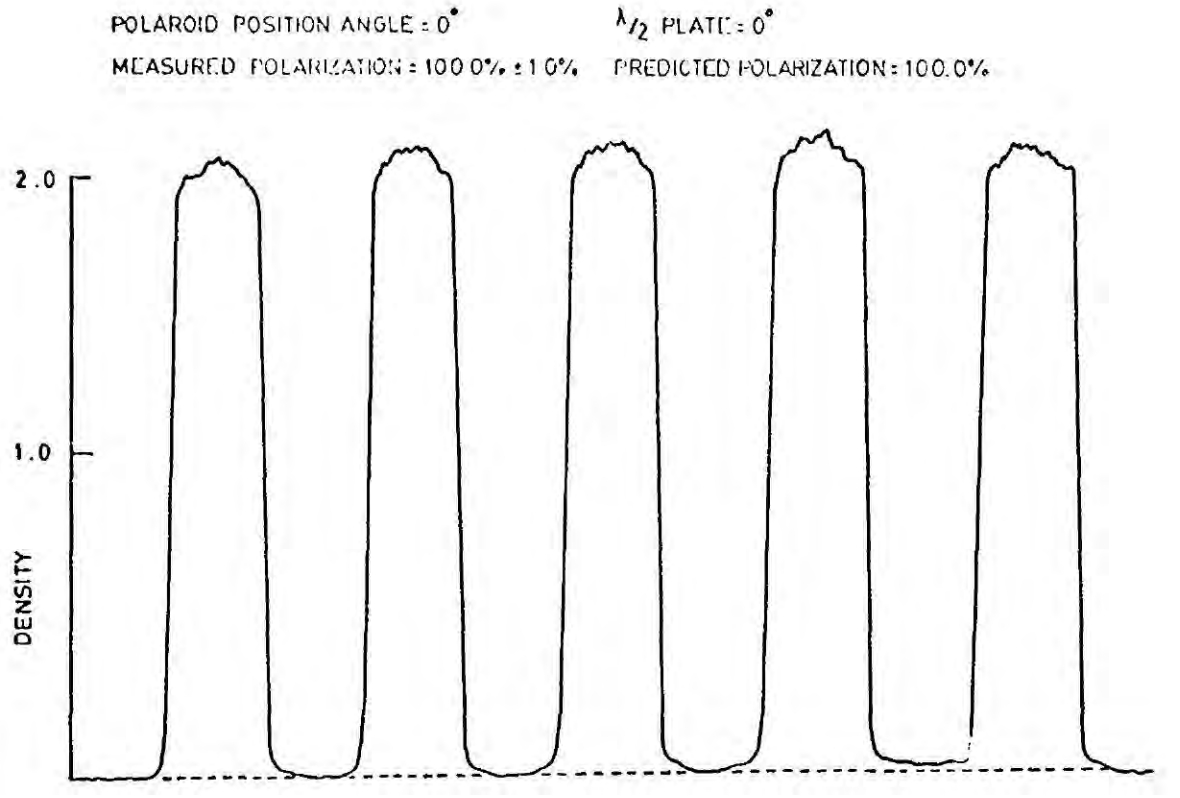

(b)

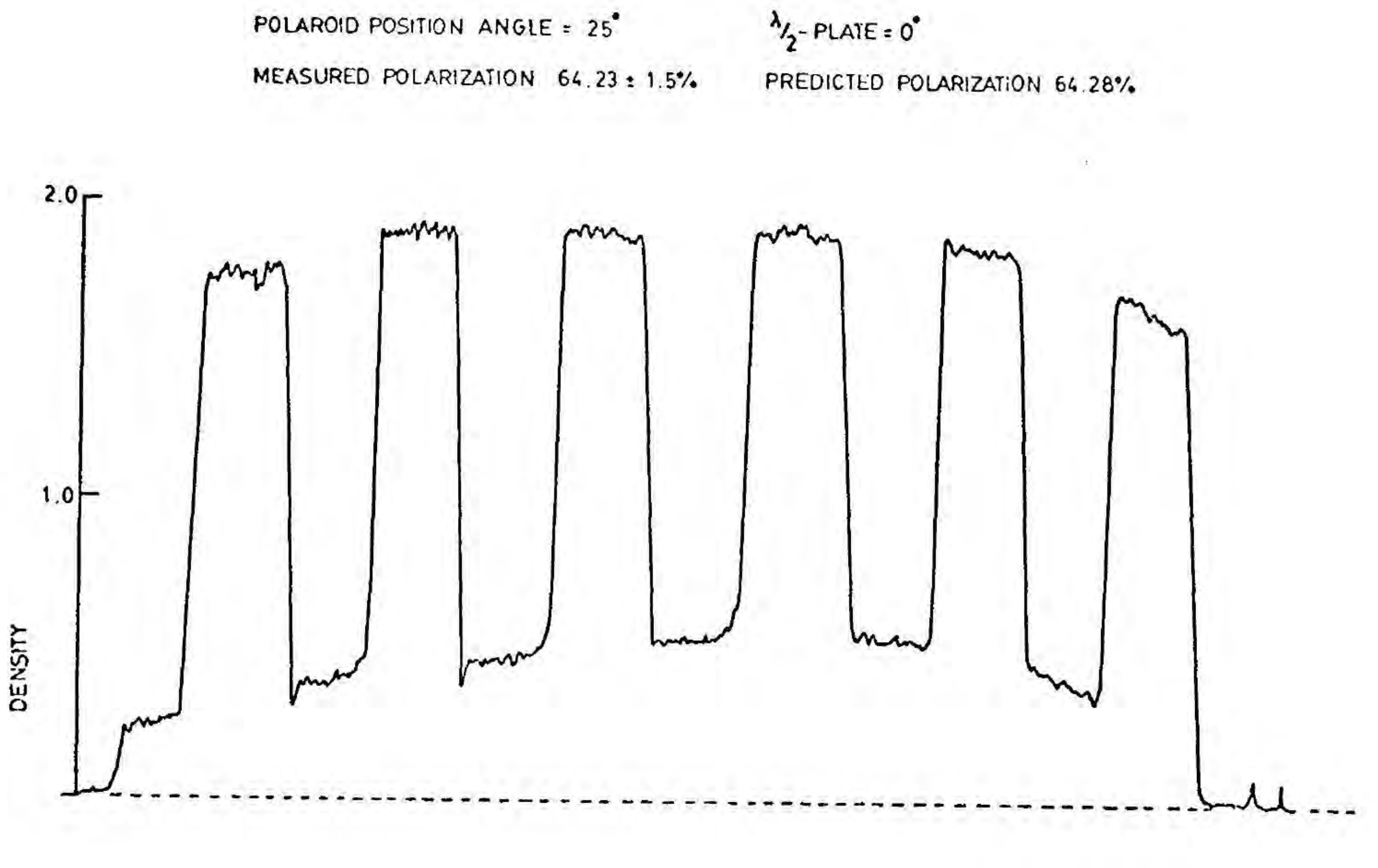

<u>Figure 5.9</u> Density traces from the laboratory polarization measurements

(c)

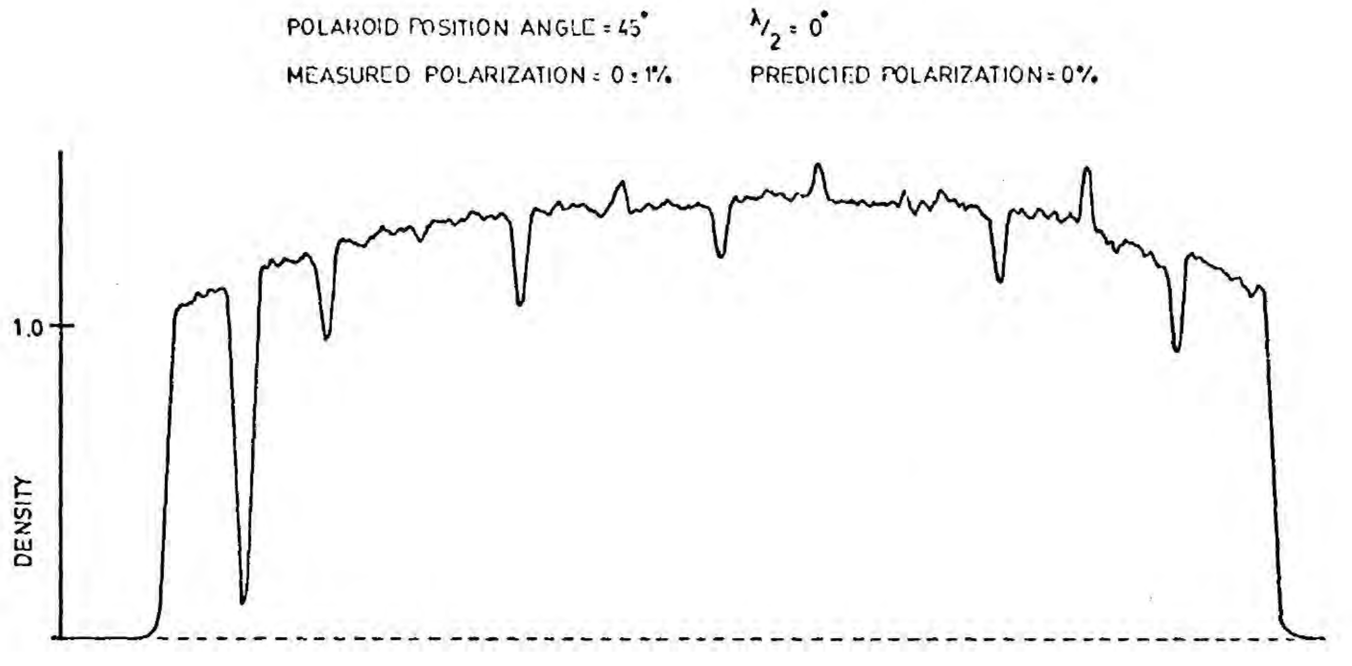

(d)

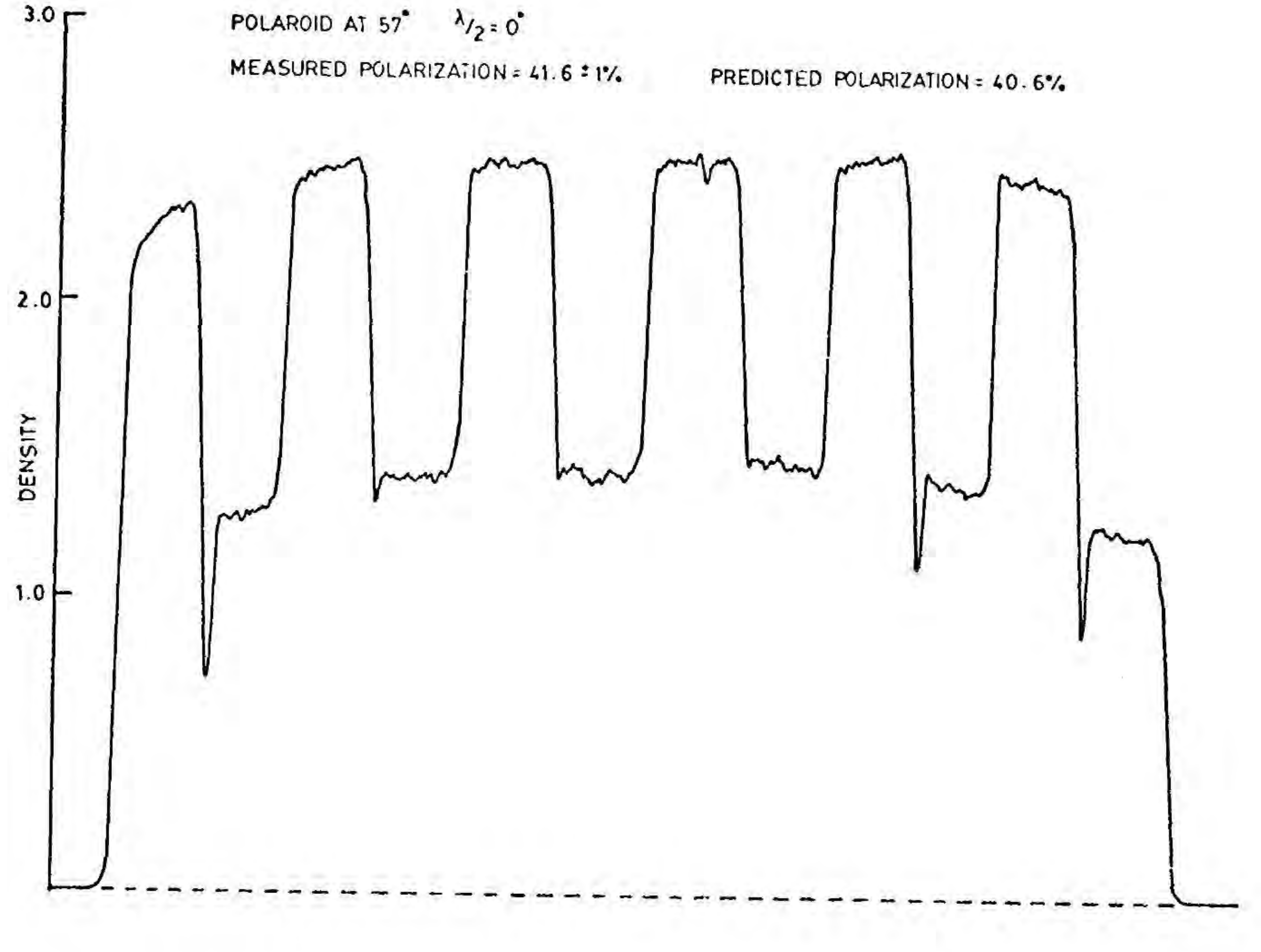

Figure 5.9 continued

(e)

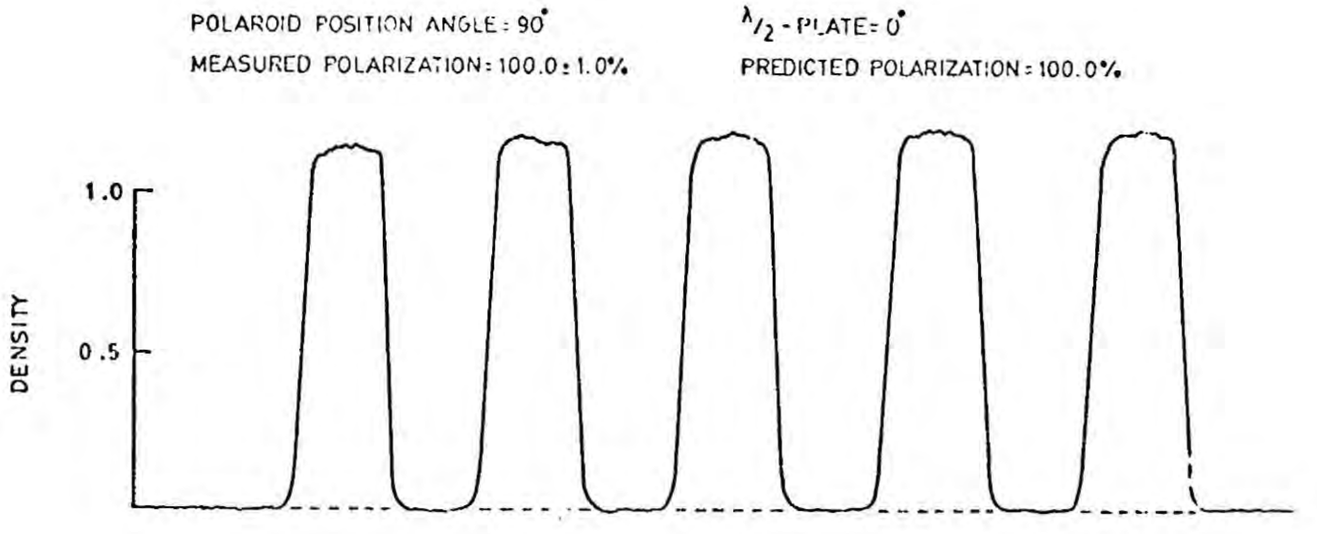

(f)

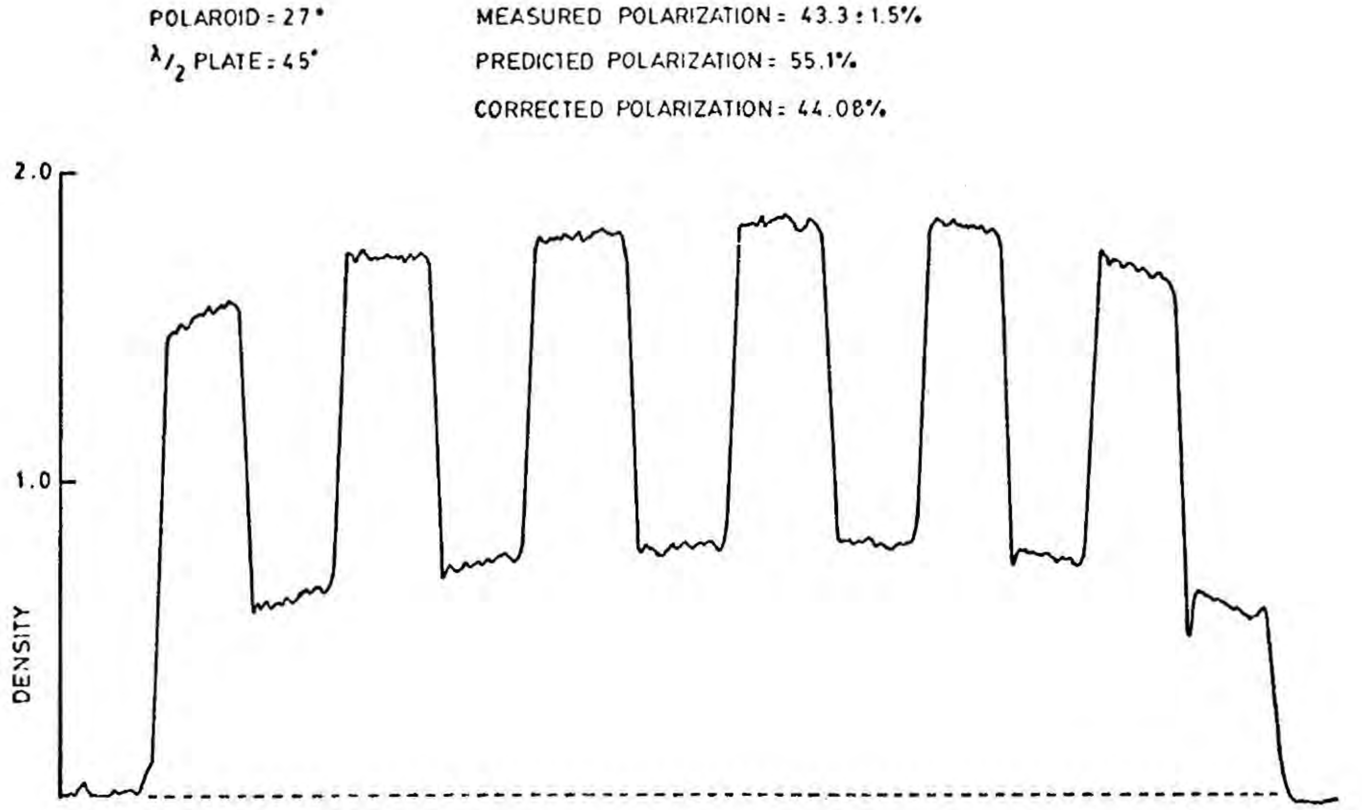

Figure 5.9 continued

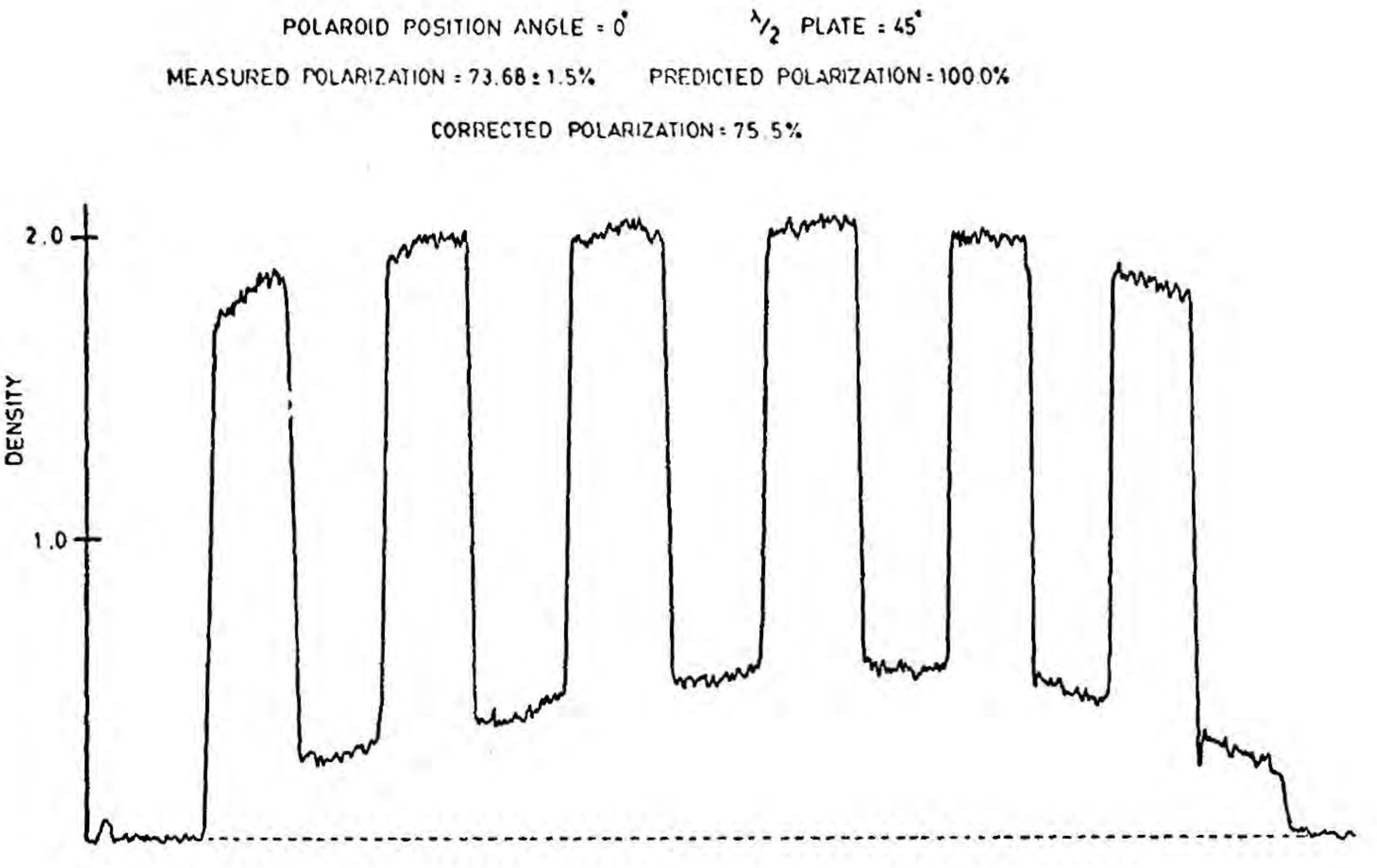

(g)

Figure 5.9 (continued)

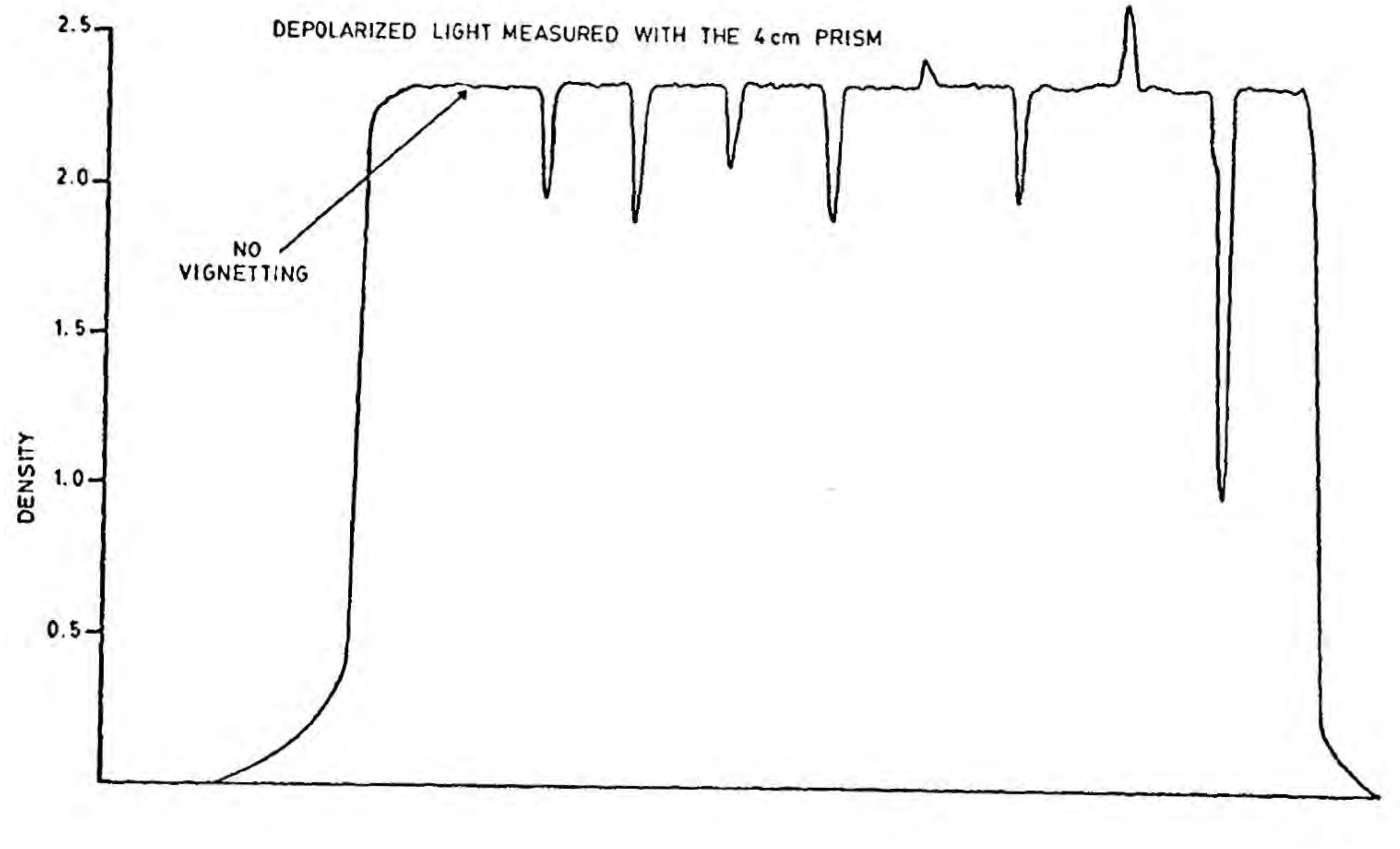

Figure 5.10 Intensity profile with the 4 cm prism.

$$f_1' = \left(\frac{I_2' \cdot I_6'}{I_1' \cdot I_5'}\right)^{\frac{1}{2}} = f_1$$

which, as before, is a true estimate of the cathode sensitivity. However,

$$f_2' = \left(\frac{I_8' \cdot I_4'}{I_7' \cdot I_5'}\right)^{\frac{1}{2}} \cdot \left(\frac{1 + 0.122Q/I_4}{1 - 0.122Q/I_3}\right)^{\frac{1}{2}} = f_2 \cdot \left(\frac{1 + 0.122Q/I_4}{1 - 0.122Q/I_3}\right)^{\frac{1}{2}} \qquad (5.19)$$

and no longer determines the cathode sensitivity correctly. In order to estimate the magnitude of the error caused by using f_2' instead of f_2, let us assume typical polarizations $\lesssim$ 10%, so that $Q/I \lesssim 0.1$. Expanding the square root terms as power series, and taking $I_4 \sim I_3 \sim I/2$ we have

$$f_2' \sim f_2 \, (1 + 0.3 \, Q/I) \sim 1.03 \, f_2 \qquad (5.20)$$

We therefore overestimate f by 3%, but this error will be masked by those from other sources, which are typically ~ 5 to 6% (c.f. Figures 4.13), and thus equations 5.16 and 5.17 can be applied directly to the M82 polarization data to correct for the $\lambda/2$-plate depolarization effects.

5.1.4 Corrections for Instrumental Vignetting

Figures 5.9 clearly show the vignetting across the field of view of the polarimeter produced by the 2 cm prism. This has two consequences: Firstly an artificial polarization will be produced, but fortunately this effect is corrected for by the use of the f-factor (this is an alternative explanation of the shift of the f-factor distribution peak to 1.01), and secondly the Sky background intensity will be a function of position in the field of view and this is the effect that we are concerned with here. In practice a separate determination of the Sky Stokes' parameters I_{sky}, Q_{sky} and U_{sky} was made for each strip pair and so

TABLE 5.2 Photographic Verification of the Depolarization Corrections

$\lambda/2$-plate orientation	Polaroid Position Angle	Observed Stoke's Parameter %	True Stoke's Parameter %	Depolarized Stoke's Parameter %
0	0	100.0 ± 0.5	100.0	100.0
0	5	97.75 ± 2.0	98.48	98.48
0	10	94.59 ± 1.0	93.97	93.97
0	17	71.5 ± 2.0	82.9	82.9
0	25	64.23 ± 2.0	64.28	64.28
0	37	28.8 ± 2.5	27.56	27.56
0	45	0	0	0
0	57	41.6 ± 2	40.6	40.6
0	60	- 53.85 ± 2.0	-50.0	50.0
0	77	- 90.91 ± 1.0	-89.9	89.9
0	85	- 96.78 ± 1.0	98.48	98.48
0	90	-100.0 ± 0.5	100.00	100.00
22½	0	10.26 ± 2	0	12.24
22½	5	17.5 ± 3	17.36	26.8
22½	10	33.77 ± 2	34.2	40.58
22½	25	78.8 ± 1	76.6	72.96
22½	45	89.9 ± 1	100.0	75.6
22½	60	77.1 ± 2	86.6	79.9
22½	90	100.0 ± 0.5	100.0	100.0
45	0	72.2 ± 1	100.0	75.6
45	5	65.2 ± 2	98.48	78.8
45	10	63.39 ± 2	93.97	65.77
45	25	43.3 ± 2	64.27	48.2
45	45	0 ± 1.5	0	0
45	60	40.0 ± 2	50.0	37.4
45	90	76.5 ± 1	100.0	75.5
67½	0	- 10.26 ± 2	0	- 12.2
67½	5	+ 3.0 ± 0.5	+ 17.36	+ 2.77
67½	10	13.2 ± 1.0	34.2	17.6
67½	25	57.1 ± 1.0	76	59.4
67½	45	100.0	100.0	100.0
67½	60	- 89.0	- 86.6	- 82.7
67½	90	- 15.9	0	- 12.2

vignetting corrections need only be applied in the X direction. These were determined from photographic measurements of a uniformly-illuminating-depolarized light source using an analogue analysis method. The intensity profile obtained was very similar to that of Figure 5.9C and is given in Table 5.3. Though a 25% light loss occurs for pixels between 1 and 25 and 475 and 512, the electronographs only contain useful data between pixels 50 and 450 and thus the corrections amounted to no more than 10%. Since the Sky background was estimated from the regions 50 to 100 and 450 to 400 the Sky parameters subtracted from the galaxy had to be larger, and crude scaling was therefore applied to the Sky parameter at intervals of 50 pixels using values determined from Table 5.3 by interpolation. As M82 was situated between locations 175 and 400, this meant that a virtually constant set of Sky parameters, with values 1.1 times the measured values were used. The final polarization map obtained after applying the depolarization and vignetting corrections is presented, and discussed in detail, in section 5.3.

In order to remove the vignetting the 2cm prism was replaced by an identical 4 cm prism and the observations made with this later prism show no signs of this effect (Figure 5.10).

5.2 Calibration Measurements at the Telescope

5.2.1 Observations of Standard Stars

Recalling our discussion of Chapter 3, the standard star observations serve two purposes :

(i) They enable the calculation of the "zero-point" correction required to convert the natural position angle measurements into the true equitorial system.

Table 5.3

The Vignetted Intensity Profile of the Polarimeter

Y - coordinate (pixels)	Recorded Intensity % (All measurements ± 0.5%)
1	74.8
25	82.9
50	90.0
100	98.8
150	100.0
250	100.0
350	100.0
400	98.6
450	90.0
475	84.3
512	75.5

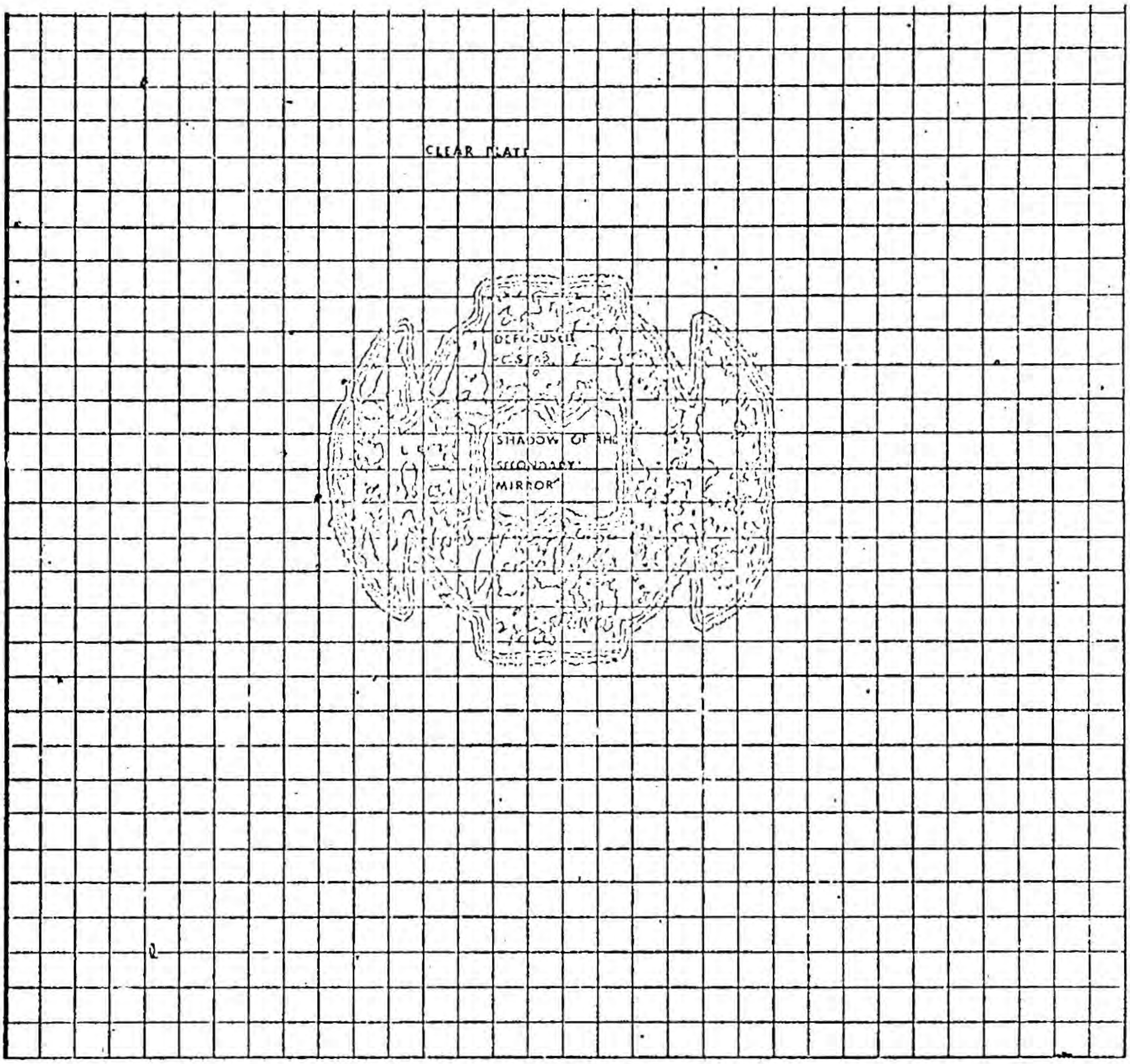

<u>Figure 5.11</u> *Isophote map of a defocussed Standard Star image.*

(ii) They determine the accuracy of our observations and the instrumental polarization.

In this work both focused and defocused standard stars were observed. The analysis of both types of standard star image proceeded along the lines described in Chapter 4. The focused images were registered using the locations of their centroids. The polarization was then calculated for each star from the average of the polarization in 5 x 5 cells, and the spread about the mean value was used to estimate the errors in p and θ. The motivation for using defocused star images was that they resembled extended objects, and might thus provide a more realistic estimate of our accuracy in the M82 observations. However, though more 5 x 5 cells are contained in the defocused images (Figure 5.11) this does not confer any real advantage, as the image registration is more difficult and demanding. In practice we used the centroid of the shadow of the secondary mirror for this purpose. The contour map of Figure 5.11 also shows the variations in the primary minor reflectivity.

Observations with the Chromatic $\lambda/2$-plate

Because the photocathode used for the M82 observations was prematurely destroyed only 6 sets of observations of standard stars had been made with the chromatic $\lambda/2$-plate. The results of these observations, before and after correction for the depolarization effect of the $\lambda/2$-plate are compared with the accepted values in Table 5.4. In each case the errors quoted on the accepted values are estimated by the author from the scatter between the results of different observers, and are consequently far larger than the figures of $\pm 0.1\%$ and $\pm 0.5°$ generally quoted for the accuracy of photoelectric

TABLE 5.4 : OBSERVATIONS OF STANDARD STARS MADE WITH THE CHROMATIC $\lambda/2$-PLATE

STAR	Accepted Value		This Work			
			Uncorrected		Corrected	
	P%	Θ(Deg)	P	Θ	P	Θ
μ cas	0.09 ± 0.06	24 ± 1	0.9 ± 0.8	37.7 ± 20	1.05 ± 0.8	30.9 ± 20
ρ cas	1.32 ± 0.1	55 ± 3	1.6 ± 0.8	64.0 ± 5	1.66 ± 0.8	59.3 ± 5
			1.0 ± 0.8	68.0 ± 5	1.11 ± 0.8	61.0 ± 5
ρ cas depolarised with Lyot depolariser	0.0	-	0.6 + 0.8	40.0 ± 20	0.76 ± 0.8	
			0.8 ± 0.8	25.5 ± 20	1.2 ± 0.8	

TABLE 5.5 : COMPARISON BETWEEN OUR MEASUREMENTS OF THE POLARIZATION OF STANDARD STARS WITH THE ACHROMATIC $\lambda/2$-PLATE AND THE PUBLISHED VALUES (AXON + ELLIS 1976). AN ASTERISK INDICATES THAT A DEFOCUSSED IMAGE WAS USED.

STAR	Accepted Value		This Work	
	p%	θ^o	p%	θ^o
HD43384	2.7 ± 0.4	170 ± 3	2.3 ± 0.5	172 ± 5
HD122945	0.1 ± 0.01	56 ± 1	0.3 ± 0.5	69 ± 10
HD155528	4.6 ± 0.2	93 ± 1	4.3 ± 0.5	90 ± 5
HD80083	0.13 ± 0.01	140 ± 2	1.4 ± 0.5	128 ± 10
μcas*	0.09 ± 0.01	24 ± 1	0.65 ± 0.5	22.5 ± 10
ρcas*	1.32 ± 0.06	55 ± 3	1.26 0.5	58.3 ± 5

polarimetry of stars (Gehrels 1974). The observations of the unpolarized μcas and the polarized ρcas, depolarized with a Lyot depolarizer, show the absence of any instrumental polarization greater than the accuracy limit of the observations or larger than 0.8%. Below about 1% polarization, the noise from the PDS grey-scale dominates and the position angles are ill-defined. The results for the polarized ρcas do nevertheless agree with the accepted values allowing for our large uncertainties. The position angles are certainly better determined than for the unpolarized star, and this would seem to imply a sharp transition between polarizations when we can and cannot accurately determine the position angle at about 1%. Realistically however, we have such a limited number of observations that no firm conclusions as to the size of our errors can be reached. In order to derive reliable estimates of our errors we combine these measurements with the cloth measurements reported in the next section, and use the internal accuracy of our M82 data together with a comparison of the M82 data with previous photoelectric observations; this analysis is reported in section 5.4

Observations with the achromatic $\lambda/2$-plate

A more extensive series of standard star observations were made with the achromatic $\lambda/2$-plate and provide a measure of the accuracy of the polarimeter with the improved optical system. The results are summarized in table 5.5 and show very good agreement with the accepted values. As for the observations with the achromatic $\lambda/2$-plate, the PDS noise sets a lower limit on the polarization beyond which our measurements are inaccurate, but we estimate this figure to be slightly lower than before, i.e. 0.5%. However, even for such low polarizations, the errors in the position angles are significantly smaller with the achromatic $\lambda/2$-plate. The results for the polarized standards are in excellent agreement with the accepted values with mean uncertainties of $\pm$ 0.5% in p and $\pm 5^{\circ}$ in θ. Though this accuracy does not approach that of the very best photoelectric work it is still good enough to be acceptable, and comparable to, that of most photoelectric polarization measurements of stars. The defocussed standard star observations did not yield substantially different results, implying that additional sources of systematic error are not inherited in the instrument's measurement of the polarization in extended objects. On the basis of these observations we consider that it is unnecessary to apply corrections to either the polarizations or position angles obtained with the improved version of the polarimeter. Future observations of extended objects with the instrument are therefore expected to have a far greater accuracy than the measurements reported here.

5.2.2 Cloth Measurements

The "cloth" measurements described here are aimed at providing a straightforward method of carrying out calibrations at the telescope using electronographic detection. Our basic requirements are therefore that we should have a uniform, unpolarized source, as totally or partially polarized light may be obtained by inserting appropriate polarizers at known position angles. The two measurements in which we are primarily interested are the direct measurement of the photocathode sensitivity variations, so enabling corrections to be made to the sky subtraction as described in Chapter 4, and the calibration and determination of the errors in the electronographic polarization measurements.

If we uniformly illuminate the photocathode and take an exposure, the variation of density over the electronograph will give the variation of the photocathode sensitivity. The resulting map will also take into account any irregularities in the transmission of the filters and the other optical components of the instrument, which would be of particular importance for narrow band observations. The standard approach is one developed by Penny (1976) in which exposures of the twilight sky are taken when it is bright compared to the tube background and any field stars present. In practise the method is difficult to apply, as considerable experience is required in judging when,

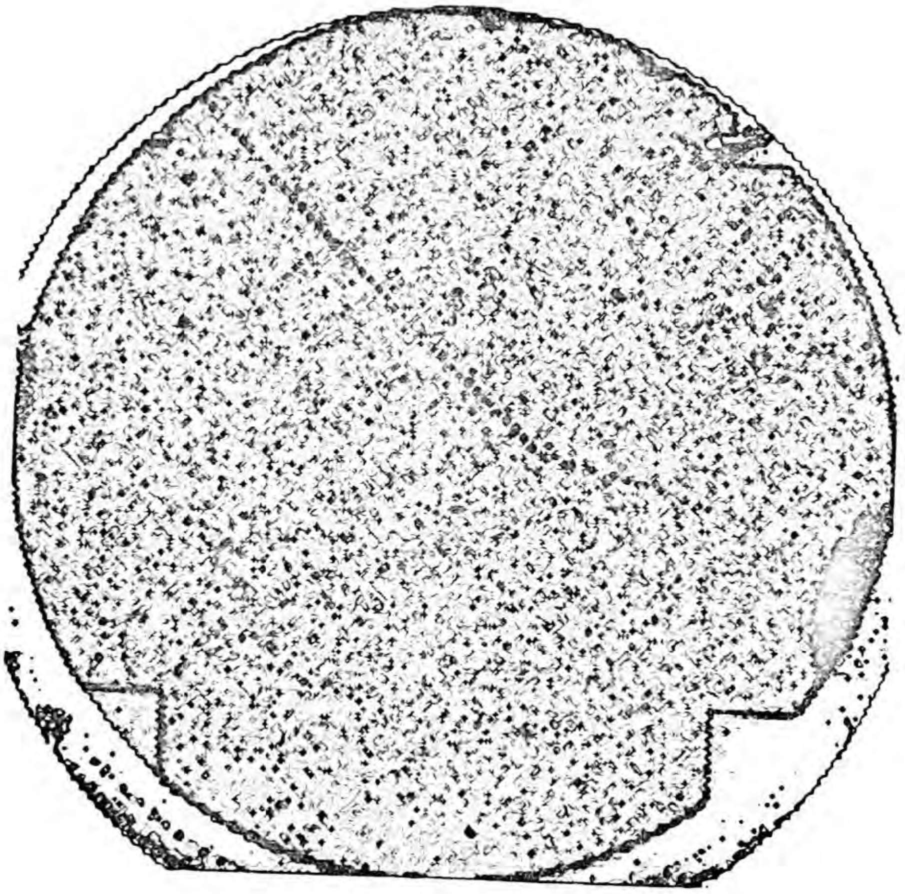

Figure 5.12a. Contour map of the photocathode sensitivity. The contour level is at the 1% variation level.

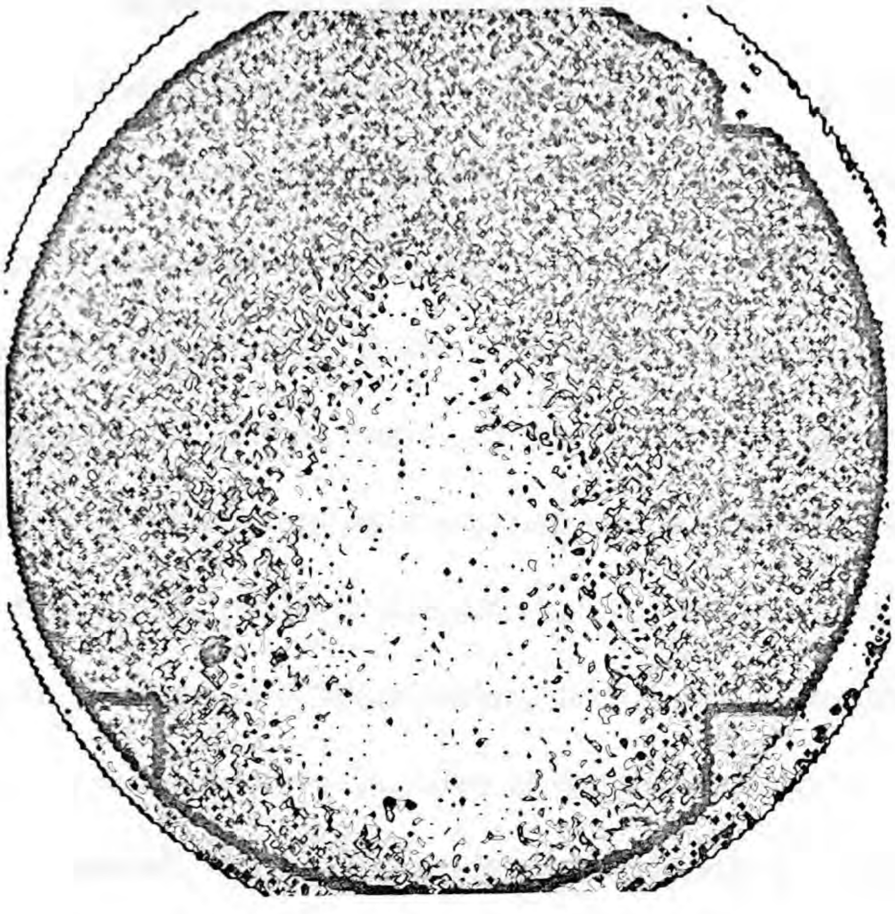

Figure 5.12b. Contour map of the photocathode sensitivity. The contour level is at the ½% level. A scratch and numerous emulsion defects are visible as dark spots.

and for how long, each exposure should be taken so that the tube is not damaged or such short exposures are required that the shutter action produces non-uniform illumination. The prohibitive objection as far as we are concerned is, however, that the twilight sky is highly polarized (up to 40%) by Rayleigh scattering (Ashburn, 1952). As an alternative we have developed the "cloth" method. Uniform, unpolarized illumination is obtained by draping a white sheet over the telescope aperture. This is so close to the telescope that it is out of focus, and the effects of wrinkles and shadows cast by the secondary mirrors are then not significant. As an extra precaution, a second sheet is mounted on the dome wall and viewed with the instrument. The illumination is provided by the dome lights and thus a suitable intensity can be readily and reproducibly obtained. The cloth acts both as a diffuser and a depolarizer, and from our previous discussion we know that the incoming light will be depolarized to better than 0.01%, which is adequate for our purposes. Our first consideration is therefore the uniformity of illumination. In figure 5.12 we present two independent cathode maps of the whole 4 cm. area of the photocathode obtained in the B-band with the prism removed, and these provide a substantially polarization independent measurement. The maps are uniform to at least the same accuracy as those obtained by Penny (1976) using the sky method and moreover clearly show the sensitivity variations we wish to measure. Except where a major defect in the photocathode occurs, the variations in sensitivity are always less than $\pm$ 10%, and generally less than $\pm$ 5% in localized regions of the photocathode. The instrumental polarization has also been measured using the cloth method by repeating the above exposure with the prism inserted and the chromatic $\lambda/2$-plate at four successive position angles. The registration of these plates was achieved using the grid outline and the polarization was analysed in 10 x 10 pixel cells. The e-factors (figure 5.13a) show remarkable consistency over the field of view and the f-factors once again show variations in

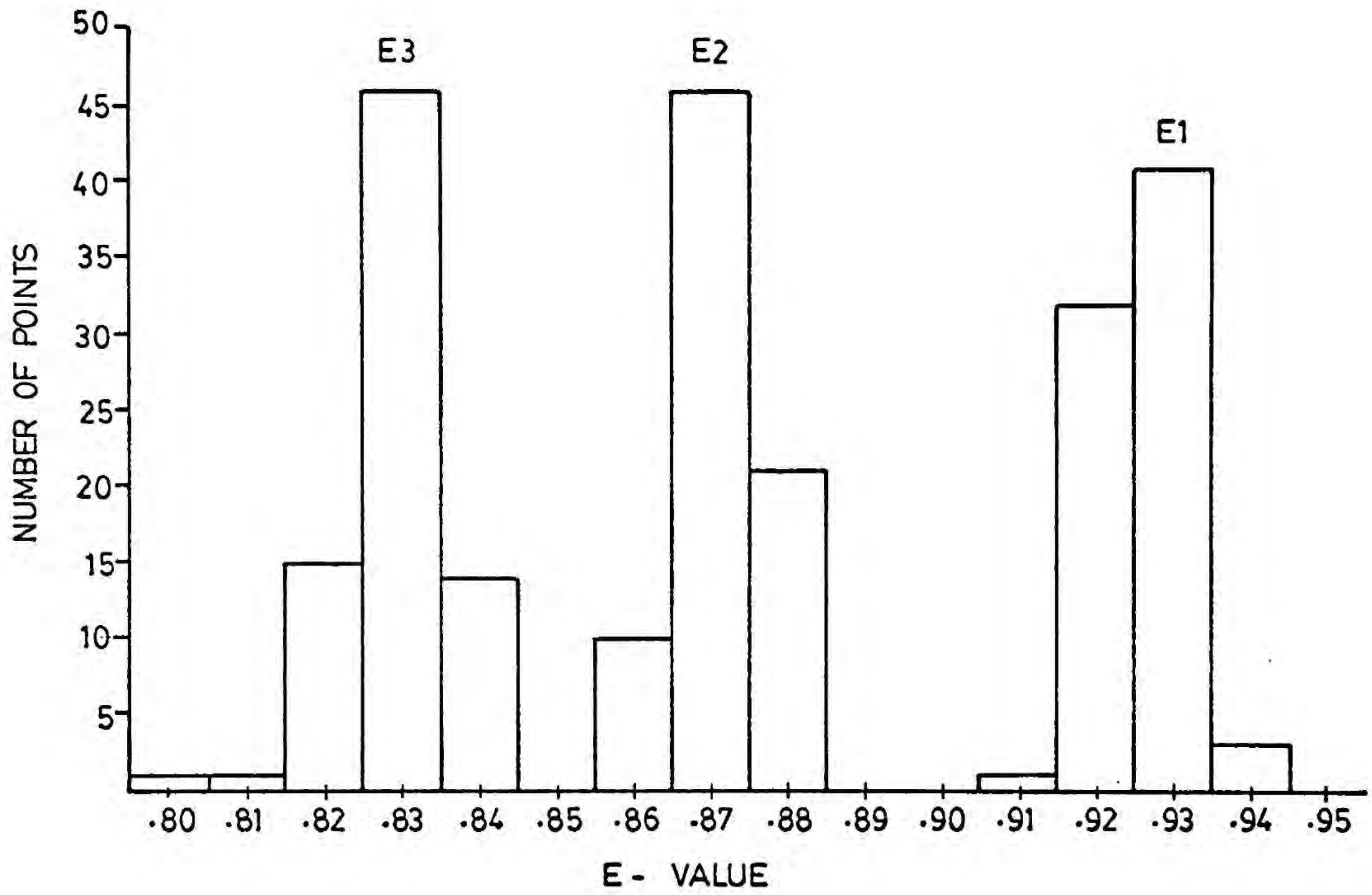

Figure 5.13a *The e-factors from plates 44 to 48.*

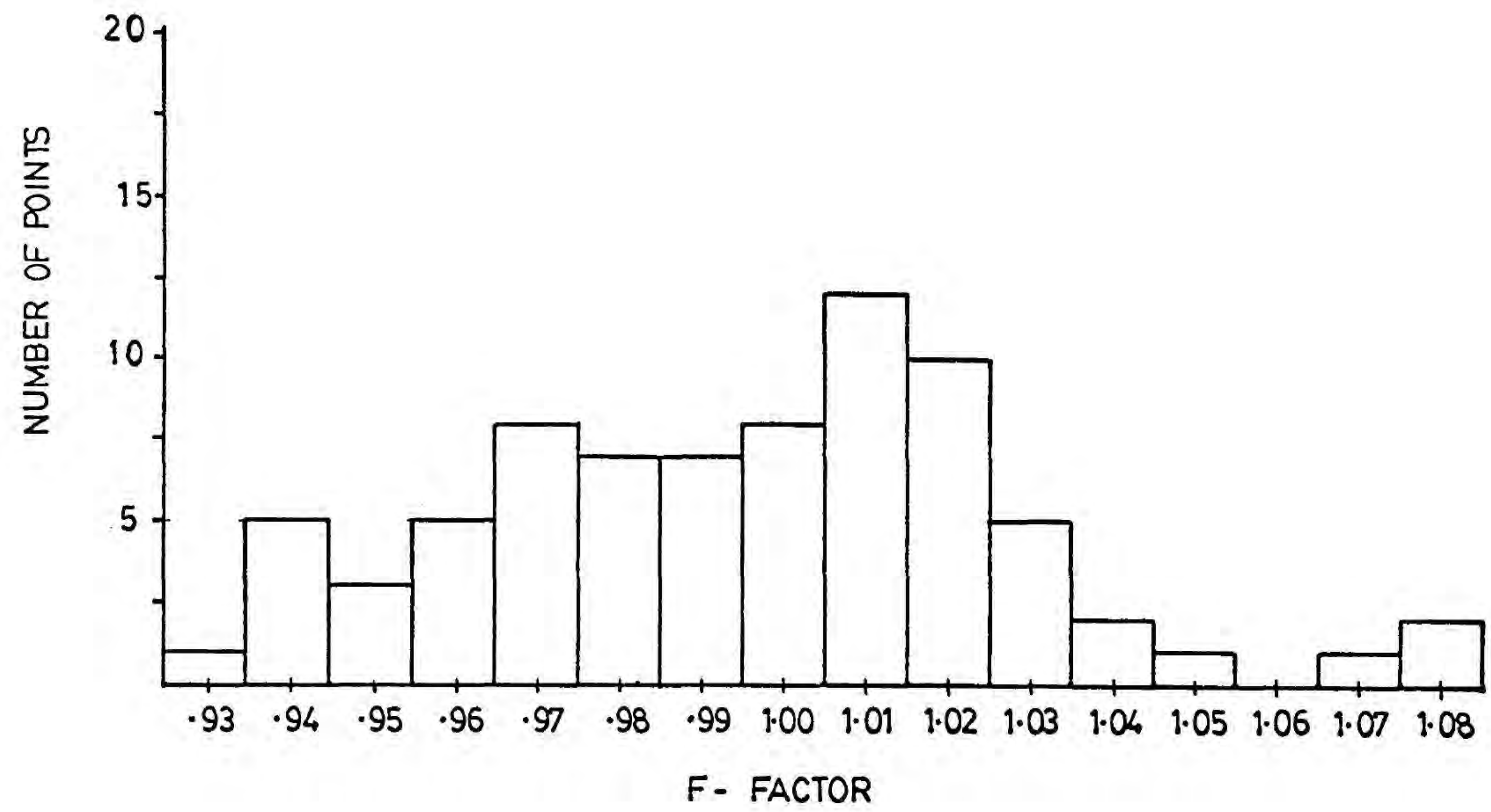

<u>Figure 5.13b</u> *The mean f-factor distribution from plates 44 to 48.*

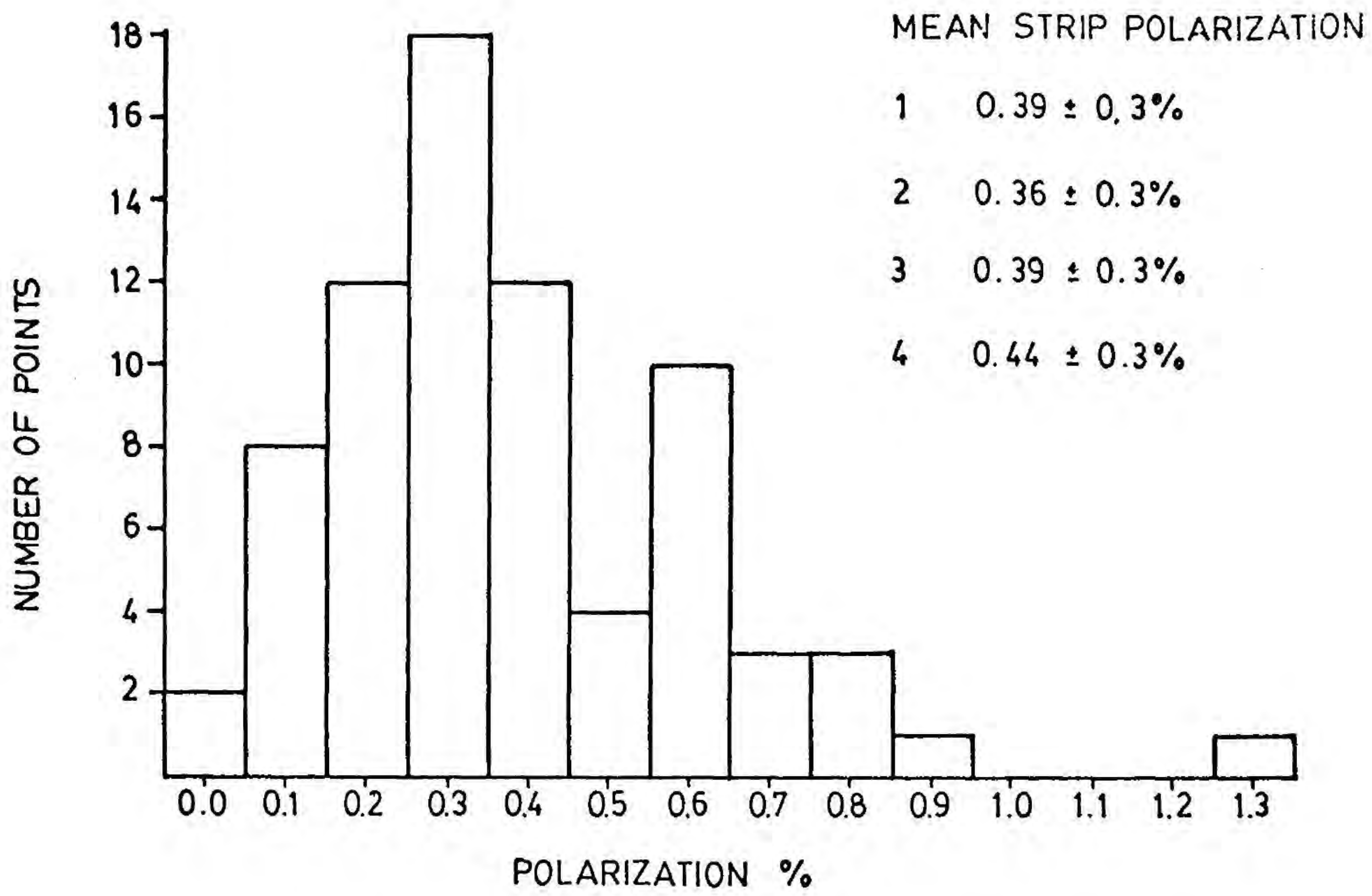

Figure 5.13c Measured polarization obtained from plates 44 to 48.

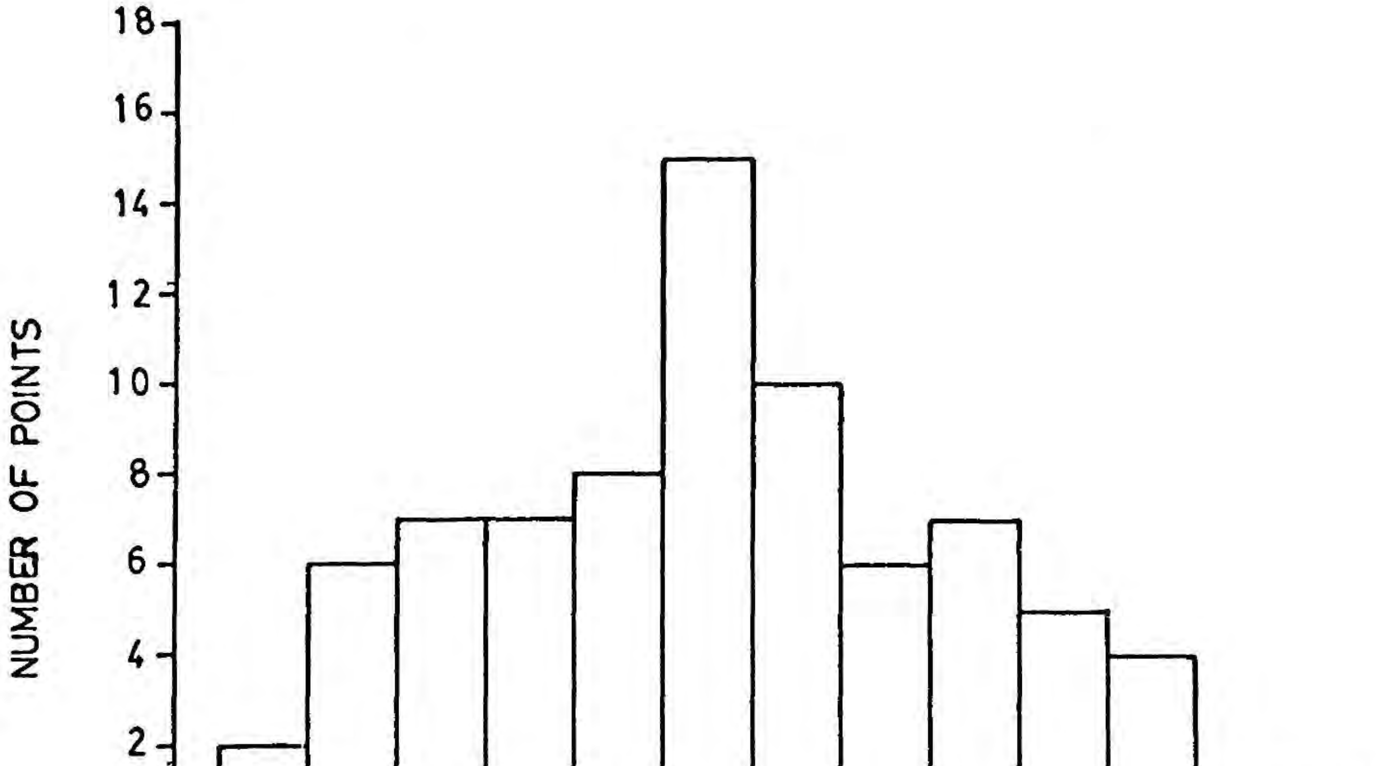

Figure 5.13d (P1-P2) plot for plates 44 to 48.

sensitivity between strips of less than $\pm$ 5%. The measured polarizations range between 0.0 and 0.9% (figure 5.13c) and the mean values obtained for the four strips measured are 0.39, 0.36, 0.39 and 0.44%. From the (P1-P2) plot we estimate our uncertainty to be only $\pm$ 0.3%, which is smaller than the precision of our M82 observations and can be easily accounted for by grey-scale noise. The position angles obtained showed no sensible preferred direction for reasons discussed previously and are therefore not presented. Similar observations to these should be used to obtain cathode sensitivity maps rather than direct measurements so that polarization effects are taken into account. The method of deriving a cathode map from these data has been described in Chapter 4, but because our observations of M82 were obtained with a different photocathode we refrain from presenting one here. By inserting a sheet polaroid at a known orientation, similar measurements may be used to calibrate the instrumental position angles and determine the instrumental depolarization. In figures 5.14 we present results of measurements made with the polaroid at a position angle of 45^{o}. This choice of orientation enables us to check the U correction equations 5.16 and 5.17 virtually independently of the Q_2 correction because U is very much bigger than Q. The observed polarizations are shown in figure 5.14a and the mean value obtained was 83.8 $\pm$ 2% due to depolarization by the chromatic wave-plate. After applying the correction equations we obtain a mean polarization of 98.6% (figure 5.14b) with an uncertainty of $\pm$ 2% estimated from the (P1-P2) plot (figure 5.14c). The effect of the corrections to the position angles is small, because U dominates Q; a plot of the corrected angles is shown in figure 5.14d and the (ANG1-ANG2) plot in figure 5.14e. These plots show that the position angles are remarkably well determined, because of the dominance of U. The mean position angle is 44.9 $\pm$ 0.3^{o}. Allowing for the rather large scatter in p these results give a further indication that the correction equations accurately compensate for the instrumental depolarization. We

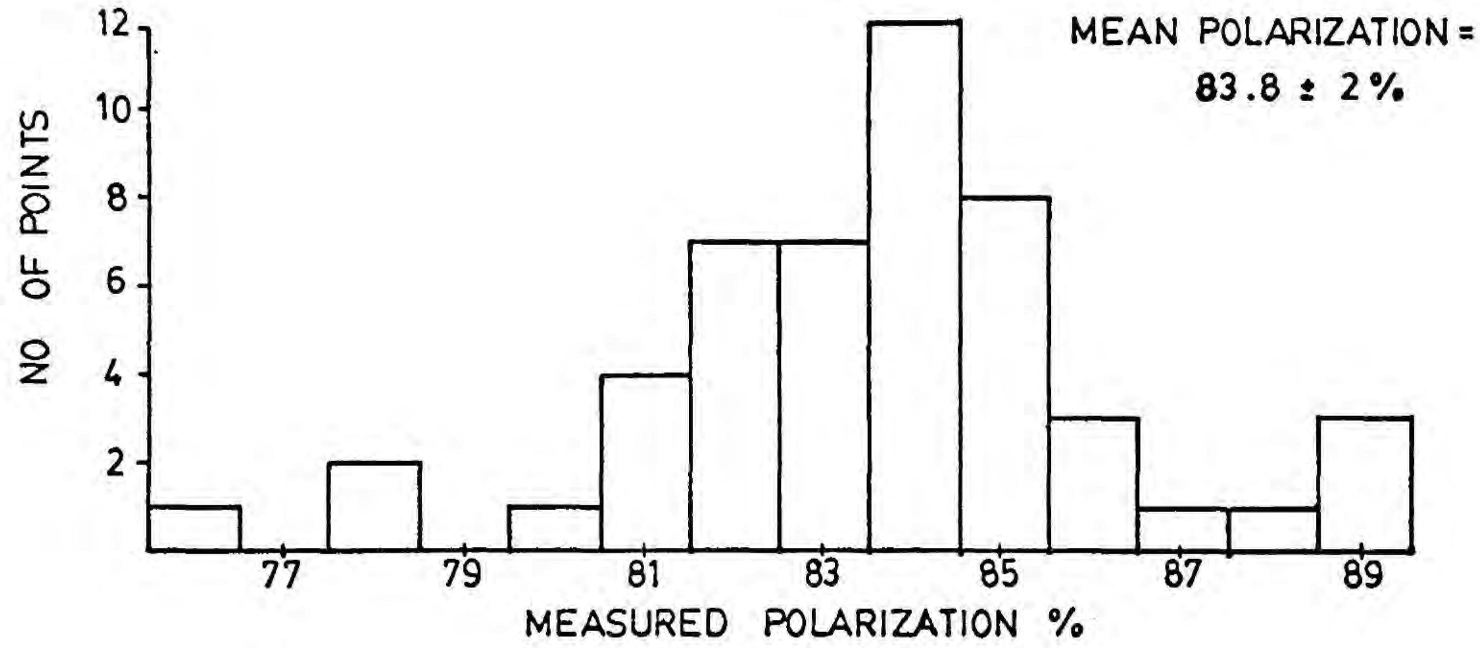

Figure 5.14a *Observed polarization from plates 52 to 56 (Polaroid inserted at 45° position angle).*

(b)

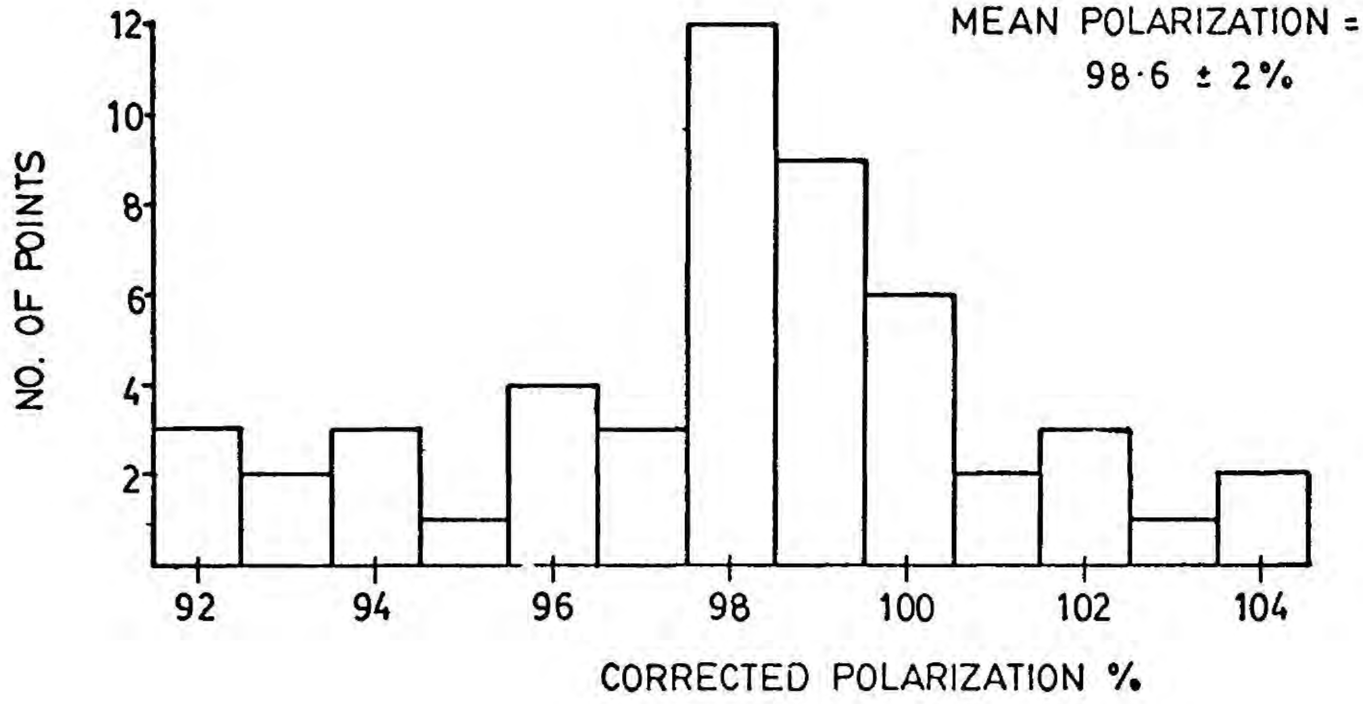

(c)

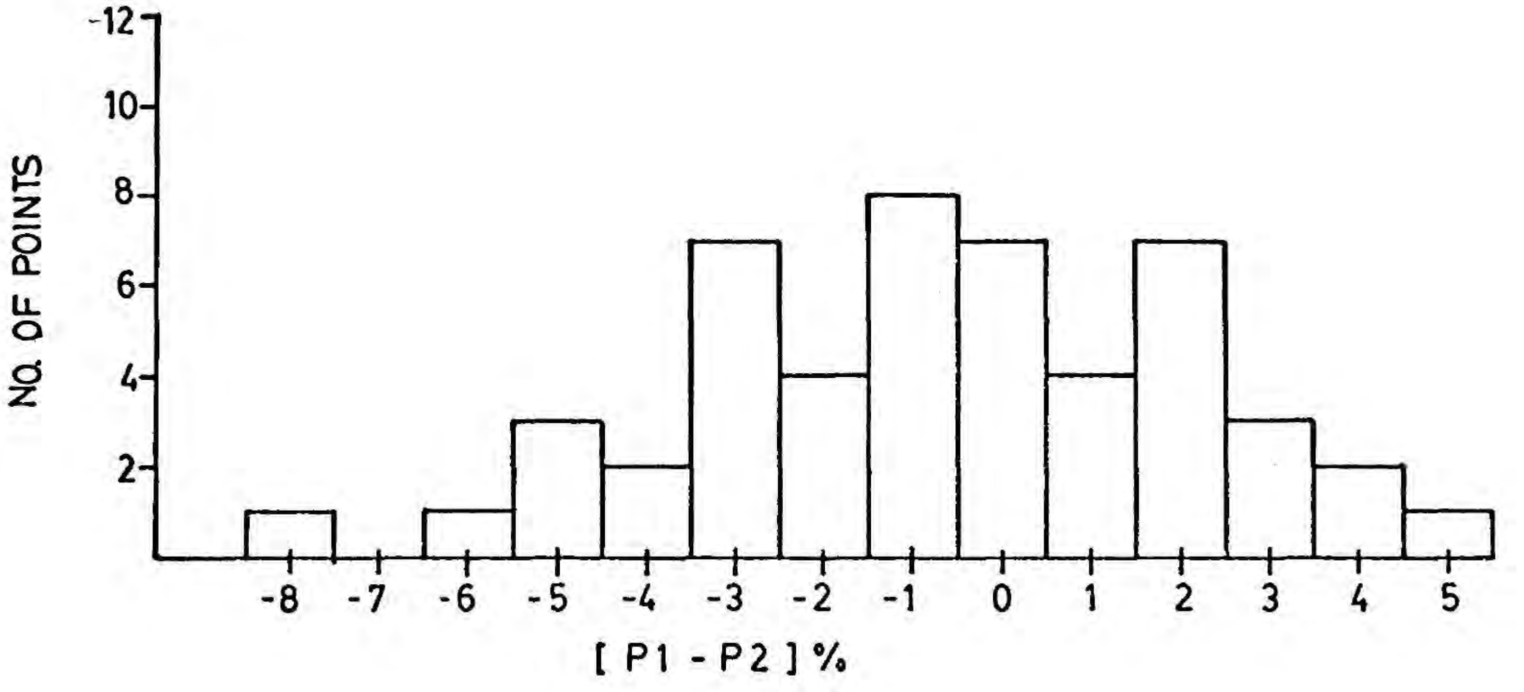

Figure 5.14 (b) Corrected polarization
(c) (P1 − P2) plot.

(d)

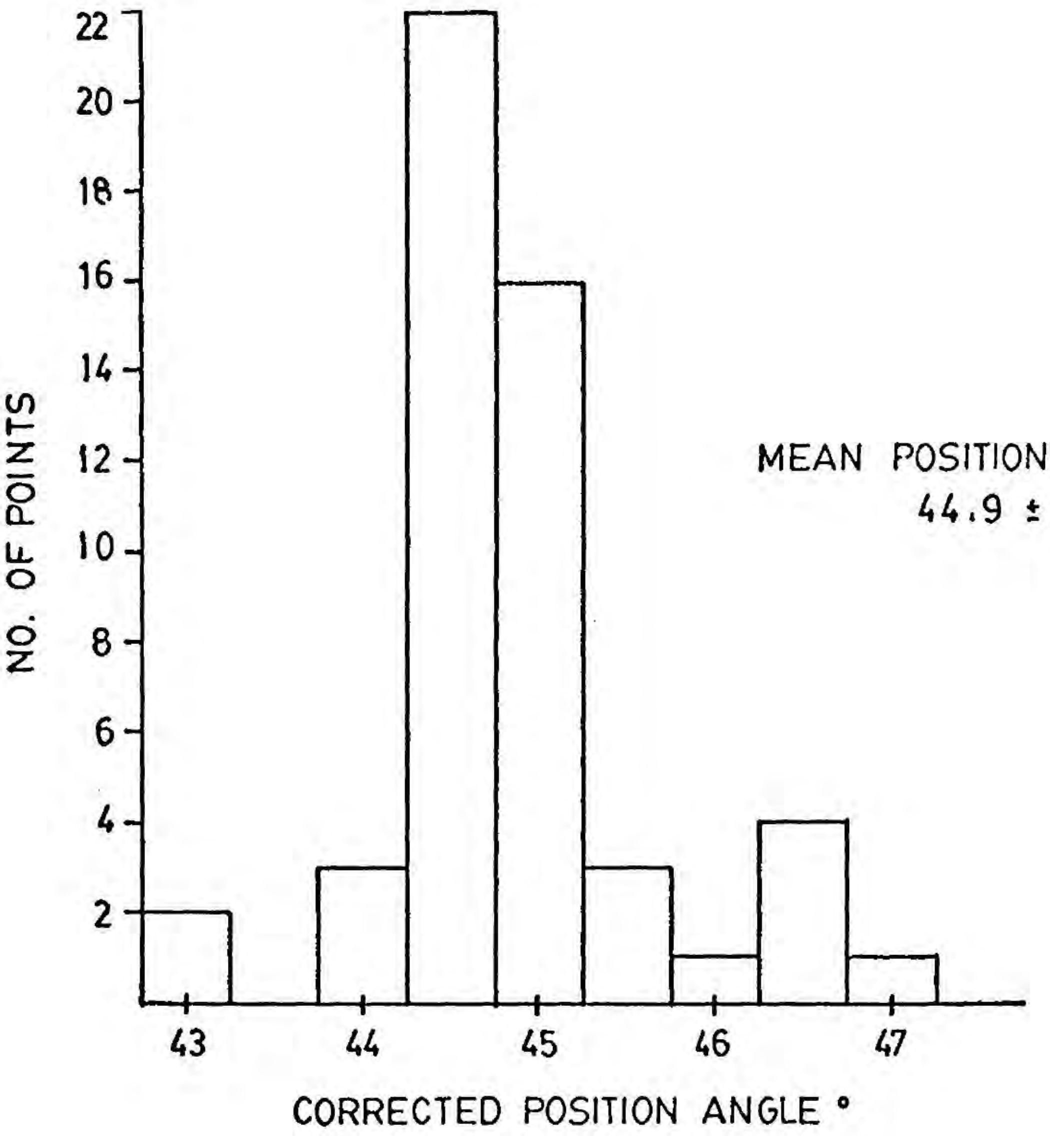

(e)

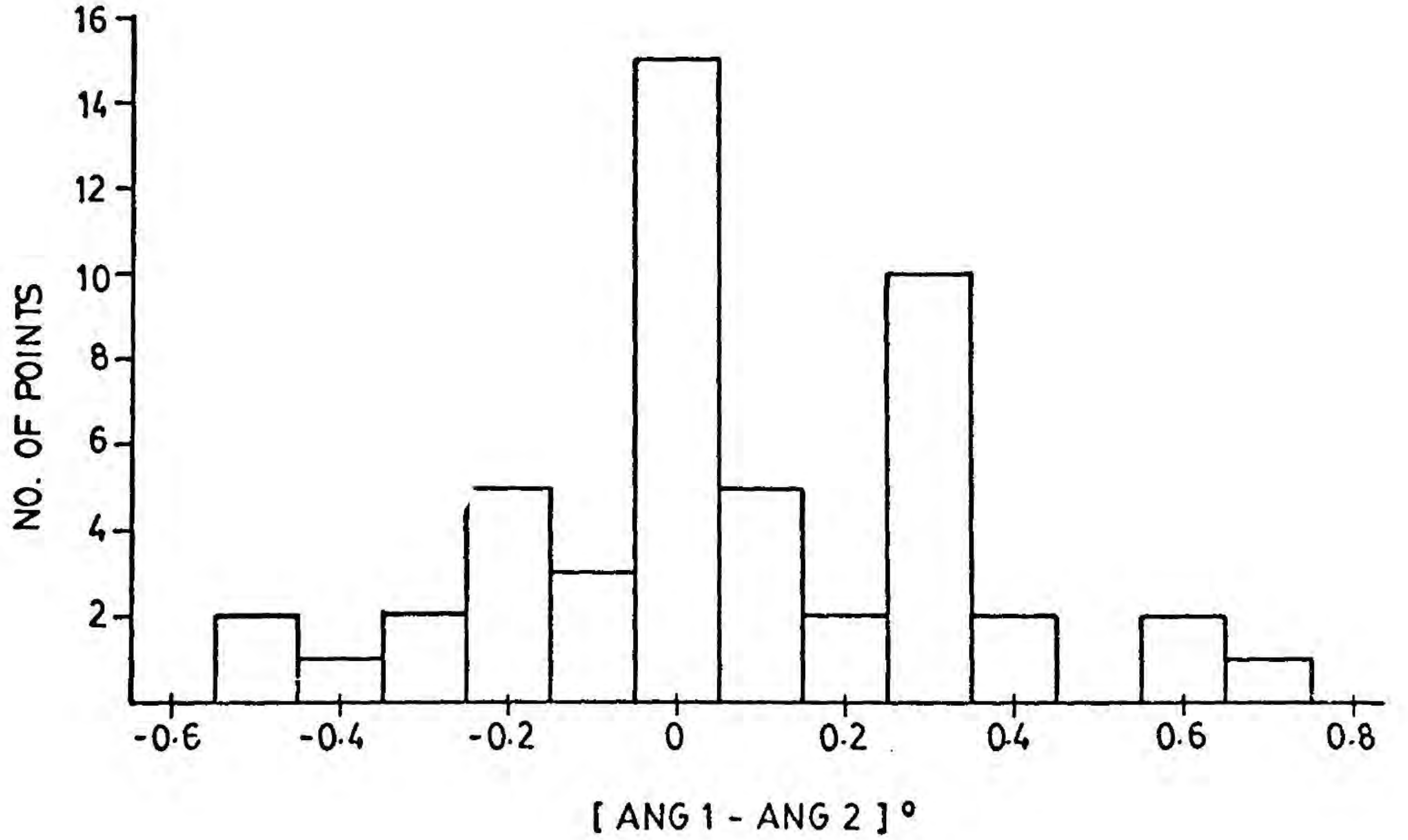

Figure 5.14 (d) *corrected position angles*

(e) *(ANG 1 - ANG 2) plot.*

(d)

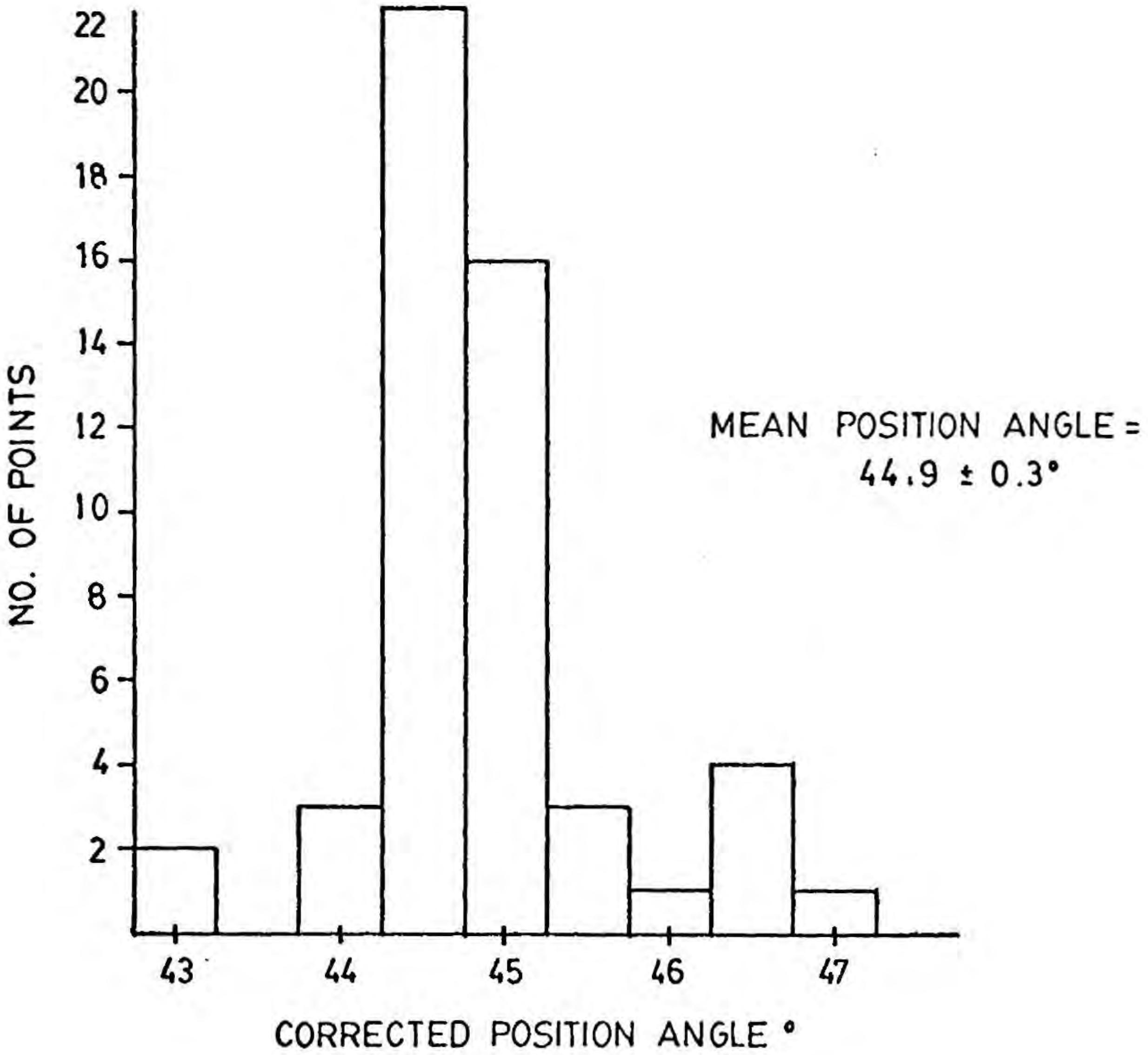

(e)

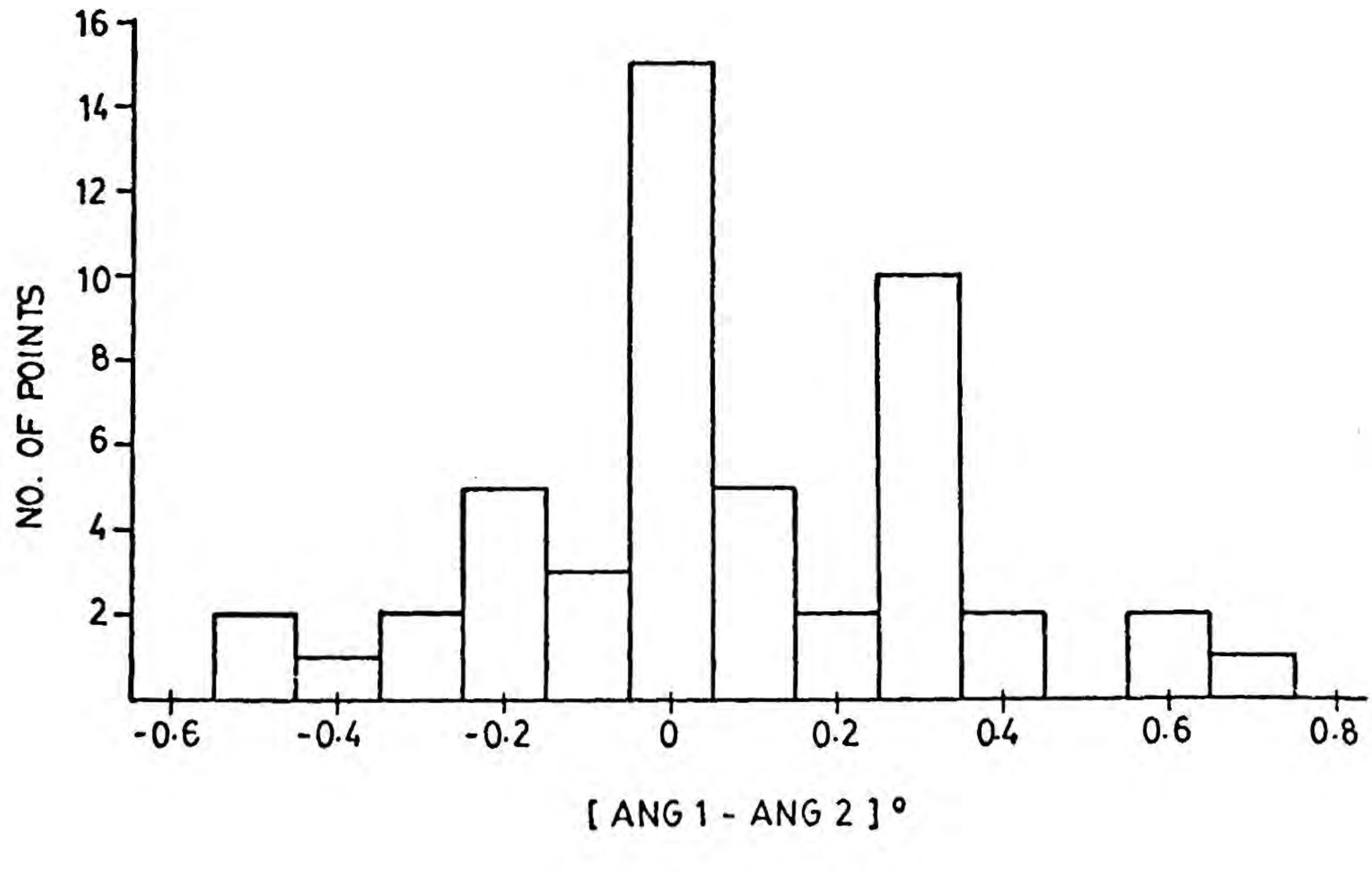

Figure 5.14 (d) *corrected position angles*

(e) *(ANG 1 - ANG 2) plot.*

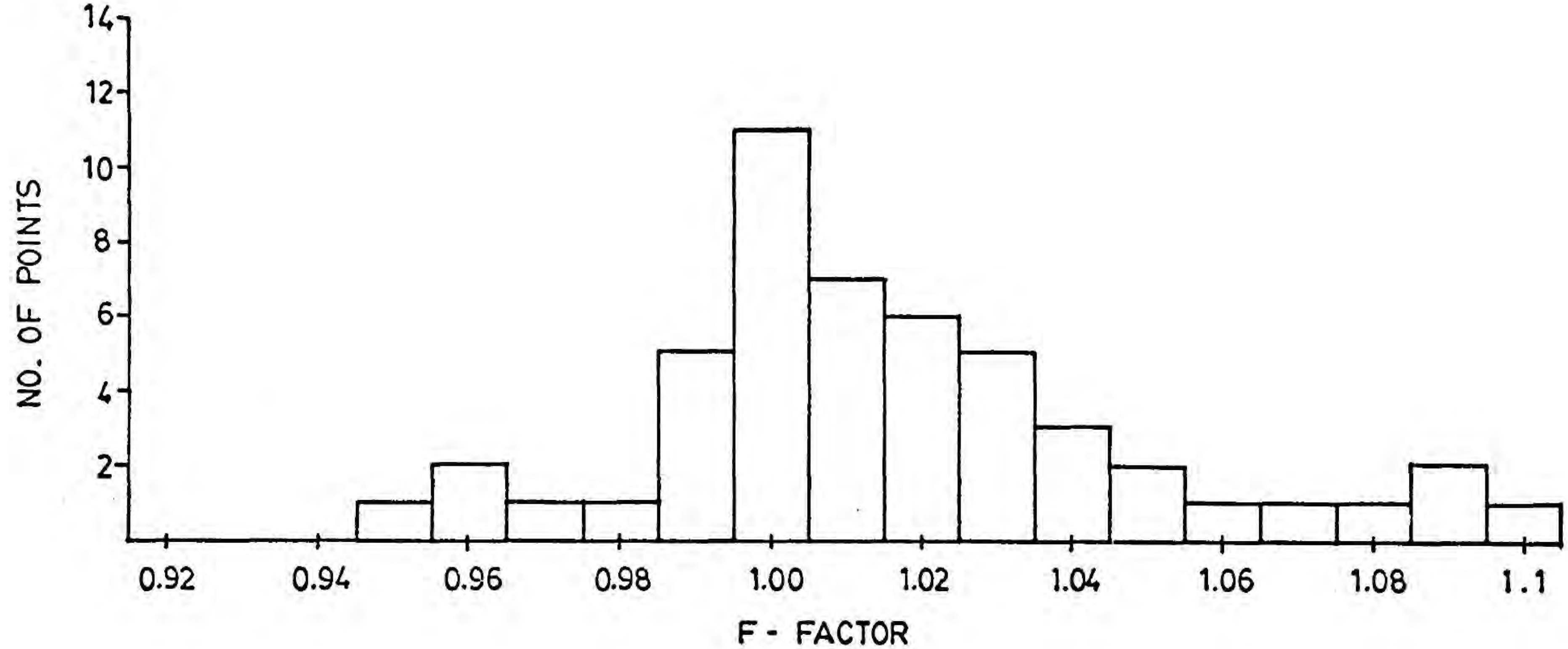

Figure 5.14 (f) *The mean f-factor distribution from plates 52 to 56.*

conclude that the cloth technique is potentially very powerful and yields high precision results; it will provide valuable additional measurements of our accuracy in future work.

5.3 The M82 polarization results

M82 has a galactic lattitude b $\sim 35^{o}$ and the interstellar polarization in this direction will therefore be small. For stars close to the direction of M82, and more distant than 400pc (this distance gives a z height $\sim$300pc, c.f. thickness of galactic disk $\approx$ 250pc). Behr (1959) detected polarizations less than 0.3% with position angles $\sim 93 \pm 10^{o}$. Similarly Loden (1961) and Hall (1958) obtained polarizations less than 0.5%.

The contribution to the observed M82 polarization from interstellar polarization is therefore negligible and we have not applied corrections to the data for its effect.

The final polarization map of M82 obtained after the application of the corrections, detailed earlier in the Chapter, is shown in Figure 5.15. Each measurement is represented by a line centred on the point observed, whose orientation, measured anticlockwise from North, gives the position angle of the e-vector and whose length is proportional to the magnitude of the polarization, as indicated on the accompanying scale. Each determination is made over an area $\sim$6" x 6" arc. The map is plotted in 1950 equatorial coordinates and the stars used for astronometric purposes are identified by the letters A to F. In order to maintain the clarity in an already complicated map we have not superimposed it on a photograph of the galaxy, but the relationship of the polarization pattern to the optical structure of the galaxy can be established by comparing the map with Figure 5.16. This is a 20 minute electronograph of M82 in the B-band, obtained by the author at the f/7.5 Cassegrain focus of the 40" telescope, Wise Observatory, Israel.

These observations show the polarization at more than 20 times the total number of points previously observed, with a spatial resolution between five and seven

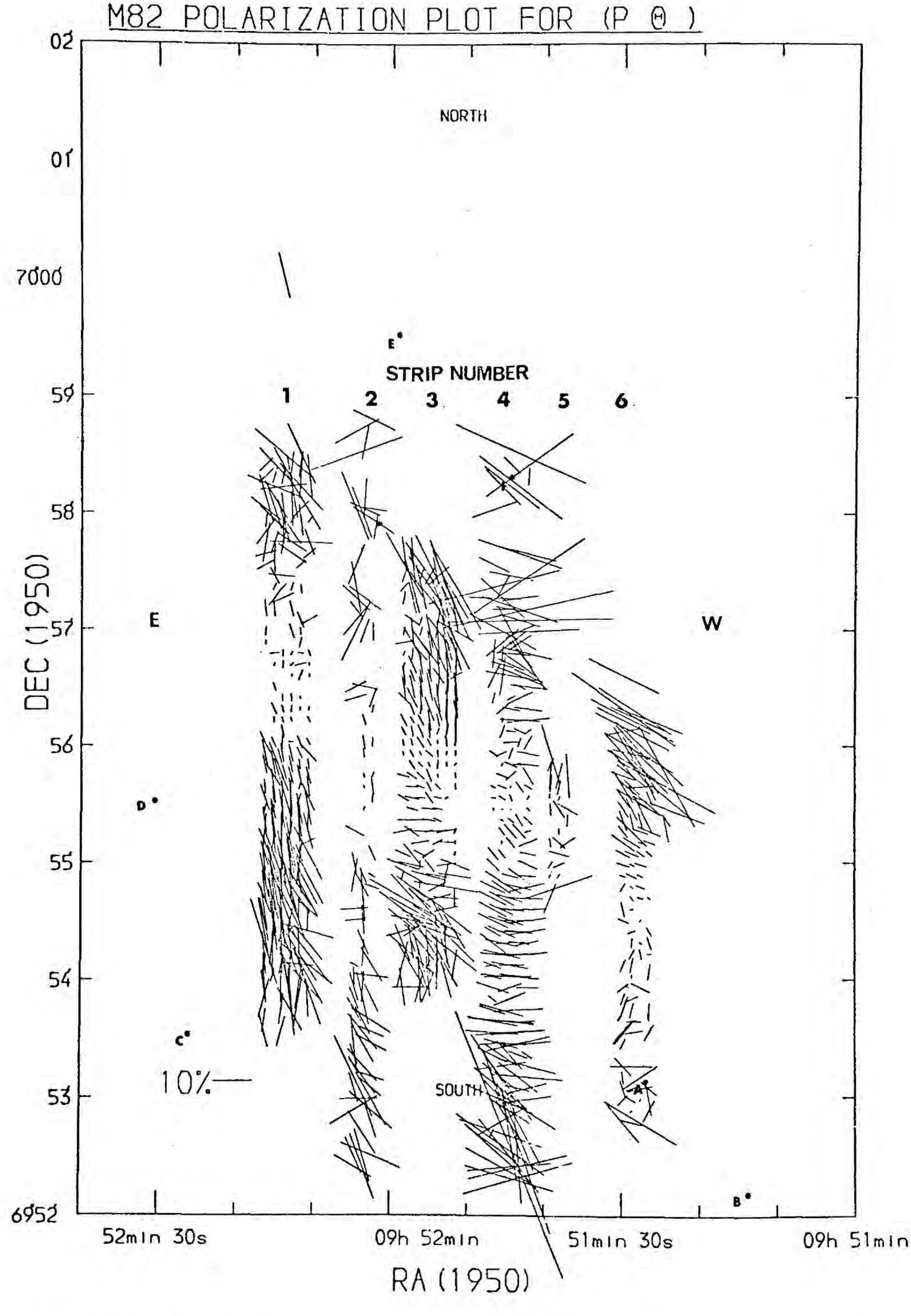

Figure 5.15 The final polarization map. For details of the notation see the text.

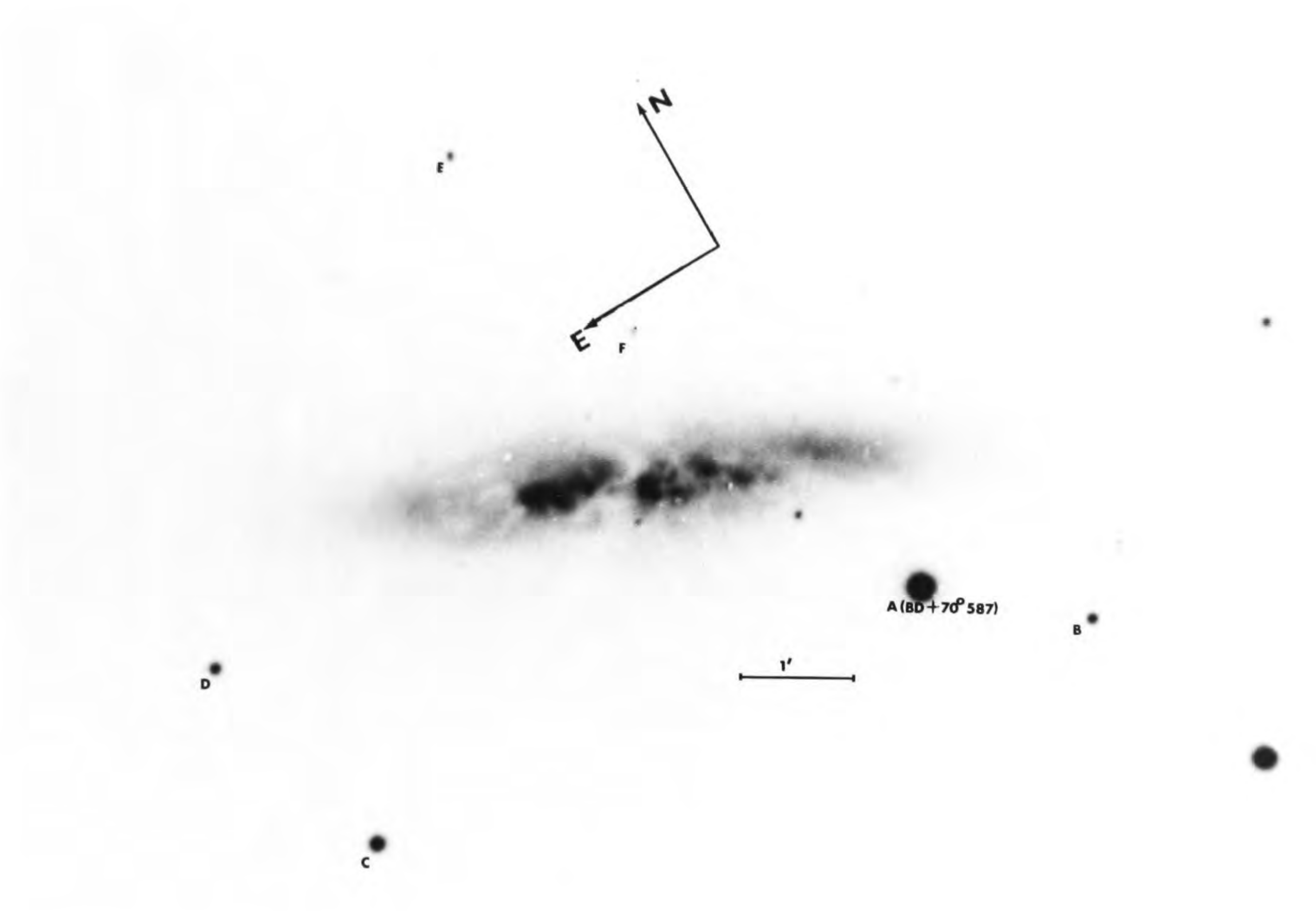

FIGURE 5.16 A B-BAND ELECTRONOGRAPH OF M82

time as fine. Though complete maps of the polarization structure in extragalactic objects at radio wavelengths are common, this is not the case at visible wavelengths and in fact these results are the first such complete mapping of the polarization in any extragalactic object. A comprehensive interpretation of these results is given in Chapter 7, but a preliminary note of the more outstanding features is given below.

The most obvious feature of the map is that the polarization is small in the central regions of the galaxy and increases steadily as we move outward into the halo. Noise abounds in a great many places, particularly so near the edge of the map, beyond the visible extent of the galaxy in Figure 5.16. This effect almost certainly arises from the reduced contrast of the galaxy against the sky background, which was extremely large on these plates, and introduces large random components into the data. We have tried to limit this effect by confining our measurements to points brighter than one-tenth of the sky background. Comparing the final map with the raw map of Chapter 4, to which this criterion was not applied, there has been an obvious reduction in noise but realistically points with a surface brightness below a limit of one-eighth of the sky background cannot be trusted. Adoption of this more stringent cut-off would then exclude all the points above +69 58' and all those below +69 53'. However, despite the noise, there is still real evidence for a central symmetric polarization pattern in the halo of the galaxy below about + 69 56'. The pattern is most prominent in strip 4 (at $\sim 9^h\ 51^m\ 45^s$). This feature is coincident with a "bulge" in the Hα emission profile of the galaxy (Figure 6.3, Lynds and Sandage, 1964) and appears to be centred on a bright region in the optical image of the galaxy. The circular pattern is also pronounced in strip 1 and is evident to a lesser extent in strips 2 and 3, though the latter strip contains a region of vectors whose perpendiculars do not point towards the body of the galaxy. A more serious discrepancy occurs in strip 6 in the area below + 69 53' where the vectors do not follow the expected flow pattern. This region contains the bright star BD+70 587 (identified by the letter A in Figure 5.15) and the confused vectors are probably a consequence of contamination from the star (the regions around other field stars are similarly affected). The circular pattern does appear in strip 6 above + 69 56', but this is the only evidence of the assumed structure above this declination, and indeed the majority of the vectors in the other strips seem to totally contradict the evidence in the lower half of the map. This marked contrast between the upper and lower regions of the map is extremely hard to account for since it encompasses both half maps of the galaxy. In strip 1 in the region North of + 69 57' where there are many confused vectors we have probably simply reached the sky limit. However, in strips 2 and 3, where the vectors appear to be regularly aligned at the wrong orientations, a possible explanation is that there has been an incorrect sky subtraction. Here the magnitude of the galaxy stokes parameters is ($Q \sim 40, U \sim 40$), comparable to those of the sky. A small alteration in the sky parameters will produce a considerable change in the orientation of the vectors. Such a change in the sky parameters would arise if this region were situated in a large cathode irregularity, which covered both the O and E strips and would then be undetectable in the f-factors. A change in the sky parameters would then be required to take this effect into account. Since we cannot obtain further information on such cathode irregularities, we can only speculate as to the probability of the existance of the effect or other possible causes.

The central symmetric polarization pattern apparent in the bottom half of the map was originally identified in the photoelectric data by Solinger (1969). It is currently thought to arise from the reflection of light from the bright nuclear region, or galactic disk of M82, in an extensive halo of dust particles. In order to understand why other mechanisms are precluded we must also take into account the other observational data. A review of the evidence is therefore given in Chapter 6. We will now turn our attention to analysing the precision of our results by comparing them with the previous observations, and will return to a more detailed discussion of the implications and origins of the optical polarization in Chapter 7.

5.3.1 Polarization error analysis: A comparison with previous observations

In this section we make a quantitative comparison of the electronographic results with the photoelectrically-measured polarizations of Elvius (1964, 1967, 1969), designated by the letter E in table 5.11, Visvanathan and Sandage (1969), designated VS, and Angels et al (1975), designated A. The photoelectric measurements were all made with circular apertures considerably larger than the areas used in our analysis, which corresponds to the size of the seeing disc; Elvius used a diameter of 40" arc and Visvanathan and Sandage and Angels et al used 30" arc. It should be immediately noticed that because such large apertures have been used for the photoelectric measurements (i.e. 5 to 7 times the seeing disc), real polarization information will have been smeared out, whereas our electronographic measurement will record the variations. To enable us to compare the electronographic and photoelectric results we have summed the Stokes parameters from each 6" x 6" arc area of the electronographic map into square areas of equivalent sizes to those used by the photoelectric observers. Any discrepancy from comparing square and circular areas will be small and has therefore been neglected. All the regions identified in the last section as containing dubious electronographic measurements were excluded from the comparison (this has little effect as there are few points in common in these regions). This leaves a total of 37 points in common and the results of the comparison are recorded in table 5.11.

Elvius does not quote errors on her observations beyond saying that the instrumental polarization was less than 0.5%. However some locations were observed more than once, and these showed a scatter of between 1% and 6% in p and 6^{o} and 20^{o}

TABLE 5.11 : COMPARISON BETWEEN PREVIOUS OBSERVATIONS AND OUR MEASUREMENTS

NO	LOCATION		ELECTRONOGRAPHIC		PHOTOELECTRIC		Source	Area	I_{gal}/I_{sky}
	E*	N**	P%	θ°	P%	θ°		□" arc	
1	21.9	139.3	1.5 ± 1.0	85.9 ± 4	0.0 ± 1.0	-	E	42	1.5
2	23.9	90.0)	3.8 ± 1.5	136.8 ± 4	2.5 ± 0.3	120 ± 3	A	31	1.0
		)			1.6 ± 1.0	136 ± 8	E	42	1.0
3	25.9	287.1	26.5 ± 2.5	62.8 ± 4	32.4 ± 3.0	60 ± 3	VS	32	0.2
4	26.4	113.4	5.2 ± 1.5	142.1 ± 4	5.7 ± 1.0	132 ± 8	E	42	2.0
5	26.4	145.0	1.8 ± 1.5	26.8 ± 4	0.7 ± 0.5	20 ± 18	E	42	3.0
6	26.5	204.7	1.2 ± 1.5	43.3 ± 4	3.3 ± 2.0	21 ± 8	E	42	0.75
7	26.4	237.0	13.7 ± 1.5	58.0 ± 4	4.5 ± 1.0	37 ± 8	E	42	0.25
8	28.6	212.7	10.1 ± 1.5	42.0 ± 4	4.7 ± 1.0	28 ± 8	E	42	0.67
9	29.9	274.0	22.6 ± 2.5	60.4 ± 4	22.5 ± 3.0	53 ± 3	VS	32	0.2
10	30.2	290.0	20.2 ± 2.5	64.0 ± 4	21.8 ± 2.0	62 ± 8	E	42	0.2
11	30.9	138.0	0.8 ± 1.0	145.0 ± 15	0.3 ± 0.5	-	E	42	2.0
12	32.2	134.7	0.8 ± 1.0	158.0 ± 15	0.4 ± 0.5	10 ± 8	E	42	2.0
13	37.4	212.7	5.3 ± 1.0	74.5 ± 4	4.3 ± 1.0	50 ± 8	E	42	0.5
14	38.4	209.4	5.1 ± 1.0	74.0 ± 4	4.6 ± 1.0	46 ± 8	E	42	0.5
15	43.69	114.0)	12.1 ± 2.5	73.3 ± 4	14.0 ± 2.0	80 ± 8	E	42	0.5
	41.69	114.3)			0.4	19 ± 8	E	42	0.8
	42.8	116.6)	9.1 ± 2.5	72.6 ± 4	1.3 ± 2.0	4 ± 8	E	42	0.5
16	43.6	180.0	6.5 ± 2.5	82.4 ± 4	3.0 ± 1.0	65 ± 8	E	42	3.0
17	43.6	145.9	12.8 ± 2.5	86.8 ± 4	10.2 ± 2.0	79 ± 8	E	42	1.4
18	43.6	115.6	9.9 ± 2.5	87.1 ± 4	7.6 ± 2.0	81 ± 8	E	42	1.0
19	43.6	104.2	10.2 ± 2.5	61.2 ± 4	12.1 ± 2.0	61 ± 8	E	42	0.5
20	47.5	144.0	9.8 ± 2.5	69.4 ± 4	12.3 ± 2.0	59 ± 8	E	42	1.4
21	47.6	280.0	10.9 ± 2.5	94.8 ± 4	8.0 ± 2.0	84 ± 8	E	42	0.3
22	47.1	136.6	10.2 ± 2.5	75.0 ± 4	11.1 ± 3.0	78 ± 8	E	42	1.0
23	47.5	270.0	7.9 ± 2.5	112 ± 4	6.8 ± 1.0	91 ± 8	E	42	0.3
24	48.4	160.0	9.0 ± 2.5	65.7 ± 4	9.5 ± 2.0	48 ± 8	E	42	2.0
25	48.6	86.3	18.5 ± 2.5	69.7 ± 4	24.7 ± 1.0	75 ± 1	VS	32	0.3
26	49.6	264.0	1.2 ± 1.0	109.1 ± 4	1.4 ± 1.0	112 ± 8	E	42	0.5
27	52.4	204.0	2.4 ± 1.0	52.5 ± 4	0.6 ± 0.4	49 ± 8	E	42	2.0
28	53.2	250.8	2.4 ± 1.0	112 ± 4	1.4 ± 1.0	112 ± 8	E	42	1.5
29	55.6	148.5	10.7 ± 1.0	40 ± 4	14.1 ± 0.6	41 ± 1	VS	32	0.3
30	58.8	136.6	12.0 ± 2.5	19.6 ± 4	16.0 ± 3.0	31 ± 8	E	42	0.25
31	61.2	130.0	11.1 ± 2.5	50.6 ± 4	15.8 ± 0.9	43 ± 2	A	31	0.25
32	62.4	292.0	5.0 ± 2.5	156 ± 4	2.2 ± 1.0	123 ± 8	E	42	0.5
33	60.4	176.7	7.2 ± 2.5	44.6 ± 4	3.4 ± 1.0	28 ± 8	E	42	0.67

TABLE 5.11 (continued)

NO	LOCATION E^{*}	N^{**}	ELECTRONOGRAPHIC P%	Θ^{o}	PHOTOELECTRIC P%	Θ^{o}	Source	Area " arc	I_{gal}/I_{sky}
34	69.0	238.0	3.7 ± 1.5	175.7 ± 4	1.0 ± 1.0	172 ± 13	E	42	1.5
35	75.2	127.0	9.3 ± 1.0	44.3 ± 4	11.3 ± 2.0	44 ± 5	A	31	0.33
36	75.5	298.0	4.3 ± 1.0	111.0 ± 4	5.8 ± 1.0	128 ± 8	E	42	2.3
37	78.2	271.0	2.2 ± 1.0	146.5 ± 4	1.9 ± 1.0	154 ± 8	E	42	2.3

*In seconds of time relative to 9h 51m.

**In seconds of arc relative to $+69^{o}52'.0$.

N.B. 1 minute of time = 5.13 minutes of arc at $+69^{o}55'$.

TABLE 5.12 : ERRORS IN THE MAGNITUDE OF POLARIZATION

I_{gal}/I_{sky}	No. of Points	σ_T%	σ_{PE}%	σ_E%
>2	9	1.6	1.1	1.4
1 to 2	7	2.0	1.7	1.1
1 to 0.5	10	3.3	1.4	3.0
	8	2.6*	1.4	2.2
<0.5	11	4.5	2.0	4.0
	10	3.7**	2.0	3.1

*Excluding points numbers 8 and 15.

**Excluding point No. 7.

TABLE 5.13 : ERRORS IN POSITION ANGLE

I_{gal}/I_{sky}	No. of Points	δ_{θ}^{o}	δ_{PE}^{o}	δ_{E}^{o}
>2	8	12.0	8.0	8.9
1 to 2	6	8.6	7.4	4.4
1 to 0.5	7	13.0	8.0	10.2
<0.5 (All)	11*	10.4	5.8	8.6
Viswanathan + Angels only	6	4.9	2.9	4.2
Elvius only	5*	11.0	8.0	7.5

*Excluding point number 7

in θ. For locations in common with our data we have used the observed scatter in her data where available. For the other points we have followed Solinger (1964) in adopting a mean error of $\pm 8^{o}$ for θ, we estimate the mean error in p to be $\pm$ 1% for polarizations less than 7% and $\pm$ 2% for larger polarizations. For the data of Angels et al (1976) and Visvanathan (1969) we have used the errors quoted by the authors. The errors quoted on our electronographic results are mean values derived directly from the (P1-P2) and (ANG1-ANG2) data for each point on the map. As we noted in Chapter 4 the errors are different for each half-map of the galaxy. The mean error in p for strips 1, 3 and 5 (i.e. plates 13 to 16) is very consistent up to polarizations of ~15% and has a value of $\pm$ 1%, it then increases to $\pm$ 2% for larger polarizations. The mean error in p is somewhat larger for strips 2, 4 and 6 (plates 9 to 12). Points with a polarization less than ~10% have an uncertainty of $\pm$ 1.5%; between 10% and 25% the uncertainty is $\pm$ 2.5% and above 25% the error is $\pm$ 4%. The mean error of the position angles is $\pm 4^{o}$. A plot of the electronographic versus photoelectric polarizations is shown in Figure 5.17. The random scatter of the points about the ideal line indicates that no overall systematic error exists in the electronographic measurements. As might be expected the amount of scatter increases with decreasing intensity. This is shown quantitatively in table 5.12 which lists the computed rms difference σ_T between the photoelectric and electronographic measurements as a function of the ratio I_{gal}/I_{sky}. In general, σ_T will be composed of two independent quantities: the intrinsic rms error of the photoelectric measurements from the true value σ_{pE}; and a similar quantity σ_E for the electronographic results. If we assume that the photoelectric errors are entirely random then σ_{pE} will be equal to the quoted accuracy of each measurement. The values of σ_E representing the intrinsic rms errors of the electronographic polarization measurements from the true values can then be calculated from

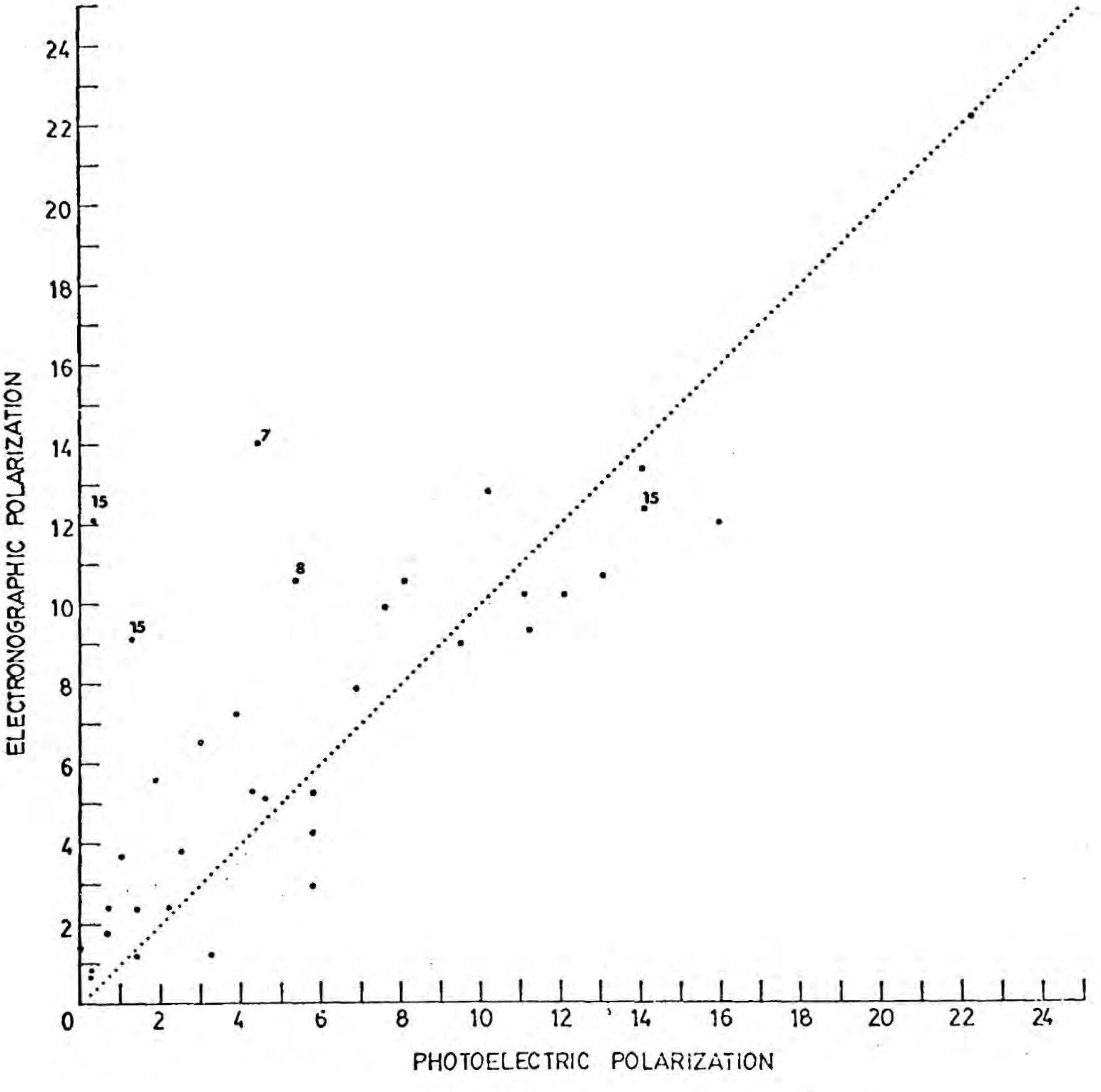

Figure 5.17 Plot of the electronographic polarizations against photoelectric polarizations of Elvius (1964, 1967, 1969), Viswanathan & Sandage (1969) and Angel et al (1975).

$$\sigma_T^2 = \sigma_{pE}^2 + \sigma_E^2 \qquad (5.21)$$

The computed rms values of σ_{pE} and σ_E are also listed in table 5.12. For the regions of the galaxy brighter than the sky background the electronographic error is comparable in size with the photoelectric error, being between 1% and 1.4%. This figure agrees well with the mean error derived from our internal consistency. For regions fainter than the sky background the electronographic error increases by between 3% and 4%, which is about twice the photoelectric error, and is slightly larger than the estimate from our internal consistency. If we examine table 5.11 more closely we see that two of the points, numbers 7 and 8, with brightness ratios less than 1.0 have electronographic polarizations over 3 times the observed photoelectric polarizations. Such large discrepancies do not appear elsewhere in the data except for possibly point 15 where the three measurements made by Elvius are wildly different. Comparing this point with point 18, which is almost coincident, we concluded that the two low polarization measurements are anomalous and have not used them in the error analysis. For points 7 and 8 the explanation appears to lie in a localized patch of dubious measurements in either our data or Elvius' data (which it is is not clear because the polarization changes rapidly in this vicinity). If we exclude points 7 and 8 from the error analysis the electronographic error becomes appreciably smaller: it drops to $\pm$ 2.2% for points with a brightness ratio between 0.5 and 1.0 and $\pm$ 3.1% for points fainter than 0.5. Both these figures are in good agreement with the error estimates obtained from the (P1 - P2) data.

A similar comparison can be made for the position angle results. Table 5.13 lists the computed rms difference in position angle δ_θ as a function of the brightness ratio I_{gal}/I_{sky}. Also included are the values of δ_{pE} and δ_E representing the intrinsic errors from the true values of position angle for the photoelectric and

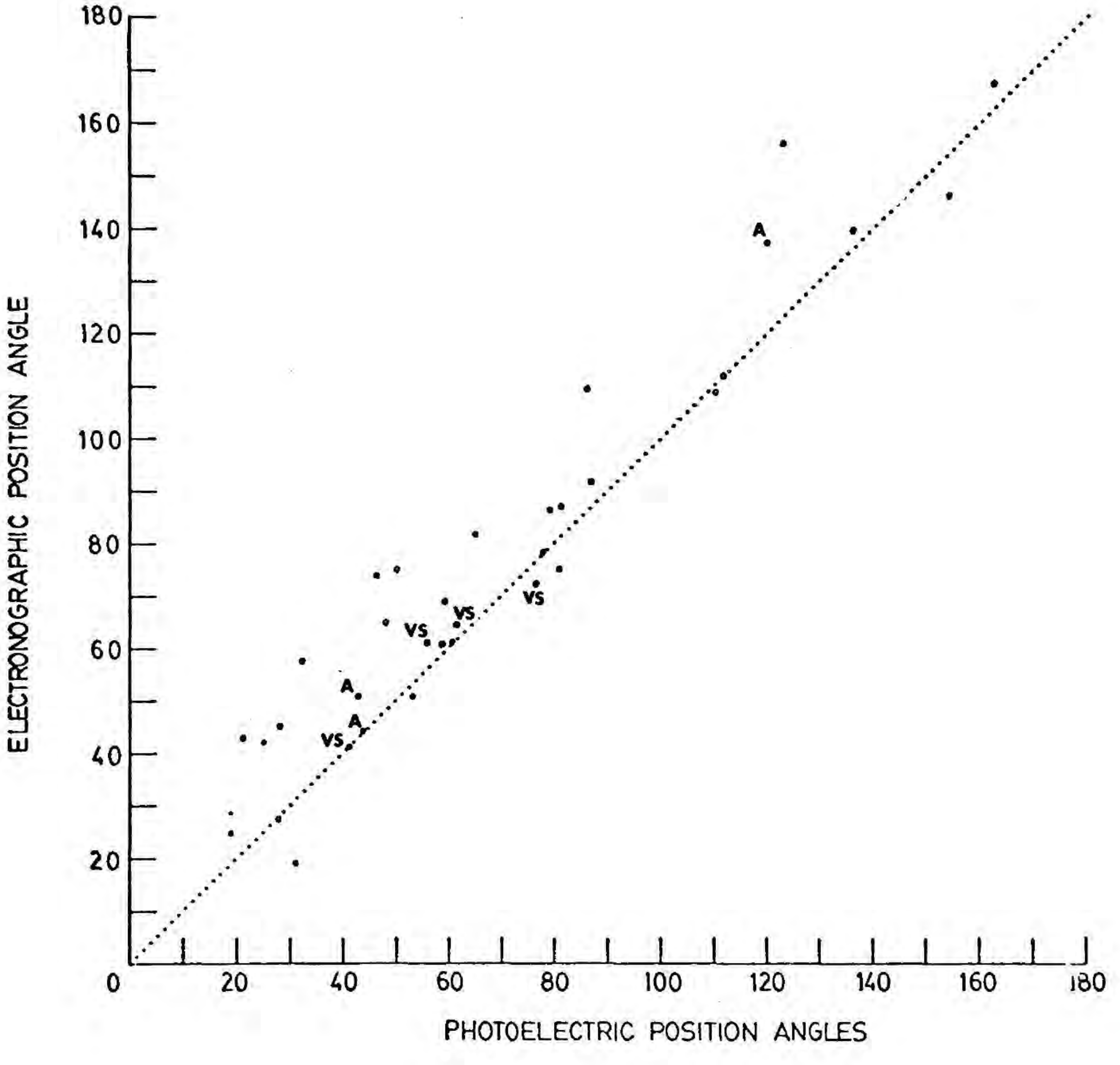

Figure 5.18 *Plot of electronographic position angles against photoelectric position angles of Elvius (1964, 1967, 1969), Viswanathan & Sandage (1969) and Angel et al (1975).*

electronographic measurements, respectively. There is no apparent systematic trend in the variations of δ_θ. For points with a brightness ratio between 1 and 2 the computed δ_E is $\pm 4.4^o$ which agrees very well with the estimate from the (ANG1-ANG2) data. For points with a brightness ratio greater than 2 the error is $\pm 8.7^o$, about twice that predicted. However the accuracy in determining the position angle depends not only on the intensity of the light but also on its polarization. For polarizations less than 2% the position angles must be regarded as being rather ill-defined and this accounts for the increased uncertainty in both δ_θ and δ_E. Points with a brightness ratio between 0.5 and 1.0 have a mean rms uncertainty of ± 10.2 and point fainterthan 0.5 have an uncertainty of $\pm 8.6^o$. Both these figures are comparable in size to the photoelectric uncertainties (ie 8.0^o and 5.8^o respectively) but are twice the value expected on the bases of the (ANG1 - ANG2) data. It might be argued that the value of δ_E is artifically low because we have overestimated the size of the error in the Elvius position angles, which comprise most of the photoelectric data. To examine this possibility we have segregated the Elvius data from that of Angels and Visvanathan and repeated the analysis for the two groups. Since the VS and A data is confined to faint regions this was only possible for points with a brightness ratio less than 0.5. The results of the analysis are given in table 5.13. Taking the E data alone the rms difference between the photoelectric and electronographic position angles is $\pm 11.0^o$ whereas for the VS + A group it is only $\pm 4.9^o$. Even though the rms error on the VS + A observations is only $\pm 2.9^o$ we still obtain a value of δ_E of only $\pm 4.2^o$, whereas the E data gives a δ_E of $\pm 7.5^o$ even using a δ_{pE} value of $\pm 8^o$! There is thus a considerable difference in the quality of the agreement between our data and the two photoelectric groups, and contrary to the above assumption the Elvius data gives the largest discrepancy. The value of $\pm 4.9^o$ for the

VS + A data agrees well with out accuracy calculated from our internal consistancy whereas the value for the E data is twice as large. At face value this suggests that we have underestimated the error in the Elvius position angles, or alternatively that they are systematically different from those of Visvanathan, Angels et al and ourselves. However we must also reconcile this result with the smaller error obtained for the E data points with brightness ratios between 1 and 2. Assuming that we have satisfactorily explained the larger error for points of low polarization (i.e. brighter than 2) a systematic difference between points fainter and brighter than the sky background could be produced by an incorrect sky subtraction. Since the effect is not apparent in the magnitude of the polarization the problem is only in the position angle of the background polarization. The evidence is however inconclusive and it is most probable that we have merely underestimated the error in the Elvins angles; the result implies that the error should in fact be $\pm 10.2^{o}$ for points fainter than 0.9.

The mean difference in position angle for the photoelectric and electronographic data is 7.7^{o}, and since the standard error on this mean is 8.5^{o}, the result shows that there is no effective difference between the angles of the two data sets.

On the basis of the results of this analysis we do not consider it necessary to apply systematic corrections to either the electronographic polarizations or position angles. Furthermore, combining these results with the cloth measurements, standard star observations and our internal consistency we estimate the standard error on the polarization to be 1.4% for polarizations less than 10%, 2.2% for polarization between 10% and 25% and 3% for polarization larger than 25%, and the standard error on the position angles to be 4.2^{o}. These errors compare favourably with those of Elvius. Visvanathan and Sandage (1969) achieved accuracies of 1% in p and 1.5^{o} in θ in bright regions of the galaxy and 6% in p and 8^{o} in θ for faint regions (Visvanathan and

Sandage 1972). The accuracy of our polarization measurement is comparable with theirs and so is our measurement of the position angle for the fainter regions of the galaxy, but they are more accurate in determining θ in the bright regions.

Similar conclusions hold for the photoelectric observation of Angels et al (1975). However, our observations have at least 5 times the spatial resolution are 20 times more numerous and have been obtained in a small fraction of the time required for the photoelectric measurements. The merits of the technique of electronographic polarimetry developed in the thesis therefore speak for themselves.

References

Axon, D.S. and Ellis, R.S. 1977 M.N.R.A.S.

Angels, J., Schmidtt, G. and Cromwell, R. 1975 Preprint, Ap. J. in press.

Ashburn, E.V. 1972 J. Geophys. Research 57, p. 85.

Behr, A. 1959 Verofferiluchangen U. Streriwarte Gottingen No. 126.

Billings, B.H. 1957 J. Opt. Soc. Amer., 41, p. 966.

Elvius, A. 1964 Lowell Obs. Bull., 5, p. 271.

1967 A. J., 72, p. 794.

1969 Lowell Obs. Bull., 7, p. 14.

Gehrels, T. 1974 Planets, Stars and Nebulae Studied with polarimetry, U. of Arizona Press.

Gerrant, A. and Birch, J.M. 1975 Introduction to matrix methods in optics, Appendix D, p. 315, Wiley.

Hall, J.S. 1958 Pub. U.S. Naval Obs. and Ser. Vol. 17, No. VI.

Loden, L.O. 1961 Stockholm Obs. Ann., 21, No. 7.

McMullan, D. 1975 Private Communication.

Penny, A.J. 1976 PhD. thesis, University of Sussex.

Shurcliff, W.A. 1962a Polarized light, p. 123, Oxford University Press.

1962b ibid, p. 23, table 2.1.

Solinger, A.B. 1969 Ap. J. (Letters), 158, L25.

Visvanathan, N. and Sandage, A. 1969 Ap. J., 157, p. 1065.

1972 Ap. J., 176, p. 57.

Worthing, A.U. 1926 J. Opt. Soc. Amer., 13, p. 635.

CHAPTER 6

OBSERVATIONAL PROPERTIES OF THE GALAXY M82

M82 (NGC 3034) is a peculiar-shaped galaxy of dimensions 13.4' x 8.5' arc, and is situated in Ursa Major (R.A. (1950) 9H 57.9M, DEC. (1950) + 69^{o} 56'). Holmberg (1950, 1958) has classified it as Irr II, which means that the galaxy shows no rotational symmetry; and photographic images show no signs of resolution into stars, as well as the presence of prominent dust features.

For a long time M82 has been believed to be associated with the nearby galaxy M81. Figure 6.1 shows the four constituent members of the M81 group; M81 and NGC 2403, both of which are Sc type galaxies, and M82 and NGC 3077 both of which are type Irr II. Very few Irr II galaxies are known, and it is quite remarkable that two such objects should occur in the same region of the sky. Recent 21 cm observations by Davies (1969) (Figure 6.2) provide conclusive evidence that the galaxies do indeed form a physically connected system. Neutral hydrogen is clearly visible beyond the Holmberg radii of the constituent galaxies, bridging them together (there is in fact twice as much neutral Hydrogen outside the Holmberg radii as inside). Of particular interest is the presence of a neutral Hydrogen companion to the SW of M81, 0.7^{o} x 0.5^{o} across, and 0.7^{o} SW of M81, without an optical counterpart, which

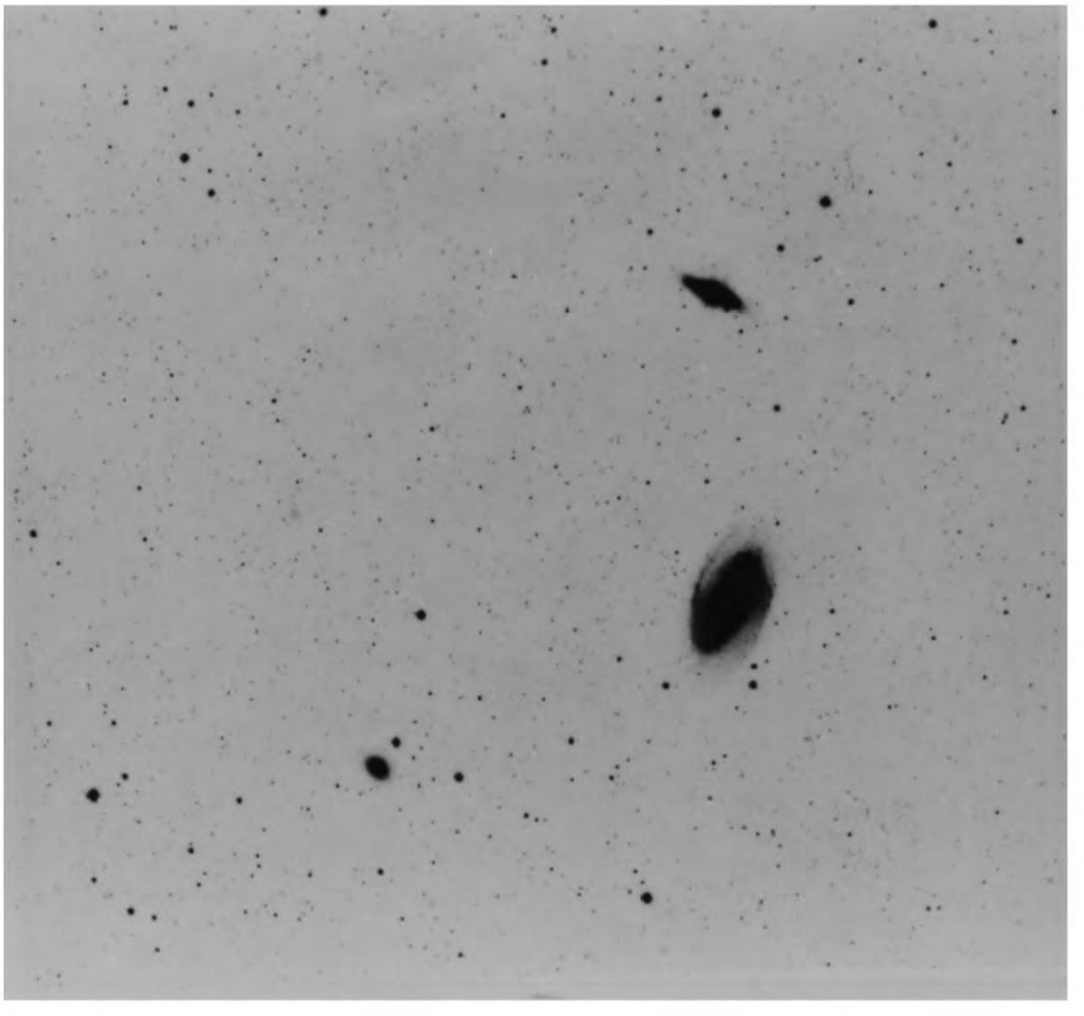

Figure 6.1 The M81 GROUP

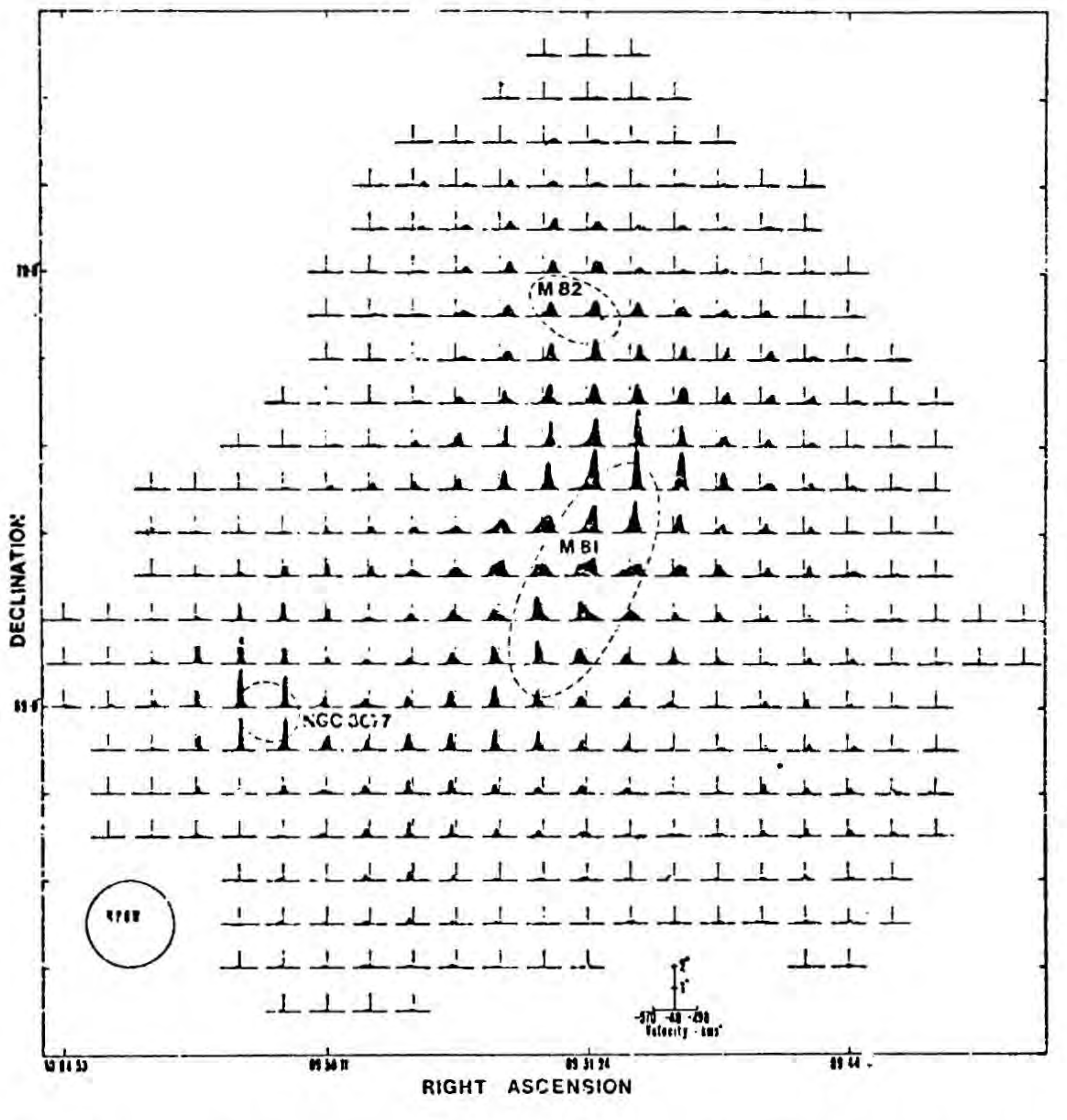

Figure 6.2 *Neutral hydrogen spectra taken in the M81/M82/NGC 3077 group. The central velocity of each spectrum is -40 km s^{-1} relative to the Sun; each spectrum extends $\pm$ 530 km s^{-1}. The survey was continued in each direction until the signal fell to below 0.2K in brightness temperature. Holmberg optical dimensions for each galaxy are shown by a broken line. (From Davies 1969).*

lends further support to the hypothesis that this is a region of unusual activity. Examination of the velocity directions shows co-rotation with M81, except in the region of NGC 3077 and the SW companion, and on this basis we may establish the distance of M82 as 3.2 Mpc, or 9.8×10^{24} cm (Tamman and Sandage 1968). The importance of establishing the distance of M82 is that it enables the geometry of the galaxy, and the size of its optical features to be determined. Assuming overall dimension similar to our galaxy, and applying simple geometry yields, the useful results

$$1 \text{ arc sec} \sim 16 \text{ parsecs}$$
$$1 \text{ arc min} \sim 960 \text{ pc} \sim 1 \text{ kpc}$$

M82 has a visual magnitude of $9^{m}.68$ (i.e. it has a similar surface brightness to the crab nebula), and has an integrated spectral type of A5 (a young spectral type, c.f. the Sun is G2) (Humason, Mayall and Sandage 1956), which contrasts with its colour indices (de Vaccouleurs 1961).

$$B - V = 0.^{m}87 \quad (0.^{m}73 \text{ after correction for galactic reddening})$$
$$U - B = 0.^{m}33$$

N.B. The typical B-V colour index for an 'A-type galaxy' is $0.^{m}6$ (Humason et al 1956). This discrepancy, to the red, of the colour index with respect to the spectral type has been put down to dust scattering (Morgan and Mayall 1959), and has been estimated as being $\sim 3^{m}.0$ (Peimbert and Spinnrad 1970).

The velocity of recession, as measured from optical absorption lines, is found to be + 281 km Sec^{-1} (Mayall 1960), and suggests from the tilt of the lines, that the galaxy is rotating about its minor axis. This value has

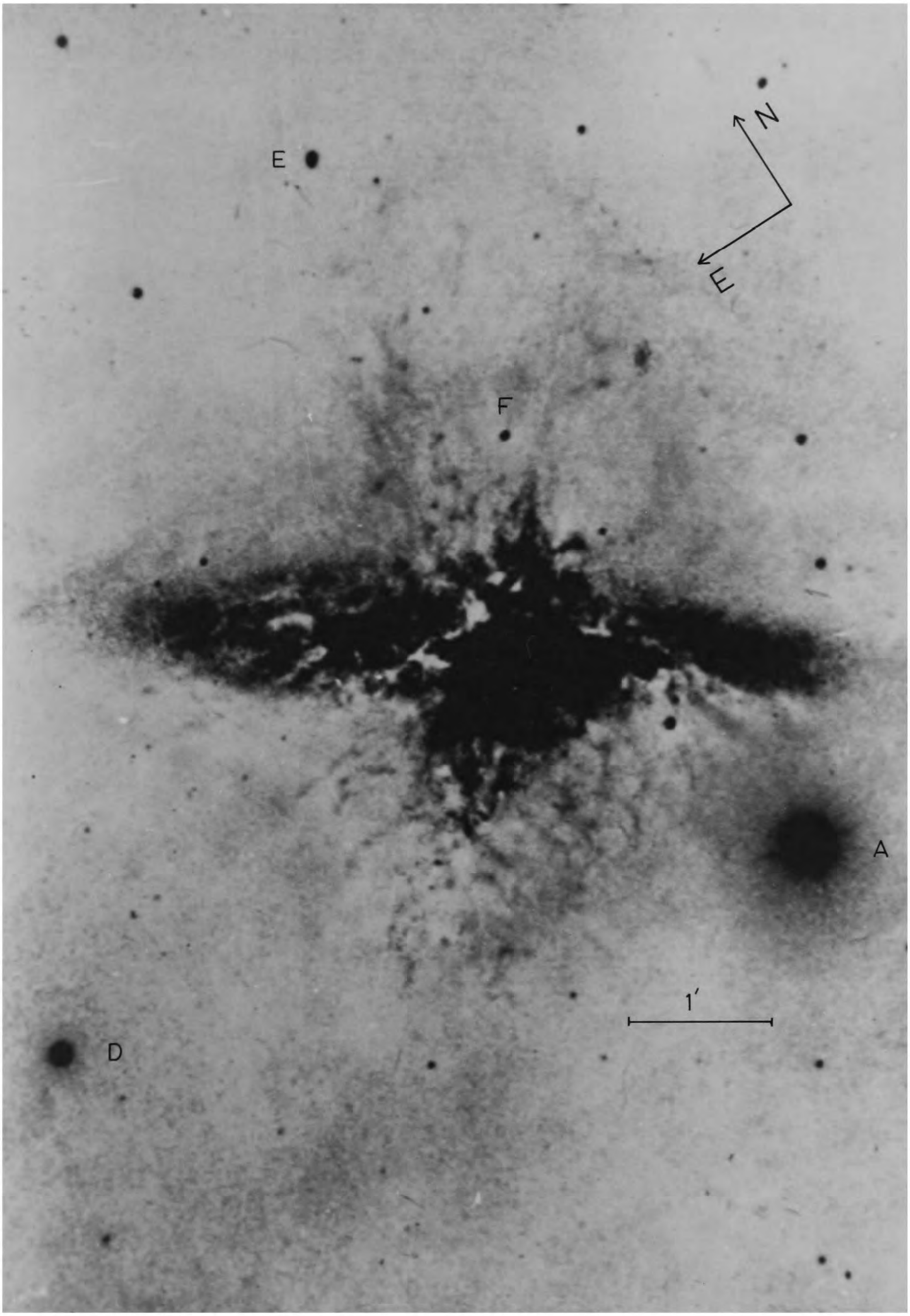

FIGURE 6.3 A PHOTOGRAPH OF M82 IN Hα EMISSION LIGHT SHOWING THE FILAMENTS [LYNDS & SANDAGE 1964]

been disputed by Volders and Hogbom (1961), who found a value for the recessional velocity of + 190 km Sec^{-1}, based on 21 cm emission line measurements. However, Solinger (1969) has pointed out that their measurements must be viewed with scepticism, because of their poor resolution. Since then, Guelin and Weliachew (1970), and Weliachew (1971) have determined the recessional velocity from 21 cm absorption lines, and found a somewhat higher value of + 379 km Sec^{-1}. The importance of these discrepancies will be discussed in detail later.

The most remarkable feature of M82 is the system of luminous filaments eminating from the centre of the galaxy in the direction of the minor axis. Direct photographs of the galaxy in Hα emission light (Figure 6.3, Lynds and Sandage 1964) showed that the filaments radiate mainly at this wavelength (6500 A^{o}), and extended to some 3'arc (3000 pc) from the galactic centre. The appearance of looping structures seemed to indicate that they were a consequence of magnetic field lines, and comparison with the Crab nebula (Figure 6.4) shows great structural similarity, possibly implying a similar explosive origin.

Previously, Lynds (1961) had identified M82 with the radio source 3C231, and measured its radio spectrum between 1.5 and 3.0 GHz, and discovered that it was very flat, having a spectral index $\alpha = -0.17$ (α is defined as d (log S_ν)/d log ν where S_ν is the flux at frequency ν), which was very similar to that of the Crab nebula ($\alpha = -0.23$). This led Lynds to suggest that the observed optical luminosity of the filaments might be explained by an extrapolation of the radio spectrum, if the synchrotron process was operating in the galaxy. In their paper of 1964, Lynds and Sandage also

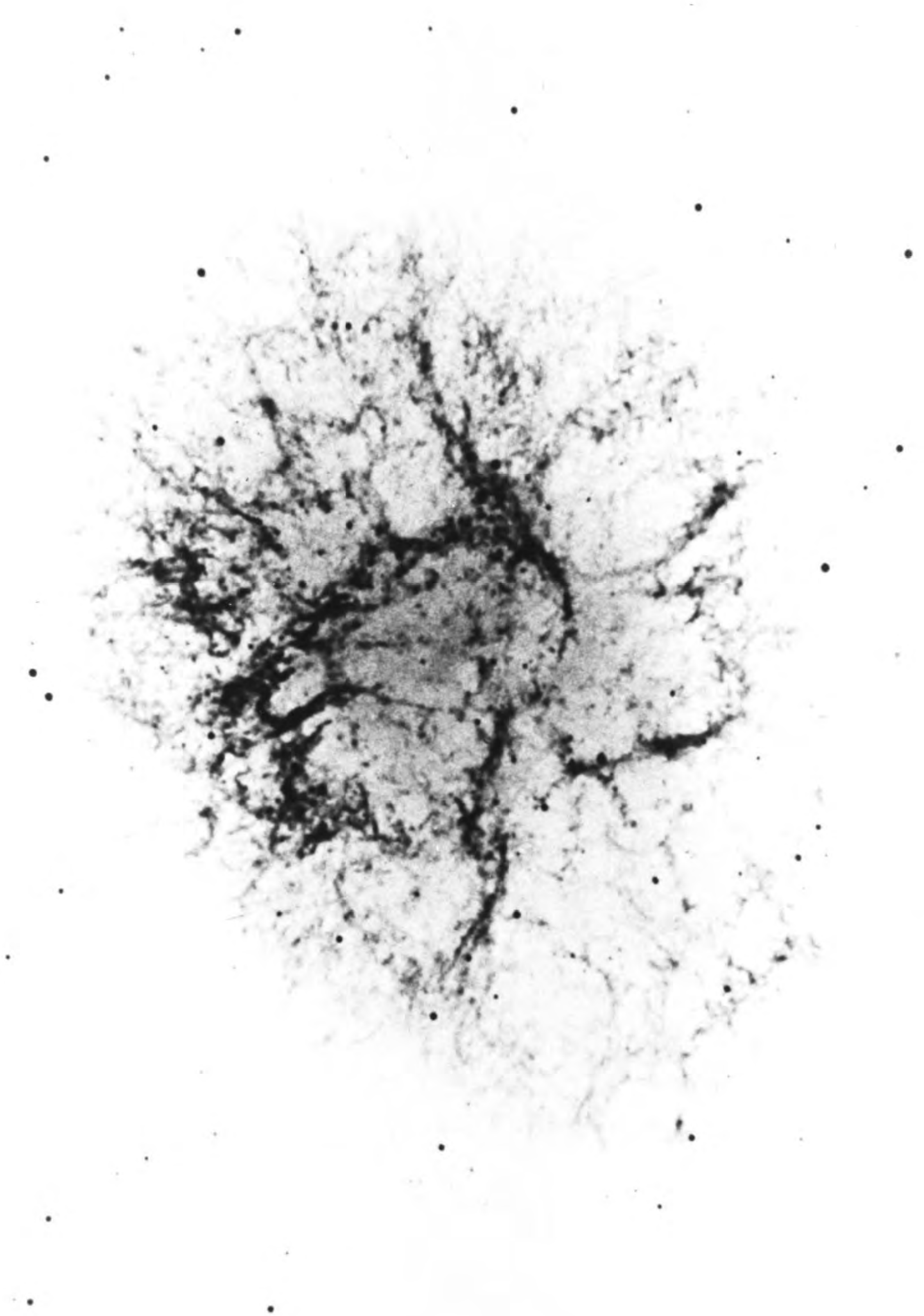

FIGURE 6.4 THE CRAB NEBULA IN Hα LIGHT
[Trimble, Private communication]

presented the results of an emission line spectrum study of the galaxy. The spectrograms where orientated along the minor axis of the galaxy. The spectra showed strong emission lines of $H\alpha$, $H\beta$, $H\delta$ and forbidden lines of [N II], [S II], [O II], and [O III], out to 2′ arc from the galactic centre (Figure 6.5). The lines were inclined to the dispersion direction, indicating a velocity component orthogonal to the major axis of the galaxy. In order to determine whether this was consistent with an explosion or an implosion the orientation of the galaxy had to be determined. By studying the asymmetry of dust features they concluded that the galaxy was inclined by 8^{o} to the line of sight, such that the Northern side was farthest away. Applying this geometry, and combining their results with the recessional velocity, and rotation curve measurements of Mayall (1960), they interpreted the slope of the lines as due to movement of gaseous matter away from the centre of the galaxy with a velocity 1000 km Sec^{-1}. Lynds and Sandage extended and refined Lynds earlier suggestion and proposed that the filaments were indeed forced out by an explosion, and traced out the magnetic field lines in the galaxy in a manner similar to those of the Crab nebula. Although the initial explosion may have been isotropic they argued that debris in the fundamental plane, the build up of magnetic pressure, or possibly inelastic collisions with the abundant gas inhibited such expansion, resulting in most of the ejected matter travelling, in the direction of least constraint, i.e. along the minor axis. If sufficient energy could be put into relativistic electrons then the observed radio spectrum, optical luminosity, colour distribution, and emission line structure of the galaxy could be accounted for by synchrotron emission. From the narrowness of the observed emission

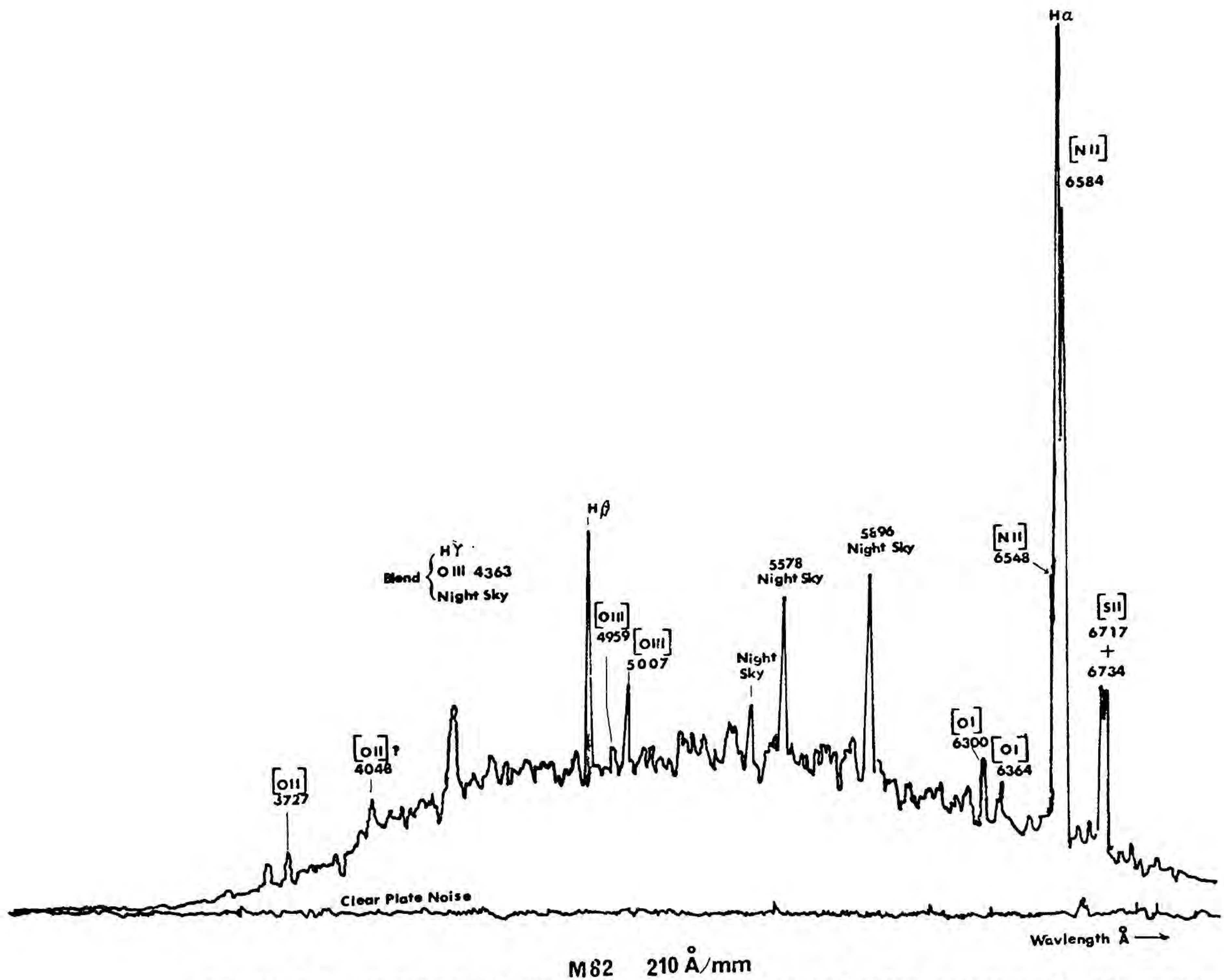

Figure 6.5 *Spectrum of M82 taken on the 90" Isaac Newton Telescope by the Author.*

lines they further concluded that the filaments were optically thin.

Shortly afterwards Burbridge, Burbridge and Rubin (1964) reported the results of a more extensive emission line study of the galaxy, and broadly confirmed the results of Lynds and Sandage.

The most important consequence of this model is that since the synchrotron mechanism is invoked, the light from M82 should show a high degree of linear polarization ($P \gtrsim 70\%$), and the plane of polarization should be orthogonal to the field direction, i.e. orthogonal to the filaments. This prompted polarization studies of the filaments in an attempt to prove the hypothesis.

6.1 Optical Polarization of M82; the Historical Development

Initial photographic polarization measurements in the filaments of M82 by Sandage and Miller (1964) indicated that they were very highly polarized, as much as 100% in some regions, and that the E-vectors were perpendicular to the filamentary directions. This appeared to be dramatic confirmation of the synchrotron hypothesis of Lynds and Sandage. However, photoelectric polarization measurements made by Elvius (1963) gave small polarizations ($P \sim 1\%$) in the main body of the galaxy, and polarizations increasing up to a maximum of only 16% as the distance from the fundamental plane of the galaxy increased. Though her measurements were confined to the central region of the galaxy, and some of the observed polarizations were large, they were still considerably smaller than those reported by Sandage and Miller, who had used a rather dubious photographic masking technique in deriving their results. (Subsequent measurements have shown that their technique is completely unreliable for polarization studies e.g. Elvius (1969)). Further to her measurements Elvius (1963) proposed an alternative mechanism for producing the observed polarization. Her argument was that light from bright parts of the galaxy (later to be refined to a bright galactic nucleus) was scattered by numerous dust clouds, by a mechanism such as Rayleigh scattering, thus producing highly polarized light. If this were the case, and the light source was the nucleus of the galaxy, the E-vector of the polarized light would be expected to be orthogonal to the radius vector at that point rather than the filamentary direction, thus enabling the two hypotheses to be distinguished. Later measurements by Elvius (1967, 1969) and Elvius and Hall (1967), using more refined techniques, extended and confirmed her previous measurements but were confined to bright regions in the lower reaches of the filamentry structure, though polarizations as high as 40% were reported.

Based on the symmetry of the observed polarization pattern Solinger (1969, a, b, c) proposed a third alternative, in which the polarization was produced by Thompson scattering by electrons which were ejected by an explosion. The filamentary medium being forced out by this event, and subsequently heated by a following shock-wave. A more detailed discussion of the requirements and predictions of this model will be given later, but the salient point for the present discussion is that again the polarizations would be expected to be large, with the E-vector orthogonal to the radial direction. Sandage and Viswanathan (1969) made photoelectric polarization and colour measurements of areas in the outer regions of the filamentary structure, at distances varying from 66" to 196" arc from the galactic nucleus. The results showed polarizations varying from 12 to 32%. The position angles of the E-vectors were in general perpendicular to the direction of the associated filaments. Unfortunately the measurements were made very close to the minor axis of the galaxy, where the radial and filamentary directions were virtually coincident, and thus the results were consistent with all the models. By extrapolating the synchrotron spectrum into the optical

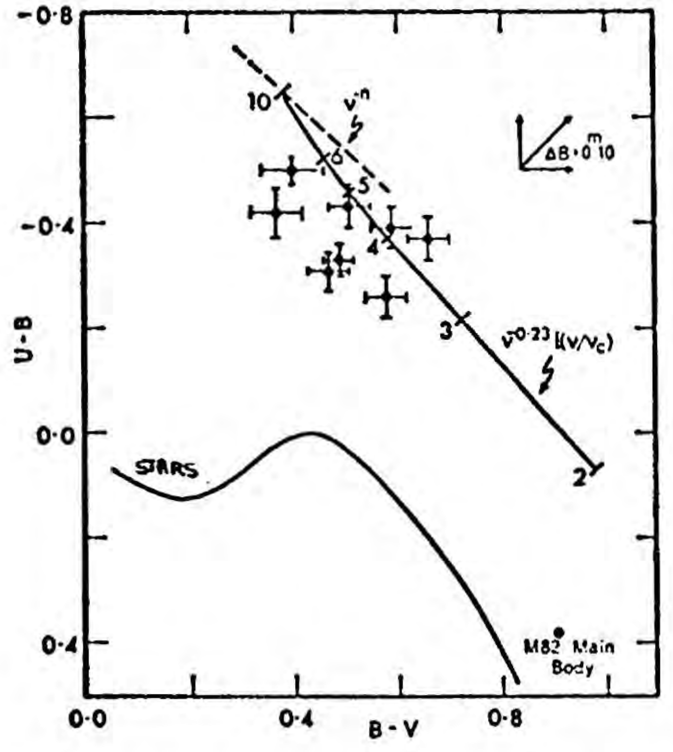

Figure 6.6(a) (U-B, B-V) diagram. Dashed line is for power law spectrum. Solid line gives result from electron cut off at ν_c. (Sandage and Viswanathan 1969).

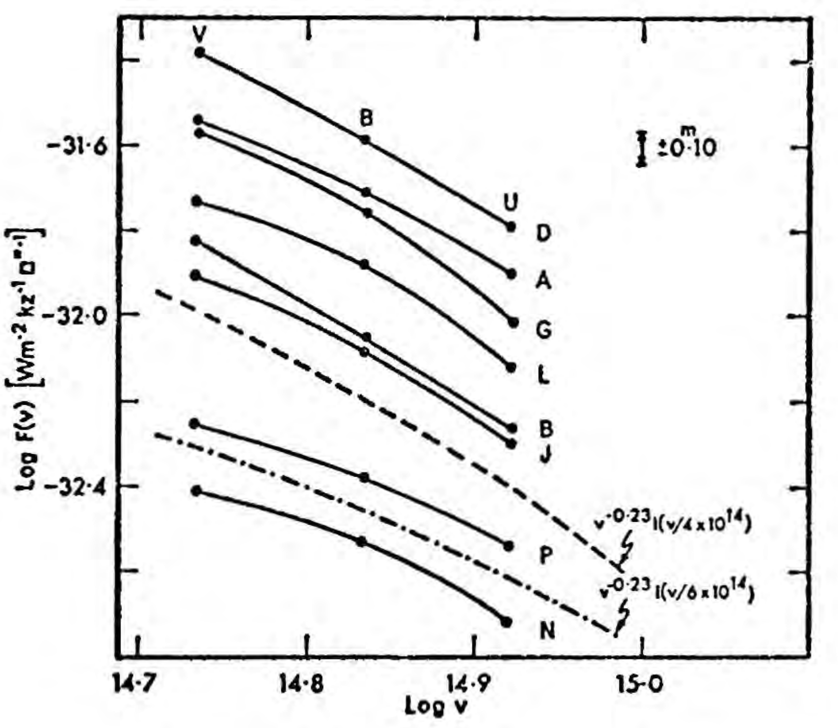

Figure 6.6(b) Continuum spectra of eight regions shown in (a) in absolute flux units. Segments of two theoretical synchrotron spectra arbitrarily normalized are shown as dashed and dotted lines. (From Sandage and Viswanathan 1969).

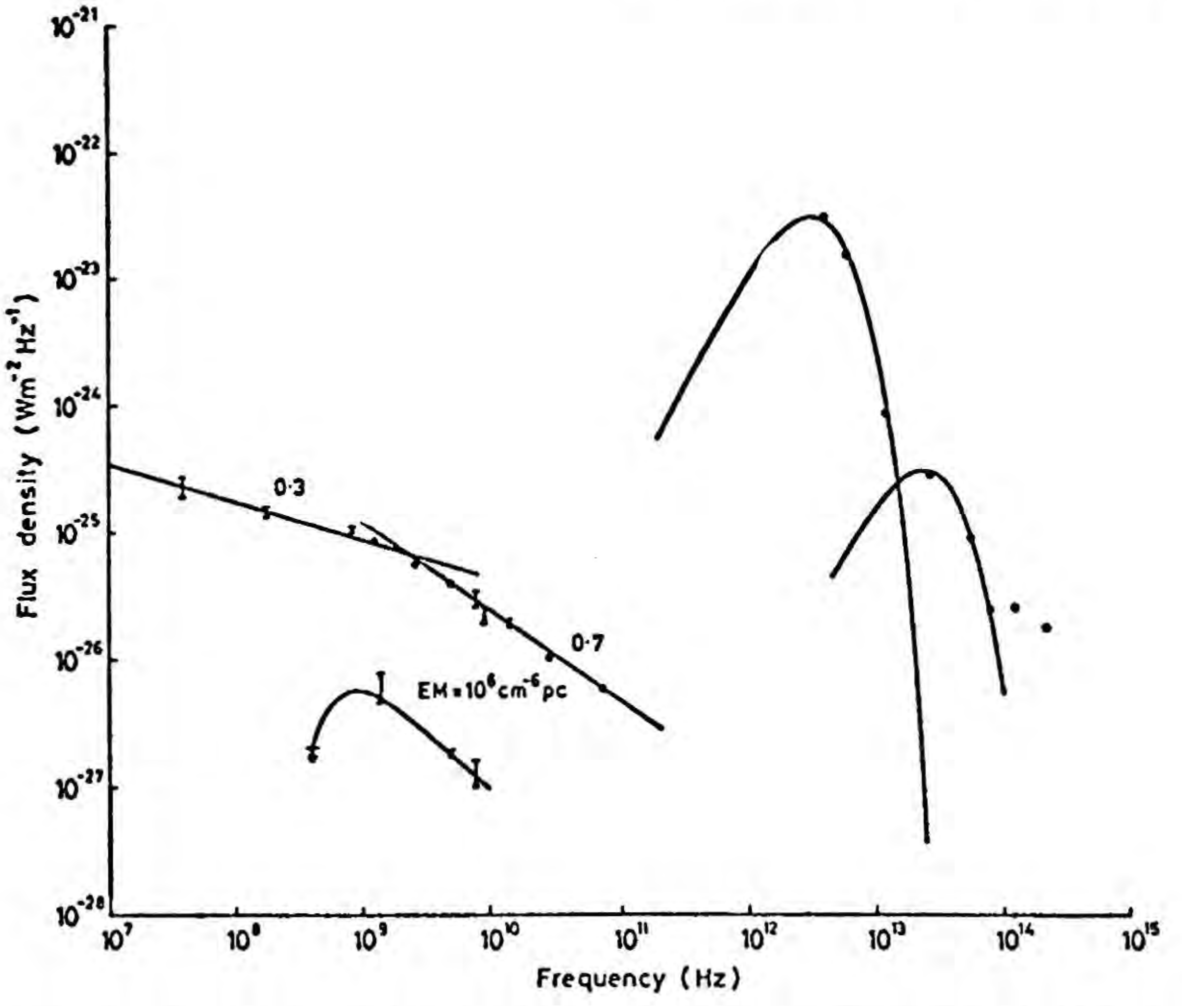

Figure 6.7 The Radio Spectrum of M82. The lower curve is that of the compact source designated A by Hargrave (1974) and comparison spectra for black bodies with T = 60 and 45^{O}K are shown. (From Hargrave 1974).

region they also showed that it was possible to explain the observed colours in the galaxy (Figures 6.6). However, attempts to account for the observed Hα emission by a further extrapolation of the spectrum below the Lyman limit produced an intensity of Ultra Violet (U.V.) photons that was too small by an order of magnitude. Further observations were obviously required to distinguish between the models, and the results of these and the consequences for each model will be discussed separately.

6.2 Failure of the Synchrotron Hypothesis

Lynds and Sandage had originally suggested the synchrotron hypothesis for three reasons:

1. It linked together the radio spectrum and the observed polarization.
2. It provided a mechanism for producing the Hα emission, and the observed variations in colour index.
3. It explained the structure of the galaxy by analogy to the smaller scale explosion in the Crab nebula.

Some discussion on each of these points has already been presented, and though the observational data did not conclusively support the model, it did not exclude it either. The new observational data discussed below was to destroy the agreement with the model and force its abandonment.

6.2.1 The Radio Spectrum

The original predictions of Lynds and Sandage were based on an extrapolation of the flat radio spectrum ($\alpha = -0.23$) observed by Lynds (1961) in the range 1.5 - 3 GHz. Later measurements by Kellerman (1964) at 21 cm gave a spectral index $\alpha = -0.29 \pm 0.006$, and in the range 21 - 10 cm $\alpha = -0.3$, which were eminantly consistent with Lynds result.

However, measurements at 3.75 cm by Dent and Haddock (1965) gave a flux which was smaller than that predicted by $\alpha = -0.30$, being more consistent with a spectral index $\alpha = -0.57$ (Dent 1965). Further measurements by Dent and Haddock (1966), Berge and Seielstad (1969), Kellerman and Pauliny-Toth (1969, 1971) and Kellerman et al (1969) confirmed that above 3 GHz there was a sharp change of slope in the spectrum, but not to $\alpha = -0.57$, but to $\alpha = -0.7$ (Figure 6.7), thus invalidating the original extrapolation. The revised spectrum gave a U.V. photon flux two orders of magnitude lower than that predicted by $\alpha = -0.3$, eliminating any possibility that synchrotron emission could explain the Hα emission, or the colour distribution in the galaxy (Peimbert and Spinnrad 1969). The optical measurements discussed below also disagreed with the predictions of the theory and showed it to be unworkable in M82.

Moreover, measurements at 5 GHz by Hargrave (1974) have subsequently shown that the radio emission is actually confined to a region 50" x 15" arc in the centre of the galaxy , implying a negligible radio flux in the filaments. More important, however, Hargrave's (1974) attempt to map the linear polarization of the galaxy at this frequency resulted in the discovery that no part of the source was measurably polarized, thus providing conclusive evidence that the synchrotron model is incorrect. (The possibility of complete Faraday depolarization in the radio and yet not in the visible seems unlikely).

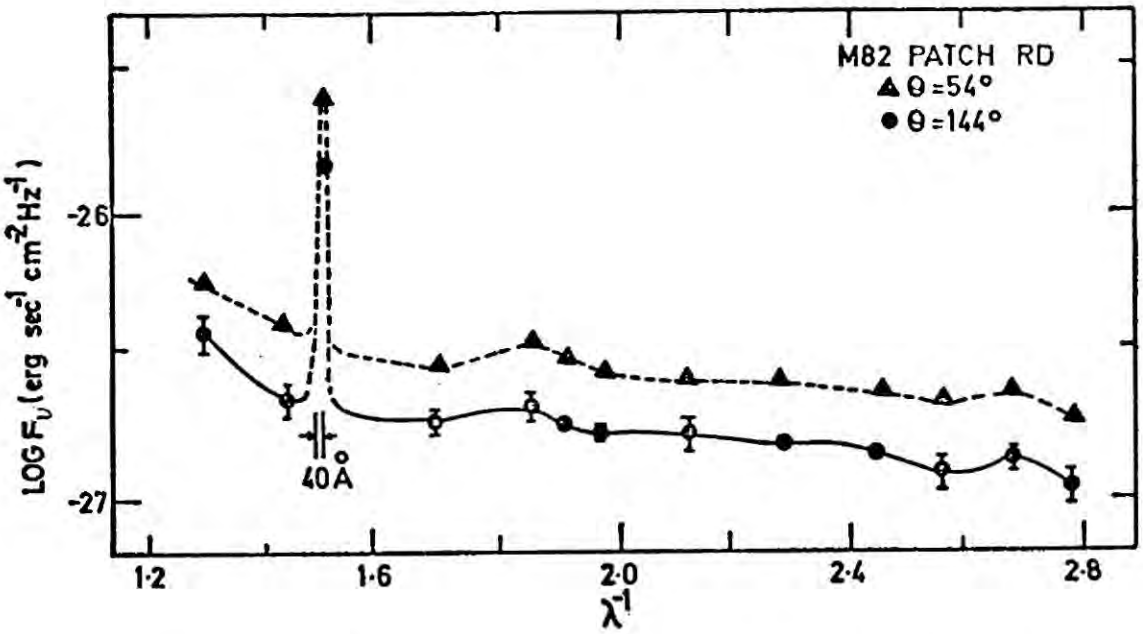

Figure 6.9 Energy distribution of Patch Rd reduced to absolute units (per area of the entrance aperture of diameter 9.9") for the external polarization angles 54° and 144°. The 40 Å band pass is shown with the Hα + [N II] complex superposed. (From Viswanathan and Sandage 1972).

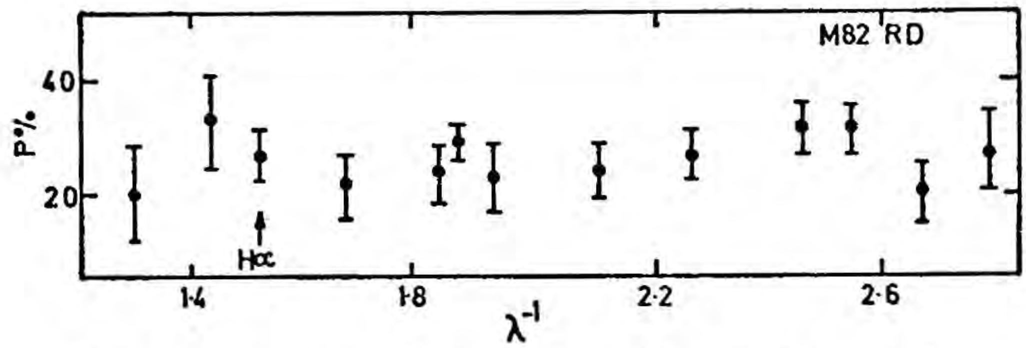

Figure 6.10 Polarization of radiation from Patch Rd in each channel of the scanner as a function of wavelength. Error-bars are 1σ in length. (From Viswanathan and Sandage 1972).

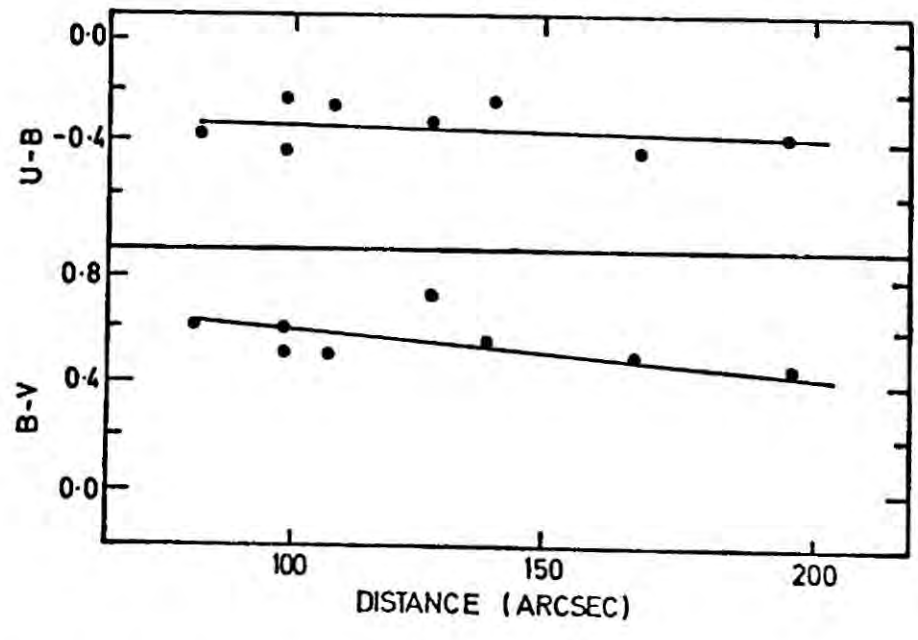

Figure 6.11 Change of colour of the filaments with distance from central M82A region. (From Viswanathan and Sandage 1972).

6.2.2 Optical Polarization Measurements in the Outer Filaments and the Polarization of the Hα Emission Line

In order to provide a conclusive test to decide between the synchrotron model and the scattering models Viswanathan and Sandage (1972) observed five new regions, in the outer filamentary structure, which were chosen so that the perpendicular to the filament in each region made an appreciable angle to the radius vector. These five regions were exceedingly faint, and for the faintest patch the signal was less than 1% of the sky background. The measurements of θ (the position angle of the E-vector) agreed to within 2σ (two standard deviations) with those predicted by the scattering models, but differed by 4 to 9σ from the predictions of the synchrotron model (Table 6.1 and Table 6.2). The data thus suggested that the filaments could not be producing the polarized light by synchrotron emission but were producing it by a scattering process. One region (designated patch RD by Viswanathan and Sandage) was measured for polarization in the wavelength range 0.34 - 0.8 μm with a multichannel spectral scanner and polarimeter in order to determine the wavelength dependence of the polarization. One of the channels was centered on the Hα emission line, using a band width of 0.004 μm, so that there was little contamination from the continuum. Unexpectedly the observations showed that the Hα + [N II] emission lines (unresolved with the system) were highly polarized with $P = 27 \pm 3\%$ and with a position angle $\theta = 54 \pm 3^{\circ}$. The total intensity in the emission line being 5.6 times as large as that in the continuum, in the range investigated, showed that contamination was unimportant (Figure 6.9). However, this result became even more remarkable when comparisons with the continuum showed that this was also highly polarized (as expected), but with the same magnitude and at

Table 6.1 Comparison of Predicted and Observed Polarization Angles on the Synchrotron Hypothesis (Viswanathan and Sandage 1972).

Name (As designated by V and S 1972)	Predicted Angle (degrees)	Observed Angle + rms (degrees)	$\Delta\theta/\sigma$
QC	40^{o}	80 ± 10	4.0
QV3	24^{o}	58 ± 9	3.8
QV1	16^{o}	55 ± 10	3.9
QB	64^{o}	120 ± 6	9.3
QP	0^{o}	5 ± 5	1.0

Table 6.2 Summary of Predicted and Observed Polarization Angles for Scattering From a Central Source (Viswanathan and Sandage 1972).

Name (As designated by V and S 1972)	Predicted Angle (degrees)	Observed Angle	$\Delta\theta/\sigma$
A	76.4	75.0 ± 1	- 1.4
B	53.7	53.4 ± 2	- 0.1
C	29.1	41.0 ± 1	+12.0
D	51.6	54.0 ± 2	+ 1.2
G	54.1	58.5 ± 3	+ 1.5
J	48.3	60.0 ± 3	+ 3.9
K	93.4	94.0 ± 1	+ 0.6
L	63.1	67.5 ± 2	+ 2.2
M	51.6	54.5 ± 2	+ 1.4
N	78.3	78.0 ± 3	- 0.1
P	91.7	90.0 ± 4	- 0.4
QB	107.4	120.0 ± 6	+ 2.1
QF	8.7	5.0 ± 5	- 0.7
RD	50.0	54.0 ± 2	+ 2.0
QL	82.6	80.0 ± 10	- 0.3
QV1	61.4	55.0 ± 10	- 0.6
QV3	80.0	58.0 ± 9	- 2.4

the same position angle as the $H\alpha$ radiation. If, as previously supposed, the $H\alpha$ emission was due to recombination radiation in the filaments, then the $H\alpha$ line should be unpolarized, or at least depolarized relative to the continuum. Clearly this was not the case, and the only conclusion that could be drawn from this observation was that the $H\alpha$ and continuum radiation had the same origin, namely, scattered light from the nucleus. The observed wavelength dependence of the continuum polarization was very flat (Figure 6.10). If the scattering was due to dust then this implied that the grains were fundamentably different in their size distribution from those in our galaxy, because a strong wavelength dependence is observed locally. In the transmitted light from reddened stars (the Davis-Greenstein mechanism cf. Coyne and Wickramasinghe 1967) the polarization reaches a maximum near $\lambda \approx 5000\ A^{o}$, and is smaller at both longer and shorter wavelengths. In the reflected light from grains in reflection nebulae the polarization rises monotonically towards the long wavelengths (Gehrels 1960, Hall 1965, Elvius and Hall 1966, Zellener 1970). Viswanathan and Sandage argued that this meant that either the scattering grains were much larger than the wavelength of the light, which they considered unlikely in view of the results in our galaxy, or that the scatters were electrons, which would give a "grey" (flat) wavelength dependence. This then appeared to be evidence in support of Solingers model. The observed equivalent widths of emission lines in the filaments were very narrow which contradicted this evidence, and the whole issue was confused even more when examination of the distribution of colour with distance from the centre of the galaxy showed a trend for blueing with distance (Figure 6.11), which was exactly the opposite to that expected from dust scattering models.

Though the results presented in the present and previous sections had ruled out the synchrotron model it had left both the other proposed models with different problems, neither of them fully explaining the observations.

6.3 The Electron Scattering Model

In Solingers model the filaments are assumed to have been forced out by an unspecified cataclysmic explosion of energy $\sim 10^{60}$ ergs. The explosion is then followed by a shock wave which propagates out from the origin of the blast and heats and compresses the ambient medium. The result of the process is that very large temperatures, $\sim 10^{8}$ °k, are produced behind the shock front, thus the gas will be highly ionized, and there will be a large abundance of free-electrons.

If the kinetic temperature of these electrons is greater than 10^{7} °k then significant bremstrahlung will be expected, in which case M82 should be on X-ray source. The observed line emission is intrinsic to the filaments, and results from collisional ionization and subsequent recombination behind the shock front. The observed polarization is accounted for by Thompson scattering by the plentiful free-electrons that are present, and is expected to be wavelength independent, and large. The appearance of a concentric polarization pattern in the observations implies that the source of illumination is a small bright nucleus, supposedly at the centre of the explosion. If the filaments are optically thin, then the expected polarized intensity should be (Solinger 1969b).

$$Q \approx < \frac{d\sigma_t}{d\Omega} > \frac{L}{4\pi R_S^{\,2}} N_e R_S \, d\Omega \tag{6.1}$$

where $< \frac{d\sigma_t}{d\Omega} >$ = the average Thompson cross-section $\sim 5.95 \times 10^{26} m^2$

$d\Omega$ - solid angle observed ($1 \text{Sec}^2 = 2.24 \times 10^{-11}$ steradians)

R_S = radius of the shock front $\sim$ 3 kpc

N_e = electron density $\sim 10 \text{ cm}^{-3}$ (Lynds and Sandage 1964)

Q $\sim 5 \times 10^{15} \text{ erg Sec}^{-1} \text{ cm}^{-2}$

L = optical luminosity of the nucleus.

Substitution into equation 6.1 gives a value for the optical luminosity of the nucleus of $\sim 3 \times 10^{43}$ erg Sec^{-1}, which might imply that it is similar to a Seyfert nucleus. If this were true it would be expected to radiate strongly in the infra-red with a luminosity $\sim 10^{43}$ erg Sec^{-1}.

How do these predictions compare with the observations ?

Measurements in the infra-red band (3 - 300 μm), (Kleinman and Low 1970 a, b, Low and Auman 1970, Joyce et al 1972, Harper and Low 1973) have confirmed this latter prediction and give a luminosity 2×10^{44} erg Sec^{-1}, which is in very good agreement with that predicted by the model. X-ray measurements, made with the UHURU satellite, (Giocanni et al 1974) in the 2 - 6 kev energy range gave a flux of four counts Sec^{-1} which at the distance of M82 corresponds to a flux of 9×10^{40} erg Sec^{-1} which is in good agreement with that expected from bremstrahlung or alternatively inverse Compton scattering of infra-red photons by free-electrons. The predicted optical luminosity is however, considerably larger than that of a typical Seyfert galaxy, e.g. NGC 5151 ($L \sim 10^{41}$ erg Sec^{-1}, Oke and Sargent 1968), and measurements of the luminosity of the optical centre adopted by Burbridge et al, by Peimbert and Spinnrad (1970) give a luminósity $\sim 6.2 \times 10^{41}$ erg Sec^{-1}, which is considerably smaller than predicted by the model. Further, Peimbert and

Spinnrad (1970) also report that the observed intensity ratios of the [OI], [OII], [OIII] emission lines are impossible to produce by collisional ionization as required by this model.

The energy involved in the explosion is extremely large, being four orders of magnitude larger than required by Lynds and Sandage (1963) and Burbridge et al (1964), who found great difficulty in maintaining their energy requirements. This is an obvious problem with the model.

The wavelength dependence of polarization in the range 3585-8000 A^o has been discussed previously and is in excellent agreement with the prediction of the model. The polarization of the $H\alpha$ line (Viswanathan and Sandage 1972) presents a serious difficulty for the model, because as Viswanathan and Sandage (1972) and Sanders and Balamore (1971) point out the model supposes that this radiation is due to recombination. If this were the case, then the emission line would be expected to be depolarized relative to the continuum. Sanders and Balamore (1971) have presented a detailed discussion of the problem, attempting to amend Solinger's original suggestion by supposing that the polarized $H\alpha$ radiation observed in the filaments, like the continuum radiation, is nuclear light scattered by free electrons, in which case the polarization would follow naturally. The equivalent widths of the emission lines in the filaments are very narrow $\sim 10\ A^o$ (Viswanathan and Sandage 1971, Heckathorn 1972), and this seems unreconcilable with an electron temperature of $10^8\ {}^o k$, at which they should be $> 500 A^o$, and would therefore be so wide as to be undetectable. The observed widths suggested that the temperature in the filaments is only $\sim 10^5\ {}^o k$. Sanders and Balamore find that if this temperature is adopted then the luminosity of the nucleus in $H\alpha$ light must be three orders of magnitude greater than observed for the nucleus of a typical Seyfert galaxy ($\sim 10^{44}$ erg Sec^{-1}), and they thus conclude that the production of the line polarization by scattering off electrons is unreasonable.

A suggestion by Blerkom et al (1973), that fluorescence could produce the Hα polarization seemed to re-establish the model on a firm footing. However, the mechanism is only applicable to the emission lines of Hydrogen, and the discovery that the [N II] forbidden line is also polarized (Viswanathan 1974), with the same magnitude, and at the same position angle as the continuum and Hα line, argues very strongly against this idea.

The inability of the electron scattering model to explain the emission line widths and polarizations argues against this model. Even if this does not totally rule out such a mechanism, it appears that large modifications will be required to enable the model to account for the observations.

6.4 Dust Scattering

At present the only mechanism that appears to be capable of producing narrow polarized emission lines is the scattering of light by dust grains. The number density of grains, n_g, required to produce the observed Hα polarization has been estimated to be

$$n_g \sim 2 \times 10^{11} \text{ cm}^{-3} \quad \text{(Sanders and Balamore 1973)}$$

and if the specific density of grains is assumed to be one, this yields a mass density in grains of

$$\rho_g \approx 1 \times 10^{-25} \text{g cm}^{-3}$$

By assuming that the mass in gas is 100 times that in grains (Spitzer 1968), Sanders and Balamore (1973) obtained an estimate for the total mass contained in the filament

$$M_{tot} \approx 4 \times 10^6 \ M_{\odot}$$

which is comparable with the estimate made by Lynds and Sandage (1964) on the basis of intrinsic $H\alpha$ line formation in the filaments, but several orders of magnitude lower than that predicted by Solinger's theory.

Since the chemical composition, scattering properties, and shape of interstellar grains are not very well known, it is difficult to decide what would be feasible choices of these parameter for the dust in M82. However, the observed flat wavelength dependence of polarization does imply that if grains are present they cannot have a unique characteristic size.

Mathis (1973) has investigated the problem of producing a flat wavelength dependence from a mixture of different sized spherical particles, assuming that they are dielectrics with a range of refractive indices similar to those matched to the known properties of interstellar grains by Gilra (1971).

Unlike other shapes of grain, the scattering properties of spherical grains are well known (Van de Hulst 1957, Wickramasinghe 1967, Greenberg 1968) and depend on the dimensionless quantity

$$x = \frac{2\pi a}{\lambda} \tag{6.2}$$

where

a = radius of the grain.

λ = wavelength of the light.

In the Rayleigh limit of small particles ($x \ll 1$) the scattered intensity is proportional to $x^4 (1 + \cos^2 \theta)$ (see Chandresakhar 1959), and the polarization is identical to that produced by Thompson Scattering from electrons, namely

$$P \propto \frac{1 - \cos^2\theta}{1 + \cos^2\theta} \qquad (6.3)$$

where θ is the angle of scattering (i.e. the angle between the line of sight and the direction of incidence of the light). The scattered intensity is symmetric about $\theta = 90^o$ and the x^{-4} dependence means that the light will be very much bluer than the incident light. The polarization is thus extremely large, and by inspection of equation (6.3) it can be seen to be 100% when $\theta = 90^o$. For particles whose size is of the order of the wavelength of the light ($x \sim 1$) the scattered intensity becomes peaked in the forward direction, and is proportional to x, and is thus still blue, but to a much lesser extent than before. The polarization produced is small $\lesssim 10\%$ and is governed by the refractive indices of the grains, as is the value of x at which the transition from Rayleigh Scattering takes place. When the grains are much bigger than the wavelength of the light ($x >> 1$) the scattering behaviour becomes very complicated, and is dominated by diffraction effects, and similarly depends strongly on the refractive indices of the grains (see Kerker 1969, Van de Hulst 1957, for details). In general the scattered intensity is wavelength independent and the polarization is extremely small (~ 0) or even in a direction orthogonal to that produced by the smaller particles.

If we now reconsider Viswanathan and Sandage's (1972) argument that the colour of the continuum light should necessarily become redder as we move away from the central source, due to interstellar type extinction, we see that this is a rather naive suggestion. The actual colour of the light will depend on the relative importance of the contrasting effects of extinction and the scattering, and hence on the actual size distribution of grains. The contribution of the scattering to the colour of the light is governed by the need to meet the more exacting requirement of the wavelength dependence of the polarization, demanding that the number of small, highly polarizing and blue scattering grains be diluted with sufficient large grains to produce the observed magnitude and wavelength dependence of polarization. The choice of the size distribution for the grains, within the above limitations, is fairly arbitrary. Mathis (1973) assumed that the grains sizes, by an analogy to interstellar grains, followed an Oort-Van de Hulst distribution (Oort and Van de Hulst 1946).

$$N(a, \langle a \rangle) = \exp[-0.693 \, (a/\langle a \rangle)^{2.6}] \qquad (6.4)$$

where $\langle a \rangle$ is the mean grain size, the values of which range between 0.05 - 0.2 μ . No single Oort-Van de Hulst distribution was capable of producing a large wavelength independent polarization, because more smaller particles relative to the large ones were required to produce the polarization, than the distribution contained. However, by combining three different Oort-Van de Hulst distributions Mathis (1973) was able to obtain a good fit to the observations after applying a Whitford (1958) reddening to the central source radiation. The degree of reddening was chosen to make the final scattered intensity, relative to the source, equal at 3500 A^{o} and 8000 A^{o}. The reddening assumed was 1.9 magnitudes at V, which is somewhat less than that found by Peimbert and Spinnrad (1970) to apply to the central source ($\sim$3.5 mags at V). As Peimbert and Spinnrad (1970) point out the application of the Whitford law is an over estimate, as this takes into account the total extinction, when really only the absorption should be allowed for, thus the amount of dust required will be underestimated. The most alarming consequences of this approach is that exact cancellation of the reddening and scattering effects has to occur in order to produce identical colours in the filaments and the central source as observed, such cancellation would appear to be purely fortuitious and makes the model seem rather contrived. Furthermore, the Oort-Van de Hulst distribution for interstellar grains is correct only on the basis of one particular destruction mechanism (Wickramasinghe 1967). A physically more realistic distribution

$$N(a, \langle a \rangle) = \exp[-a/\langle a \rangle] \tag{6.5}$$

follows if other destruction mechanisms are taken into account (Wickramasinghe 1965, Wickramasinghe et al 1966). Unfortunately this distribution makes the problem of too few small grains even more accute, and matching the observed wavelength dependence can still only be achieved by invoking a combination of several such distributions. It is quite apparent that these calculations are very arbitrary and must be accepted with a degree of caution, and are certainly not conclusive evidence for a dust scattering mechanism, but merely indicate that the mechanism is feasible.

REFERENCES

Berge, G.L. and Seielstad, G.A.	1969	Ap. J., 157, p. 35
Blerkom, D. Van, Castor, J.I., Auer, L.H.	1973	Ap. J., 179, p. 85.
Burbidge, G.R., Burbidge, E.M and Rubin, V.	1964	Ap. J., 140, p. 942
Coyne, G.V. and Wickramasinghe, N.E.	1969	A.J. 74, p. 1179
Davies, R.D.	1969	I.A.U. Symposium
Dent, V.A.D. and Haddock, F.T.	1965	Quasi-Stellar Sources and Gravitational collapse ed., E. Soching, I. Roos, A. Shild, (C.U.P.), p. 381.
Dent, V.A.D.	1965	Unpublished Thesis, University of Michigan.
Dent, V.A.D., and Haddock, F.T.	1966	Ap. J., 144, p. 568
Elvius, A.	1962	Lowell Observatory Bull., 5, p. 271.
Elvius, A.	1967	A.J., 72, p. 794.
Elvius, A.	1969	Lowell Observatory Bull., 7, p. 117.
Elvius, A., and Hall, J.S.	1967	Lowell Observatory Bull., 6, p. 257.
Gehrels, T.	1960	Lowell Observatory Bull., 4, p. 30.
Giacconi, S., Murray, S., Gursky, H., Kellog, E., Schreir, E., Matalsky, T., Kock, D., and Tananbaum, H.	1974	Ap. J. Suppl. 27, p. 37.
Gilra, D.P.	1971	Nature, 229, p. 237.
Hargrave, P.J.	1974	M.N.R.A.S., 168, p. 491.

Guelin, M., and Weliachew, L. 1970 Astr. and Astrophys. 9, p.155.

Hall, R.C. 1965 Published A.S.P., 77, p.158.

Harper, D.A., and Low, F.J. 1973 Ap. J. 182, L89.

Holmberg, E. 1950 Medd. Lund. Serr II, 128.

Holmberg, E. 1958 ibid., 136.

Humason, M.L., Mayall, N.U. and Sandage, A.R. 1956 A.J., 61, p.97.

Joyce, R.R., Gizari, D.Y. and Simon, M. 1972 Ap. J., 171, L67.

Kellerman, K.I., and Paulin-Toth, I.I.K. 1969 Ap. J. 155, L71.

Kellerman, K.I. and Paulin-Toth, I.I.K. 1971 Astrophys. Letts., 8, p.153.

Kellerman, K.I. and Paulin-Toth, I.I.K. and Williams, P.J.S. 1969 Ap. J., 157, p.1.

Kleinman, D.E., and Low, F.J. 1970a Ap. J., 159, L165.

Kleinman, D.E., and Low, F.J. 1970b ibid., 161, L203.

Low, F.J. and Auman, H.H. 1970 Ap. J., 162, L79.

Lynds, C.R. 1961 Ap. J., 134, p.659.

Lynds, C.R., and Sandage, A.R. 1963 Ap. J., 137, o.1005.

Mathis, J.S. 1973 Ap. J., 183, p.41.

Mayall, N.U. 1960 Ann' d'Ap. 23, 344.

Morgan, N.W. and Mayall, N.U. 1959 Science, 130, p.1421.

Peimbert, M. and Spinnrad, N. 1970 Ap. J., 160, p.429.

Sandage, A.R. and Miller, E.C. 1964 Science, 130, p.1421.

Sandage, A.R. and Viswanathan, N.J 1969 Ap. J., 157, p.1065

Sanders, R.H. and Balamore, D.S.	1971	Ap. J., 166, p. 7.
Solinger, A.B.	1969a	Ap. J., 155, p. 403.
Solinger, A.B.	1969b	Ap. J., (Letters), 150, L21.
Solinger, A.B.	1969c	ibid, 158, L25.
Solinger, A.B. and Market, T.A.	1975	Ap. J., 197, p. 309.
Tamman, G.A. and Sandage, A.R.	1972	Ap. J., 178, p. 623.
Vaucouleurs, G. de	1961	Ap. J. Suppl., 5, p. 233.
Vaucouleurs, G. de, and Vaucouleurs, A. de.	1964	Reference Catalogue of Bright Galaxies (Austin, University of Texas Press).
Viswanathan, N.J.	1974	Ap. J., 192, p. 319.
Viswanathan, N.J. and Sandage, A.R.	1972	Ap. J., 176, p. 57.
Volders, L. and Hogbom, J.A.	1961	B.A.N., 15, p. 307.
Weliachew, L.	1971	Published A.S.P., 83, p. 609.
Zellener, B.	1970	A.J., 63, p. 201.
Van de Hulst, H.C.	1959	Light Scattering by Small Particles, Wiley, New York.
Greenberg, J.A.	1968	Stars and Stellar Systems, Vol. 7, University of Chicago Press p. 221.
Wickramasinghe, N.C.	1967	Interstellar Grains, Chapman and Hall, London.
Kerker, M.	1969	The Scattering of Light and Other Electromagnetic Radiation, New York, Academic Press.

Spitzer, L.	1968	Diffuse Matter in Space, J. Wiley, London.
Chandreskhar,	1959	Radiative Transfer.
Oort, J.H. and Van de Hulst, H.C.	1946	B.A.N., 10, p.187.
Wickramasinghe, N.C.	1965	M.N.R.A.S., 131, p.177.
Wickramasinghe, N.C., Ray, W.D. and Wyld, C.	1966	ibid, 132, p.137.

CHAPTER 7 THE POLARIZATION STRUCTURE OF M82

7.1 Introduction

For reasons discussed in chapter 6, the polarization in M82 is thought to arise by reflection of the light from the bright nuclear region, or galactic disc (Solinger and Markert 1976) in an extensive halo of dust particles. Consequently, observations of the polarization can give information about the position and luminosity of the energetic nuclear region, and about the scattering mechanism. Other outstanding questions about M82 include the existence and nature of a compact nucleus, and the morphological and evolutionary state of the whole galaxy.

Our two-dimensional polarization study provides data for the construction of an improved model of M82. For example, the fairly clear division of the map into regions of high and low polarization represents a separation in depth, at least near the centre of the map. The edge-on view of the galaxy shows the unobserved near side along the central band, whereas on each side of the disc an unobscured line of sight passes through highly polarized regions directly illuminated by the bright central source, and with large scattering angles. In this chapter we attempt to characterize the central source by fitting models to the observational data. Some smaller contributions to the polarization by other mechanisms is also to be expected and may be apparent in one or two features of the galactic disk in figure 5.15; these most probably arise from the properties of the disk rather than the halo material, and may show that there is some magnetic alignment in this irregular object.

7.2 The Centre of Symmetry of the Polarization Pattern

The perpendiculars to the e-vectors indicate the effective centre of illumination as seen by the scattering particles. If the illumination is provided by a bright nucleus the perpendiculars from all regions of the map will meet at the same point. To investigate this we divided the data into 8 groups, each containing more than 30 measurements.

covering at least 60" x 60" arc areas of the map. We excluded the regions of strips 1, 2 and 3 North + 69 57' from the analysis because of the high noise levels discussed previously. For each datum point in a group we computed the quantity δ_i given by

$$\delta_i = (N_i - \overline{N}) \cos \theta_i + (E_i - \overline{E}) \sin \theta_i \qquad (7.1)$$

where (E_i, N_i) is the equatorial coordinate of the measurement, θ_i the position angle of the e-vector at that point and $(\overline{E}, \overline{N})$ is an initial guess of the position of the centre of illumination (Solinger 1969). The quantity δ_i measures the distance between the radius vector from $(\overline{E}, \overline{N})$ to (E_i, N_i), and the normal to the e-vector at that point. The centre of illumination is then found by minimising the total sum of square separations S for each group given by

$$S = \Sigma w_i \delta_i^2 \qquad (7.2)$$

using the optimization routine described previously (chapter 4) with $\overline{E}$ and $\overline{N}$ as free parameters of the fit. The summation i is taken over all points in the group and the w_i are appropriate weight factors. Two different weights were used; initially the weight was taken as unity and then, since the accuracy of the position angle is dependent on the degree of polarization, we included a term proportional to the measured polarization at each point

$$w_i = p_i \qquad (7.3)$$

Convergence was accepted when the total sum of squares changed by less than 1×10^{-6} between iterations. The confidence interval for each solution was computed from the residual sum of squares S and the hessian matrix, G, at the solution, given by

$$G = 2J^T J \qquad (7.4)$$

where J is the first derivative matrix

$$J_{ij}(x) = \left(\frac{\partial \delta_i}{\partial X_j}\right)_{\underline{x}} \qquad (7.5)$$

evaluated at $\underline{x} = (\overline{E}, \overline{N})$. An unbiased estimate of the variance of the ith fit parameter x_i is then

Table 7.1 Centre of Symmetry of the Polarization Pattern from Various Locations in the Galaxy

	Region of Map		Centre of Symmetry		Standard Deviation		No. of Points	Confidence Limits			
No.	RA*	DEC**	RA*	DEC**	$\pm\sigma_{RA}$	$\pm\sigma_{DEC}$		$\pm$ 99%		$\pm$ 90%	
								RA	DEC	RA	DEC
1	22 to 30	0 to 300	38.7	132.0	6.7	6.6	57	18.2	17.6	11.2	11.0
2	38 to 46	60 to 120	43.7	194.8	1.06	3.26	36	2.94	9.06	1.80	5.57
3	38 to 46	120 to 180	41.4	184.8	0.69	1.54	36	1.88	4.2	1.17	2.6
4	38 to 46	180 to 240	41.7	207.6	2.18	2.36	47	5.89	3.66	6.37	3.94
5	38 to 46	240 to 360	46.3	278.3	7.0	10.8	55	18.6	28.7	11.7	18.0
6	51 to 58	140 to 190	54.9	160.0	1.9	2.9	31	5.2	8.0	3.2	4.9
7	60 to 70	< 180	53.1	184.9	8.3	7.0	64	22.1	18.6	13.9	11.7
8	70 to 80	120 to 240	69.0	182.4	10.3	3.8	119	27.0	17.1	10.0	6.3

* RA in seconds of time relative to 9H 57M

** DEC in seconds of arc relative to + 69^{o} 52'

Table 7.2 Centre of Symmetry Obtained with a Weight Proportional to the Observed Polarization

	Region of Map		Centre of Symmetry		Standard Deviation		No. of Points	Confidence Limits			
No.	RA*	DEC**	RA*	DEC**	$\pm\sigma_{RA}$	$\pm\sigma_{DEC}$		$\pm$ 99%		$\pm$ 90%	
								RA	DEC	RA	DEC
1	22 to 30	0 to 300	33.5	138.2	7.0	9.8	57	18.6	26.1	11.7	16.4
2	38 to 46	60 to 120	44.2	192.6	0.80	3.05	36	2.2	8.4	1.36	5.2
3	38 to 46	120 to 180	41.4	188.4	0.59	1.34	36	1.6	3.7	1.0	2.3
4	38 to 46	180 to 240	41.4	206.7	2.07	2.48	47	5.6	6.7	3.5	4.2
5	38 to 46	240 to 360	43.5	292.0	1.73	3.4	59	4.6	8.8	2.9	5.5
6	57 to 58	140 to 190	55.4	156.3	1.77	3.05	31	4.8	8.4	3.0	5.2
7	60 to 70	< 180	52.3	183.8	7.96	7.1	64	21.1	18.8	13.3	11.9
8	70 to 80	120 to 240	56.7	178.2	9.8	3.8	119	25.7	10.0	16.3	6.3

* RA in seconds of time relative to 9H 51M.

** DEC in seconds of arc relative to + 69^{o} 52'.

$$\text{var } x_i = \frac{2S}{m-2} H_{ii} \qquad i = 1, 2 \tag{7.6}$$

where H is an approximation to G^{-1} and m is the total number of points in the group. If $\underline{x}^*$ is the true solution then the 100 (1-β) confidence interval on $\underline{x}$ is

$$x_i - \sqrt{\text{var } x_i} \cdot t(\beta/2, m-2) < x_i^* < x_i + \sqrt{\text{var } x_i} \cdot t(\beta/2, m-2) \tag{7.7}$$

where $t(\beta/2, m-2)$ is the $100\beta/2$ percentage point of the t-distribution with m-2 degrees of freedom (Wolberg 1967). The results of the analysis are summarised in table 7.1 and 7.2. The differences between tables 7.1 and 7.2 for areas with RA's between 38.0 and 48.0 are small and the errors in the positions are less than $\pm$ 2.0^s and $\pm$ 2.0" in RA and Dec respectively. The differences are larger for other areas but so are the errors and no real difference exists between the estimates with the two weights. The illumination centres are not coincident they are spread over a region of ~ 120", suggesting that the illuminating source is extended rather than a point nucleus. The idea that the nucleus provides all of the illumination is in any case naive, for as Solinger and Markert point out even in the brightest Seyfert galaxies the nucleus is between 1 and 4 magnitudes fainter than the disk (Sandage 1971). The disk must therefore contribute significantly to the illumination and the polarization pattern will depend on the ratio of the nuclear to disk lummosities $R = L_N/L_D$. From the additivity of the Stokes parameters the total Stokes parameters Q and U produced by scattering at any point in the galaxy will be the sum of the nuclear and disk Stokes parameters Q_N, U_N and Q_D U_D

$$\begin{aligned} Q &= Q_N + Q_D \\ U &= U_N + U_D \end{aligned} \tag{7.8}$$

These quantities will be proportional to the luminosity of their respective sources, the scattering crossection and some functions depending on the geometry of the scattering only q_N, u_N, q_D, u_D (Solinger and Markert 1976)

$$Q_N = L_N \sigma q_D \qquad Q_D = L_D \sigma q_D$$
$$U_N = L_N \sigma u_N \qquad U_D = L_D \sigma u_D \tag{7.9}$$

Thus in the ratio of U/Q the unknown quantity σ drops out and

$$\theta = \tan^{-1} \left(\frac{Ru_N + u_D}{Rq_N + q_D}\right) \tag{7.10}$$

Using the observed position angles ϕ, simple scattering models can be fitted to data by minimizing the sum of square differences

$$\psi^2 = \sum_{i=1}^{n} \left(\frac{\phi_i - \theta_i}{\delta \phi_i}\right)^2 \tag{7.11}$$

where the $\delta \phi_i$ are the uncertainties in the observed position angles (i.e. 4^o for our data). Thus the observed polarization pattern not only determines the position of any illuminating nucleus, but also yields information on the light distribution in the disk, and the ratio R, which would otherwise be unobservable quantities. Solinger and Markert (1976) have described such a model and fitted it to the photoelectric polarization data. The more numerous polarization results reported here, with their more precise position angles gives us the opportunity to make a more reliable fit to the model.

7.3 Scattering Models

We assume that the scattering particles are spherical and small compared to the wavelengths of the light, so that Rayleigh scattering occurs (chapter 6.4). The particles are non-interacting and the assumption of optical thinness is made so that multiple scattering can be neglected.

The Stokes vectors of the incident light $\hat{I}_o$ and the scattered light $\hat{I}$ are related by $\hat{I} = \underline{M} . \hat{I}_o$ where $\underline{M}$ is the Mueller matrix which characterizes the scattering particle. The Stokes vectors $\hat{I}_o$ and $\hat{I}$ are measured relative to axes which are parallel and perpendicular to the scattering plane (that is the plane containing the incident and scattered light) and it is convenient to adopt the notation of Chandrasekhar

(1959) and write them in terms of the intensities I_{11} and $I_{\perp}$ in each of these directions respectively i.e. $\hat{I}_o = (I_{11}\ I_{\perp},\ u,\ v)$. The Stokes parameters I and Q are then given by $I = I_{11} + I_{\perp}$ and $Q = I_{11} - I_{\perp}$. The scattering matrix M is given by Chandrasekhar (1959)

$$\underline{M} = \begin{bmatrix} \cos^2\theta & 0 & 0 & 0 \\ 0 & 1 & 0 & 0 \\ 0 & 0 & \cos\theta & 0 \\ 0 & 0 & 0 & \cos\theta \end{bmatrix} \tag{7.12}$$

where θ is the scattering angle (i.e. the angle between the incident and scattered light). However, rather than measure the Stokes parameters relative to the scattering plane we must measure them relative to axes fixed in the plane of the sky (i.e. equatorial system) so we can compare them with the observations. This involves multiplications by a linear transformation matrix R which is given by Chandrasekhar (1959).

$$\underline{R} = \begin{bmatrix} \cos^2\psi & \sin^2\psi & \frac{1}{2}\sin 2\psi & 0 \\ \sin^2\psi & \cos^2\psi & \frac{1}{2}\sin 2\psi & 0 \\ -\sin^2\psi & \sin 2\psi & \cos 2\psi & 0 \\ 0 & 0 & 0 & 0 \end{bmatrix} \tag{7.13}$$

where ψ is the angle between the scattering plane and the reference direction (Equitorial North). Our scattering equation therefore becomes

$$\hat{I} = \underline{R} \cdot \underline{M} \cdot \hat{I}_o \tag{7.14}$$

For unpolarized incident light $I_{11} = I_{\perp} = \frac{1}{2}I_o$ and $U = V = 0$ hence we obtain

$$\hat{I} = \begin{pmatrix} I_{11} \\ I_{\perp} \\ U \end{pmatrix} = \frac{3}{4} \begin{pmatrix} \cos^2\theta\cos^2\psi + \sin^2\psi \\ \cos^2\theta\sin^2\psi + \cos^2\psi \\ (1 - \cos^2\theta)\sin 2\psi \end{pmatrix} I_o \tag{7.15}$$

The problem of calculating the Stokes parameters Q and U for any particular model therefore reduces to evaluating θ and ψ from the models geometry. We consider two simple cases, the model of Solinger and Markert (1976), details of which are given in appendix II, and a point source nucleus with line of sight integration (appendix III).

The Solinger and Markert model assumes that all the scattering occurs in the plane containing the nucleus and perpendicular to the line of sight. The light source is taken to be a point source at the centre of an assymmetric disk which is orientated edge-on to the observer. The disk luminosity Σ varies radially as a standard spiral (Freeman 1971) i.e. it falls of as exp $(-r_D/k'')$ to a cut-off at $r_D = 5.2'$ (where the notation of appendix II has been used) and k is an arbitrary constant. We have made one slight alteration to their model by fixing the position angle of the disk to be along the obvious optical axis at position angle 65^o. The position of the nucleus (E, N), the ratio R and the scale length k are allowed to be free parameters of the fit, and their best values chosen by using the least squares optimization routine described previously to minimize ψ^2. Convergance was accepted when the value of ψ^2 changed by no more than 1×10^{-3} between itterations. The two-dimensional integral for the disk Stokes parameters was evaluated numerically using a Chebyshev method (Clenshaw and Curtis 1960). For comparison we have also evaluated the model for Solingers case C which the best fit they obtained to the photoelectric data; and have computed the residual value of ψ^2 per point for various areas of our map. The inclusion of the exponential term in the radial integral proved to be difficult to handle in the numerical integral. The routine failed to obtain the desired accuracy (0.0005) for the integral for about 10% of the data and these errors obviously propagate into the optimization. This is illustrated quite dramatically by the fact that the optimization routine altered k preferentially and converged to a best solution with a Negative value for k i.e. the disk luminosity increasing with distance from the nucleus! Clearly such a situation is unrealistic and so to overcome the problem we modified the model so that the disk luminosity was a constant. The one-dimensional integrals for the point source nucleus model (equations C10) were evaluated using a fast-Fourier transform method (Gentleman 1970). The best fit values for the model parameters and their standard deviations (determined as in section 7.2) in each of the three cases are summarized in table 7.3, and the resultant ψ^2- values per point in table 7.4. Referring to table 7.3 we see that the point source nucleus model gives a solution very close to Solingers case C, with a comparable residual ψ^2 (Table 7.4). A close examination of Table 7.4 shows why both models fit the data well in regions 1 to 8, with the exception of region 5 where the polarization pattern is dominanted by direct contribution from the disk, these regions are centered around the nucleus and the nuclear light contribution will dominate there. Neither model provides a satisfactory fit in the more distant region of the polarization pattern where the disk is expected to dominate. This is rather hard to understand for Case C, however as Solinger and Markert (1976) point out, far from the nucleus the polarization pattern from both disc and nucleus is circular and thus the elliptical pattern from the disc only appears to contribute in intermediate distances. The discrepancy for case C could be explained if the photo-electric data contained little data at intermediate distances, the model would then tend to a point source fit, however the small value of R argues very strongly against this and this is substantiated by the results of the best fit Solingers model. This is clearly the best fit to the data with small residual values of ψ^2 in all the regions except 1 and 11 which are in the upper half of our map and thus badly affected by noise. The RA coordinate for this model is very close to that of Case C and indeed the point source model as well and the confident interval is small. The declination position is however some 13" of arc different even allowing for the uncertainties. This could be a consequence of assuming a constant disc luminosity but is more likely to be due to the uncertainties in the position angles. The ratio L_N/L_D is about half of Case C but is not substantially different when the standard deviations are taken into account. Our final conclusions are that the polarization pattern is produced by illumination from an extended source consisting of a point nucleus embedded in a axismetric disk. The RA position of the nucleus is well determined and lies at 42.7 $\pm$ 0.3 and the nucleus luminosity is about 2% of the disk, conclusions are virtually identical to those of Solinger and Markert (1976). There is however some difference in our estimate of the declination of the nucleus. The best value is 205 $\pm$ 1.2, and at the momer it is not clear what the cause of this is. An explanation must await improved data with the new polarimeter optics and with a lower sky background.

If observations at several wavelengths could be made then the composition and grain shape and size could be investigated using calculations similar to these. Of particular importance would be observations at infra-red wavelengths. This would provide a crucial measure of the observed "greyness" of the continuum polarization. For example if Mathis's (1973) suggestion of an assembly of different sized particles were correct then the polarization would increase at infra-red wavelengths whereas if the particles were Rayleigh scatters as assumed here the polarization would decrease (Abadi, private communication).

Table 7.3 Parameters Determined by the Models

PARAMETER	BEST FIT TO SOLINGER MODEL	POINT NUCLEUS	SOLINGER CASE C
RA POSITION OF NUCLEUS	42.7 $\pm$ 1.4	43.3 $\pm$ 0.003	42.6 $\pm$ 0.6
DEC POSITION OF NUCLEUS	205.0 $\pm$ 1.2	188.2 $\pm$ 3.4	187.0 $\pm$ 3
RATIO L_N/L_D	0.024 $\pm$ 0.01		0.05 $\pm$ 0.07 0.03

Table 7.4 Residual ψ^2-Values for the Models.

No	Location RA	Location DEC	Number of Points	Residual value of ψ^2 per point: SOLINGER CASE	POINT NUCLEUS	SOLINGER BEST FIT
1	48 to 60	>190	49	6.19	1.73	14.75
2	48 to 60	<190	43	2.01	2.11	0.32
3	36 to 48	60 - 120	38	0.83	0.63	0.71
4	36 to 48	120 - 180	55	1.44	0.71	0.23
5	36 to 48	180 - 240	47	4.74	3.04	3.13
6	36 to 48	240 - 360	33	1.22	1.24	0.63
7	<28	>190	28	1.00	0.90	0.42
8	<28	<190	22	2.63	1.39	2.78
9	60 to 70	<180	46	10.04	8.96	1.29
10	>70	180 - 240	39	26.52	25.53	1.08
11	>70	>240	30	8.73	2.38	14.33
12	>70	120 - 180	25	21.46	18.53	2.43
TOTAL ψ^2			455	2.87834×10^3	2.3136×10^3	1.7511×10^3

7.4 The central region of M82

A detailed plot of the structure of the central region based on the radio map of Kronberg and Wilkinson (1975) with the other optical and infra-red features, summarized in table 7.5, superimposed is shown in Figure 7.1. The radio structure is obviously complex, these are many compact components lying close to the optical axis of the galaxy along position angle 65^{o} (Burbidge et al 1964). The most conspicuous of these is the strong unresolved feature M82A (marked by the letter A) discussed in detail by Hargrave (1974). Each of the other compact sources is identified, using the notation of Kronberg and Wilkinson, according to its position relative to $\alpha = 9^{H}\ 51^{M}\ 00^{S}$, $\delta = 69^{o}\ 54'\ 00$. Turning now to the optical features. The optical bright spot often assumed to be the centre of the galaxy (Burbidge et al 1964) is identified by a solid square and the dynamical centre adopted by Heckathon (1972) is denoted by the letter H inside an open square. The two dotted circles give the positions and approximate sizes of the two remarkable large HII regions studied by Peimbert and Spinnrad (1970) and Recillas-Cruz and Peimbert (1970). We have also marked on the map the various position indicated by the polarization data: the open circle with the letter S is the position of the nucleus in Solinger and Markerts "case C", B is the equivalent position obtained by fitting their model to our data and N the position indicated by a point source fit to our data with line of sight integration. Also marked for completeness are the centres of symmetry from different regions of our map as given in section 7.2.

The remaining features on the map are from the infra-red; the centre of the 10μ emission is marked by the cross (Kleinman and Low 1970) and that of the 2μ emission by an open star containing the number 2 (Axon et al 1977). The solid circles dotted throughout the region are the bright spots detected in near infra-red photographs by Van den Bergh (1971). Some previous writers have tried to emphasize that

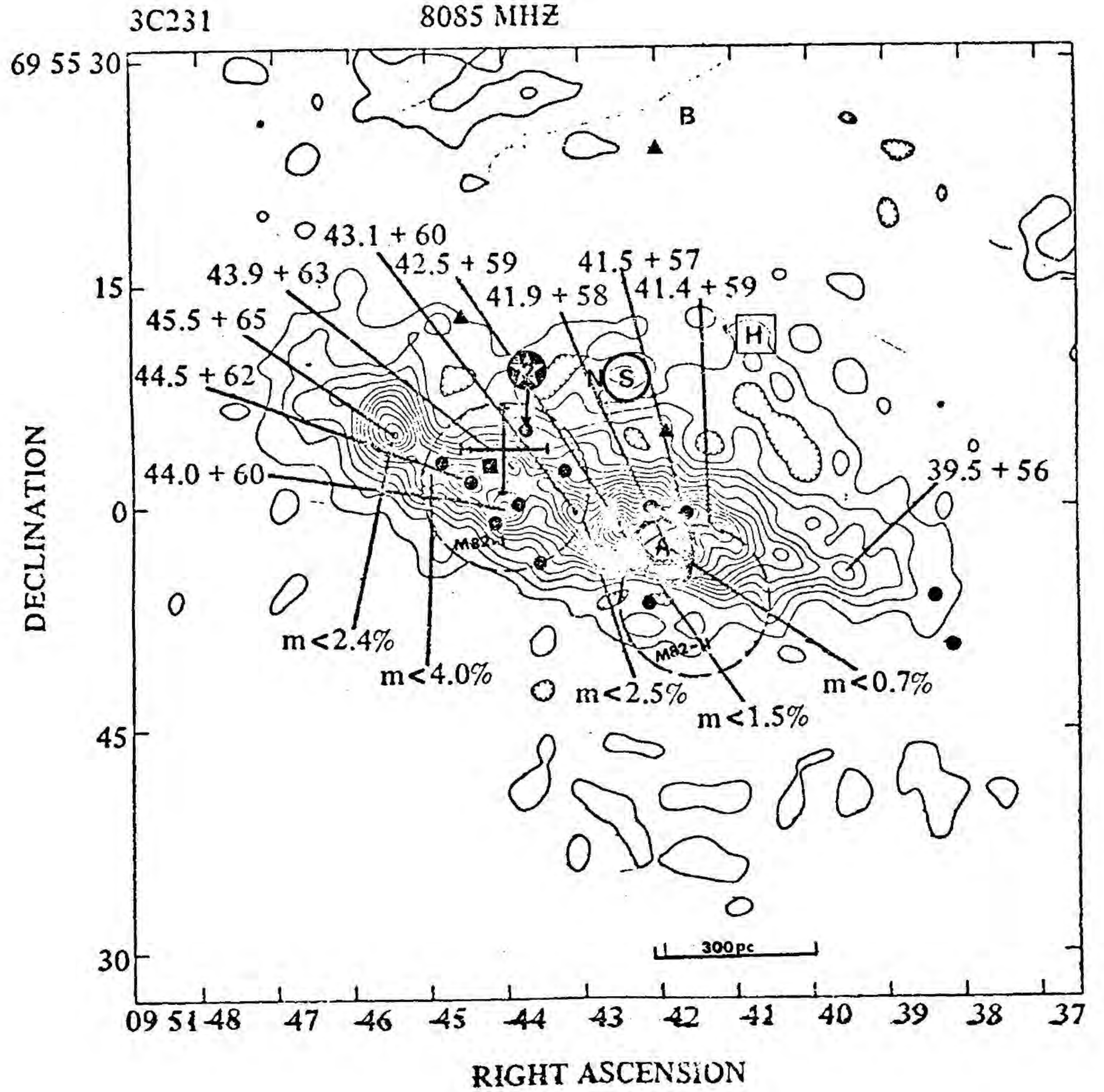

Figure 7.1 Map of the central region of M82 based on the radio map at 8085 MHz given by Kronberg and Wilkinson (1975) with the optical features superimposed (as identified in the text). The contour interval is 3.94 mJy beam^{-1} (14.9k) and the compact radio features are labelled by their positions relative to $\alpha = 09^h\ 57^m\ 00^s.0$ $\delta = 69^o\ 54'\ 00''.0$.

Table 7.5 Central Source Positions in M82

Reference	RA (1950)	DEC	Method
Burbidge, Burbidge, and Rubin (1964)	$9^{H}\ 51^{M}\ 44.2^{S}$	69° 55' 03"	optical bright spot
Solinger and Markert (1975)	$9^{H}\ 51^{M}\ 42.5^{S}$	69° 55' 07"	polarization pattern
Volders and Hogbuum (1961)	1' SW of the optical centre $9^{H}\ 51^{M}\ 54.6^{S}$	 69° 54' 10"	peak of 21 cm emission
Heckathorn (1972)	21" from optical centre at PA 290° $9^{H}\ 51^{M}\ 40.4^{S}$	 69° 55' 11"	centre of filaments as determined from rotation curve
Hargrave (M82A) (1974)	$9^{H}\ 51^{M}\ 42.0^{S}$	69° 54' 58"	unresolved peak of the 5GHZ emission
Axon et al (1977)	$9^{H}\ 51^{M}\ 43.4^{S}$	69° 55'10"	peak 2.2μ emission
Kleinman and Low (1975)	$9^{H}\ 51^{M}\ 44.1^{S}$	69° 55" 04'	peak of 10μ emission

the various central features in M82 are almost coincident, but we would like to point out that there is no detailed correspondence between them, such as might be expected if a true nucleus were present. The compact source A is close to the HII region M82-II towards the periphery of the radio contours and though there are 3 adjacent IR knots it has no special position in the 10μ and 2μ sources and is only near to the other features. Consider also the optical bright spot which is sometimes assumed to be the centre of the galaxy in dynamical studies, this is very close to the peaks of the 10μ and 2μ emission it is surrounded by a wealth of lesser compact radio sources and IR knots, and the whole ensemble is engulfed in the HII region M82-I, and yet clearly it is not coincident with the centres of symmetry and nuclear positions determined from the polarization data. Furthermore there is no real correlation between the IR knots and the compact radio sources, only two cases of coincidence occur, and the other sources have radio fluxes less than about 3mJy (Hargrave 1974). As Hargrave points out this is perhaps not so surprising since the optical features are viewed through high observation, but still the overall picture argues against a unique nucleus. This idea is also strongly supported by the 2μ data, for a highly obscured optical nucleus might well be expected to be visible at this wavelength, on the contrary however the data shows a remarkably smooth extended source disk like in shape with a dimension of $\sim 120''$ arc along the major axis and less than $\sim 5''$ width along the minor axis. On the basis of the evidence there seems little justification for assuming the existence of a unique nucleus and this clearly does not support the idea that M82 contains a Seyfert type nucleus (e.g. Solinger 1969); it does not however preclude that possibility that M82 has some resemblance to a Seyfert galaxy, and indeed we suggest that it is very much so. We argue that M82 like a class 2 Seyfert galaxy is powered thermally by many luminous stars along the lines proposed by Adams and Weedman (1975). The idea of thermally powered Seyferts followed from a study of several peculiar galactic nuclei from Sersic-Pastoriza (S-P) list of "hot-spot" galaxies (Sersic and Pastoriza (1969) in which Osmer et al (1974) showed that large numbers of hot young stars can exist in galactic nuclei but be inconspicuous because of reddening. The intrinsic luminosity found for the stars in these galaxies are comparable to those required in Seyfert 2's, though as Adams and Weedman point out such high luminosities can only arise from a transitory burst of star formation and cannot persist over the lifetime of a galaxy. There is also other empirical evidence that hot stars in galactic nuclei can lead to luminosities comparable to those of NGC1068. The nucleus of NGC4685 (Markarian 52) is a representative example of a bright condensed nucleus, that seems to contain large number of hot stars; it emits strong narrow emission lines with strengths comparable to those of HII regions (Weedman 1973) and is also a strong IR source (Reicke and Low 1972) which is explained by re-radiation from dust. Rather interestingly one of the galaxies also studied by Osmer et al was an irregular II, NGC5253 and they concluded that as for the S-P galaxies this was also powered by young stars. Can we justify such a model for M82?

There is strong evidence for the existence of large number of young stars in the core of M82. The many infra-red knots in the central region have been convincingly identified by Van den Bergh (1971) as unusually luminous associations of very early type stars. The 12 IR knots are ~ 100 times brighter than any cluster in our own galaxy with the total luminosity in the clusters ~ 10^{43} ergs s^{-1}, which is about 5% of the observed infra-red luminosity. It also is important to note that there is no sign of such knots outside the central core and Van den Bergh has argued that this implies a recent outburst (within the last 10^7 years) of star formation in the core. From the assumption that the two bright HII regions M82 I and II are energized by young stars Recillas-Cruz and Peimbert (1969) and Peimbert and Spinnrad (1970) estimate that $\sim 1.8 \times 10^6$ main sequence o6 stars are required, which is already many more than exist in our galaxy. In view of the high observation in the central region (Peimbert and Spinnrad 1970), ~3 - 4 magnitudes at Hβ, this figure may reprisent only a fraction of the total number of stars present as further unobserved H II regions could exist and probably do, indeed if the low-frequency turnover in the spectrum of the compact radio source M82A is due solely to foreground HII absorption then there must be much unobserved ionized Hydrogen (Kronberg and Wilkinson 1975). It is therefore highly possible that all of the 0.8 to 2μ radiation can be explained in this way. The model also offers an equally attractive explanation of the 10μ radiation as reradiation from the prefuse amounts of dust present (Kleinmann and Low 1969). The energy absorbed by the dust in the 3500-1100 A^{o} region, derived from reddening corrections, amounts to ~ 4 x 10^{42} ergs sec^{-1} which is close to the figure ~8.8 x 10^{42} erg sec^{-1} for the energy emitted in the 5 - 22μ region (Piembert and Spinnrad). This excess of young stars in the central region would also explain the difference between the Balmer jump of the core and the out regions of the galaxy (Peimbert and Spinnrad 1970). This leads us directly to the theory of the Seyfert phenomenon proposed by McCrea (1975) which he ascribes to supernova events at a rate of perhaps one per ten years, in a limited volume (no direct triggering of the events is called for, but star formation may be stimulated by previous outbursts). Since the core of M82 appears to contain a very large number of massive stars and is the seat of a recent accelerated burst of star formation it is conceivable that the supernova rate is considerably higher than our own galaxy and could be is high as this figure of 1 per ten years (after all this is only 3 or 4 times the average supernova rate for our galaxy), and the large amounts of dust will help to produce the high mass levels required. Most of the supernova would of course be invisible because of the heavy observation in the core. Kronberg and Wilkinson (1975) have discussed M82A in terms of a possible supernova remnant: it has a non thermal spectrum, its size < 1.2 pc, and integrated radio luminosity 4.8 x 10^{37} erg sec^{-1}, imply a minimum total energy in relativistic electrons

$< 2 \times 10^{49}$ ergs which is comparable to Cas A (1.1×10^{49} ergs) Rosenberg (1970) and would be equal to that of Cas A if the size were smaller than 0.5 pc (in fact the source is now known to be ~ 0.002 pc in diameter Gehzahler et al 1977) and it would then lie on the surface brightness- diameter diagram for supernovae remnants (Iloviasky and Lequeux 1972). The other compact sources could also be supernova remnants with such a high supernova rate and the whole radio emission might be explained in this manner. If the expanding supernovae shells are producing the relativistic electrons the magnetic field would be highly turbulent accounting for the lack of radio polarization (Kronberg and Wilkinson 1976). McCrea's theory appears very attractive but it must be modified somewhat in order to apply it to M82 as the active region we have discussing is ~ 300 pc i.e. about 10 times the size of a Seyfert nucleus however even if this is not the triggering mechanisms a thermally powered M82 fits in well with the observations. The existence of such strong infra-red emission might also explain both the filaments and the velocity field in the galaxy (Hargrave 1974).

7.4.1. The Velocity Field

In the old regime of intrinsic emission line production the observed velocity difference between the nucleus and the filaments was interpreted as the line of sight component of the expulsion velocity of the filament i.e. $V_R \sin \theta$, where θ is the angle between the line of sight and the direction of expulsion of the filaments, and V_R is the velocity away from the central source. Since θ was small $\sim 8^{\circ}$ (Lynds and Sandage 1964) this led to a $V_R \sim 1000 \mathrm{kms}^{-1}$, a value consistent with a very energetic explosion.

The Hα polarization implies however that we are seeing the light in reflection, in which case the velocity differences will be the result of the motion of the filamentry material not only with respect to observer but also away from the centre of the galaxy. Consequently the velocity differences observed are indicative of the true velocity of the material i.e. $\sim 100 - 200 \mathrm{kms}^{-1}$ rather than $\sim 1000 \mathrm{kms}^{-1}$. The energy required

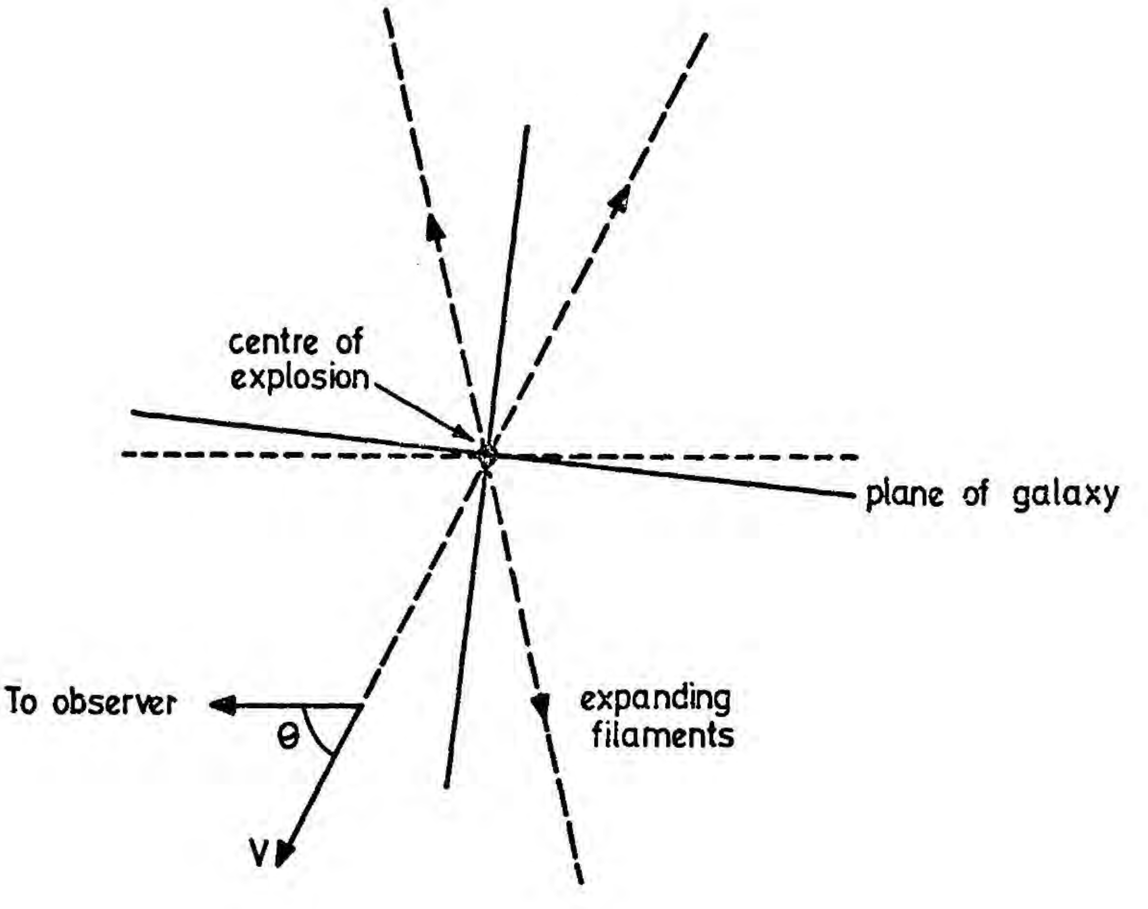

Figure 7.2 Velocity field expected from expelled dust grains.

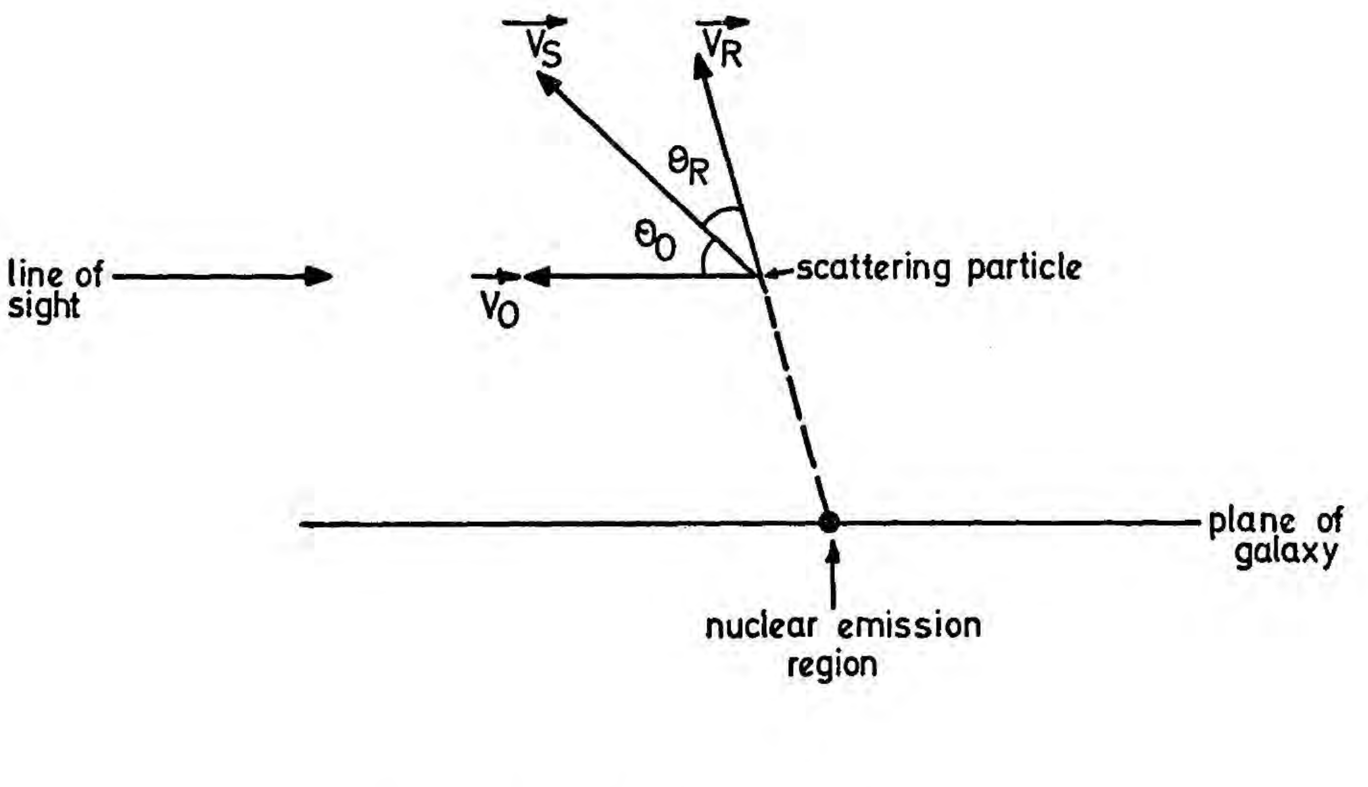

Figure 7.3 Explanation of the velocity field by the inclusion of orbital motions (Sanders and Balamore 1971)

to expel the filaments is therefore reduced to $\sim 4 \times 10^{53}$ ergs with a consequent increase in the time scale to 10^7 years (Sanders and Balamore 1971).

There is however another immediate consequence of equal importance. if the ejected particles are assumed to be moving in the radial direction only, with a relative velocity V_R, away from the nucleus, then the observed velocity difference between the point in the filaments at which the scattering takes place and the central light source is given by

$$V = V_R (1 - \cos\theta) \qquad (7.16)$$

where θ is the scattering angle (Figure 7.2). Since V_R is positive everywhere then V must similarly positive everywhere. Hence all the emission lines should appear redshifted. However large regions are known to exist where the spectral lines are observed to be blueshifted (Heckathorn 1971, Burbidge et al 1964) and thus the particles cannot be travelling in the manner just described (Sanders and Balamore 1971). Sanders and Balamore (1971) and Heckathorn (1971) propose to overcome this problem by including orbital velocity components (Figure 7.3). They argue if the filamentry structure is expanding and if the light from the apparent optical nucleus is being scattered then the observed radial velocity V_S, can only occur if the velocity of the particle towards the observer, V_0, is greater than the velocity of the particle away from the optical nucleus, V_R, i.e. $V_o > V_R$ or $\theta_R > \theta_o$. This then implies that non-radial velocity components exist with respect to the nucleus so that it is still possible to have $V_o < V_R$ in some places and so produce redshifted lines.

Recently Solinger (et al 1977) have critisized this idea because they feel the inclusion of orbital motion is ad hoc, and because Sanders and Balamore ignore some blueshifts near the nucleus towards the south of the galaxy. They argue that no plausible outflow model can be reconciled with the observed velocity field, and propose to explain the observed velocities by having the whole galaxy ploughing through a giant intergalactic dust cloud which engulfs the whole M81 group, rather in the way suggested by Elvius (1972). In this model M82 is supposed to be an interlopper in the group and thus acquires enough velocity relative to the dust cloud to produce the required blue shift in some places in the galaxy. We wish to argue very strongly against such a model, for we see no reason to adopt such a contrived situation, and secondly the model does not really account for the structure of the velocity field. Our first point is that the observed blueshifts are by no means well established experimentally, considerable anomalies exist in the data, Burbidge et al's data was obtained with a dispersion ~ 420 A^{o}/mm which even assuming very accurate measurement of the spectra leads to an uncertainty of $\pm$ 200 km/s in the velocities, more than sufficient to convert the blue shifts to red shifts. We note that Solinger et al do not compare their model with Heckathorn's measurements, which have an uncertainty of only $\pm$ 50 km/s and we therefore feel their conclusions are rather unsound. Even Heckathorn's measurements contain anomalies, for example, measurements of the $H\alpha$ and [NII] lines yield velocities differing by as much as 90 km/s in the same position of the galaxy. Many of the blueshifts may therefore be artifacts of measurement errors, particularly in the fainter regions of the galaxy where the difficulty in measuring the lines increases. A reinvestigation of the velocity field at a much higher dispersion is called for; say at 10 A^{o}/mm ($\pm$ 5 km/s) or 45^{o}A/mm ($\pm$ 25 km/s), we are currently undertaking such a programme (Axon et al 1977). Secondly, the majority of the blueshifts occur near the nuclear region (Axon et al 1977) and it is not clear why this should be preferentially so in their model. It seems quite natural that these motions should occur from bulk motion away from the central region itself, particularly so in the scenario we have just described. The method we invoke is due to Hargrave (1974). He abandons the explosive model in favour of driving the grains away from the central region by radiation pressure from the strong central infra-red source. He shows clearly that sufficient radiation can be present to easily produce the much lower expulsion velocities of the dust scattering model, this supply of pressure could be maintained long enough to expel the grains well away from the nucleus; Bohuski (1976) has deduced empirally from studies of HII regions that the conversion efficiency from radiative energy of the ionizing stars to kinnetic energy in the gas is ~ 0.01 over the lifetime of the HII region. Assuming the efficiency to hold for M82 it requires that the infra-red source $\sim 10^{42}$ ergs sec^{-1} last for $\sim 6 \times 10^{5}$ years to produce the observed total kinnetic energy of the filaments $\sim 4 \times 10^{53}$ ergs, this is a modest requirement. The subsequent motion of the grain will depend on the relative contribution of this driving force, gravitational attraction, retardation by collision with the gas atoms and effects due to other mechanisms. The dust grains might also become charged through photoionization and could thus follow magnetic field lines if their radius of gyration is small enough. Clearly such effect can readily produce the nonradial velocities required, and particularly so near the core of the galaxy where the "stopping" material is the densest. This seems to be more plausible than Solinger et al's suggestion and fits in well with our general view of the galaxy.

7.4.2. The evolutionary status of irr II galaxies

If M82 is thermally powered and has mild or partial Seyfert characteristics it opens up the intruiging possibility that such galaxies could represent an evolutionary link between Seyfert and normal galaxies. The main characteristics for comparison are, strong emission-line structure, especially in the bright nuclear region, the presence of a bright infra-red nucleus, Xray and radio emission, and high dust and gas content. The original Seyferts, such as NGC 1068 and NGC 1275 are of course extreme in these respects and in the velocities of gas motions. Further impetus is given to the idea of connections between these objects in that in both M82 and NGC 1068 the emission lines are polarized identically to the continuum (Visvanathan 1974, Angels et al 1976). Of equal interest are the similarities between M82, Seyfert and active spirals such as NGC 253, which is a prominent prototype of a special subgroup of Sc galaxies, whose morphology is dominated by a dust pattern of great complexity, and is apparently releasing energy in its central region, resulting in the ejection of matter (Demoulin and Burbidge 1970) in a similar manner to M82, NGC 253 likewise has a strong-emission-line structure, is a radio source and has a bright infra-red nucleus comparable to those in M82 and NGC 1068 (Reike and Low 1975).

Galaxies of these active types have been variously classified in the past simply as "peculiar" or as members of the hetrogeneous class denotted irregular II. No systematic work has been carried out on them and it is therefore of some importance for their detailed properties to be investigated as a class, to investigate this possible evolutionary link. It is indeed an intriguing and interesting idea to finish on, that there might by a link between all the forms of active galaxies from the narrow emission galaxies such as M82 and NGC 253 to the broader Seyfert 2's and the broad lined class 1 Seyfert galaxies.

REFERENCES

Adams T. F. and Weedman D. W. 1975 ApJ., 199, p 19.

Axon D. J., Adams D., Hough J. and Jameson R. F. 1977a in preparation

Axon D. J., Bingham R. G., Peat D., Taylor K. 1977b in preparation

Bohuski T. J. 1973 ApJ., 184, p 93.

Burbidge E. M., Burbidge G. R., Rubin V.C. 1964 ApJ., 140, p 942.

Clenshaw C. N. and Curtis A. R. 1960 Numerische Mathematik, 2, p 197.

Chandrasekhar S. 1959 Radiative Transfer, Dover.

Elvius A. 1972 Astron and Astrophys.

Freeman K. C. 1971 ApJ., 161, p 802.

Gentleman 1972 C. A. C. M., 15, p 353.

Geldzahler B. J., Kellerman K. I. Shaffer D. B. and Clark B. G. 1977 ApJ (Letters), 215, L5.

Goss W. M., Allen R. J. Ekers R. D. and De Bruyn A. G. 1973 Nature, Phys. Sci., 243, p 42.

Hargrave P. J. 1974 M. N. R. A. S., 168, p 491.

Heckathorn H. M. 1972 ApJ., 173, p 501.

Harper D. A. and Low F. J. 1973 ApJ (Letters), 182, L89.

Ilovaisky S. A. and Lequex J. 1972 Astron and Astrophys., 18, p 169.

Kleinmann D. E. and Low F. J. 1969 129 meeting of the AAS.

Kleinmann D. E. and Low F. J. 1970 ApJ., 161, L203.

Kronberg and Wilkinson 1975 ApJ., 200, p 403.

Lynds C. R. and Sandage A. 1963 ApJ., 137, p 1005.

Mathis J. S. 1975 ApJ., 583, p 41.

McCrea W.H. 1975 Tercentenary Symposium, Royal Greenwich Observatory, Bulletin No. 182.

Osmer P.S., Smith M.G. and Weedman D.W. 1974 ApJ., 189, p 187.

Peimbert E. and Spinnrad H. 1970 ApJ., 160, p 429.

Recillas-Cruz E. and Peimbert M. 1970 Bol Obs Tannizintala y Tacubaya No 35 p 247.

Reicke G.H. and Low F.J. 1972 ApJ (Letters), 176, L95.

Rosenberg I. 1970 M.N.R.A.S., 147, p 215.

Sandage A. 1971 Nuclei of Galaxies (New York: America Elsevier)

Sanders R.H. and Balamore D.S. 1971 ApJ., 166, p 7.

Solinger A.B. 1969 ApJ., 158, L21.

Solinger A.B. and Markert T. 1975 ApJ., 197, p 309.

Solinger A.B., Morrison P. and Markert T. 1977 ApJ., 211, p 707.

Sersic J.L. and Pastoriza M.G. 1965 Astrophys and Space Sci., 77, p 287.

Ven Den Bergh S. 1971 Astron and Astrophys., 12, p 474.

Volders and Hogbaum 1961 B.A.N., 15, p 307.

Weedman D.W. 1973 ApJ., 183, p 29.

Wolberg J.R. 1967 Prediction Analysis, Van Nostrand.

Viswananathan 1974 ApJ., 192, 319.

Reicke G. and Low F.J. 1975 ApJ., 197, p 17.

Angel, J.R.P. et al 1976 ApJ., 206, L5.

CONCLUDING REMARKS

In the second part of this thesis we have been concerned with the measurement of the spatial variations in the polarization of galaxies and other nebulae. The work has fallen into three categories: the development of the technique of electronographic polarimetry, the digital analysis of electronographic images and polarization measurements of the galaxy M82.

The major innovation of the Nebula polarimeter is its use of electronographic detection which combines the traditional advantage of photographic measurement, the simultaneous measurement of the polarization at many points, with the precision and linearity of photoelectric instruments.

We have investigated the performance of conventional analogue reduction methods and have shown convincingly that they are a serious source of error due to poor image registration. This almost certainly accounts for the notorious inaccuracy of photographic polarimetry. We have therefore been led to develop digital analysis methods which overcome this problem and enable us to take advantage of the full potential of the Nebula polarimeter.

Using this method, we have been able to handle large amounts of data on sensible time scales, remove sizeable image defects, subtract the emulsion and sky backgrounds. correct for saturation effects and reject suspect measurements. The most important advantages of the method are, however, that corrections for the sensitivity variations in the photocathode and the emulsion and for the different exposures of each plate, can be applied to the data. The image registration has been shown to be better than 0.2 increments, which is 2μ for the increment we have used, and this currently represents the state of the art in the subject. The method is, however, only in its early stages of development and considerable refinement is possible. We have discussed many of the obvious improvements in the text and will not reiterate them here, but there are a couple of points worth commenting on. At present the uncertainty in the grey-value of an individual pixel is $\sim$ 0.5% at full scale deflection, which is improved by a factor of 5(i.e. $\sqrt{n}$) when the seeing-disc cells are formed. A significant improvement would result immediately by sampling more frequently, with the same aperture size; for example, sampling every 1μ would give an accuracy of $\pm$ 0.004% at full scale. This could best be accomplished by modifying the PDS machine software to enable these smaller samples to be summed and dumped in 25μ bins, on-line. Secondly, defects on the films are an important problem and more care must be taken in their manufacture, and less handling before use would also be advantageous.

Obviously the method has other applications, and could be readily adapted for two-dimensional photometry. An important topic would be the study of the variations in the physical conditions, from emission line ratios, in active galaxies via narrow band electronographic photometry.

Turning our attention to the experimental work, a major part of this work has been devoted to testing and improving the instrument. The measurements reported here are the first obtained with the instrument and, as might be expected, with a new technique, problems have been experienced. Most of the observations were made with a chromatic half-wave plate, as the achromatic plate was still being manufactured, and the ensuing instrumental depolarization has involved us in a complicated series of corrections. A method of measuring the wavelength variations of its retardance has been evolved and laboratory measurements combined with a theoretical treatment of the problem used to determine the corrections.

A simple, but powerful, method of making calibration measurements at the telescope has been developed which is superior to the twilight sky method proposed by Penny (1976), and enables the photocathode sensitivity to be mapped. These maps enable the sensitivity changes to be taken into account during the sky subtraction. Unfortunately, this was not possible for our data because the photocathode was destroyed before it could be mapped, but it will have an important part to play in future work. The results of the laboratory calibration measurements and standard star observations are in reasonable agreement with the accepted values, after the application of the corrections.

The polarization measurements of M82 are the first astronomical observations made with the instrument. Previously little work of substance has been carried out in the field and these results therefore represent a major advance in the subject as they are the first complete polarization map of a galaxy at optical wavelengths. Despite the high noise levels in the faint regions of the map, caused by the large sky background at Herstmonceux, and the instrumental problems, the results are in surprisingly good agreement with previous observations, are of comparable accuracy and are 20 times more numerous.

Our attempts at interpretating the results have been somewhat limited mainly because the most crucial areas of interest are those in which the noise is important. The basic results have been that there is a marked difference between the disk of the galaxy where the polarization follows the luminosity structure and the dust lanes and the halo of the galaxy where a circular pattern predominates. We interpret the pattern in terms of dust scattering and have compared two models with the data, a point source nucleus, and the model of Solinger and Markert. Unfortunately the results are inconclusive. The distribution of the centres of symmetry from different areas of the map congregate in an extended core of diameter $\sim 120''$ and we suggest that the illumination is provided mainly by such a active central feature. We have discussed the structure of the central region of M82 and suggested that it is a "hot-spot", containing many young stars whose formation has been triggered by supernovae explosions and who thermally power the galaxy in a manner very similar to the way Adams and Weedman propose to power class 2 Seyferts. The many observational similarities between the two types of galaxy has led us to speculate that irr II galaxies are an intermediate stage between Seyferts, and active spirals, and normal galaxies.

Preliminary observations with an achromatic half-wave plate show a considerable improvement over those obtained with the chromatic plate and have a precision comparable to photoelectric stellar polarimeter. At the time of writing observation of M82 with the improvedoptics have now been made (Bingham, McMullan, Pallister, White, Axon and Scarrott 1976, Nature 259 page 443) and confirm the results obtained here but show the expected enhanced signal to noise. A similar map has recently been published by Angels, Schmidtt and Cromwell (1976 ApJ, 206, p888) and was obtained using the technique developed by Woltjer for his now classic work on the Crab nebula. Since they do not publish their data we have been unable to make a detailed comparison with our results, but their technique perhaps helps to put this work and its apparent inadequacies in perspective, for even the application of correction for cathode sensitivity variations are neglected, let alone the many other problems tackled in the work.

To sum up, the future of the instrument is extremely bright, significant contributions to our knowledge of the polarization structure in galaxies and nebulae can be expected and fundamental advances in understanding of origin of the polarization will almost certainly follow. The instrument can be used in UBVR and the wavelength dependence of the polarization can therefore be studied. The use of interference filters or perhaps a diffraction grating will enable narrow wavelength ranges to be studied, leading to the possibility of investigating the polarization of emission lines in galaxies with all the intriguing possibilities that unfolds.

APPENDIX I : THEORY OF THE MEASUREMENT OF THE WAVE-PLATE RETARDANCE

Suppose we have linearly polarized light incident on a retarder at an angle θ relative to the fast axis of the plate. Let X and Y be the 'fast' and 'slow' components of the light vector along the OX and OY directions respectively. The amplitudes of these components are given by $A = C \cos \theta$ and $B = C \sin \theta$ respectively (C will be taken as unity), and the components are

$$X = A \sin \omega t \qquad Y = B \sin \omega t \tag{A.1}$$

On emerging from the retarding plate these components are then

$$X = A \sin \omega t \qquad Y = B \sin (\omega t - \delta) \tag{A.2}$$

Eliminating t yields

$$\frac{X^2}{A^2} + \frac{Y^2}{B^2} - \frac{2XY \cos \delta}{AB} = \sin^2 \delta \tag{A.3}$$

This equation represents the vibration pattern of the vector whose components are X and Y, and is in general an ellipse in the XY plane which is inscribed in a rectangle whose sides are of length 2A and 2B respectively. The shape of the ellipse is given by the ellipticity e which is the ratio of the major and minor axes $e = b/a$. The position of the ellipse is given by the azimuthal angle ϕ between the ellipse major axis and the retarder fast axis (Figure A.1).
Now suppose that the amplitudes of the components in the major and minor axis directions are measured (X'Y' directions). The equation of the waveform is then

$$\frac{x'^2}{a^2} + \frac{y'^2}{b^2} = 1 \tag{A.4}$$

By applying a single coordinate rotation the amplitudes A and B can be related to a and b and ϕ can be related to θ and δ

$$x' = x \cos \phi + y \sin \phi \qquad y' = -x \sin \phi + y \cos \phi \tag{A.5}$$

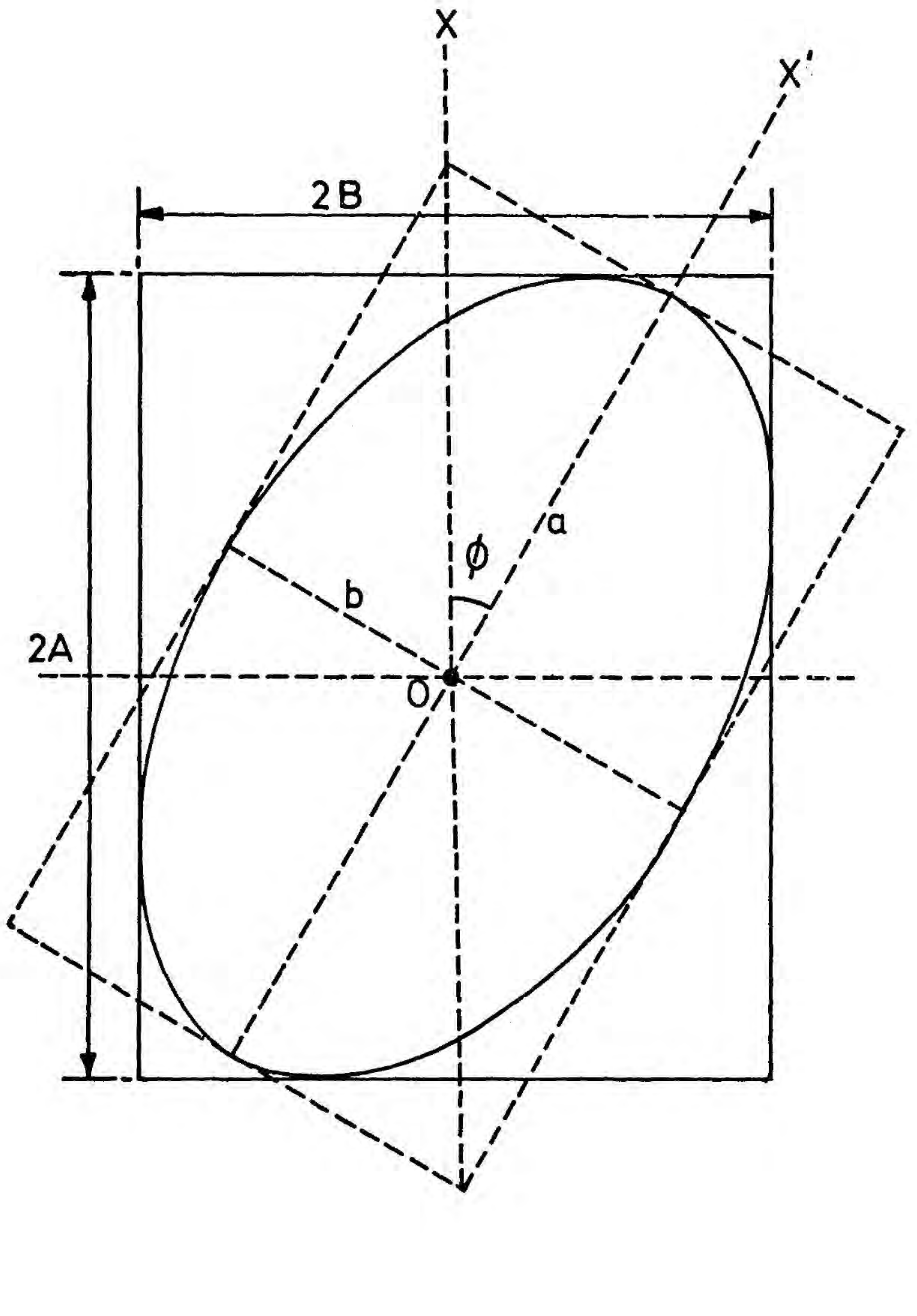

Figure A.1 *The relationship between the parameters specifying the form and azimuthal angle of the outgoing waveform.*

Substituting A.5 in A.4 and comparing coefficients with A.3 yields

$$\frac{\cos^2 \phi}{a^2} + \frac{\sin^2 \phi}{b^2} = \frac{1}{A^2 \sin^2 \delta} \qquad (A.6)$$

$$\frac{\sin^2 \phi}{a^2} + \frac{\cos^2 \phi}{b^2} = \frac{1}{B^2 \sin^2 \delta} \qquad (A.7)$$

$$\sin 2\phi \left(\frac{1}{b^2} - \frac{1}{a^2}\right) = \frac{2 \cos \delta}{AB \sin^2 \delta} \qquad (A.8)$$

Subtracting A.6 and A.7 and dividing by A.8 gives

$$\tan 2\phi = \frac{2AB \cos \delta}{A^2 - B^2} \qquad (A.9)$$

or

$$\tan 2\phi = \tan 2\theta \cos \delta \qquad (A.10)$$

When θ is $\pm 45^\circ$ then ϕ will always be $\pm 45^\circ$ unless δ is $\pm\frac{\pi}{2}$ when the light is circularly polarized and ϕ is indeterminate.

Further manipulation of equations A.6 - A.8 yields

$$\frac{b^2}{a^2} = \frac{\varepsilon - \cos \delta}{\varepsilon + \cos \delta} \qquad (A.11)$$

where $\varepsilon = \sin 2\phi / \sin 2\theta$

which, when $\theta = 45^\circ$ implying $\phi = 45^\circ$ is reduced to

$$\frac{I_{min}}{I_{max}} = \frac{1 - \cos \delta}{1 + \cos \delta} \qquad (A.12)$$

where $b^2 = I_{min}$ and $a^2 = I_{max}$, the measured minimum and maximum intensities respectively.

APPENDIX II : THE SOLINGER AND MARKERT (1976) MODEL

In this model due to Solinger and Markert (1976), the scattering is assumed to occur in the plane of the sky passing through the galactic centre. The illumination is provided by a point source nucleus embedded in a circular disk whose surface brightness falls off as $\exp(-r_D''/62'')$ where r_D is the distance from the nucleus in the plane of the disk. The scattering matrix (Chapter 7) can be evaluated provided the scattering angle, Θ, and the rotation angle between the reference direction and the scattering plane, ψ, can be calculated. Both Θ and ψ are determined from the geometry of the model which is shown in figure B.1.

The Stokes' Parameters from the Disk

The angles Θ and ψ arising from scattering at a point Z above the galactic disk at a distance Y from the minor axis of light from a disk element da located at (r_D,ϕ) are given by

$$\cos^2\Theta = r_D^2\cos^2\phi/R^2 \qquad \text{(B.1)}$$

$$\cos^2\psi = (r_D\sin\phi - Y)^2/(R^2 - r_D^2\cos^2\phi) \qquad \text{(B.2)}$$

where

$$R^2 = Y^2 + Z^2 + r_D^2 - 2r_D Y\sin\phi \qquad \text{(B.3)}$$

R is the distance from the disk element $da = r_D dr_d d\phi$ to the point (Y,Z), and r_D is the distance from the nucleus to da.

The differential incident flux dI_o at (Y,Z) due to the light from da with a surface brightness $\Sigma(r_D)$ is

$$dI_o = \frac{\Sigma(r_D)da}{4\pi R^2} = \frac{\Sigma_o\exp(-r_D/62)da}{4\pi R^2} \qquad \text{(B.4)}$$

The surface brightness is normalized so that $\int \Sigma da = L_D$ where L_D is the disk luminosity which gives, taking the limit of integration to be 310" arc,

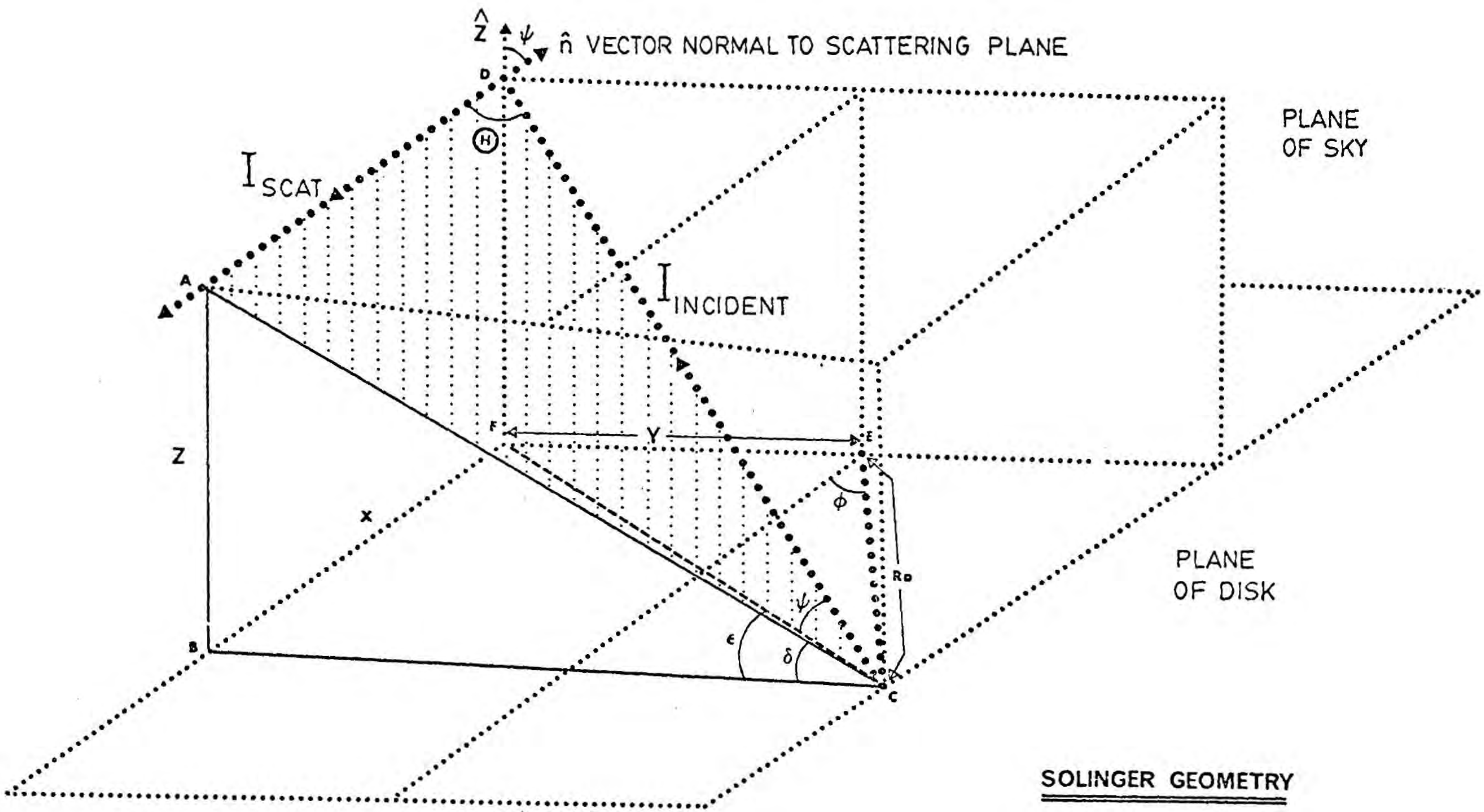

Figure B.1 *Solinger Geometry*

$$dI_o = \frac{2L_D(62)^2 \exp(-r''_D/62'')}{(4\pi)^2 R^2(1-6e^{-5})} da \tag{B.5}$$

Evaluating the scattering matrix the Stokes' parameters from the disk Q_D and U_D are

$$Q_D = L_D\sigma q_d = \frac{3\sigma\Sigma_o}{16\pi}\int_0^{310}\int_0^{2\pi} da \exp(-r_D/62)\{Z^2-(Y-r_D\sin\phi)^2\}/R^4$$

and (B.6)

$$U_D = L_D\sigma U_D = \frac{3\sigma\Sigma_o}{16\pi}\int_0^{310}\int_0^{2\pi} da \exp(-r_D/62)(Y-r_D\sin\phi)Z/R^4$$

In these equations σ is the total effective cross section of scatterers at (Y,Z).

<u>The Stokes' Parameters from the Nucleus</u>

Since the scattering occurs in the plane of the sky passing through the nucleus the scattering angle Θ for nuclear light is 90^o. Referring to figure B.1 again we have

$$\sin^2\psi = \frac{Z^2}{D^2} \tag{B.7}$$

$$\cos^2\psi = \frac{Y^2}{D^2} \tag{B.8}$$

and $$\sin 2\psi = \frac{2YZ}{D^2} \tag{B.9}$$

where $D^2 = Z^2 + Y^2$.

The differential incident flux dI_o is

$$dI_o = \frac{L_N}{4\pi} \tag{B.10}$$

where L_N is the nuclear luminosity, and the Stokes' parameters Q_N, U_N

due to scattering of nuclear light follow immediately as

$$Q_N = \frac{3}{4} \frac{Z^2 - Y^2}{D^2} \frac{L_N \sigma}{4\pi}$$

$$U_N = \frac{3}{4} \frac{2YZ}{D^2} \frac{L_N \sigma}{4\pi} \tag{B.11}$$

The extension of Solinger and Markert's model to a more realistic line of sight scattering model is straightforward. Again, the calculation of the Stokes' parameters from a bright nucleus embedded in a thin galactic disk simply requires us to evaluate the scattering equation. This follows directly from the scattering geometry shown in figure C.1.

The Disk Stokes' Parameters

We now introduce the distance X from the nucleus along the line of sight. R, the distance from the point of scatter to the point in the disk providing the illumination, becomes

$$R^2 = (Y + r_D \sin\phi)^2 + (r_D \cos\phi - X)^2 + Z^2 \qquad \text{(C.1)}$$

with the same notation as before.

The terms in the scattering matrix are

$$\sin^2\Theta = \frac{AC^2}{R^2} = \frac{(Z^2 + \{Y + r_D \sin\phi\}^2)}{R^2} \qquad \text{(C.2)}$$

$$\cos^2\Theta = (r_D \cos\phi - X)^2/R^2 \qquad \text{(C.3)}$$

$$\sin 2\psi = \frac{2Z}{R^2} \sqrt{R^2 - Z^2} \qquad \text{(C.4)}$$

The Stokes' parameters Q_D and U_D are then calculated as in Appendix II with an additional X integral between ± the radius of the disk i.e. ±310".

$$Q_D = L_D \sigma q_D = \frac{3}{4} \frac{\sigma\Sigma_o}{4\pi} \int_{-310}^{+310} dX \int_0^{2\pi}\int_0^{310} da \exp(-r_D/62) \left\{ \frac{(R^2-2Z^2)(\{r_D\cos\phi-X\}^2-R^2)}{R^4} \right\}$$

(C.5)

$$U_D = L_D \sigma u_D = \frac{3}{4} \frac{\sigma\Sigma_o}{4\pi} \int_{-310}^{+310} dX \int_0^{2\pi}\int_0^{310} da \exp(-r_D/62) \left\{ Z^2+(Y+r_D\sin\phi)^2 \right\} \left\{ \frac{2Z\sqrt{R^2-Z^2}}{R^4} \right\}$$

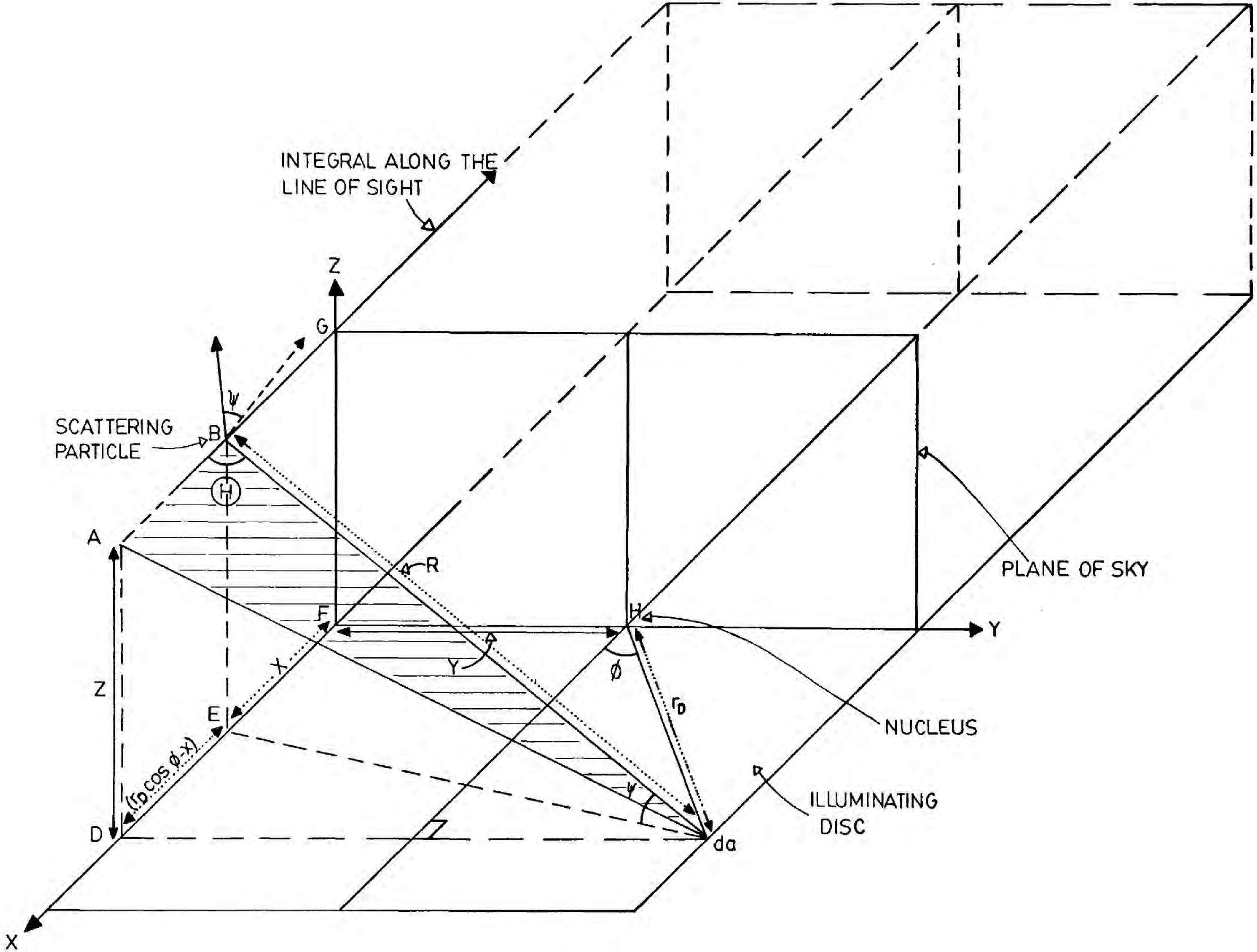

FIG. C1 LINE OF SIGHT INTEGRATION GEOMETRY

The Nuclear Stokes' Parameters

These also require an integration along the line of sight with the angles Θ and ψ being given by

$$\sin^2\Theta = \frac{Z^2 + Y^2}{R^2} \tag{C.6}$$

$$\cos^2\Theta = \frac{X^2}{R^2} \tag{C.7}$$

$$\sin 2\psi = \frac{2Z}{R^2}\sqrt{X^2 + Y^2} \tag{C.8}$$

where $R^2 = Y^2 + Z^2 + X^2$ (C.9)

Hence Q_N and U_N are

$$Q_N = \frac{3}{4}\frac{L_N\sigma}{4\pi}\int_{-310}^{+310}\frac{1}{R^4}(X^2 - R^2)(R^2 - 2Z^2)\,dX$$

(C.10)

$$U_N = \frac{3}{4}\frac{L_N\sigma}{4\pi}\int_{-310}^{+310}\frac{2Z(Z^2 + Y^2)\sqrt{X^2 + Y^2}}{R^4}\,dX$$

ACKNOWLEDGEMENTS

I wish to express my gratitude to my supervisor, Dr S. M. Scarrott, for his academic and moral guidance throughout my years as an undergraduate and research student at Durham.

Professor Arnold Wolfendale FRS first suggested the problem of the structure of the galactic magnetic field to me and I have had many useful discussions with him on the subject. I would also like to thank him, in his capacity as Chairman of the Physics Department, for allowing me to use its facilities.

Dr Richard Ellis has been both a stimulating collaborator during the work on the local magnetic field and a friend whose advise has been of great value. His many critical comments, together with those of Dr Keith Taylor of the RGO, have helped me considerably in writing this thesis. I am especially grateful to Dr Richard Bingham of the RGO for teaching me to become a skilled observer and for many useful discussions.

I am indebted to successive Directors of the RGO, Professor E. M. Burbidge FRS, Dr A. Hunter and Professor F. G. Smith FRS, for allowing me to use the 36" telescope and the PDS microdensitometer. Here a special mention should be given to Dr John Pilkington for his tireless assistance with the digitization of the electronographs. I am extremely grateful to Dr Dennis McMullan for allowing me to use his superb electronographic camera, to Dr Ralph Powell for initiating me in its use, and to Dave Bonnick and Bill Matthews for their excellent technical support.

Many useful discussions on the statistical aspects of my work have been held with Dr Peter Kiraly. Dr J. L. Osborne is thanked for useful discussions on the irregular structure of the galactic magnetic field.

A great deal of expert help with programme errors has been rendered by Dr Ian Bell and Mr Alan Lotts of the High Energy Physics Group.

The friendly assistance of the operations staff of the Computer Services Department at Durham: Brian Lander, Malcolm Alexander, Colin Iley, Harry Baker, Ian Rosethorne, Miss Gerry Brittain, Miss Angela West and Miss Mary Crosby, made the digital analysis possible.

It is a pleasure to acknowledge the fine craftsmanship of the technicians of the Physics Department workshops who built the nebula polarimeter. In this context I would especially like to thank Phil Armstrong and Alan Coulson. I would also like to thank Dennis Jobling for allowing me to use the student workshops and David Jobling for preventing me chopping off my fingers whilst there.

I am exceedingly grateful to Professor Leon Mestel FRS for allowing me to write my thesis while a Research Fellow at the Astronomy Centre, University of Sussex.

The research work was carried out with the financial support of the Science Research Council, who provided me with a 3-year studentship and a 4-month extension.

My terrible handwriting has been turned into an immaculately typed thesis by Jean Hafner, Marie Tait and Hazel Freeman, who is also thanked for much encouragement. The beautiful illustrations are the work of Angela Elliott and Audrey Gregory.

I would like to thank Kathy Whaler for her meticulous proof reading of the thesis and her continuous encouragement and patience while I wrote it.

The warmest thanks go to my parents, without whose support, generosity and encouragement none of this would have been possible.

Throughout my years as a research student, many people have helped me and I would like to have mentioned them all, but the space available is small and with the passage of time many of the names have been forgotten. I hope that I have mentioned all those whose help has been vital in my work and if I have forgotten someone I hope they are not offended as their help is deeply appreciated.

David Axon *August 1977*